transactions of the ASME

Published Quarterly by
The American Society of
Mechanical Engineers
Volume 93 • Series C • Number 1
FEBRUARY 1971

journal of heat transfer

EDITORIAL OFFICES are at ASME Headquarters, United Engineering Center, 345 East 47th Street, New York, N. Y. 10017. Cable address, "Mechaneer," New York.
PUBLISHED QUARTERLY at 20th and Northampton Streets, Easton, Pa. 18042. Second-class postage paid at Easton.
CHANGES OF ADDRESS must be received at Society headquarters seven weeks before they are to be effective. Please send old label and new address.
PRICES: to members, $3.00 a copy, $10.00 annually; to nonmembers, $6.00 a copy, $20.00 annually.
Add 75 cents for postage to countries outside the U. S. and Canada.
STATEMENT from By-Laws. The Society shall not be responsible for statements or opinions advanced in papers or . . . printed in its publications (B13, Par. 4).

INDEXED by the Engineering Index, Inc.

J. BRENT TURNER
Atlantic Richfield Company,
Richardson, Texas

C. PHILLIP COLVER
Director and Associate Professor,
School of Chemical Engineering and
Materials Science,
University of Oklahoma,
Norman, Okla.

Heat Transfer to Pool-Boiling Mercury From Horizontal Cylindrical Heaters at Heat Fluxes up to Burnout

Reproducible and consistent data were obtained for heat transfer to pool-boiling mercury from horizontal, 304 stainless steel, cylindrical heaters at heat fluxes up to 1,100,000 Btu/hr· ft². One actual burnout determination was made during the course of the study. In other runs, a heat-flux level was reached where the slope of the boiling curve decreased significantly so that subsequent increases in heat flux were accompanied by large increases in ΔT. This heat-flux level was termed the "departure heat flux." Observed maximum departure heat fluxes ranged from 400,000 Btu/hr·ft² for a 2-in. pool depth above the heater to 950,000 Btu/hr·ft² for an 8.5-in. depth. The burnout correlations of Noyes [17, 22][1] and Addoms [1] satisfactorily predicted the maximum departure heat fluxes for each pool depth studied.

Introduction

Most previous pure mercury-boiling studies have encountered problems of wettability between the liquid and the heat-transfer surface with the resultant lack of consistent behavior, particularly in the nucleate boiling regime. Consequently, in an attempt to obtain better wetting characteristics investigators have either altered the heat-transfer surface or introduced additives to the mercury test liquid. For example, Bonilla, et al. [5] found that parallel scratches spaced about two bubble diameters apart on the boiling surface increased the heat-transfer coefficient considerably for boiling mercury. Others [4, 8, 14, 18, 19] on adding trace amounts of magnesium and titanium hydride have enhanced mercury wettability. In one case [4] prolonged aging of the boiling surface also appeared to enhance surface wetting.

In such cases where wetting was obtained for pure pool-boiling mercury [4, 23], data have been reported up to maximum heat-flux levels of about 125,000 Btu/hr·ft². Even where additives have been used, reported heat-flux levels for pool boiling have not exceeded 200,000 Btu/hr·ft². In a thermal-syphon mercury-boiling loop, Romie, et al. [25] operated an electrically heated, copper-plated tube with heat fluxes reported up to 600,000 Btu/hr·ft² with no apparent indication of reaching burnout. However, their calculated heat flux was an upper limit since significant electrical power was dissipated in liquid mercury flowing through the test section. It should be further noted that the test section was located about 4 ft below the condenser in one leg of the U-loop.

In the present work it was desired to study the effects of pressure, liquid depth, and different heaters on the pool-boiling characteristics of mercury. It was further hoped to achieve a wetted surface condition without resorting to additives. Where conditions premitted, it was hoped to extend the experimental boiling curves to heat fluxes up to and including burnout.

Apparatus

The experimental apparatus, shown schematically in Fig. 1, was comprised of the insulated boiling vessel, bayonet test heater, condenser, knockout drum, charge vessel, manifold system, power supply, and instrumentation. All vessels containing mercury were fully contained in a vented enclosure. Since the entire experimental apparatus has been completely described elsewhere [26], only the most important components will be detailed here.

Boiling Vessel and Associated Components. The boiling vessel was fabricated from an 8-in. length of 316 stainless steel seamless pipe (5.76-in. ID by 6.625-in. OD) and two 6-in. schedule 80S stainless welding caps. Fig. 2 gives details and dimensions of the vessel. Note that thermowells in the boiling vessel were staggered from side to side so temperature measurements could be made at 1-in. depth intervals in the boiling liquid. Chromel–alumel thermocouples (28 gauge) were used for all thermowell temperature measurements. Holes for the three auxiliary heaters

[1] Numbers in brackets designate References at end of paper.

Contributed by the Heat Transfer Division for publication (without presentation) in the Journal of Heat Transfer. Manuscript received by the Heat Transfer Division, May 21, 1970. Paper No. 70-HT-R.

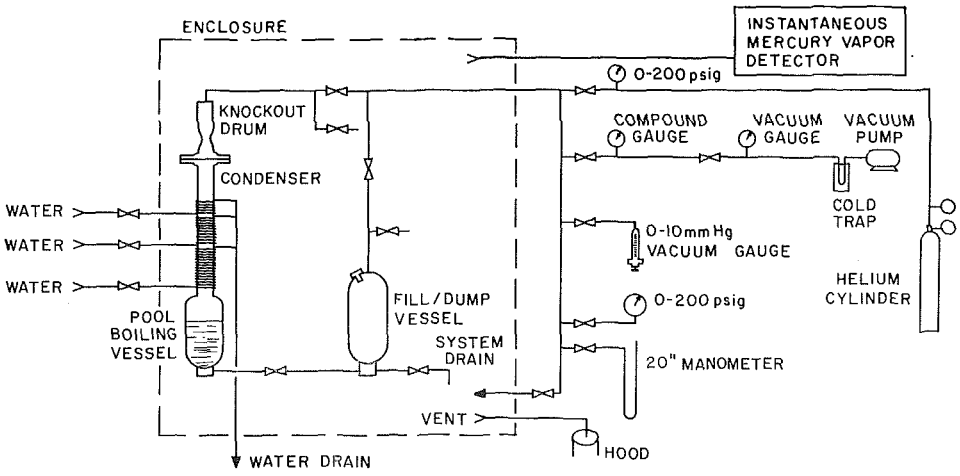

Fig. 1 Schematic diagram of experimental apparatus

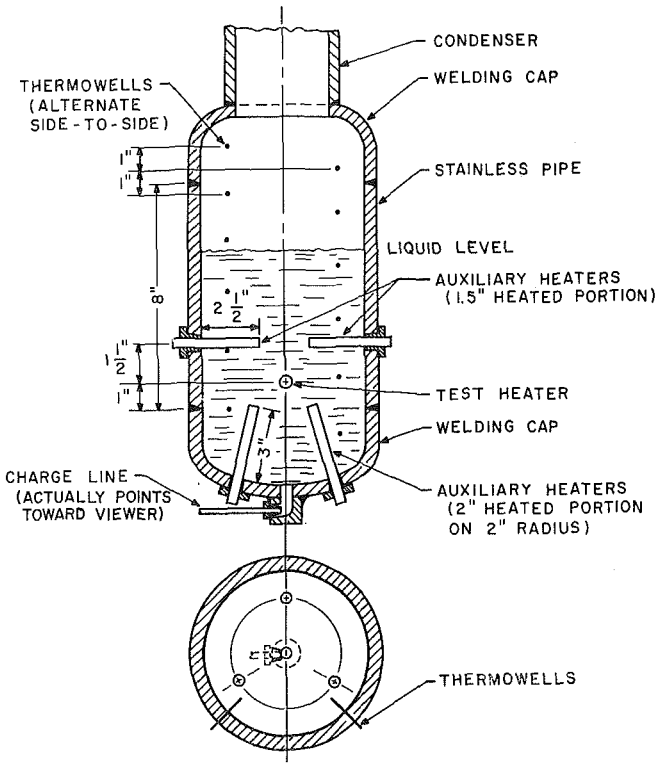

Fig. 2 Boiling vessel

entering through the bottom welding cap were drilled on a 2-in. radius and spaced at 120-deg intervals. The other two auxiliary heaters entered the vessel on opposite sides, 5 in. from the bottom of the vessel. Auxiliary heating required to maintain the pool at saturation temperature was supplied by 5 Watlow firerods with a combined capacity of 1800 watts.

The condenser was constructed from a 30-in. length of 316SS seamless pipe (3.35-in. ID by 4.0-in. OD), with five thermowells spaced at 5-in. intervals along its length. An iron pipe was split in half longitudinally, tinned inside with soft solder, clamped around the stainless condenser pipe and spot-welded to hold securely. This was done to lessen chances of damaging the stainless steel by thermal stresses and to give a surface to which cooling coils were more easily soldered. Three sets of cooling coils (with 5, 10, and 15 turns respectively) were soldered to the condenser.

One end of the condenser was then welded to the boiling vessel and the other end to a 3.5-in. schedule 40S flange. An O-ring groove was machined in the flange to accommodate a Viton rubber O-ring which could withstand temperatures up to 600 deg F. This flange served as the connection between the condenser and the knockout drum, which consisted of an 8-in. length of 316 SS pipe (4-in. ID by 4.5-in. OD) containing stainless steel gauze. The gauze was to facilitate condensation of any vapor that migrated past the condenser.

A charge vessel was formed from a 12-in. length of 6-in. stainless pipe with welding caps making up the ends. A THY-442 Hoke bellows valve was installed in the fill line between the charge vessel and the boiling vessel. The Hoke bellows valve, with a maximum operating pressure of 600 psia at a temperature of 1200 deg F, had a 316 stainless body and a 347 stainless bellows seal welded to the body, permitting all wetted parts of the valve to be metal. A flexible shaft leading to the bellows valve with a rotating seal through the enclosure wall allowed remote operation of the valve when the enclosure door was in place.

The system was equipped to obtain data over the pressure range from about 1 mm mercury to 200 psig. This required the use of vacuum pumps for subatmospheric pressures and a helium cylinder to provide inert cover gas pressures above atmospheric. The vacuum pumps and helium cylinder were connected to the system through the manifold arrangement shown in Fig. 1. Proper use of the valves allowed the system, or any part thereof, to be adjusted to the desired pressure level. For pressure runs (above the capability of the mercury manometer) a calibrated 10-in-dia 0–200 psig Marsh gauge was used. A mercury manometer was used for subatmospheric runs from 1 in. mercury to atmospheric pressure. For 0–10 torr pressures, a Gilmont cartesian-diver vacuum gauge was used.

Test Heater. The bayonet heater has shown itself to be quite versatile and capable of producing the high flux levels required in liquid metal boiling studies [7, 22]. However, thermocouple placement in such heaters has presented considerable difficulty. In both the studies of Noyes [22] and Colver and Balzhiser [7], thermowells or sheathed thermocouples were brazed into longitudinal grooves cut in the external surface of the heater. In both instances, extensive erosion and/or melting of the brazing material occurred during operation (especially during burnout determinations). Noyes suggested that in his work, "premature burnout may have been in some way caused by the thermocouple grooves and/or the associated brazing alloy." In at least one case, a heater used by Colver failed by splitting lengthwise along a thermocouple groove. Colver also encountered some difficulty in accurately extrapolating measured temperatures to the heater surface. Since the thermal conductivity of the braze material

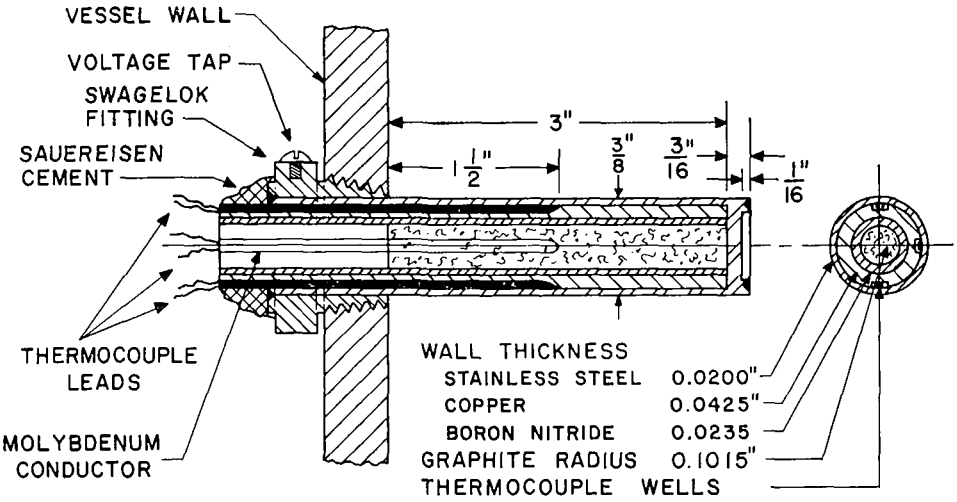

Fig. 3 Cross section of test heater

surrounding the heater thermocouples was not precisely known, certain approximations were necessary.

Though the present design is similar in many aspects, the thermocouple installation represents considerable improvement from the brazing method used by Noyes and Colver. The composite heater consisted of a 304 stainless sheath, a grooved cylinder of tinned copper for thermocouple placement, a machined boron nitride tube, and a graphite-rod heating element. A detailed view of the assembled test section is shown in Fig. 3. The use of a Swagelok male connector (No. 600-1-8-316) allowed easy interchange of heaters.

The outside surface of the copper tube was tinned with solder and all excess solder was wiped away leaving a smooth shiny surface. The thermocouple grooves (0.050 in. wide by 0.025 in. deep) were then milled longitudinally in the copper surface at 90-deg intervals. The grooves extended to the midpoint of the heater, except for two heaters which were equipped with one or two grooves extending to the midpoint as before, but the other two extended to within 1/4 in. of each end. The placement of thermocouples near the ends of the heater allowed a determination of any longitudinal temperature variations. Insulated 30 gauge chromel-alumel thermocouple wire was used for internal heater temperature measurements. After assembly of each heater, with thermocouples in place, Sauereisen cement was used to cover the exposed copper and to affix the thermocouple leads in place, avoiding undue flexing or breakage.

Heater Surface Treatment. The surfaces of test heaters used in the preliminary water work were finished in a lathe with 400C grit silicon carbide paper. Test heater 1 (used in the first mercury runs) was further smoothed with 600 grit paper. A final finish was obtained by hand rubbing the surface with crocus cloth. Previous studies [2, 14] have shown that mercury does not readily wet stainless steel; consequently this surface was silvered by the technique described by Watt, et al. [27]. Test heater 2 was electroplated with silver, since it was felt a wetting condition could possibly be achieved by plating with a material which was completely wetted by mercury.

Power Supply and Instrumentation. A 20-kva Udylite rectifier supplied d-c power to the test heater. A stepless variable transformer controlled the output from 0–1000 amp at 0–20 v with no more than 5 percent ripple. A 50-mv, 800-amp shunt was used along with a calibrated Simpson multirange d-c millivoltmeter to measure heater amperage. Test heater voltages were measured with a calibrated Simpson multirange d-c voltmeter and a Sanborn recorder. Though the recorder readings did not yield the accuracy afforded by the meter, the continuous voltage trace along with simultaneous thermocouple traces gave an easily discernible record of each power increase and resultant temperature increase.

To protect against failure of test heaters, a controlling pyrometer and control module by Assembly Products automatically cut off the rectifier when temperatures in the heater exceeded a set-point value. Two 11-position Leeds and Northrup thermocouple switches were used to obtain selective readings from the various thermocouples. For added convenience a 3-way, double-pole switch was employed so that signals from each thermocouple switch could be relayed to a Hewlett-Packard digital voltmeter without changing leads. For monitoring pool and vapor temperatures, a Leeds and Northrup Speedomax W 12-point recorder was connected to the top 4 thermocouples in the pool and 8 others located in the vapor space above the boiling pool. The three test heater thermocouples were connected, respectively, to the controlling pyrometer setup, a fast-response oscillographic recorder, and a standard strip-chart recorder. The fast-response, variable-range oscillographic recorder gave this equipment excellent capability for recording rapid temperature fluctuations.

Experimental

Preliminary Preparation. All instrumentation was checked for operability and calibrated where possible before incorporating it into the experimental system. Each component of the apparatus making contact with the test liquid or vapor was thoroughly cleaned with dichloroethylene prior to installation, to remove any oil or grease films present. After installation, the entire system was vacuum-checked for leaks. In addition, the system was pressured to 200 psig and found to hold nicely at this level.

To refine the operating procedure and acquaint the operator with the system, 16 experimental runs were made with de-ionized distilled water. Though no subatmospheric runs were made with water, nucleate boiling runs were made at pressures up to 200 psig and heat fluxes up to 790,000 Btu/hr-ft^2. The test water was dumped from the system and replaced with fresh water 5 times during the 16 runs, so that dissolved impurities would be flushed from the system.

To prepare the system for charging mercury, the water was dumped from the system and the test vessel heated to about 500 deg F while the vacuum pumps continued evacuating the system. Condensed moisture collected and froze in the liquid nitrogen cold trap and had to be removed twice when the trap became clogged with ice. After a few hours, no further collection

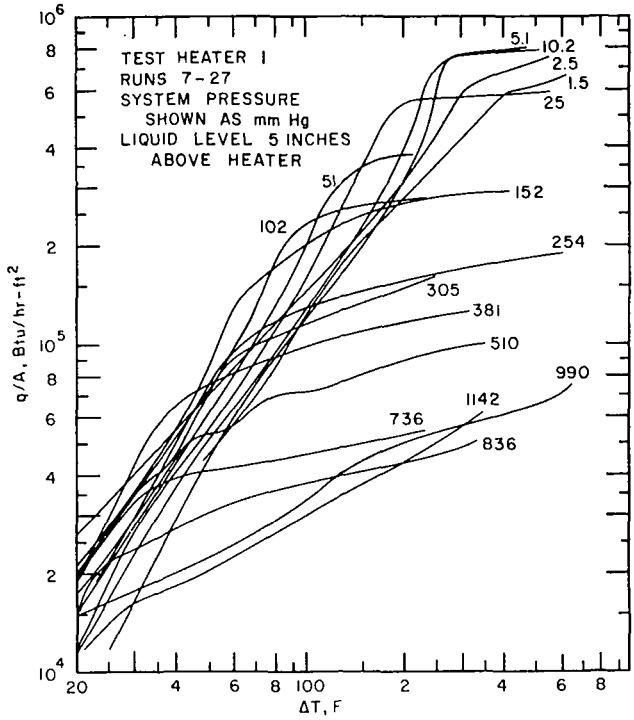

Fig. 4 *Mercury results for a 5-in. liquid depth above test heater 1*

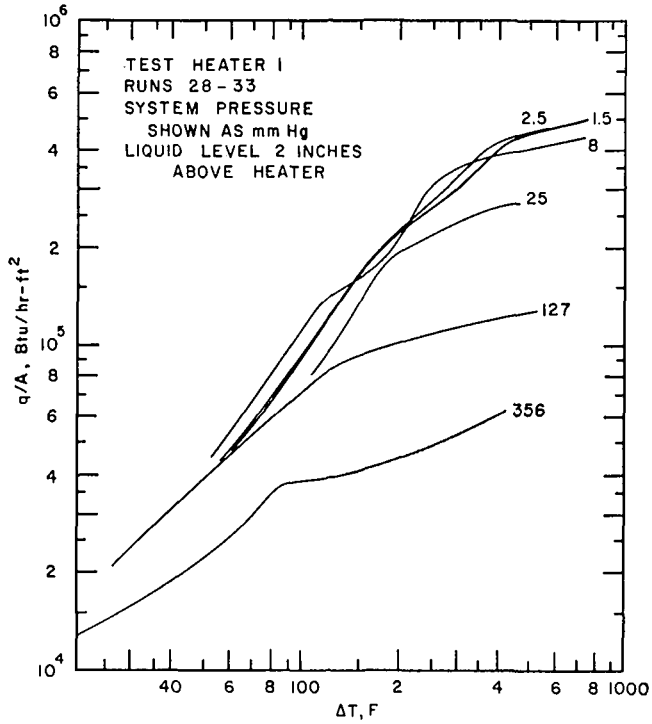

Fig. 5 *Mercury results for a 2-in. liquid depth above test heater 1*

of water occurred and the system was allowed to cool after being filled with helium to maintain a slight positive pressure.

Each time the system had been filled with water, a 1-gal quantity was sufficient to give a 10-in. liquid level in the boiling vessel. Since the test heater location was at the 3.5-in. level and the upper auxiliary heaters at the 5-in. level, 100 lb of mercury (0.887 gal) was charged to the system through the charge vessel, giving a maximum liquid level of 8.5 in. After filling, the charged vessel was evacuated and repressurized with helium.

Mercury was transferred to the boiling vessel by evacuating it and opening the transfer valve. Reverse transfer from the boiling vessel to the charge vessel was likewise accomplished by evacuating the charge vessel and opening the transfer valve. This procedure was required only when it was desired to change heaters or change the liquid level. The mercury remained in the boiling vessel between runs except when one of the above changes was made.

Experimental Procedure. To begin a run, the auxiliary heaters were turned on and set at about 670 w total input to the pool. At this setting, the heat-flux level in each heater was 19,000 Btu/hr·ft². As the pool temperature approached saturation, power to the auxiliary heaters was decreased to a heat flux slightly above 10,000 Btu/hr·ft².

During heat-up, system pressure was always initially set above the operating pressure to allow the pool temperature to exceed the desired saturation value. The pressure was then dropped to the desired level with the resulting boil-off assuring saturated conditions. At this point, the liquid level was determined by taking thermocouple readings along the entire depth of the boiling vessel and condenser.

Once all preliminary thermocouple readings were made, the system pressure was again checked (and adjusted if needed, as it was after each power increase) before turning on the rectifier. Power to the test heater was increased incrementally with the following information being recorded: test heater voltage, amperage, heater thermocouple readings, and liquid thermocouple readings. At low heat fluxes, very short times were required for the system to reach steady state after a power increase; at high levels, longer times were required as shown by the continuous heater thermocouple traces. In each case, sufficient time for steady state was allowed before taking the above readings. At intermediate heat fluxes, the pool temperature was again recorded along its entire depth.

Initially, small induced voltages were observed in the heater thermocouple signals. These induced voltages were observed and measured by the method described by Davenport, et al. [9] and later used by Mednick and Colver [21]. With the fast-response oscillographic recorder monitoring thermocouple output, the rectifier was quickly turned off and on. Induced voltage could then be read directly as the amplitude difference between the "off" and "on" thermocouple output. After a few runs, no induced voltage was observed. This was taken to mean that the free end of the heater achieved good electrical contact with the mercury pool so that the pool carried a major portion of the current. Comparing the overall voltage drop and heater voltages observed in both the water and mercury studies, it was concluded that negligible power dissipation occurred in the mercury pool.

To obtain maximum information from each run, and to detect any aging of the surface during high heat-flux operation, the power level was adjusted stepwise upward until it was felt that burnout was imminent or until the temperature exceeded the pyrometer set-point, which automatically turned off the rectifier. The power was then adjusted stepwise downward with pertinent information being recorded at each setting. In case of pyrometer cut-off, the rectifier powerstat was turned down slightly and the rectifier reactivated to accomplish the downward cycle.

With the peculiar behavior observed for boiling mercury, a clearly defined burnout point was only observed once; however, a change in nucleate boiling behavior was easily detectable in the test heater thermocouple traces. Though only constant-pressure boiling curve determinations were made for mercury, the "decreasing pressure" method of burnout determination used by Noyes [22] and Colver and Balzhiser [7] was employed successfully to obtain 5 burnout values for water at various pressures. In addition, 15 burnout determinations were made for water at 6 different pressures using the increasing heat-flux approach.

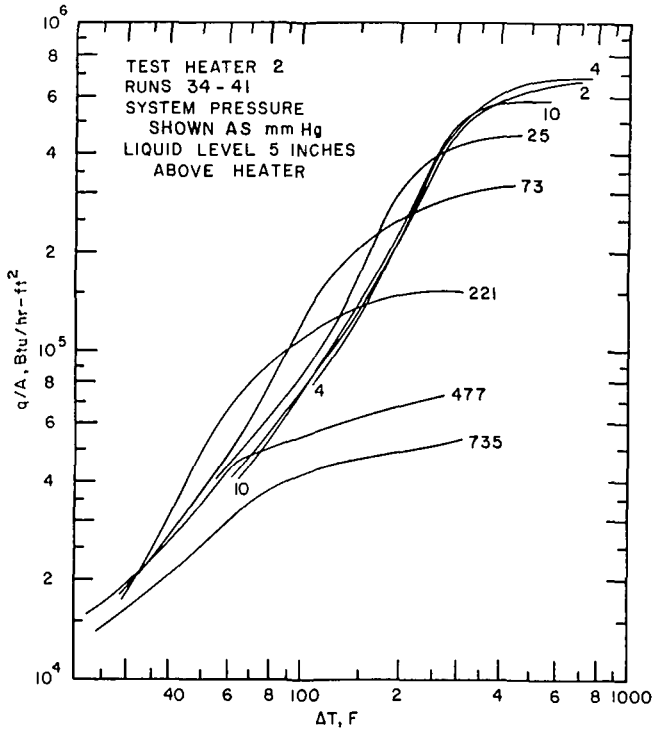

Fig. 6 Mercury results for a 5-in. liquid depth above test heater 2

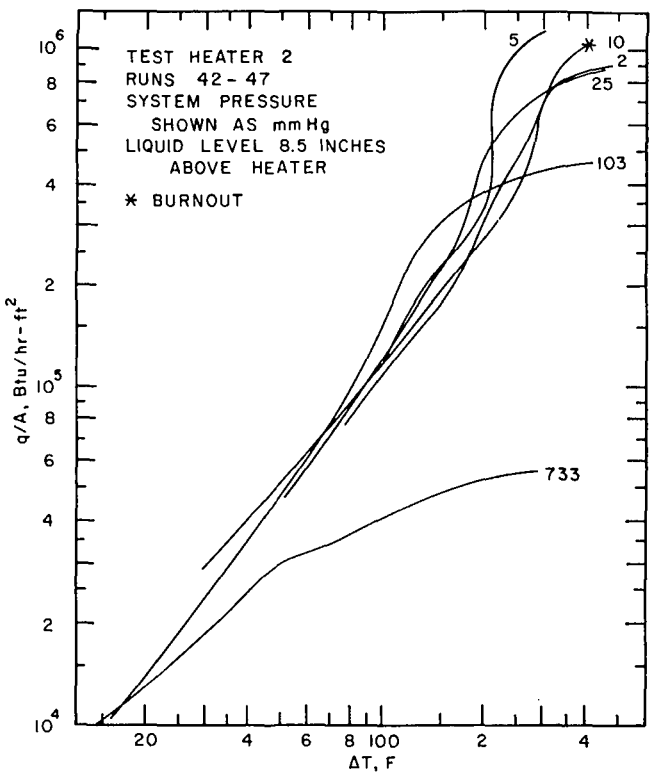

Fig. 7 Mercury results for an 8.5-in. liquid depth above test heater 2

Results and Discussion

Water Experiments. A preliminary study using water was performed to improve and finalize the test heater design, and for the purpose of comparing results from the present apparatus to published data. Although not shown, the nucleate boiling water results compare favorably with other investigations using tube heaters [18] and horizontal plate heaters [3, 12].

In each nucleate boiling run, the heat flux was increased incrementally until a large instantaneous temperature rise in the test heater indicated burnout. In addition to these burnout determinations, five burnout determinations were obtained at a constant heat flux by gradually decreasing the system pressure until burnout ensued. For these determinations, the pyrometer turned off the rectifier at the onset of burnout. Good agreement was achieved for burnout values obtained by either method. Water burnout data ranged from about 200,000 Btu/hr·ft² at atmospheric pressure to 790,000 Btu/hr·ft² at 200 psig.

Boiling Mercury Experiments. Two test heaters were used in carrying out the boiling mercury investigation. Test heater 1 was used for 33 runs at system pressures ranging from 1 mm to 1143 mm mercury (45 in. mercury). Fourteen additional runs were made with test heater 2 over a comparable pressure range. Plots and tables of the data from all individual runs are included in the thesis [26]. Heat fluxes extended to 1,100,000 Btu/hr·ft² when operating with the greatest liquid pool depth (8.5 in. above the heater) at a system pressure of 5 mm mercury.

Runs 1 through 6 exhibited considerable hysteresis and lacked the consistency observed in subsequent nucleate boiling runs. Specific behavior encountered in these runs will be discussed later, as undoubtedly, the surface of test heater 1 was not yet fully conditioned to boiling mercury. The present discussion will then be restricted to runs which gave representative data for a conditioned surface. Boiling curves for runs 7 through 27, made with test heater 1, are shown in Fig. 4. These runs were made with an 8.5-in. liquid depth in the boiling vessel, but since the test heater was located 3.5 in. from the bottom of the pool, this corresponded to a 5-in. liquid level above the heater. Runs 28 through 33 were made with the liquid level 2 in. above the heater. Boiling curves for these runs are shown in Fig. 5. Fig. 6 shows the results of runs 34 through 41 made with a 5-in. liquid level above test heater 2. Runs 42 through 47, shown in Fig. 7, were made with an 8.5-in. liquid level above the heater. Individual curves in each figure are presented to best reflect the average trend of the data in each run, and in most cases the boiling curves were from data obtained both on the upward and downward cycles of the boiling curve. Note that each set of runs in Figs. 4–7 forms a homologous group of curves. Moreover, it is readily seen in the figures that in each run, a heat-flux level was reached where the slope of the boiling curve decreased markedly. This point of transition or departure, herein termed "departure heat flux," is of particular interest and will be discussed in a later section.

Reproducibility of Mercury Data. Considering the scatter often observed in liquid metal boiling studies, it was felt that exceptional reproducibility was attained in this study. Composite plots of the data shown in Figs. 4-7 give an initial indication of the consistency and, therefore, reproducibility of the data. For additional comparison, runs 10, 17, and 38 are shown in Fig. 8. Recall that runs 10 and 17 were made with test heater 1 and run 38 with test heater 2. Fig. 8 shows that exceptional reproducibility was obtained for test heater 1. Note that, while observed ΔT's in runs 10 and 17 are very close, the surface has aged slightly during the interim 4-week period to give a higher departure heat flux in run 17. Considering the slight difference in surface treatment between test heaters 1 and 2, run 38 shows very good agreement with the runs 10 and 17 made with test heater 1. It can also be seen in Fig. 8 that very close agreement was shown for the increasing and decreasing heat-flux cycles.

Effects of Surface Aging. It appeared that the heater surface of test heater 1 became conditioned to boiling mercury after run 6. However, in run 4 the ΔT increased to about 400 deg F and suddenly dropped to less than 70 deg F at a constant heat flux as shown in Fig. 9. This marked decrease in ΔT was a definite sign that nucleation had begun. The same behavior was observed

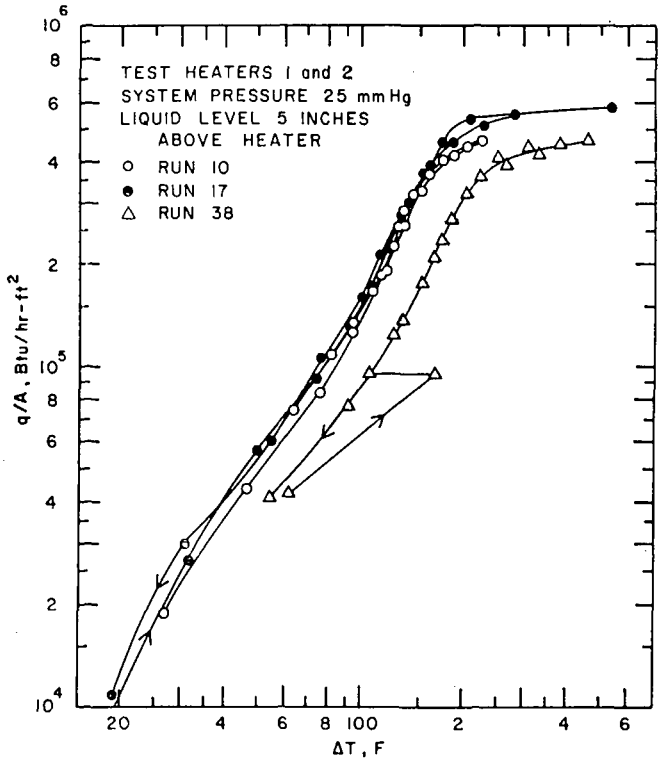

Fig. 8 Reproducibility of mercury results

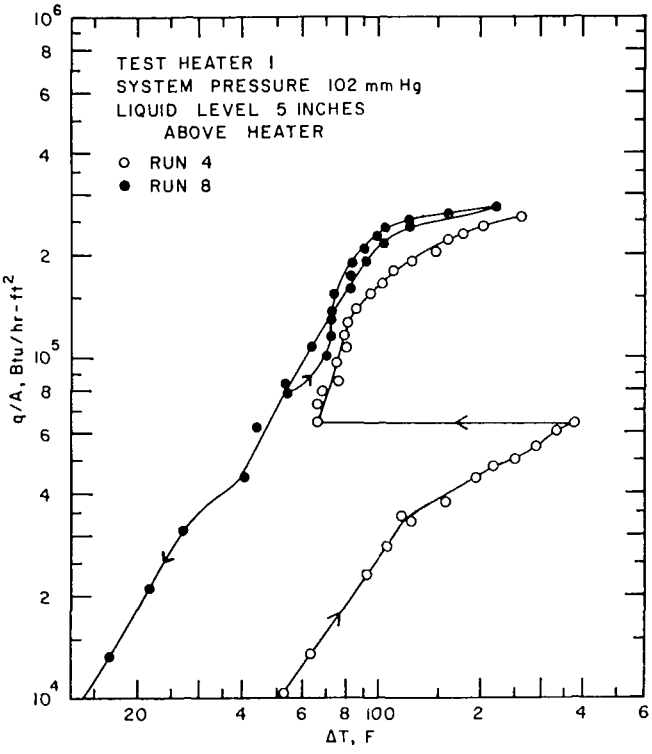

Fig. 9 Effects of aging on test heater 1

during run 5, but this drastic temperature drop was not observed in subsequent runs with test heater 1. In fact, succeeding runs exhibited much lower ΔT's for the lower (and what appeared to be totally convective) portion of the boiling curve. Run 8, also shown in Fig. 9, was made at the same pressure and pool depth as run 4. These runs agreed closely above 60,000 Btu/hr·ft², but the effects of hysteresis (apparently as the result of surface aging) gave widely varying ΔT's at lower heat fluxes. Note also that the departure heat flux (point of slope decrease) is more abrupt in run 8 than in run 4.

In later runs with test heater 1, it appeared that the surface had aged sufficiently so that the transition from apparent convective heat transfer to nucleate boiling occurred more easily. This was felt to be an indication that stable nucleation sites had been established. During run 25, the heat flux was by chance set at a heat flux (212,000 Btu/hr·ft²) where periodic changes from convection to nucleate boiling and back could be observed in the heater temperature trace. This behavior is illustrated in Fig. 10 where the surface temperature gradually rose 50 to 60 deg F, indicating destabilization of nucleation, then it would suddenly fall to its original level and repeat the cycle.

When test heater 1 was removed from the system, the surface had a frosty gray appearance, which upon immersion part way into a beaker of clean mercury showed complete nonwettability. However, a portion of the Swagelok fitting which had been in contact with boiling mercury was still wetted by mercury as the entire test heater surface had been previous to installation.

The silver-plated test heater 2 also exhibited aging, but in a different manner than test heater 1. During run 34, which was the initial run using test heater 2, the system was allowed to run for an extended period at a heat flux of about 55,000 Btu/hr·ft². After a period of time, heater temperatures rose about 200 deg F

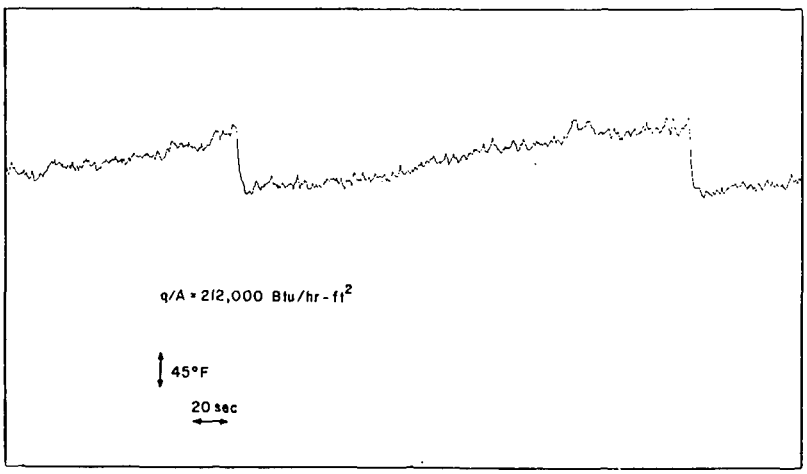

Fig. 10 Test heater temperature trace during run 25

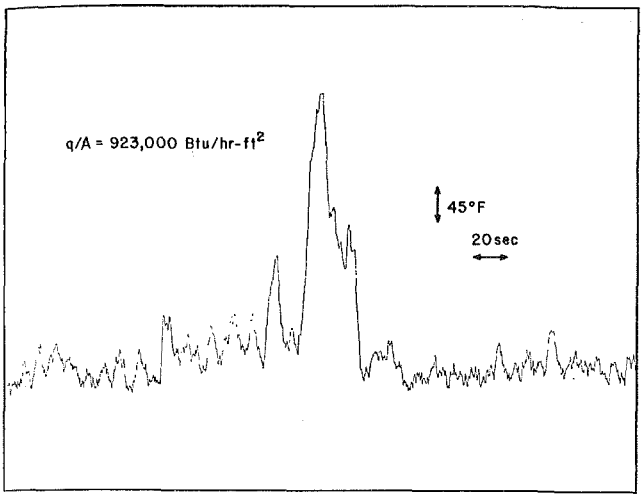

Fig. 11 Typical test heater temperature excursions above the departure heat flux

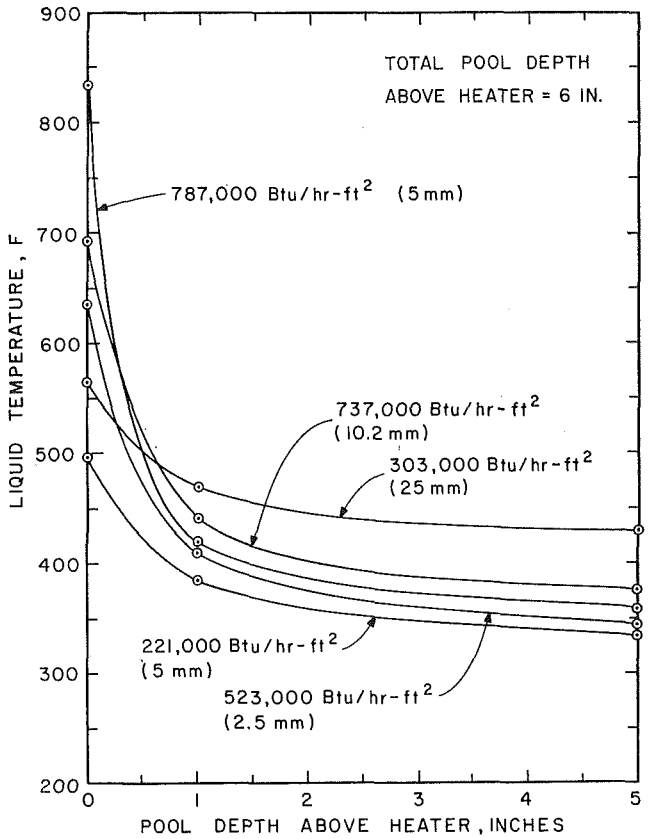

Fig. 12 Pool temperature gradients

while operating at this heat flux, indicating that perhaps the silver plating had dissolved away from the surface.

Test heater 2 never gave as smooth a change from convective to nucleate boiling as had test heater 1. Most of the boiling curves obtained with test heater 2 exhibited a discontinuity at intermediate heat-flux levels. Moreover, the apparent absence of active nucleation sites resulted in high ΔT's, but upon reaching an adequate heat-flux level, sufficient superheat was achieved at the heater surface to activate sites and provide the sudden establishment of nucleate boiling. This caused the ΔT to immediately drop to a substantially lower value. When the heat flux was increased, the temperature rose rapidly and then fell to a stable level indicating that the surface was supporting nucleation. Frequently surface temperatures rose about 200 deg F above the level corresponding to stable nucleate boiling. However, when the heat flux was further increased, more-stable boiling was achieved. This behavior was very similar to that observed by Colver and Balzhiser [7] for boiling potassium.

Other Effects. Although noise from the vacuum pumps and the cooling fan on the rectifier made it difficult to characterize low-level noises, a distinguishable rumbling sound emanated from the enclosure once nucleate boiling was established. This sound was accompanied by discernible vibration of the outer enclosure. As the heat flux was further increased, the vibration became more pronounced.

Internal heater temperature fluctuations were quite significant at all heat-flux levels. Figs. 10 and 11 show typical internal heater temperature fluctuations observed at relatively low and high heat fluxes. As noted in Fig. 11, when the departure heat flux was surpassed much larger fluctuations occurred, and were occasionaly accompanied by large temperature excursions (oftentimes >200 deg F).

The existence of pool temperature gradients have been reported in previous liquid metal studies by Colver and Balzhiser [7] and Madsen and Bonilla [20]. Similarly, it was found that such gradients existed in this study. Using readings obtained from the thermocouple positioned 1 in. above the test heater, the thermocouple in the liquid nearest the free surface, and a heater surface thermocouple, Fig. 12 was prepared. Pool thermocouples other than that 1 in. above the heater indicated that sufficient mixing was present so that most of the pool was at a fairly uniform temperature for system pressures near atmospheric and was only 10 to 20 deg F hotter than the free-surface temperature for low system pressures.

Comparison of Data With Previous Mercury Studies. Maximum heat fluxes in previous studies have been less than 150,000 Btu/hr·ft² for pure pool-boiling mercury and only 200,000 Btu/hr·ft² for pool-boiling mercury with additives. This compares to heat fluxes achieved in this study in excess of 1,000,000 Btu/hr·ft².

The nucleate boiling data of Bonilla, et al. [4], Korneev [16], Lyon, et al. [18, 19], and Farmer [23], compare favorably with the present results, particularly with respect to the slope of the boiling curve. In fact, Korneev [16] observed a departure heat flux for data at 1 atm pressure. It would also appear that the data of Bonilla, et al. [4] exhibited a departure heat flux but they did not join the two portions of their boiling curves for system pressures of 130 and 287 mm mercury.

Comparison of Data to Correlations. The prediction of Eckert [10], as modified by Hyman, et al. [15], for free-convection heat transfer from horizontal pipes to liquid metals, satisfactorily predicted the slope of experimental data in the convective region; however, predicted ΔT's were about an order of magnitude higher than the present data after the test heater surface had fully aged. The convective portion of boiling curves obtained in runs 4 and 5, in which test heater 1 was not fully aged, more nearly agreed with predicted ΔT's.

Predicted nucleate boiling curves using the correlation of Forster and Zuber [11] agreed reasonably well with the data in slope and range of ΔT's; but the correlation gives a larger shift in ΔT with pressure than the actual data.

Departure Heat Flux. As previously noted, the heat flux at which the slope of the boiling curve decreased markedly was designated the "departure heat flux," $(q/A)_D$. After reaching this heat flux, further small increases in heat flux caused large increases in ΔT. Further, temperature fluctuations in the region above the departure heat flux were much more pronounced as previously discussed and shown in Fig. 11.

Fig. 13 shows that plotting the departure heat flux versus system pressure gives an envelope for each liquid level studied, with the highest heat fluxes being achieved at low system pressures and high liquid levels. Notice, however, that the envelope

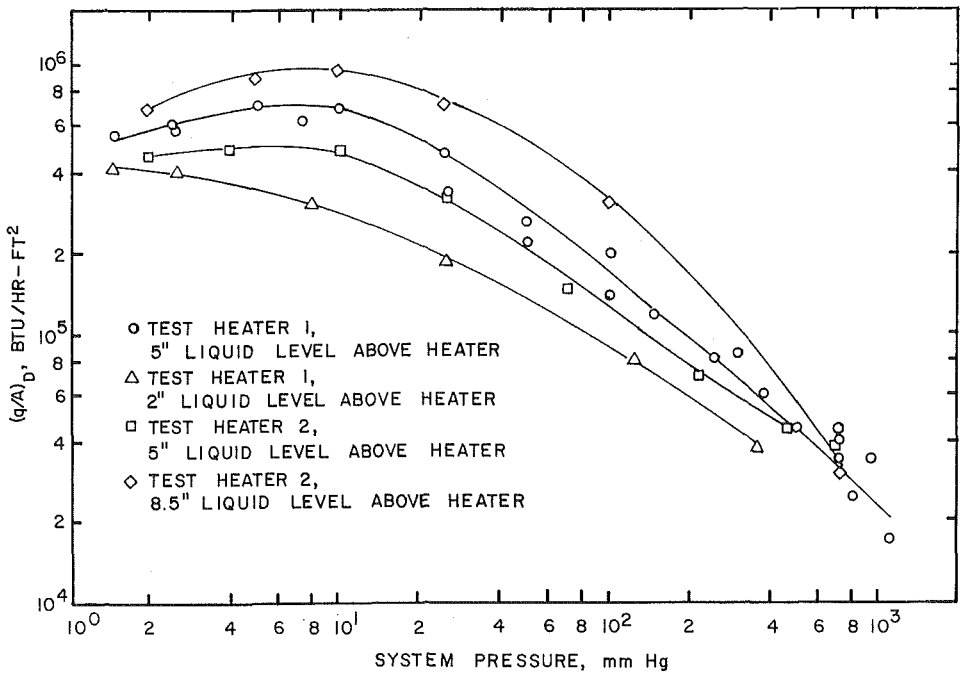

Fig. 13 Dependence of departure heat flux on system pressure and pool depth

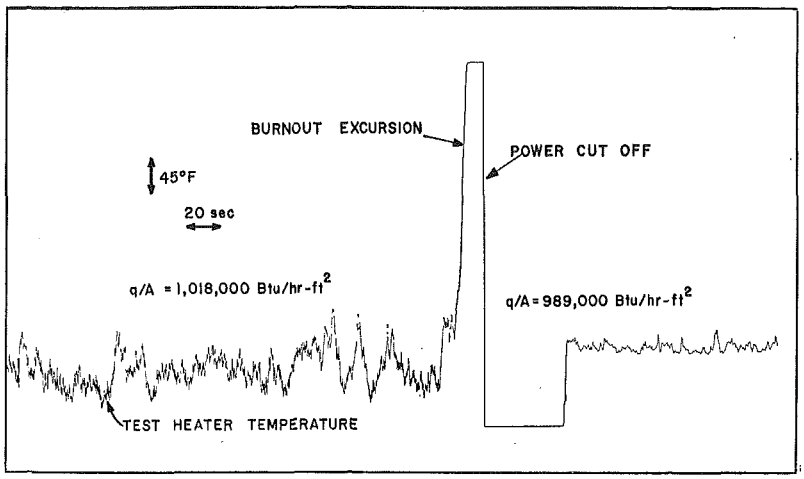

Fig. 14 Test heater temperature trace in run 45 during burnout determination

for a 5-in. level with test heater 2 lies slightly below the envelope for the corresponding level with test heater 1. Observed ΔT's at the same pressure, liquid level, and heat-flux level were generally higher for test heater 2 than for test heater 1, and it is felt that this perhaps resulted from test heater 2 not being fully conditioned or aged in the interval between its installation and the time the runs were carried out.

It can be seen in Fig. 13 that each envelope exhibits a maximum in the low pressure range. These maxima vary from slightly over 400,000 Btu/hr·ft² for a 2-in. liquid level above the heater to almost 1,000,000 Btu/hr·ft² for an 8.5-in. level. Run 46 extended to a heat flux of 1,100,000 Btu/hr·ft² although the departure heat flux was reached at about 900,000 Btu/hr·ft².

Burnout. The boiling behavior observed for the system operating near the heat-flux levels and system pressures corresponding to the maxima of the departure heat-flux envelopes more closely resembled expected behavior for a system near the burnout heat flux. During run 45, a very large temperature excursion was observed (the recorder stylus went off-scale after a 400 deg F rise) which might be justifiably called a burnout. This temperature excursion, shown in Fig. 14, occurred at a heat flux of 1,018,000 Btu/hr·ft². The observation of this burnout and indications in other low-pressure runs that burnout was imminent seemed to indicate that at low pressure, the system was demonstrating behavior normally expected for a wetting liquid. For this reason, the observed departure heat fluxes were plotted versus total pressure, i.e., system pressure plus static head above the heater. Fig. 15 shows that plotting the departure heat flux in this manner effectively separates the maxima exhibited for each liquid level and shows a consistent variation of the maxima with total pressure. Burnout correlations of Addoms [1] and Noyes [17, 22] are included in Fig. 15. Notice that these correlations very nearly predict the observed variation of the maximum departure heat flux. Other correlations by Rohsenow and Griffith [24], Zuber and Tribus [28], and Caswell and Balzhiser [6] fall below those shown in Fig. 15. Physical properties for saturated conditions at the heater were used in evaluating the correlations. The favorable comparison of the maximum de-

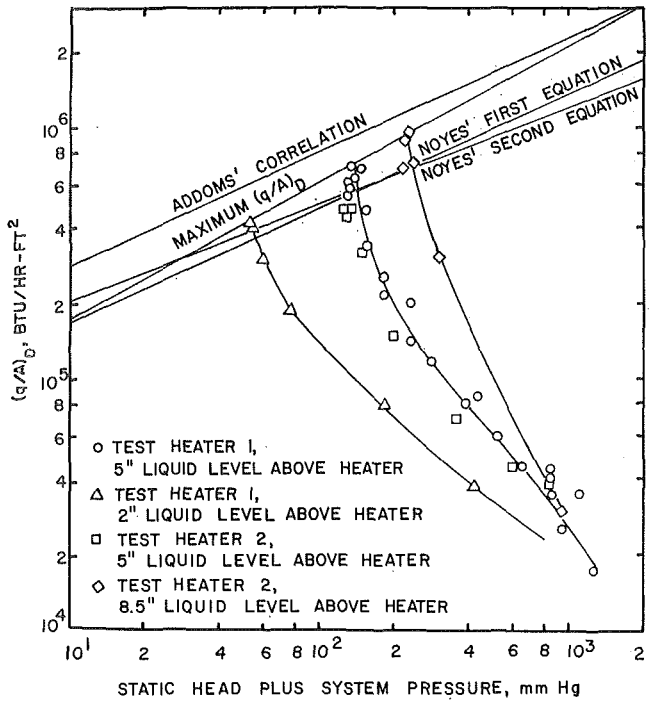

Fig. 15 Comparison of departure heat flux with correlations of Addoms [1] and Noyes [17, 22]

parture heat flux with burnout correlations further suggests that at low pressure the system exhibited boiling behavior quite similar to that expected for most wetting liquids.

Pressure Effect on the Departure Heat Flux. It has previously been noted that increasing the pool depth shifts the nucleate boiling curve to lower ΔT's. Fig. 13 displays the fact that increased departure heat fluxes were obtained with higher liquid levels. Each of these results would be expected as manifestations of pressure effects on boiling. However, one would not normally expect the departure heat flux to increase with decreasing system pressure as observed. To explain this, it was desired to find some property or feature of boiling mercury which varied with system pressure in a manner that would allow such behavior.

While endeavoring to understand why the departure heat flux increased with decreasing system pressure, many explanations were considered and discarded. It was finally concluded that the lack of pool temperature gradients except near the heater may perhaps most satisfactorily point to the reason for increased departure heat fluxes with decreases in system pressure. For low system pressures, a very steep temperature gradient (corresponding to the static pressure gradient) must exist in the pool for equilibrium saturated conditions to be present at all levels of the pool. However, it was shown in Fig. 12 that mixing in the pool resulted in fairly uniform pool temperatures (except near the heater) corresponding closely to saturated conditions for the system pressure. Consequently this had a net effect of producing inherent subcooling in the pool which increased with increasing pool depth and decreasing system pressure. The resultant effect is clearly illustrated in Fig. 16 which is a plot of departure heat flux versus inherent liquid subcooling. The ultimate consequence, of course, would be an increased departure heat flux with decreasing pressure as observed. By direct comparison, it is well known that subcooling enhances heat transfer during nucleate boiling and increases the burnout heat flux, and that this enhancement is greater at lower pressures [13, 29]. Similar enchancement should be observed for any high density boiling liquid.

Possible Boiling Mechanism Above the Departure Heat Flux. To better understand the departure heat flux, and to formulate some idea of the type of boiling occurring above this level, the data were carefully scrutinized and the literature was carefully surveyed. Previous mercury investigators [4, 16, 18, 19] have observed instances where the slope of the boiling curve was

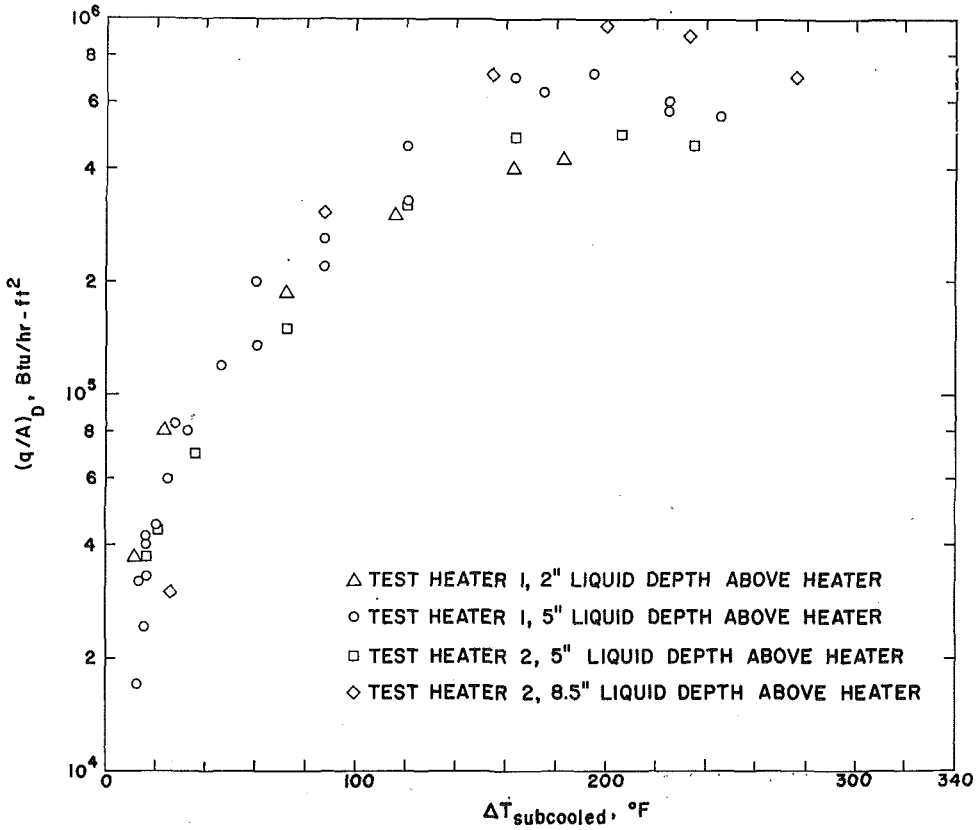

Fig. 16 Dependence of departure heat flux on inherent liquid subcooling near the test heater.

very small, and they attributed this to film boiling due to nonwetting of the surface. Observations made in this study indicated that the small slope may have indeed been a manifestation of nonwetting, but it is doubtful that fully developed film boiling was present. It is felt that the observed phenomenon can best be compared to the second transition region hypothesized by Gaertner [12] for nucleate boiling water. The second transition is the point where a change in slope for the water boiling curve was observed at a high heat-flux level. Gaertner observed that the transition occurred when vapor mushroom stems became unstable and collapsed. Considering this and the large temperature fluctuations observed above the departure heat flux as shown in Fig. 11, it is suggested that this region is likewise characterized by formation and collapse of vapor patches on the surface. This explanation for the small slope of the boiling curve is quite plausible since additional heat would generate more vapor patches which in turn would decrease the heat-transfer coefficient. This analysis is further substantiated by the observed occurrence of large temperature excursions above the departure heat flux.

Conclusions

1 Reproducible, consistent results were obtained for pool-boiling mercury even though the test heater surface was apparently unwetted.

2 Heat fluxes for boiling mercury extended to levels never before achieved on wetted or nonwetted surfaces. Heat fluxes up to 1,100,000 Btu/hr·ft^2 were obtained at ΔT's less than 400 deg F.

3 At a particular nucleate boiling heat-flux level, the slope of the boiling curve decreased significantly so that subsequent increases in heat flux were accompanied by large increases in ΔT. The heat flux at which this pronounced decrease in slope occurred was termed the "departure heat flux."

4 Departure heat fluxes plotted versus system pressure for different pool depths above the heater formed envelopes, which exhibited maxima at a system pressure less than 25 mm mercury. Maximum observed departure heat fluxes ranged from 400,000 Btu/hr·ft^2 for a 2-in. liquid level above the heater to 950,000 Btu/hr·ft^2 for an 8.5-in. level above the heater.

5 The maximum departure heat fluxes showed good agreement with burnout correlations of Addoms [1] and Noyes [17, 22] when plotted as a function of total pressure at the heater.

6 Heater temperature fluctuations observed were very similar to those observed for other boiling liquid metals.

7 Nearly uniform temperatures existed in the boiling pool except near the test heater where high superheats were present.

Acknowledgment

Fellowship support was provided by the National Science Foundation. Much of the auxiliary equipment was purchased through a grant from the National Aeronautics and Space Administration (NGR 37-003-026).

References

1 Addoms, J. N., "Heat Transfer at High Rates to Water Boiling Outside Cylinders," ScD thesis, M.I.T., 1948; also McAdams, W. H., *Heat Transmission*, 3rd ed., McGraw-Hill, New York, 1954.

2 Balzhiser, R. E., et al., "Investigation of Liquid Metal Boiling Heat Transfer," Fifth Quarterly Report, University of Michigan, September, 1964.

3 Bobst, R. W., and Colver, C. P., "Temperature Profiles up to Burnout Adjacent to a Horizontal Heating Surface in Nucleate Pool Boiling Water," *CEP Symposium Series*, Vol. 64, No. 82, 1968, pp. 26–32.

4 Bonilla, C. F., Busch, J. S., Stalder, A., Shaikmahmud, N. S., and Ramachandran, A., "Pool-Boiling Heat Transfer with Mercury," *CEP Symposium Series*, Vol. 53, No. 20, 1957, pp. 51–57; also NYO-7638.

5 Bonilla, C. F., Grady, J. J., and Avery, G. W., "Pool Boiling Heat Transfer from Scored Surfaces," *CEP Symposium Series*, Vol. 61, No. 57, 1965, pp. 280–288.

6 Caswell, B. F., and Balzhiser, R. E., "The Critical Heat Flux for Boiling Liquid Metal Systems," *CEP Symposium Series*, Vol. 62, No. 64, 1966, pp. 41–46.

7 Colver, C. P., and Balzhiser, R. E., "A Study of Saturated Pool Boiling Potassium up to Burnout Heat Fluxes," *CEP Symposium Series*, Cleveland, Vol. 61, No. 59, 1965, pp. 253–263.

8 Clark, L. T., and Parkman, M. F., "Effects of Additives on Wetting During Mercury Pool Boiling Heat Transfer," ASME Paper No. 64-WA/HT-22, New York, 1964.

9 Davenport, M. E., Magee, P. M., and Leppert, G., "Thermocouple Attachment to a Direct-Current Heater," JOURNAL OF HEAT TRANSFER, TRANS. ASME, Series C, Vol. 84, No. 2, May 1962, pp. 187–188.

10 Eckert, E. R. G., and Soehnghen, E., "USAF Tech. Report No. 5747," Wright-Patterson AFB, Dayton, Ohio, 1939.

11 Forster, H. K., and Zuber, N., "Dynamics of Vapor Bubbles and Boiling Heat Transfer," *AIChE Journal*, Vol. 1, No. 4, 1955, pp. 531–535.

12 Gaertner, R. F., "Photographic Study of Pool Boiling on a Horizontal Surface," JOURNAL OF HEAT TRANSFER, TRANS. ASME, Series C, Vol. 87, No. 1, 1965, pp. 17–29.

13 Gambill, W. R., "A Survey of Boiling Burnout," *British Chemical Engineering*, Vol. 8, No. 2, 1963, pp. 93–98.

14 Hochman, J. M., "Mercury Wetting and Its Effects on Heat Transfer," Atomics Int'l. Report No. NAA-SR-10315, August, 1964.

15 Hyman, S. C., Bonilla, C. F., and Ehrlich, S. W., "Heat Transfer to Liquid Metals and Non-Metals at Horizontal Cylinders," *CEP Symposium Series*, Vol. 49, No. 5, 1953.

16 Korneev, M. I., "Heat Transfer in Mercury and Magnesium Amalgams During Boiling Under Conditions of Free Convection," *Teploenergetika*, Vol. 2, No. 4, 1955, p. 44.

17 Lurie, H., and Noyes, R. C., "Boiling Studies for Sodium Reactor Safety, Part II," AEC Report NAA-SR-9477 (Atomics Int'l.), October, 1964.

18 Lyon, R. E., "Boiling Heat Transfer with Liquid Metals," PhD thesis, University of Michigan, 1953.

19 Lyon, F. E., Foust, A. S., and Katz, D. L., "Boiling Heat Transfer with Liquid Metals," *CEP Symposium Series*, Vol. 51, No. 17, 1955, pp. 41–47.

20 Madsen, N., and Bonilla, C. F., "Heat Transfer to Sodium-Potassium Alloy in Pool Boiling," *CEP Symposium Series*, Vol. 56, No. 30, 1960, pp. 251–259.

21 Mednick, R. L., and Colver, C. P., "Heat Transfer from a Cylinder in an Air-Water Spray Flow Stream," *AIChE Journal*, Vol. 15, No. 3, 1969, pp. 357–361.

22 Noyes, R. C., "An Experimental Study of Sodium Pool Boiling Heat Transfer," JOURNAL OF HEAT TRANSFER, TRANS. ASME, Series C, Vol. 85, No. 2, 1963, pp. 125–131; also Atomics Int'l Report No. NAA-SR-6769, December, 1960.

23 Poppendiek, H. F., "Liquid-Metal Heat Transfer," *Heat Transfer Symposium*, University of Michigan Press, 1953, pp. 77–100.

24 Rohsenow, W. M., and Choi, H. Y., *Heat, Mass, and Momentum Transfer*, Prentice-Hall, New York, 1961, pp. 211–236.

25 Romie, F. E., Brovarney, S. W., and Geidt, W. H., "Heat Transfer to Boiling Mercury," JOURNAL OF HEAT TRANSFER, TRANS. ASME, Series C, Vol. 82, No. 4, 1960, pp. 387–388; also AEC R & D Report No. ATL-A-102, Adv. Tech. Labs., October, 1959.

26 Turner, J. B., "Heat Transfer to Pool Boiling Mercury from Horizontal Cylindrical Heaters at Fluxes up to Burnout," PhD thesis, University of Oklahoma, 1968.

27 Watt, D. A., O'Connor, R. J., and Holland, E., "Tests on an Experimental D-C Pump for Liquid Metals," Atomic Energy Research Est. Report No. R/R 2274 (British), 1957.

28 Zuber, N., and Tribus, M., "Further Remarks on the Stability of Boiling Heat Transfer," AECU-3631, January, 1958.

29 Zuber, N., Tribus, M., and Westwater, J. W., "The Hydrodynamic Crisis in Pool Boiling of Saturated and Subcooled Liquids," TRANS. ASME, Vol. 27, 1961, pp. 230–236.

R. M. HOLDREDGE
Assoc. Professor,
Department of Mechanical Engineering,
Utah State University, Logan, Utah
Mem. ASME

P. W. McFADDEN
Head, School of Mechanical Engineering,
Purdue University, West Lafayette, Ind.
Mem. ASME

Film Boiling on Horizontal Cylinders in Helium II

The analysis of Rivers and McFadden for film boiling heat transfer from horizontal cylinders immersed in Helium II is briefly reviewed and results are recapitulated. Experimental measurements of film boiling heat transfer are made for horizontal cylinders of 0.145 cm and 0.245 cm dia immersed in Helium II baths at 1.78, 1.96, and 2.1 K at wall heat fluxes up to 2.84 w/cm². The nondimensionalized experimental results are compared with the accepted correlations of Bromley and Breen and Westwater to demonstrate the inability of the usual film boiling correlations to predict film boiling in Helium II. The nondimensionalized experimental results are compared with the predictions of the Rivers and McFadden analysis which considers Helium II properties, and the results of the analysis are substantiated.

Introduction

HELIUM, unlike any other substance, has two known liquid phases. The phase diagram shown in Fig. 1 indicates thermodynamic states which characterize each phase. The two phases are separated by the lambda line which intersects the saturation curve at the lambda point. The phase called Helium I, which occurs at higher temperatures (saturation temperatures from approximately 2.17 to 5.2 K) is very similar to other liquefied gases and noncryogenic liquids. Hence, heat transfer between a solid exterior surface and Helium I should be adequately predicted using standard dimensionless groups and heat transfer correlations. Even pool boiling involving a bath of Helium I should agree with accepted standard correlations.

However, the low temperature phase of liquid helium (saturation temperatures below approximately 2.17 K) called Helium II has several properties which make it unlike any other known fluid. For example, Helium II exhibits an unusually large capacity to transmit heat. Although it does not obey the Fourier-Biot law of heat conduction in the usual sense, if this law is applied to Helium II, the effective thermal conductivity can be very large, up to three orders of magnitude larger than that of pure copper at room temperature. However, the effective thermal conductivity is not a constant, or even a function only of the thermodynamic state, but may in various circumstances be a function of geometry and temperature gradient as well. In addition to peculiar thermal behavior, unusual flow phenomena are found with Helium II. For example, the viscosity of Helium II when measured in a capillary tube appears to approach zero. As would be expected then, heat transfer from a solid surface to a bath of Helium II cannot be described by the usual dimensionless groups and correlations, as is documented by experimental evidence.

Consider a heated horizontal cylinder immersed in a saturated bath of Helium II. The liquid in the neighborhood of the cylinder is at state B in Fig. 1 while the temperature of the liquid bath is determined by the vapor pressure indicated by state A in Fig. 1 and is essentially uniform (except close to the heated surface) because of the excellent heat transport characteristics of the bath. If heat Q is transferred radially from the cylinder of surface area A and surface temperature T_s to the bath at temperature T_b, then several regimes of heat transfer are possible according to the size (D) of the test cylinder, the surface heat flux $q\left(=\frac{Q}{A}\right)$, the bath temperature, and the immersion depth L. The regimes of heat transfer are qualitatively illustrated in Fig. 2.

In regime 1 the Kapitza resistance is controlling; this regime has been investigated extensively, both experimentally and analytically, since this unexpected resistance was first reported in 1941 [1].[1] Phenomenologically, it is postulated that phonons are radiated from the solid surface into the Helium II, hence the heat flux is proportional to $(T_s^4 - T_b^4)$. As the heat flux is increased, there is a $(T_s - T_b)$ for which additional thermal resistance comes into play and the Kapitza resistance is no longer controlling [2]. More experimental results are needed to confirm and to describe completely this region (regime 2, Fig. 2).

Finally, there is a heat flux at the solid surface which cannot be supported by the liquid at the solid-liquid interface. This condition is often defined as burnout, or the peak flux condition as in ordinary fluids, and when it occurs, the surface experiences a sharp increase in temperature (typically to 10 K or more) as a film of helium vapor forms between the solid surface and the liquid bath. An additional increase in heat flux causes an in-

Contributed by the Heat Transfer Division and presented at the Fluids Engineering, Heat Transfer, and Lubrication Conference, Detroit, Mich., May 24–27, 1970, of THE AMERICAN SOCIETY OF MECHANICAL ENGINEERS. Manuscript received at ASME Headquarters, January 12, 1970. Paper No. 70-HT-3.

[1] Numbers in brackets designate References at end of paper.

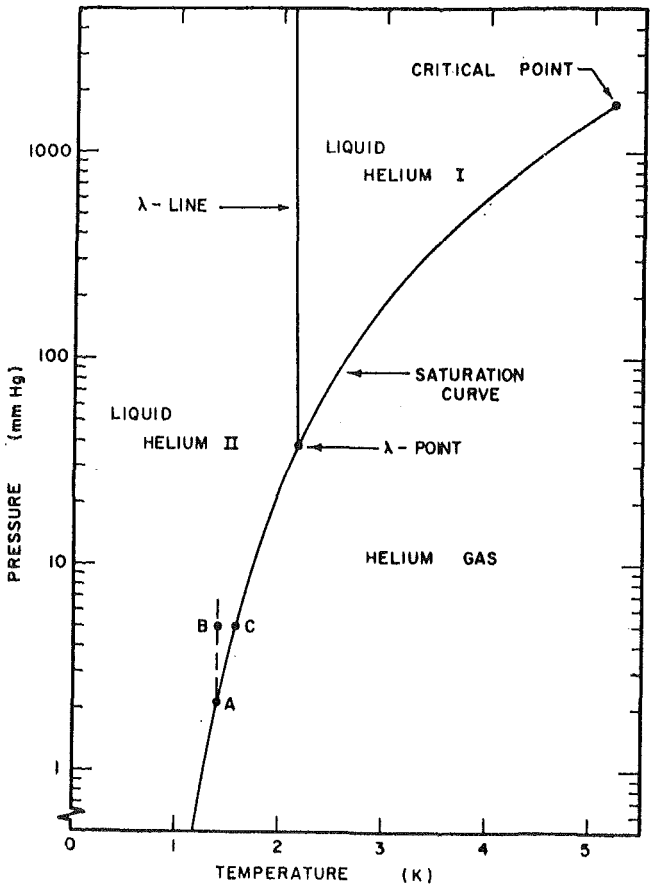

Fig. 1 Helium phase diagram

crease in T_s and changes in the vapor film. (It should be noted that no nucleate boiling has ever been reported in Helium II.) Regime 3 then represents the condition similar to film boiling of ordinary liquids and is the regime of interest in the present work.

The first published results for film boiling in Helium II were presented by Rinderer and Haenseler [3]. They investigated a submerged wire and found that a nearly concentric closed film of helium gas was formed around the wire when it was heated well above the helium saturation temperature. Under steady-state conditions, there was no net production of gas, i.e., there were no bubbles leaving the film. Thus all of the heat leaving the wire must have been conducted away from the film by an "internal convection" process in the Helium II. Using the data of Rinderer and Haenseler, Frederking [4] calculated the magnitude of the heat flux in the Helium II at the film interface, q_b, and found it to be independent of the heat flux at the wire surface, q, and the temperature difference across the film (ΔT), but very dependent upon the depth of the wire in the bath. Experimental results, including the measurements of Goodling and Irey [5], suggest, then, that there is a certain maximum heat flux which the Helium II will absorb, that this heat flux is a function of thermodynamic state and immersion depth at least, and that this heat flux represents the thermal boundary condition at the liquid-vapor interface in film boiling of Helium II. Hence, as in subcooled film boiling in an ordinary liquid, the heat conducted into the liquid-vapor interface is absorbed partially in evaporating additional liquid, and the remainder is conducted into the liquid bath. However, unlike subcooled boiling in an ordinary liquid, in the case of Helium II there is no thermal resistance in the adjacent liquid bath up to a point. The bath readily accepts a heat flux of q_b at the liquid-vapor interface.

These mostly qualitative experimental results and conclusions formed the basis of the mathematical model proposed by Rivers and McFadden [6] to describe and predict film boiling in Helium II. The purpose of the present work was to obtain additional quantitative experimental data in order to compare this data and previously published data [2] with both the model and results of the Rivers-McFadden theory and standard film boiling theories. In the following, the elements of the analytical approach and results are reviewed and the experimental program and results are presented. Finally, a comparison between analysis and experiment is made and discussed.

Analysis

The mathematical model of Rivers and McFadden is reviewed to emphasize the difference between Helium II and other liquids or liquefied gases. Because of its unusual features the basic mathematical model is presented in some detail, but the solution is only summarized. (For details see reference [7].)

Consider a cylinder immersed in a Helium II bath and surrounded by a film of helium vapor, as indicated in Fig. 3. The relative thickness of the vapor film is exaggerated for illustrative purposes. The convection which occurs within the film was assumed to be laminar, steady, incompressible, plane two-dimensional, boundary layer type flow, with constant properties and negligible internal heat generation. Thus the laws of conservation of mass, momentum, and energy, when applied to this con-

Nomenclature

A = heat transfer area
C_p = specific heat at constant pressure
D = diameter
g = acceleration due to gravity
Gr = Grashof number, $gr^3\rho\Delta\rho/\mu^2$
h = average convection heat transfer coefficient, $q/(\Delta T)$
$(\Delta h)_i$ = enthalpy change across the interface, $(h_\delta - h_b)/h_{fg}$
h_{fg} = enthalpy of evaporation
H_i = interface enthalpy parameter, $(\Delta h)_i/C_p(\Delta T)$
k = thermal conductivity
K_1, K_2, K_3 = thermometer constants
L = immersion depth
Nu = average Nusselt number, hr/k
P = pressure
Pr = Prandtl number, $\mu C_p/k$
q = surface heat flux, Q/A
q_b = heat flux at the vapor–Helium II interface
Q = heat transfer rate
Q_b = interface heat flux parameter, $rq_b/k(\Delta T)$
r = cylinder radius
R = electrical resistance
T = temperature
(ΔT) = $(T_s - T_\delta)$
u = velocity component in x-direction
v = velocity component in y-direction
x = length coordinate parallel to the heater surface
y = length coordinate perpendicular to heater surface
α = thermal diffusivity
δ = film thickness
μ = dynamic viscosity
ν = kinematic viscosity
ρ = density
$\Delta\rho$ = $(\rho_b - \rho_{vapor})$

Subscripts

b = in the bulk liquid Helium II
0 = at $x = 0$
s = surface
δ = at film interface, $y = \delta$
λ = at the λ-point on the saturation curve for liquid helium
f = averaged across the film

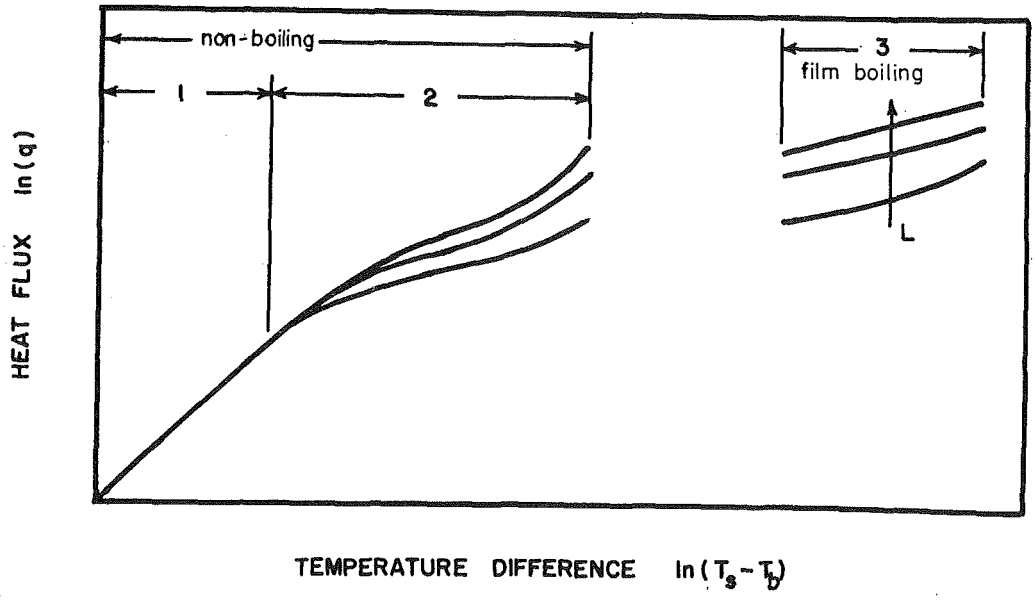

Fig. 2 The boiling curve for Helium II

vection, were expressed in the form of the boundary layer equations:

$$\frac{\partial u}{\partial x} + \frac{\partial v}{\partial y} = 0 \tag{1}$$

$$u\frac{\partial u}{\partial x} + v\frac{\partial u}{\partial y} = \nu\frac{\partial^2 u}{\partial y^2} + g\frac{\Delta\rho}{\rho}\sin\frac{x}{r} \tag{2}$$

$$u\frac{\partial T}{\partial x} + v\frac{\partial T}{\partial y} = \alpha\frac{\partial^2 T}{\partial y^2} \tag{3}$$

which are the usual formulations for boundary layer type free convection.

The basic boundary conditions on the boundary layer equations were expressed in the following form:

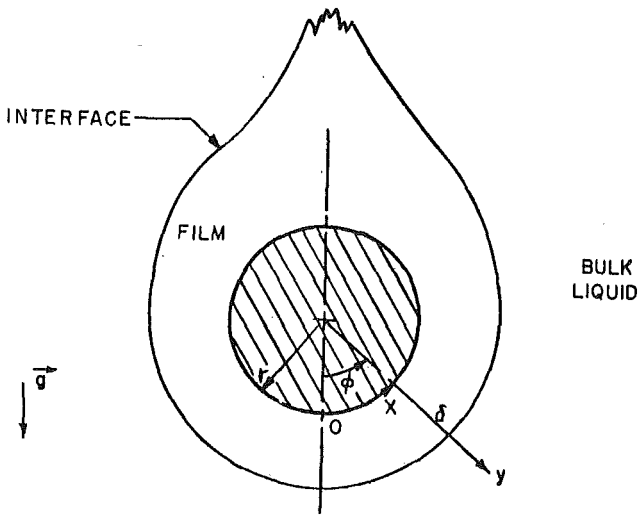

HORIZONTAL CIRCULAR CYLINDER

Fig. 3 Heat transfer configuration with coordinate system

$$\text{At } y = 0, \quad u = v = 0, \quad T = T_s \tag{4}$$

$$\text{At } y = \delta, \quad u = u_\delta, \quad v = v_\delta, \quad T = T_\delta \tag{5}$$

The temperatures T_s and T_δ were constants but the factors δ, u_δ, and v_δ were allowed to be functions of x. Thus additional boundary conditions at the interface were required.

The shear stress at the interface generated by the motion of the fluid in the film would also cause the bulk fluid immediately adjacent to the interface to move in the x-direction. This would result in $u_\delta > 0$, $\left(\frac{\partial u}{\partial y}\right)_\delta < 0$, and u_b varying from u_δ at the interface down to zero at some distance out in the bulk fluid. However, as noted earlier, for certain flow conditions the viscosity of Helium II approaches zero. For this reason the velocity profile was assumed to be discontinuous at the interface, with $u_\delta > 0$, $\left(\frac{\partial u}{\partial y}\right)_\delta < 0$, and $u_b = 0$. These idealized characteristics of the velocity variation at the interface are illustrated by the assumed, approximate form of the velocity profile in the film shown in Fig. 4.

Next, thermal boundary conditions at the interface were considered. The temperature of the vapor film was assumed to vary continuously from T_s at the heat transfer surface down to T_δ at the interface, where T_δ was taken to be the saturation temperature of the vapor. Further, T_b was assumed to be everywhere constant (in view of the experimental evidence noted previously), which yielded a discontinuous temperature drop at the interface, $(T_C - T_B)$ in Fig. 1. The idealized characteristics of the temperature distribution through the film and at the interface are illustrated by the assumed, approximate temperature profile shown in Fig. 4. Also, as based on the experimental evidence, q_b was assumed to be a function of thermodynamic state and immersion depth only, and was then a constant with respect to the processes occurring within the film.

After these idealized characteristics of the velocity and temperature profiles were established, it was then possible to derive the additional boundary conditions required at the interface by applying the laws of conservation of mass, momentum, and energy to the heat transfer and flow processes occurring at the interface. This procedure resulted in the following forms at these interface boundary conditions: The interface mass flow boundary condition,

$$\rho_b v_b = \rho \left(v_\delta - u_\delta \frac{d\delta}{dx} \right) \tag{6}$$

The interface momentum boundary condition,

$$\mu \left(\frac{\partial u}{\partial y} \right)_\delta = \rho_b v_b u_\delta \tag{7}$$

The interface energy boundary condition,

$$k \left(\frac{\partial T}{\partial y} \right)_\delta = \rho_b v_b (\Delta h)_i - q_b \tag{8}$$

For the derivation of these expressions see reference [6].

Since no similarity variable was found which would reduce the partial differential boundary layer equations to ordinary equations while simultaneously satisfying all boundary conditions, the method chosen for solving the system of equations was the familiar integral approximation method. Thus the boundary layer equations had to be transformed from their partial differential form, equations (1), (2), and (3), into their integrodifferential form.

These resulting integral equations were solved in the usual manner using fourth-order polynomials for the velocity and temperature profiles in the helium film. In nondimensionalizing the mathematical system, it was found that the nondimensional average heat transfer coefficient (Nusselt number), $\mathrm{Nu} = hr/k$, was dependent upon the following four parameters. The Prandtl number,

$$\mathrm{Pr} = \frac{\mu_f C_{pf}}{k_f}$$

The Grashof number,

$$\mathrm{Gr} = \frac{gr^3 \rho_f (\rho_b - \rho_f)}{\mu_f{}^2}$$

The "interface enthalpy" parameter,

$$H_i = \frac{(\Delta h)_i}{C_{pf}(\Delta T)_f}$$

and the "interface heat flux" parameter,

$$Q_b = \frac{r q_b}{k_f (\Delta T)_f}$$

The parameters Pr, Gr, and H_i are characteristic of film boiling problems for ordinary fluids, while Q_b is a new parameter which is characteristic of Helium II.

The integral equations were numerically integrated using a technique based on the Runge-Kutta method. Rivers and McFadden [7] presented the final results in the form $\mathrm{NuGr}^{-1/4}$ versus $Q_b\mathrm{Gr}^{-1/4}$ for various values of H_i, as shown in Fig. 5 using $\mathrm{Pr} = 0.7$, which is characteristic of helium vapor.

Examination of Fig. 5 resulted in the consideration of three film boiling regimes. For $Q_b\mathrm{Gr}^{-1/4} < 0.05$, the "convection" regime, there is considerable film growth around the cylinder. This regime is similar in nature to film boiling of ordinary liquids, and calculations indicate $\mathrm{NuGr}^{-1/4}$ is essentially independent of $Q_b\mathrm{Gr}^{-1/4}$. Rivers and McFadden concluded this result is due to q_b being so small compared to q that it has a negligible influence, and ordinary convection processes in the film dominate the heat transfer process.

Another regime is characterized by $Q_b\mathrm{Gr}^{-1/4} > 5$. For this regime there is negligible film growth around the cylinder. Results indicate the temperature variation in the film is linear with radius and consequently the dominant heat transfer process in the film is conduction, with convection exerting negligible influence. The process in this regime depends only on Q_b and $q = q_b$,[2] and hence Helium II properties dominate the heat transfer process.

Finally, a transition regime exists for $0.05 < Q_b\mathrm{Gr}^{-1/4} < 5$. In this regime both Helium II properties and ordinary convection processes must be accounted for in correlating film boiling.

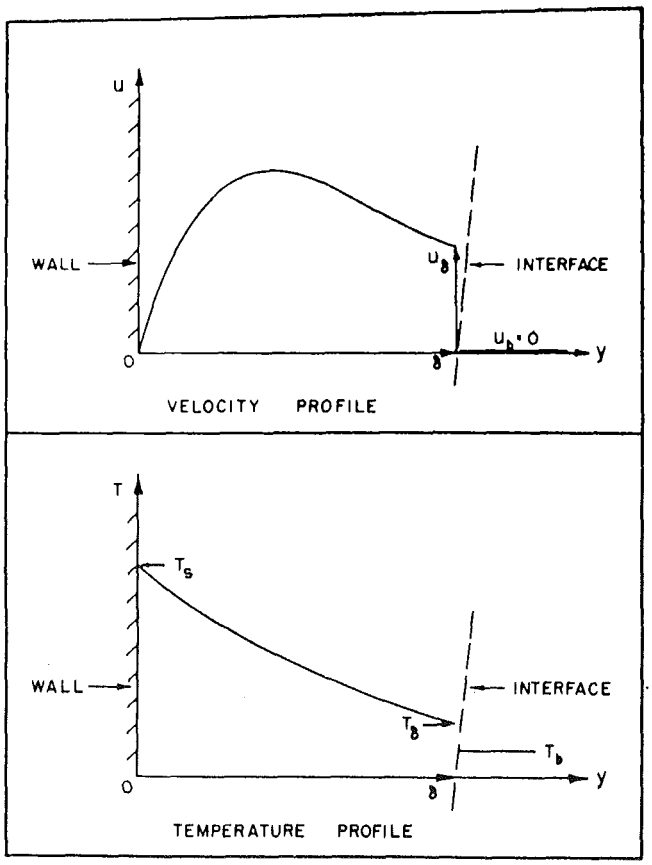

Fig. 4 The assumed approximate forms of the velocity and temperature profiles

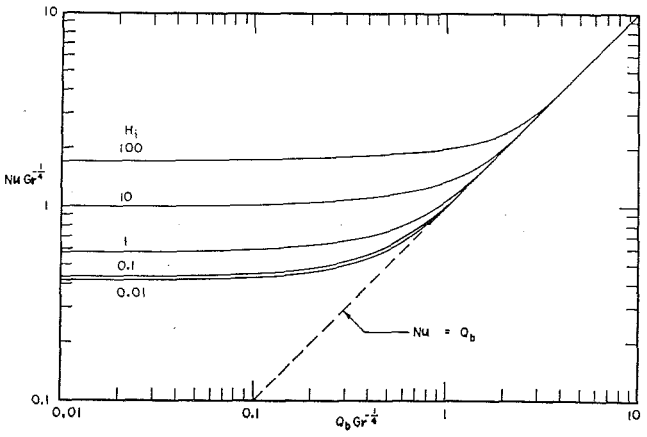

Fig. 5 Calculated results, horizontal cylinder with a helium gas film (Pr = 0.7)

[2] This is so because the analysis used a boundary layer model, and the film was therefore very thin. For thick films such as in [3], obviously $rq = (r + \delta)q_b$, although it is not known if $Q_b\mathrm{Gr}^{-1/4} > 5$ characterizes the boundary of this regime for thick films.

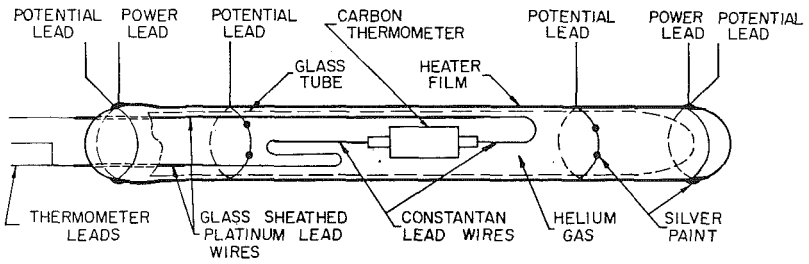

Fig. 6 Test section (schematic) film boiling data

Test Apparatus and Experimental Procedure

The experimental cryostat was a vacuum jacketed 8.9-cm-ID liquid helium dewar which was immersed in a liquid nitrogen dewar. For details of the test installation, test section construction, and thermometer calibration, see [2, 8].

A schematic of the test section is presented in Fig. 6. The surface temperature of the test section was determined by a $^1/_{10}$-w, 56-ohm fixed composition, Allen-Bradley carbon resistor which had its dia reduced until it fit inside the test section. Since alloys have a much higher thermal resistance at helium temperatures than pure metals, insulated constantan wires 0.003 in. in dia were inserted between the platinum lead wires and the resistor to add sufficient thermal resistance to insure that the thermometer measured the surface temperature. (For physical dimensions and details of construction see [2].)

End effects were minimized by taking the test surface as that portion of the test section (approximately one-half) between the inner potential leads. The energy transferred from the test surface was determined from the potential drop across the inner potential taps and the d-c current as determined by the potential drop across a standard resistor.

A Minneapolis-Honeywell calibrated germanium thermometer was used to calibrate the bath thermometer and test section thermometers from 1.78 to 76 K. For temperatures below 4.2 K, the germanium thermometer calibration was checked against the 1958 He^4 temperature scale. (For details of a calibration see [2] or [8].)

The test section surface temperature was measured to within 1.4, 1.75, 1.3, and 3 K for wall temperatures on the order of 25, 50, 60, and 150 K, respectively. Consequently, the temperature differences are felt to be accurate to within less than 5 percent error. The heat fluxes are probably accurate to within a consistent error of 5 percent and a scatter of approximately 1 percent. The immersion depths are felt to be accurate to within 0.3 cm, except for immersion depths of less than 2.5 cm at a large heat flux where the error may be as large as 0.45 cm.

Experimental Results

With this experimental apparatus, heat transfer data were taken for both Helium I and Helium II [8]. The data of particular interest to the present work is that bearing on the analytical predictions [6, 7], that is, data on the interfacial heat flux q_b, plus wall heat flux data during film boiling.

Details of the transition to film boiling for Helium II were previously reported [9]. These results showed the burnout heat flux varies approximately linearly with immersion depth for a given bath temperature and does not vary monotonically with bath temperature at a fixed immersion depth. These results are in qualitative agreement with Frederking's previous results [10]. The results also indicate that the effect of test section dia on the burnout flux is small, but the burnout fluxes are generally slightly larger for the smaller test section. The size influence has also been observed by Frederking [11] and is in the same direction as ordinary liquids.

While measurements of film thickness could not be made in the present experiments, qualitative visual observation showed the film to be very thin compared with the dia of the test section, and thus the present burnout heat flux values are roughly representative of the interface heat flux values immediately after burnout and, hence, approximate q_b. Thus q_b depends primarily on thermodynamic state and immersion depth, with some dependence on cylinder size as indicated. The approximation of q_b then was used in all subsequent analysis of experimentally determined Helium II film boiling data.

Film boiling heat transfer data were taken for both test sections in Helium II over a range of immersion depths and bath temperatures. Some of this data was presented previously [2] and is shown in Fig. 7.

No film boiling data for the 0.245-cm-dia test section at a bath temperature of 1.78 K was obtained because of insufficient pump capacity. Data seem consistent except for the 0.245-cm-dia test section at 1.96 K bath temperature near a heat flux of 1.6 w/cm^2. No explanation for this inconsistency is given. While it might seem more satisfying to present these data in the form of curves for heat flux as a function of temperature difference, with immersion depth as a parameter (as qualitatively done in Fig. 2), the method of presentation here reflects how the data were taken and requires no cross-plotting, so that only original data points are presented.

In addition to film boiling data in Helium II, data were taken for film boiling in Helium I. Since for Helium I, $Q_b = 0$, an approximate asymptote for the convection regime of Fig. 5 was obtained. The uncorrelated data are not presented here but can be found in [8].

During film boiling the vapor film in the above tests was visually observed. The vapor-liquid interface seemed smooth, except near the top of each cylinder in certain tests. Further, the film thickness seemed small compared with the cylinder dia, except for the largest heat fluxes. This qualitative observation was felt to be necessary to gain a feeling for the validity of the boundary layer assumptions when comparing these experimental results with theory. All Grashof numbers were below 10^5 which insured laminar flow in the film.

The data of Fig. 7 plus additional data from [8] were then nondimensionalized, as indicated previously, for purposes of correlation, as shown in the following section. Additional details concerning this data can be found in [8]. Since the analysis of Rivers and McFadden was developed considering constant properties, when comparing the results of experiments with the theory, average values of varying properties had to be used. In all cases properties of the vapor film were evaluated at the arithmetic average film temperature.

Discussion

Before comparing the present experimental results with Helium II theory, it was of interest to compare experimental results of film boiling in Helium II with two generally accepted correlations for ordinary liquids. It was found that the correlations of Bromley [12] and Breen and Westwater [13] successfully

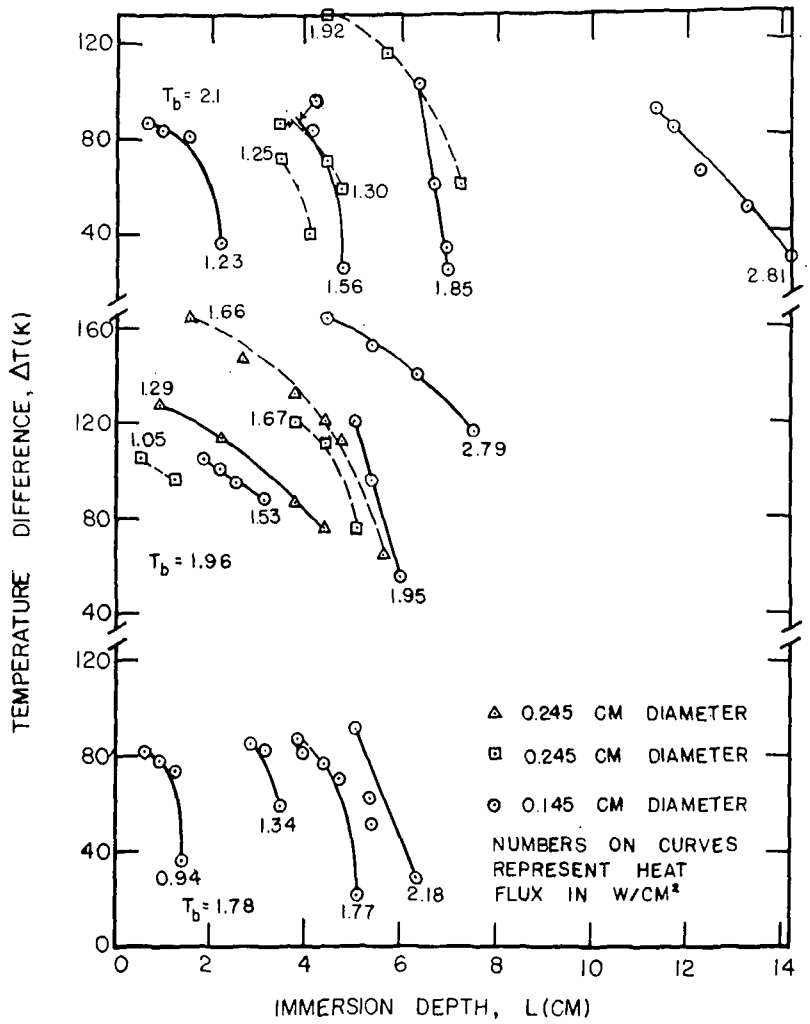

Fig. 7 Film boiling data

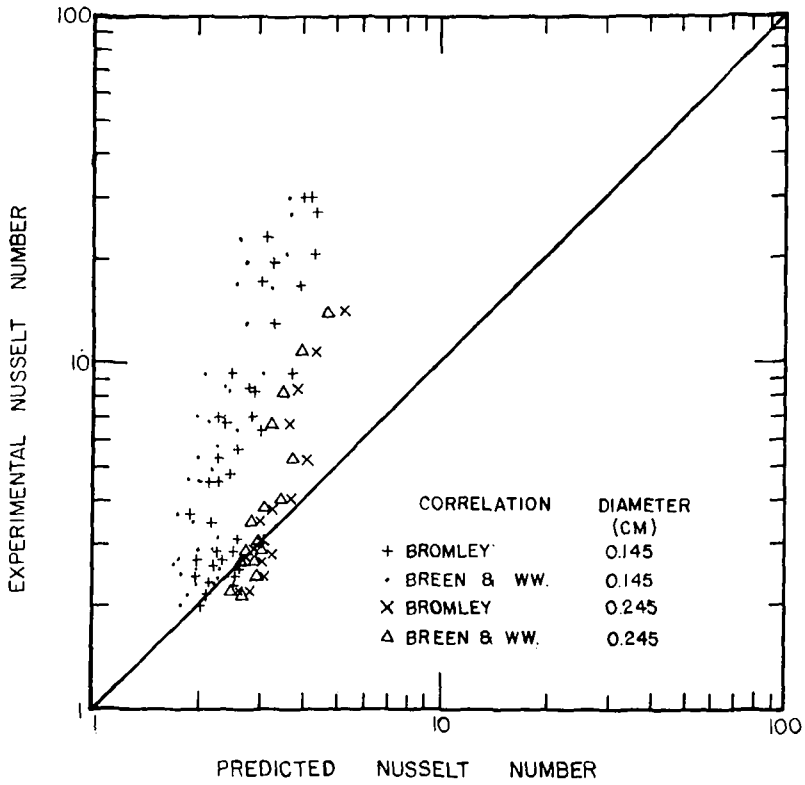

Fig. 8 Comparison of predicted Nusselt number and experimental Nusselt number

predicted the observed Nusselt numbers only for small Nusselt numbers, as shown in Fig. 8. Small Nusselt numbers correspond to large temperature differences, which in turn correspond to the convection regime shown in Fig. 5. Since this is the regime where Helium II properties are relatively unimportant and correlations for ordinary liquids obviously do not account for these properties, this agreement is expected. It is equally obvious that the vast differences between predictions of these correlations and experimental results at larger Nusselt numbers is caused by the fact that these correlations do not include Helium II properties, which the following does.

Finally, then, the data combined with the results for q_b [8] were nondimensionalized and superimposed on Fig. 5, which resulted in Fig. 9.

It should be noted that while the data do not reflect the variations of H_i (for all points $0.027 \leq H_i \leq 0.45$), this is not entirely unexpected since both the present analysis for Helium II and the analysis of McFadden [14] for ordinary liquids showed that $\mathrm{NuGr}^{-1/4}$ was becoming rather insensitive to H_i for H_i less than about one-half.

Also, as noted earlier, data for film boiling in Helium I were obtained. For all Helium I data, H_i was of the order of 0.1, and $0.32 \leq \mathrm{NuGr}^{-1/4} \leq 0.45$. Since Helium I data should be the approximate asymptote for the convection regime, it seems that the Helium II results tend toward the proper asymptote. While the analysis of [14] was only valid for $H_i \geq 0.5$, it is reasonable to expect that the asymptote for film boiling of ordinary liquids should be no smaller than the free convection, non-film boiling value of $\mathrm{NuGr}^{-1/4}$. Hermann [15] showed that for a horizontal cylinder in free convection with $\mathrm{Pr} = 0.7$, $\mathrm{NuGr}^{-1/4} = 0.313$, which means, in turn, that the Helium I data look reasonable.

Hence the present experimental results seem to support the theory of Rivers and McFadden. While local measurements of heat fluxes, film temperatures and velocities, and interfacial temperatures and velocities were not made, the average heat transfer results using constant-property calculations as indicated do agree quite well with the theory in two important respects. First, the experimental results agree with the predicted heat transfer measurements within 14 percent, when comparing the absolute value of the experimental deviations from theoretical predictions. In the transition and convection regimes the data tended to be lower than predicted analytically, indicating that convection within the film was overestimated in the mathematical model. The asymptotic analytical results for $Q_b = 0$ also indicate this.

Secondly, the three regimes of Fig. 5 were found to exist experimentally not only through correlation of heat transfer results but also through qualitative visual observation of the vapor film. Specifically, in regime 3, where Helium II properties predominate, the vapor film appeared to be extremely thin and concentric with the cylinder, in agreement with the theory [6, 7] and previous experimental results in this regime [3]. Further, in regime 1 where vapor film properties predominate, the film did grow around the cylinder, and at the top of the cylinder the film thickness was such that bubbles did break off from the surface of the film as in ordinary film boiling (although in the present case the bubbles condensed almost immediately, as would be expected in Helium II). This latter result also is expected from theory [6, 7].

Finally, Fig. 10 is a plot of Nusselt number as predicted from the present theory compared with measured Nusselt number. The agreement is indeed gratifying. It is concluded then that the Rivers and McFadden theory does offer a good method for the prediction of heat transfer rates during film boiling of Helium II. Not only are the functional relations known for laminar film boiling for the horizontal cylinder and vertical plate, see [7], but more importantly, a new parameter, Q_b, has been identified to be of sometimes paramount importance in determining Helium II film boiling heat transfer. It is suggested that functional relationships $\mathrm{Nu}(\mathrm{Gr}, \mathrm{Pr}, H_i, Q_b)$ should be investigated in the future for correlating Helium II film boiling data from other geometries, non-boundary layer type flows, turbulent films, very high heat fluxes, etc.

Acknowledgments

The authors would like to thank the National Science Foundation, Purdue Research Foundation, and the E. I. du Pont de Nemours and Company for their support of this research project.

References

1 Kapitza, P. L., "The Study of Heat Transfer in Helium II," *Journal of Physics*, USSR, Vol. 4, 1941, p. 181.

2 Holdredge, R. M., and McFadden, P. W., "Boiling Heat Transfer From Cylinders in a Saturated Liquid Helium II Bath," *Advances in Cryogenic Engineering*, Vol. 11, Plenum Press, New York, 1966, p. 507.

3 Rinderer, L., and Haenseler, F., "Heat Transfer in Superfluid Helium," *Helvetica Physica Acta*, Vol. 32, 1959, p. 322.

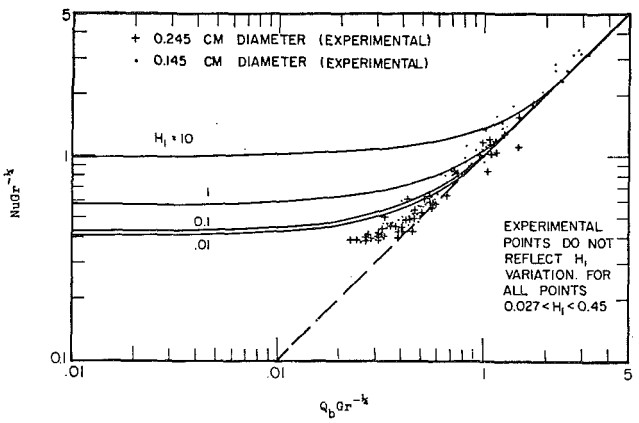

Fig. 9 Experimental results superimposed on the prediction of Rivers McFadden

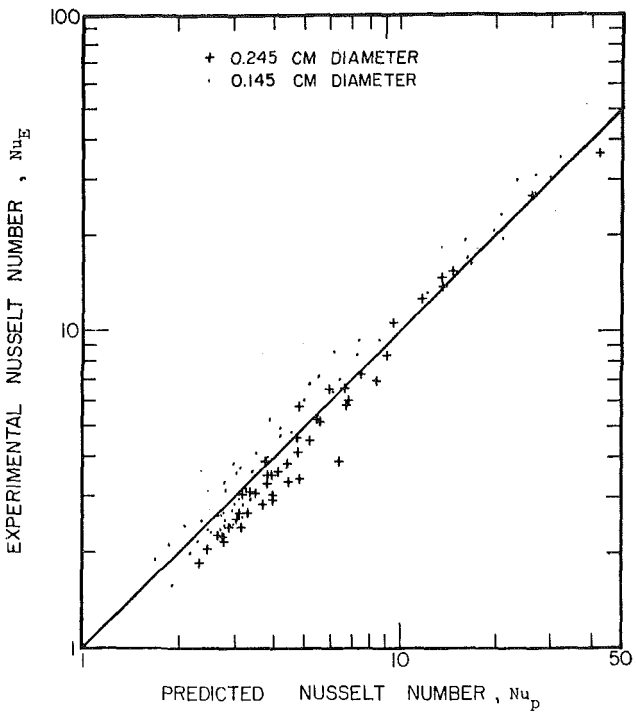

Fig. 10 Comparison of experimental results and the Rivers-McFadden prediction

4 Frederking, T. H. K., "Remarks on the Heat Transfer in Helium II at High Flux Values," UCLA Department of Engineering, Report No. 62-5, 1962, p. 22.

5 Goodling, J. S., and Irey, R. K., "Non-Boiling and Film Boiling Heat Transfer to a Saturated Bath of Liquid Helium," *Advances in Cryogenic Engineering*, Vol. 14, Plenum Press, New York, 1969, p. 159.

6 Rivers, W. J., and McFadden, P. W., "Film Free Convection in Helium II," JOURNAL OF HEAT TRANSFER, TRANS. ASME, Series C, Vol. 88, No. 4, November 1966, pp. 343–350.

7 Rivers, W. J., "An Analytical Investigation of Film Free Convection Heat Transfer to Liquid Helium II," PhD thesis, Purdue University, Lafayette, Indiana, 1964.

8 Holdredge, R. M., "Heat Transfer From Cylinders to a Saturated Liquid Helium II Bath," PhD thesis, Purdue University, Lafayette, Indiana, 1965.

9 McFadden, P. W., and Holdredge, R. M., "Heat Transfer to a Saturated Bath of Liquid Helium II," *Heat Flow Below 100 Deg K and Its Technological Applications*, Institut International du Froid and Pergamon Press, Paris, 1965, p. 259.

10 Frederking, T. H. K., "Waermeuebergang bei der Verdampfung der verfluessigten Gas Helium and Stickstoff," *Forschung auf dem Gebiete des Ingenieurwesens*, Vol. 27, 1961, p 17.

11 Frederking, T. H. K., Personal Communication.

12 Bromley, L. A., "Heat Transfer in Stable Film Boiling," *Chemical Engineering Progress*, Vol. 46, May 1950, p. 221.

13 Breen, B. P., and Westwater, J. W., "Effect of Diameter of Horizontal Tubes on Film Boiling Heat Transfer," *Chemical Engineering Progress*, Vol. 58, July 1962, p. 67.

14 McFadden, P. W., "An Analytical Investigation of Laminar Film Boiling," PhD thesis, Purdue University, Lafayette, Indiana, 1959.

15 Hermann, R., "Waermeuebertragung bei freier Stroemung am waagerechten Zylinder in zwei-atomigen Gasen," *VDT-Forschungsheft*, No. 379, Berlin, 1936.

4 Frederking, T. H. K., "Remarks on the Heat Transfer in Helium II at High Flux Values," UCLA Department of Engineering, Report No. 62-5, 1962, p. 22.
5 Goodling, J. S., and Irey, R. K., "Non-Boiling and Film Boiling Heat Transfer to a Saturated Bath of Liquid Helium," *Advances in Cryogenic Engineering*, Vol. 14, Plenum Press, New York, 1969, p. 159.
6 Rivers, W. J., and McFadden, P. W., "Film Free Convection in Helium II," JOURNAL OF HEAT TRANSFER, TRANS. ASME, Series C, Vol. 88, No. 4, November 1966, pp. 343-350.
7 Rivers, W. J., "An Analytical Investigation of Film Free Convection Heat Transfer to Liquid Helium II," PhD thesis, Purdue University, Lafayette, Indiana, 1964.
8 Holdredge, R. M., "Heat Transfer From Cylinders to a Saturated Liquid Helium II Bath," PhD thesis, Purdue University, Lafayette, Indiana, 1965.
9 McFadden, P. W., and Holdredge, R. M., "Heat Transfer to a Saturated Bath of Liquid Helium II," *Heat Flow Below 100 Deg K and Its Technological Applications*, Institut International du Froid and Pergamon Press, Paris, 1965, p. 259.
10 Frederking, T. H. K., "Waermeuebergang bei der Verdampfung der verfluessigten Gas Helium and Stickstoff," *Forschung auf dem Gebiete des Ingenieurwesens*, Vol. 27, 1961, p 17.
11 Frederking, T. H. K., Personal Communication.
12 Bromley, L. A., "Heat Transfer in Stable Film Boiling," *Chemical Engineering Progress*, Vol. 46, May 1950, p. 221.
13 Breen, B. P., and Westwater, J. W., "Effect of Diameter of Horizontal Tubes on Film Boiling Heat Transfer," *Chemical Engineering Progress*, Vol. 58, July 1962, p. 67.
14 McFadden, P. W., "An Analytical Investigation of Laminar Film Boiling," PhD thesis, Purdue University, Lafayette, Indiana, 1959.
15 Hermann, R., "Waermeuebertragung bei freier Stroemung am waagerechten Zylinder in zwei-atomigen Gasen," *VDT-Forschungsheft*, No. 379, Berlin, 1936.

DISCUSSION

T. H. K. Frederking[3]

The authors' classification of heat transfer regimes in superfluid He II appears to be quite useful when the region of large heat flux densities is considered. It is noted however, that the definition of regime 2 (Fig. 2) may not be generally acceptable in the light of the experiments of reference [5] and others. In other experiments [5] the establishment of several cooling curves in regime 2 (instead of one single function) is less obvious. In this context, it is noted that the present specimen geometry has been adopted also by Efferson.[4] Efferson's results show that the particular combination of specimen materials allows large temperature fluctuations at high heat fluxes. This point deserves attention since in cryogenic technology equipment these conditions appear to be more frequent than perfect temperature uniformity.

The major point of concern in the present paper is the applicability of the Rivers-McFadden model to He II film boiling. It is known that film boiling of subcooled liquids, aside from vapor film properties, is affected by the conditions in the *liquid* (stirring, forced convection, stratification). These effects shift the numercial values of the thermal conductances. Usually, however, the order of maguitude is not altered. Similarly, in film boiling of He II the heat transfer is influenced by the state of the *liquid* (bath temperature, liquid heat path), as demonstrated in Fig. 7 of the paper. In contrast to ordinary subcooled film boiling however, the thermodynamic conditions in the He II have not yet been resolved completely. Therefore, the related thermohydrodynamics has not yet been cast into forms which allow more detailed calculations of the present problem. In view of this state of the art, Rivers and McFadden displayed considerable intuition when they adopted the profiles of Fig. 4 for their integral treatment. As long as the range of validity of these profiles cannot yet be fully assessed, the Rivers-McFadden model gives (as documented in Fig. 10) a remarkable account of film boiling heat transfer in He II.

[3] University of California, Los Angeles, Calif.
[4] Efferson, K. R., "Heat Transfer From Cylindrical Surfaces to Liquid He I," *Journal of Applied Physics*, Vol. 40, 1969, p. 1995.

Authors' Closure

The authors would like to thank Dr. Frederking for his comments and for his analysis of the problems associated with film boiling in He II. In considering regime 2 (Fig. 2) two items should be kept in mind. First, Fig. 2 is intended as a qualitative representation and care should be taken in attaching quantitative significance. Second, Goodling and Irey [5] state,

> As noted in Figs. 2 and 3, the experimental data begins to deviate from the Khalatnikov theory at a heat flux on the order of 0.1 W/cm^2 and diverges by as much as 35% in the vicinity of the peak flux. This agrees with the data reported by Holdredge and McFadden [13].

Dr. Frederking's comments substantiate the statement in the text expressing the need for more results to confirm and describe this region.

The test section used by Efferson was somewhat different in that no provision was made to insure minimum thermal contact with the ends of the test section by way of the thermometer leads. Also, in using test sections of this design a match of thermal expansion between the film and glass is important. Helium I data were taken with the test sections used in this investigation, and the results[5] do not show the fluctuation noted by Efferson. However, Dr. Frederking's comments concerning the need for investigation in material combinations where large temperature fluctuations occur at high heat fluxes does point out a problem area.

[5] Holdredge, R. M., and McFadden, P. W., "Heat Transfer From Horizontal Cylinders to a Saturated Helium I Bath," Paper G-5, 1970 Cryogenic Engineering Conference, June 1970, Boulder, Colo., to be published in Vol. 16 of *Advances in Cryogenic Engineering*.

D. R. CASH
Chevron Research Co.,
Richmond, Calif.

G. J. KLEIN
Eastman Kodak Co.,
Rochester, N. Y.

J. W. WESTWATER
Professor of Chemical Engineering,
University of Illinois, Urbana, Ill.
Mem. ASME

Approximate Optimum Fin Design for Boiling Heat Transfer

For extended surfaces used in boiling liquids, the specified fin-base temperature may be such as to result in simultaneous nucleate, transition, and film boiling at adjacent positions on the fins. If the fins are spines of circular cross section, the optimum shape to minimize the volume of metal resembles a turnip, as shown by Haley and Westwater. The object of the new study was to develop easy-to-machine shapes using cones and cylinders. It was shown mathematically that two cones, base-to-base, give an excellent approximation to the turnip shape. Three such fins were constructed of copper and tested in Freon-113 at atmospheric pressure. The measured, peak heat duties were 5 to 70 percent higher than the predicted values, proving that the design method is conservative.

Introduction

THE EARLY *fin* formulas derived by Harper and Brown [1][1] and subsequent workers are for surfaces having uniform heat transfer coefficients. However, nonuniform heat transfer coefficients occur for applications of space radiation and for boiling liquids. For boiling, the variation in h may be in the order of 50 to 1. Photography [2, 3] demonstrates that nucleate, transition, and film boiling can exist simultaneously on a fin at adjacent positions and that such an arrangement is stable. Traditional fin formulas are not applicable for such boiling applications. Nor can one use the variable-h formulas published by Han and Lefkowitz [4], Chen and Zyskowski [5], Melese [6], and Gardner [7]. These authors were concerned with cases for which the heat transfer coefficient is a function of position rather than a function of temperature. For boiling, the value of h commonly is a known empirical function of ΔT expressed as a "boiling curve."

Lai and Hsu [8] proposed a simplified model for establishing a criterion for the incipience of nucleate boiling on a fin. They used a heat transfer coefficient that varied as the temperature difference to the nth power. A further study by Hsu [9] considered all modes of boiling on a fin, in which the heat transfer coefficients in the various boiling regions are approximated by various nth power functions of superheat.

Applications of fins in boiling liquids are increasing. The use of low-finned tubes in reboilers and in refrigeration equipment is common. Short stubby fins on large radio power tubes rejecting heat to boiling water are described by Beurtheret and others [10, 11].

A rational design method was proposed in 1966 by Haley and Westwater [12]. The key was an assumption that the heat transfer coefficient at any point on the nonisothermal heating surface is the same as would be obtained if the surface surrounding the point were at the same temperature. Thus, if the temperature at a point on the surface is known, the heat transfer coefficient at that point can be obtained from a boiling curve determined for an isothermal heating surface. This direct approach was shown to yield satisfactory agreement between numerical predictions and experimental measurements for single, cylindrical, copper fins of 0.25-in. dia tested in isopropanol and Freon-113. It was also shown that the minimum-volume spine of circular cross section (but of varying diameter) could be calculated if the heat duty and base temperature were given. The details of the numerical technique are available [12]. They are based on a method worked out by Wilkins [13, 14, 15] who was considering fins transferring heat by radiation. For all the boiling cases for which the fin-base

[1] Numbers in brackets designate References at end of paper.

Contributed by the Heat Transfer Division and presented at the Fluids Engineering, Heat Transfer, and Lubrication Conference, Detroit, Mich., May 24–27, 1970, of THE AMERICAN SOCIETY OF MECHANICAL ENGINEERS. Manuscript received by the Heat Transfer Division, June 10, 1969; revised manuscript received, November 9, 1969. Paper No. 70-HT-5.

Nomenclature

h = local heat transfer coefficient, Btu/hr sq ft deg F
k = thermal conductivity of fin, Btu/hr ft deg F
L_1 = length of first cone shown in Fig. 1(b), ft
L_2 = length of cylinder in main body in Fig. 1(b), ft
L_3 = length of second cone in Fig. 1(b), ft
L_S = length of stem, ft
Q = heat transfer rate, Btu/hr
r = radius of fin at position x, ft
R = maximum radius of main body, ft
R_S = radius of stem, ft
Δs = incremental slant length, ft
S = surface area of fin, sq ft
T = local temperature of fin, deg F
ΔT = temperature difference, metal to liquid, deg F
ΔT_B = temperature difference, metal to liquid at fin base ($x = 0$), deg F
x = distance from hot base of fin, ft

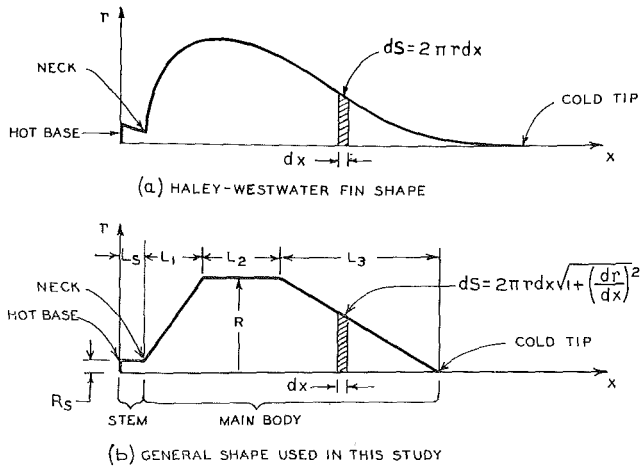

Fig. 1 General fin profiles for the optimum fin (upper sketch) and approximate optimum (lower) for heat transfer to boiling liquids. These are spines of circular cross section with symmetry about the x-axis.

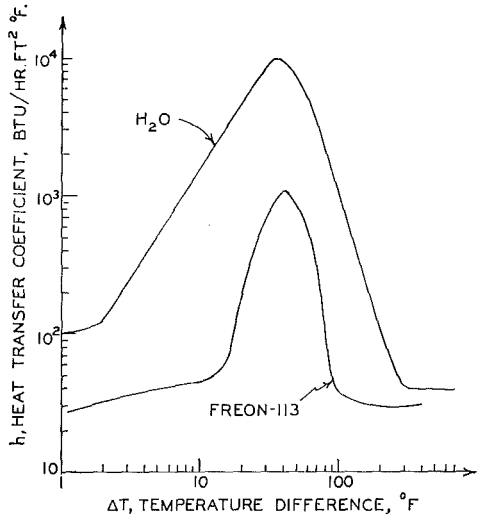

Fig. 2 Boiling curves used for prediction of fin performance. These were obtained for liquids boiling outside a 0.25-in. copper tube at 1 atm.

temperature was hot enough to correspond to film boiling at the base, the optimum spines were turnip-shaped. Photographs of a spine having this interesting shape are available [12]. Experimental data support the design. An objection to the turnip shape is that it is a complex geometric shape and is difficult to manufacture. The turnip shape can be approximated by a combination of simple geometric shapes such as cones and cylinders. The work reported in this paper considers such approximate optimum shapes.

Mathematical Analysis

Fig. 1(*a*) shows the turnip shape derived to be the optimum fin of minimum volume by Haley and Westwater [12]. Fig. 1(*b*) shows the general shape considered in the present paper. In both cases, a small stem at the hot end is the region where film boiling occurs. This is followed by a section of increasing size where transition boiling occurs. A thick region in the middle is where nucleate boiling predominates. At the cold end, each fin comes to a point, and here free convection may occur. The fin of Fig. 1(*b*) consists of a small-diameter cylinder, a cone, a large-diameter cylinder, and a second cone. The design problem becomes that of choosing the lengths and radii labeled in Fig. 1(*b*) so as to minimize the fin volume required to operate with a stated base temperature and a stated heat duty.

The problem was solved numerically on an IBM 7094 computer and also (in part) on an IBM 1800. The method was a modification of that used earlier [12]. It was assumed that the heat was transferred within the fin only in an axial direction. A detailed examination of this assumption by Kraus [16] for one earlier case showed that the assumption was satisfactory, at least for a cylindrical fin of 5 to 1 aspect ratio. For the present study the fin was assumed to be made up of 400 increments. One increment, with thickness labeled dx, is shown in Fig. 1(*b*). The heat entering the segment is given by equation (1),

$$Q = -k\pi r^2(dT/dx) = -k\pi r^2(d\Delta T/dx) \quad (1)$$

The heat transferred through the surface of the segment to the surrounding liquid is given by equation (2),

$$dQ = h\Delta T dS \quad (2)$$

All the parameters are variables. The cross section of the fin at position x is assumed to be at uniform temperature T, the radius there is r, the temperature difference between the fin and the surrounding boiling liquid is ΔT, and the heat transfer coefficient corresponding to this ΔT is h. The wetted surface area of the elemental volume is dS. Two functionalities of h versus ΔT were used, corresponding to Freon-113 (CCl_2F-$CClF_2$) and water boiling at atmospheric pressure on 0.25-in-dia horizontal copper tubes. These were taken from Haley and Westwater [12] and are reproduced in Fig. 2. The thermal conductivity of copper is a function of temperature and was so used in the equations. Four other values of k for the fins were used, but as constants, to show the effect of this parameter for water as the fluid.

The heat duty of the fin is given by the heat entering at the hot base, $Q = -k\pi R_s^2(dT/dx)_{x=0}$. This duty was assumed to be given. At the cold end, the last elemental volume receives an increment of heat dQ by conduction and must dissipate this last residue of heat according to equation (2). The digital computer was programmed so as to use a Runge-Kutta fourth-order method seeking a geometry to satisfy equations (1) and (2), the selected heat duty, and the temperature at the fin base. The print-out gave the temperature at the cold tip as well.

Design of Stem. Preliminary calculations showed that the stem of the fin corresponds to film boiling and that the fraction of the total heat duty dissipated from the surface of the stem is very small. The value is 1 percent for Freon-113 on an optimum copper spine having a tapered stem with $\Delta T_B = 400$ deg F. In addition, the stem volume is negligible compared to the total. Therefore it was decided that independent design procedures for the stem and main body of the new fin are justified. The function of the stem is to provide thermal resistance to decrease the metal temperature from that at the base to that corresponding to the film boiling crisis (minimum in the boiling curve). These minima are $\Delta T = 94$ deg F for Freon-113 and 289 deg F for water. The stem chosen was cylindrical with a diameter equal to the minimum neck diameter of the Haley-Westwater spine. Actually, any convenient small diameter is acceptable and has little effect on the fin volume. Once the neck diameter is selected it is easy to use the conduction equation (ignoring film-boiling heat transfer out the side) to compute the necessary length of the neck. Thus the size of the stem is fixed by the given heat duty, the ΔT at the fin base, the metal used, and the minimum ΔT in the boiling curve. The maximum temperature of the stem is limited only by the melting point of the metal.

Design of Main Body. For a given liquid and fin material, there were four geometric parameters to be determined for the main body with a given heat duty. Values of L_1, L_2, and R, in Fig. 1(*b*), were selected, and then an iteration was used to converge on the value of L_3, which caused the heat remaining in the fin to become zero just as the tip was reached.

One more limiting condition was imposed on the design. To assure stability in operation, the local heat flux near the cold tip should be somewhat less than the maximum flux of the boiling curve. It was specified arbitrarily that a design was satisfactory only if the cold-tip temperature was at or below the temperature corresponding to half the peak flux. These upper limits for the cold tip turned out to be a ΔT of 31.0 deg F for Freon-113 and 27.3 deg F for water.

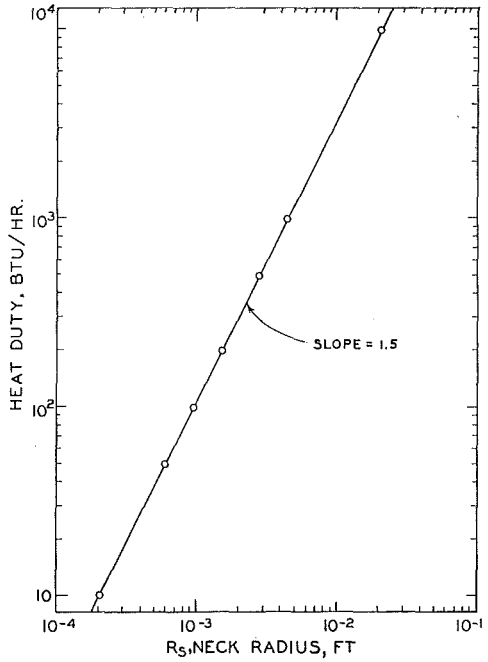

Fig. 3 Radius for optimum stem for copper spine in boiling Freon-113. The symbols here and in Figs. 4–7 show computed values.

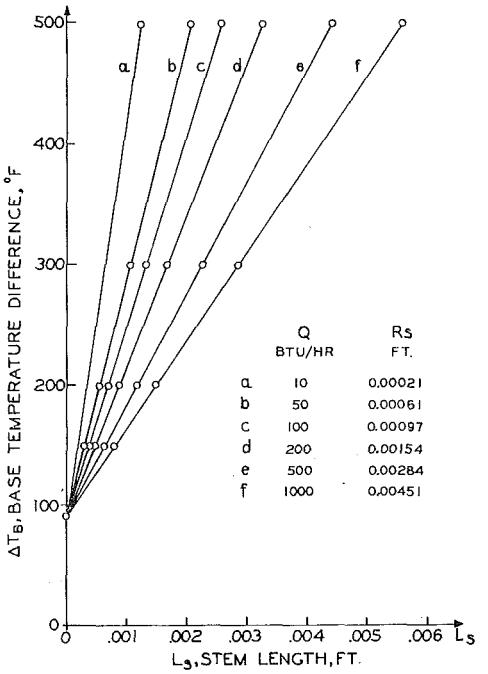

Fig. 4 Length for optimum stem for copper spine in boiling Freon-113

For each heat duty, an infinite number of combinations of L_1, L_2, L_3, and R will work. Each has a different fin volume. Graphing techniques were used to guide the selection of dimensions so as to find the fin of minimum volume within five significant figures. A detailed description of the procedure is available [17].

Predictions for Freon-113

The stem radius and stem length for Freon-113 on copper spines are given in Figs. 3 and 4. These are minimum-volume stems, but in some cases the dimensions are so small as to pose difficulties in machining. As described above, both the radius and length may be increased in a rational manner with a small penalty in volume.

For the main body of the fin, two important facts became evident. First, the cold-tip temperature usually was the highest

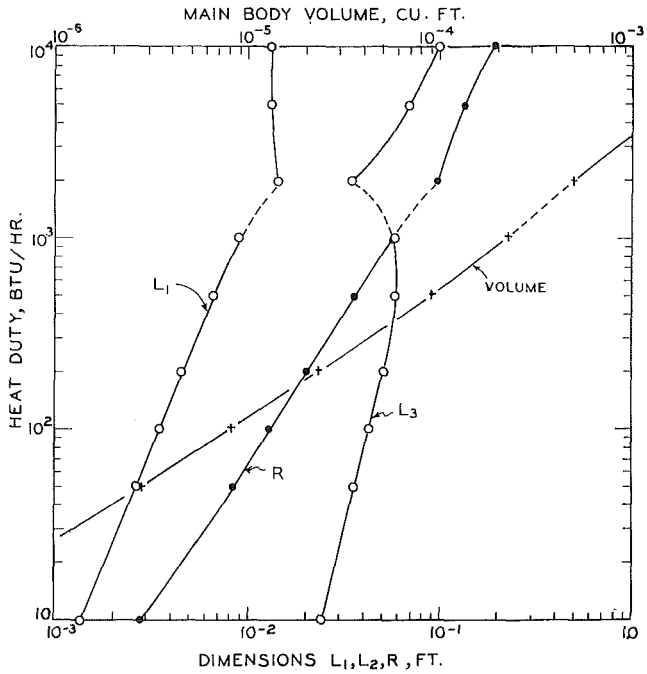

Fig. 5 Dimensions of main body of approximate optimum spine of copper in Freon-113

permitted by the rule described above. Mathematically, if the tip temperature requirement were relaxed, smaller fin volumes would result. However, such fins could become shaped like thumb tacks and in use would be unstable to perturbations in ΔT_B.

Second, the minimum fin volumes all correspond to values of L_2 equal to zero. No central cylinder should be used between the two cones. The result is that the main body is composed simply of two cones, base-to-base, and three dimensions suffice to specify the combination. Fig. 5 shows the optimum parameters for the copper–Freon-113 system. At a low heat duty such as 10 Btu/hr, the optimum fin has a length-to-diameter ratio of about 5 to 1. As the duty becomes 1000 Btu/hr, the ratio becomes 0.6 to 1. In other words, low duties call for small slender fins, whereas high duties call for large fat fins. The optimum fin volume increases smoothly with the required heat duty, although the mathematically predicted values of the cone length L_3 show a discontinuity in slope at a duty of about 2000 Btu/hr. It is believed that a smooth dimple rather than a sharp cusp would result if a true differential dx could be used rather than a finite Δx in the computations. The slope of the volume versus heat duty curve in Fig. 5 is less than unity; therefore, for a given total heat transfer rate, it is better to use many small fins rather than one large fin. The two factors which should control the final size and number of fins selected are the size of fins which can be readily manufactured and the minimum spacing needed between fins to avoid bubble interference. The spacing problem has not been studied yet.

Predictions for Water

Optimum fin dimensions for the two-cone main body of copper used with water are shown in Fig. 6. Here the discontinuity in L_3 was found to be near a heat duty of 200 Btu/hr. Similar graphs for water on aluminum, brass, mild steel, and stainless steel are available [17].

If the fin volume for a constant heat duty is considered, a surprising fact emerges. In some cases a high thermal conductivity for the metal is undesirable. Fig. 7 shows that for a duty of 20 Btu/hr copper ($k = 218$) is not the best choice. A fin of mild steel ($k = 26$) will do the job with a smaller volume. Minima in the volume versus k curves exist for water at all heat duties examined below 500 Btu/hr. At 2000 Btu/hr no intermediate minimum exists for any values of k examined, and the least volume

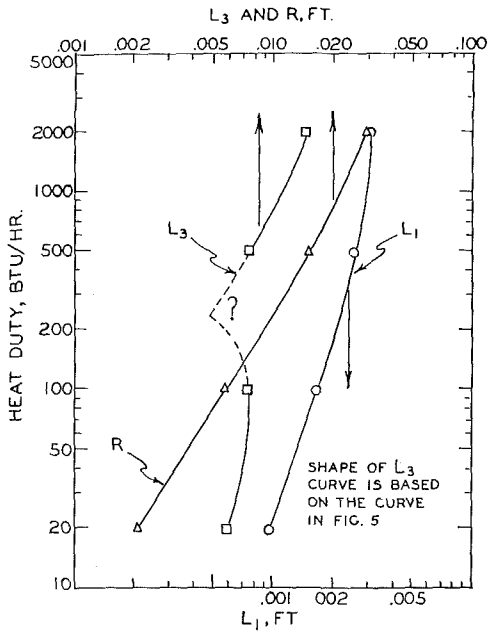

Fig. 6 Dimensions of main body of copper in water

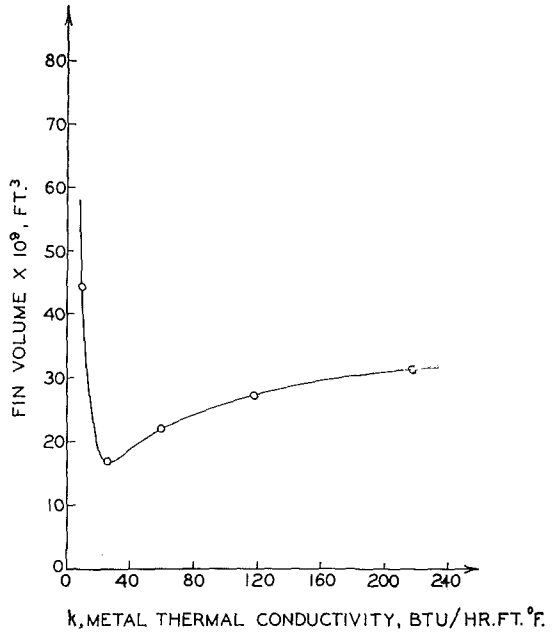

Fig. 7 Effect of thermal conductivity of a fin on its volume, in water at 20 Btu/hr

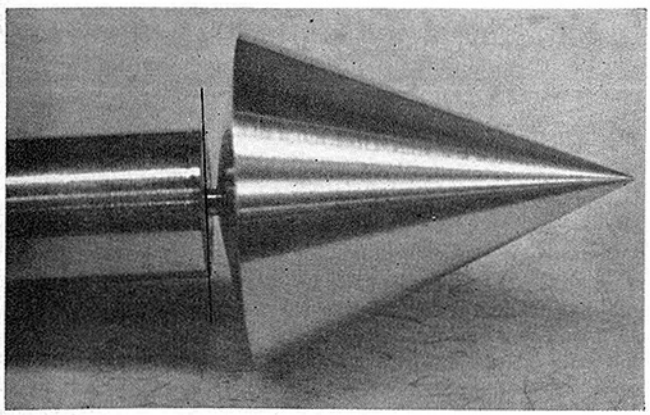

Fig. 8 Experimental Fin A, an approximate optimum shape of two cones base-to-base, of copper, designed for 254 Btu/hr in Freon-113. The wall of the boiler is indicated by a vertical line drawn on the photograph. To the left is a 0.25-in. supporting rod.

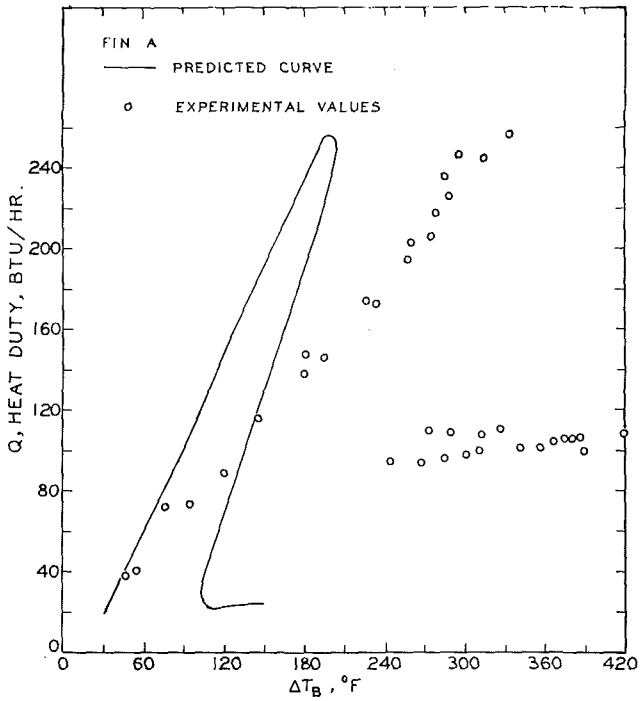

Fig. 9 Performance of Fin A in Freon-113

is obtained with the metal of highest thermal conductivity (copper). But as the duty is decreased from 500 Btu/hr to 20 Btu/hr, the best k decreases from 180 to 28 Btu/hr ft deg F. This implies that for sufficiently low heat duties a non-metal such as carbon might be the optimum material.

Experimental

Three fins were constructed of pure copper and tested to demonstrate the reliability of the design for the approximate optimum shape. They were computed for use in Freon-113 at atmospheric pressure. The dimensions are given below. Fig. 8 is a photograph of Fin A.

Table 1 Fin dimensions

	Fin A	Fin B	Fin C
Duty, Btu/hr	254	127	127
L_1, ft	0.0050	0.0037	0.0037
L_3, ft	0.0540	0.0455	0.0455
R, ft	0.0235	0.0153	0.0153
L_s, ft	0.00095	0.00077	0.0050
R_s, ft	0.00182	0.00116	0.0030
Vol., cu ft ($\times 10^5$)	3.35	1.20	1.21
ΔT_B, deg F	200	200	200

The equipment used was the same as used by Haley and Westwater [12]. It consisted of a 1-gal stainless steel boiler with glass windows. Vapor rose to an overhead condenser. Condensate was metered to obtain the heat duty. The fin and its 0.25-in. supporting rod were threaded into a 2-in-dia copper slug containing a 350-watt electric heater. In the supporting rod were three thermocouples on the geometric axis. The gradients in these gave a check on the heat duty. The heat balances closed within 15 percent. The fin was sealed in the wall of the boiler with neoprene cement and a thin brass gasket. The temperature of the fin base, namely at the boiler wall, was computed by extrapolation of the temperatures in the supporting rod. The difference between the fin base temperature and the saturated liquid temperature gave the base ΔT.

Fig. 9 shows the data for Fin A as well as the predicted curve. The predicted curve has a maximum at 254 Btu/hr. The actual fin operated successfully up to 266 Btu/hr at which point the electric heater burned out. The data shown for high values of ΔT are in the film-boiling regime and were obtained by "dry-charging," that is introducing boiling liquid into the boiler with

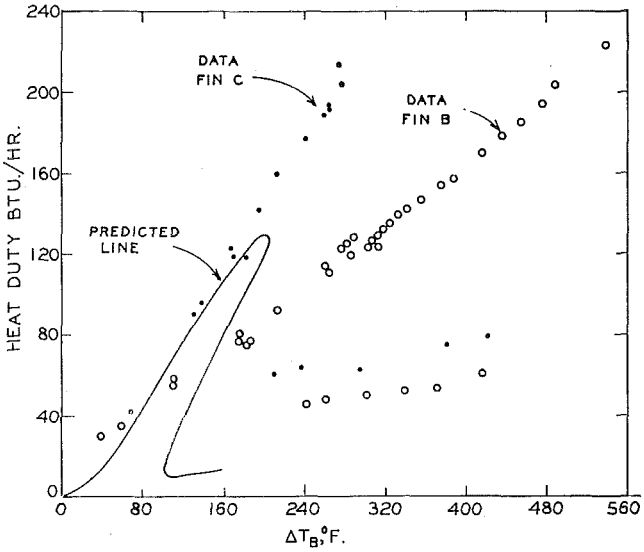

Fig. 10 Performance of Fins B and C in Freon-113. The fins had identical main bodies, but different stems.

the fin already hot enough to cause film boiling. The test showed that the design maximum heat duty was achieved with a fin having the approximate optimum shape. Using the same volume of material in the form of an optimum cylinder of constant diameter would give a heat duty of 140 Btu/hr, as computed by the method of Haley and Westwater. This heat transfer difference of 45 percent shows that the two-cone design clearly is superior to the best cylinder. The optimum turnip-shaped fin of Haley and Westwater having the same volume as the two-cone fin was described earlier [12]. It had a predicted duty of 200 Btu/hr, but actually operated at 274 Btu/hr. The underestimation of the performance was due in part to effects of turbulence on the film-boiling areas of the fin and also to underestimation of the surface area of the turnip fin. The area of the turnip fin had been based on Δx values. The accurate area requires use of the incremental slant length Δs, rather than the increment Δx. Fig. 1(*a*) makes clear the distinction. For the two-cone fin, it was easy to use the exact surface area.

The results for Fins B and C are given in Fig. 10. Fin B was used first. It had a design duty of 127 Btu/hr. During the test it was possible to traverse over the peak of the curve and achieve film boiling. The experimental maximum duty was 70 percent greater than the theoretical value. The design clearly is conservative. The experimental ΔT values at various heat transfer rates in Fig. 10 (for Fin B) as well as in Fig. 9 (for Fin A) do not match closely the predicted ΔT values. It was suspected that this could result from errors in construction of the stems of these fins. The stems are very small and high accuracy in their construction is difficult to achieve. Therefore Fin C was built. All dimensions of the main body were the same as for Fin B, and the same heat duty of 127 Btu/hr was computed. The stem, however, was made larger for Fin C so that better machining accuracy was possible. The thermal resistance of the stems for Fins B and C were intended to be identical. Fig. 10 shows that the same maximum heat duty was observed. The Q versus ΔT values for Fin C are close to the predicted functionality. It is concluded that errors in the stem construction can cause significant effects on the ΔT versus Q relationship, although the maximum heat duty is almost unaffected. It is wise to use stems larger than the optimum stems for any case in which the stem manufacture is difficult. The thermal resistance of the larger stem must equal that of the optimum stem.

Conclusions

1 A design method for fins in boiling liquids has been developed. A two-cone assembly attached to a small cylindrical neck is a good approximation to the optimum spine. The procedure is conservative and results in fins which give higher heat duties than computed.

2 The new shape has calculated heat duties per unit volume greater than calculated for cylindrical spines.

3 Calculations indicate that there is an optimum thermal conductivity for each duty. The optimum k decreases as the heat duty decreases.

4 The method used in this study can be extended to longitudinal and transverse fins.

Acknowledgment

We gratefully acknowledge the financial support of the National Science Foundation. The Union Carbide Corporation provided a graduate fellowship.

References

1 Harper, D. R., and Brown, W. B., "Mathematical Equations for Heat Conduction in the Fins of Air-Cooled Engines," National Advisory Commission Aeronautics, Report 158, 1922.

2 Haley, K. W., and Westwater, J. W., "Heat Transfer From a Fin to a Boiling Liquid," *Chemical Engineering Science*, Vol. 20, 1965, p. 711.

3 Westwater, J. W., and Haley, K. W., "Boiling Heat Transfer From Single Fins," Motion Picture, University of Illinois, Urbana, Ill., 1965.

4 Han, L. S., and Lefkowitz, S. G., "Constant Cross-Section Fin Efficiencies for Non-Uniform Surface Heat Transfer Coefficients," ASME Paper No. 60-WA-41, 1960.

5 Chen, S., and Zyskowski, G. L., "Steady-State Heat Conduction in a Straight Fin With Variable Film Coefficients," ASME Paper No. 63-HT-12, 1963.

6 Melese, G. J., "Efficacité-d'Une Ailette l'ongitudinale Avec Variation du Coefficient d'Echange de Chaleur le Long de l'Ailette," *Journal of Nuclear Energy* (London), Vol. 5, 1957, p. 285.

7 Gardner, K. A., Discussion in *Proceedings of the General Discussion on Heat Transfer*, Institution of Mechanical Engineers, London, England, 1951, p. 214.

8 Lai, F. S., and Hsu, Y. Y., "Temperature Distribution in a Fin Partially Cooled by Nucleate Boiling," *AIChE Journal*, Vol. 13, No. 4, 1967, pp. 817–821.

9 Hsu, Y. Y., "Analysis of Boiling on a Fin," NASA Technical Note D-4797, Sept. 1968.

10 Beurtheret, C., "The 'Vapotron' Technique," *Revue Technique*, Compagnie Francaise Thomson-Houston, No. 24, Paris, 1956.

11 Demange, P., Douget, E., and Le France, J. D., "Le Vapotron Nuclaire," *Revue Technique*, Compagnie Francaise Thomson-Houston, No. 38, Paris, 1963.

12 Haley, K. W., and Westwater, J. W., "Boiling Heat Transfer From Single Fins," *Proceedings of the Third International Heat Transfer Conference*, AIChE-ASME, Vol. 3, 1966, p. 245.

13 Wilkins, J. E., Jr., "Minimizing the Mass of Thin Radiating Fins," *Journal of Aerospace Sciences*, Vol. 27, No. 2, 1960, p. 145.

14 Wilkins, J. E., Jr., "Minimum Mass Thin Fins for Space Radiators," *Proceedings 1960, Heat Transfer and Fluid Mechanics Institute*, Stanford University Press, 1960.

15 Wilkins, J. E., Jr., "Minimum Mass Thin Fins Which Transfer Heat Only by Radiation to Surroundings at Absolute Zero," *Journal of the Society of Industrial and Applied Mathematics*, Vol. 8, 1960, pp. 630–639.

16 Kraus, A. D., Discussion of "Boiling Heat Transfer From Single Fins," by Haley, K. W., and Westwater, J. W., *Proceedings of the Third International Heat Transfer Conference*, AIChE, Vol. 6, 1966, p. 242.

17 Cash, D. R., MS thesis, University of Illinois, Urbana, Ill., 1969, 103 pp.

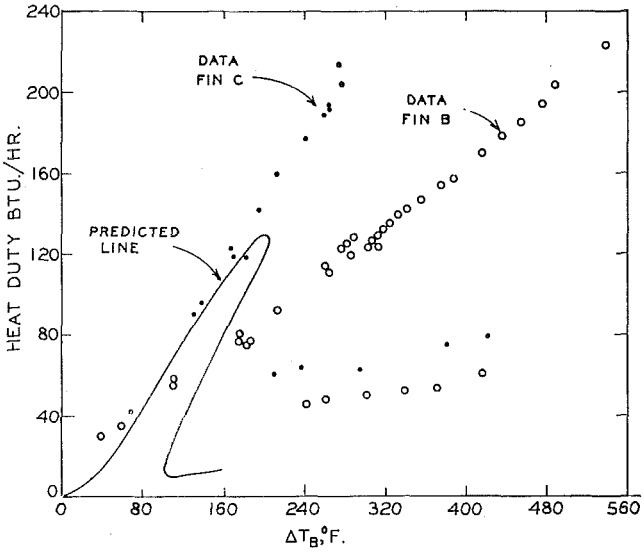

Fig. 10 Performance of Fins B and C in Freon-113. The fins had identical main bodies, but different stems.

the fin already hot enough to cause film boiling. The test showed that the design maximum heat duty was achieved with a fin having the approximate optimum shape. Using the same volume of material in the form of an optimum cylinder of constant diameter would give a heat duty of 140 Btu/hr, as computed by the method of Haley and Westwater. This heat transfer difference of 45 percent shows that the two-cone design clearly is superior to the best cylinder. The optimum turnip-shaped fin of Haley and Westwater having the same volume as the two-cone fin was described earlier [12]. It had a predicted duty of 200 Btu/hr, but actually operated at 274 Btu/hr. The underestimation of the performance was due in part to effects of turbulence on the film-boiling areas of the fin and also to underestimation of the surface area of the turnip fin. The area of the turnip fin had been based on Δx values. The accurate area requires use of the incremental slant length Δs, rather than the increment Δx. Fig. 1(*a*) makes clear the distinction. For the two-cone fin, it was easy to use the exact surface area.

The results for Fins B and C are given in Fig. 10. Fin B was used first. It had a design duty of 127 Btu/hr. During the test it was possible to traverse over the peak of the curve and achieve film boiling. The experimental maximum duty was 70 percent greater than the theoretical value. The design clearly is conservative. The experimental ΔT values at various heat transfer rates in Fig. 10 (for Fin B) as well as in Fig. 9 (for Fin A) do not match closely the predicted ΔT values. It was suspected that this could result from errors in construction of the stems of these fins. The stems are very small and high accuracy in their construction is difficult to achieve. Therefore Fin C was built. All dimensions of the main body were the same as for Fin B, and the same heat duty of 127 Btu/hr was computed. The stem, however, was made larger for Fin C so that better machining accuracy was possible. The thermal resistance of the stems for Fins B and C were intended to be identical. Fig. 10 shows that the same maximum heat duty was observed. The Q versus ΔT values for Fin C are close to the predicted functionality. It is concluded that errors in the stem construction can cause significant effects on the ΔT versus Q relationship, although the maximum heat duty is almost unaffected. It is wise to use stems larger than the optimum stems for any case in which the stem manufacture is difficult. The thermal resistance of the larger stem must equal that of the optimum stem.

Conclusions

1 A design method for fins in boiling liquids has been developed. A two-cone assembly attached to a small cylindrical neck is a good approximation to the optimum spine. The procedure is conservative and results in fins which give higher heat duties than computed.

2 The new shape has calculated heat duties per unit volume greater than calculated for cylindrical spines.

3 Calculations indicate that there is an optimum thermal conductivity for each duty. The optimum k decreases as the heat duty decreases.

4 The method used in this study can be extended to longitudinal and transverse fins.

Acknowledgment

We gratefully acknowledge the financial support of the National Science Foundation. The Union Carbide Corporation provided a graduate fellowship.

References

1 Harper, D. R., and Brown, W. B., "Mathematical Equations for Heat Conduction in the Fins of Air-Cooled Engines," National Advisory Commission Aeronautics, Report 158, 1922.

2 Haley, K. W., and Westwater, J. W., "Heat Transfer From a Fin to a Boiling Liquid," *Chemical Engineering Science*, Vol. 20, 1965, p. 711.

3 Westwater, J. W., and Haley, K. W., "Boiling Heat Transfer From Single Fins," Motion Picture, University of Illinois, Urbana, Ill., 1965.

4 Han, L. S., and Lefkowitz, S. G., "Constant Cross-Section Fin Efficiencies for Non-Uniform Surface Heat Transfer Coefficients," ASME Paper No. 60-WA-41, 1960.

5 Chen, S., and Zyskowski, G. L., "Steady-State Heat Conduction in a Straight Fin With Variable Film Coefficients," ASME Paper No. 63-HT-12, 1963.

6 Melese, G. J., "Efficacité-d'Une Ailette l'ongitudinale Avec Variation du Coefficient d'Echange de Chaleur le Long de l'Ailette," *Journal of Nuclear Energy* (London), Vol. 5, 1957, p. 285.

7 Gardner, K. A., Discussion in *Proceedings of the General Discussion on Heat Transfer*, Institution of Mechanical Engineers, London, England, 1951, p. 214.

8 Lai, F. S., and Hsu, Y. Y., "Temperature Distribution in a Fin Partially Cooled by Nucleate Boiling," *AIChE Journal*, Vol. 13, No. 4, 1967, pp. 817–821.

9 Hsu, Y. Y., "Analysis of Boiling on a Fin," NASA Technical Note D-4797, Sept. 1968.

10 Beurtheret, C., "The 'Vapotron' Technique," *Revue Technique*, Compagnie Francaise Thomson-Houston, No. 24, Paris, 1956.

11 Demange, P., Douget, E., and Le France, J. D., "Le Vapotron Nuclaire," *Revue Technique*, Compagnie Francaise Thomson-Houston, No. 38, Paris, 1963.

12 Haley, K. W., and Westwater, J. W., "Boiling Heat Transfer From Single Fins," *Proceedings of the Third International Heat Transfer Conference*, AIChE-ASME, Vol. 3, 1966, p. 245.

13 Wilkins, J. E., Jr., "Minimizing the Mass of Thin Radiating Fins," *Journal of Aerospace Sciences*, Vol. 27, No. 2, 1960, p. 145.

14 Wilkins, J. E., Jr., "Minimum Mass Thin Fins for Space Radiators," *Proceedings 1960, Heat Transfer and Fluid Mechanics Institute*, Stanford University Press, 1960.

15 Wilkins, J. E., Jr., "Minimum Mass Thin Fins Which Transfer Heat Only by Radiation to Surroundings at Absolute Zero," *Journal of the Society of Industrial and Applied Mathematics*, Vol. 8, 1960, pp. 630–639.

16 Kraus, A. D., Discussion of "Boiling Heat Transfer From Single Fins," by Haley, K. W., and Westwater, J. W., *Proceedings of the Third International Heat Transfer Conference*, AIChE, Vol. 6, 1966, p. 242.

17 Cash, D. R., MS thesis, University of Illinois, Urbana, Ill., 1969, 103 pp.

DISCUSSION

Y. Y. Hsu[2]

The authors are to be commended for taking on the difficult task of determining optimum fin design for boiling and being able to find some very interesting results. Their analysis is based upon the one-dimensional conduction model. This model might be a valid assumption if the fin is slender. However, when the fin becomes short and stubby, such as represented in Figs. 5 and 6

[2] NASA Lewis Research Center, Cleveland, Ohio.

for high heat duty, the longitudinal one-dimensional conduction assumption should be replaced by a two-dimensional approach, which, of course, is much more difficult. One possible alternative for the special case of $L/D = 1$ would be a radial-conduction approach assuming the fin is approximated by a hemisphere. When the heat duty is near the peak of the curves $Q(\Delta T)$ as shown in Figs. 9 or 10, we always have to be cautious lest a further increase of ΔT will bring the heat duty to the minimum point. One way to avoid this situation is to operate at off-design condition, say, at 50 percent of designed ΔT. But then the question to ask is whether the optimum design should be based upon the ΔT for the peak duty or ΔT for the real operating condition. It would be interesting to compare the heat duty curves of two fins optimized for two different operating conditions.

Authors' Closure

Dr. Hsu raises several important points. We are carrying out numerous two-dimensional calculations. They show, surprisingly, that the one-dimensional assumption is fairly good for predicting the heat duty even for an L/D approaching unity. The main error comes in the ΔT. Also we are making calculations for spherical segments (not necessarily hemispheres) and intend to test these experimentally.

The selection of an off-design condition such as half the critical ΔT or half the peak heat flux is a key issue. This touches the philosophy of design rather than the science of design. The answer will depend on the confidence and experience of the designer.

N. W. WILSON
Research Student.
Assoc. Mem. ASME

J. O. MEDWELL
Lecturer in Mechanical Engineering.
Assoc. Mem. ASME

Department of Mechanical Engineering,
University College of Swansea,
Swansea, Glamorgan, U. K.

An Analysis of the Developing Turbulent Hydrodynamic and Thermal Boundary Layers in an Internally Heated Annulus

The problems of the simultaneous growth of the hydrodynamic and thermal boundary layers in the entrance region of a concentric annulus with a uniformly heated core are investigated using the momentum and energy integral equations, along with a modified Reichardt momentum eddy diffusivity variation. A radius ratio range of 0.2 to 0.8 was investigated over a Reynolds number range from 10^4 to 3×10^5 for a Prandtl number of 0.7. The analysis predicts velocity and temperature profiles and local variations of normalized pressure gradients and Nusselt numbers which are in satisfactory agreement with experimental data. The analysis also shows that the flow is hydrodynamically fully developed within 10 equivalent diameters of the annulus inlet, while a further 30 equivalent diameters are required for the thermal boundary layers to reach the outer insulated wall of the annulus.

Introduction

The concentric annular geometry has many important engineering applications such as in heat exchangers and axial-flow turbomachinery. In this respect, many research workers [1–15][1] have directed their interest to the particular cases of fully developed turbulent incompressible flow in annuli in which the annulus core may or may not be heated. Frequently in practice, however, the fluid flows through relatively short lengths of annular sections so that the entry region, which precedes fully developed conditions in any ducted flow, has a considerable effect on overall pressure drop and heat transfer rates. In spite of this, relatively little research of either an experimental or theoretical nature appears to have been done on this problem.

The development of the thermal and hydrodynamic boundary layers in the entrance of an annulus obviously depends on the shape of the inlet to the annular passage. Okiishi and Serovy [16] investigated experimentally the development of the hydrodynamic boundary layer in an annulus and showed that fully developed velocity profiles are achieved in shorter distances from the inlet by using a square-edged entrance than by using a rounded entrance. This they attributed to the fact that with a rounded entrance a laminar boundary layer precedes the turbulent boundary layer, whereas for the square-edged entrance no such transition is present. Using a rounded entrance, however, does give rise to a reasonably uniform velocity profile at the entrance and this is a convenient condition, provided the boundary layers are turbulent from their initiation, from which to embark on a theoretical analysis.

Roberts and Barrow [17] approached this condition using suitable combinations of boundary layer tripping devices. Their experiments were made with air in the entry region of internally heated annuli using two radius ratios measuring local heat transfer rates. This information was used to test a modified Reynolds analogy applied to the problem.

The present work is an attempt to analyze, using the von Kármán integral techniques, the case in which the hydrodynamic and thermal boundary layers develop simultaneously in the entrance of an annulus, the core of which is heated uniformly. It is assumed that the boundary layers are initiated from the same station in the annulus entrance and that, at that position, the fluid temperature and velocity distributions are uniform. In addition, it has been assumed that all fluid properties are constant and that when fully developed flow is achieved the positions of maximum velocity and zero shear stress are coincident.

Analysis

Growth of the Hydrodynamic Boundary Layers. The momentum-integral equation for the inner wall boundary layer as described by Okiishi and Serovy may be written as

$$-\frac{d}{dx}\left\{\int_{r_1}^{r_{\delta_1}} \rho u^2 r dr\right\} + u_\delta \frac{d}{dx} \times \left\{\int_{r_1}^{r_{\delta_1}} \rho u r dr\right\} = \tau_{01} r_1 + \frac{dp}{dx}\frac{(r_{\delta_1}^2 - r_1^2)}{2} \quad (1)$$

where $r_{\delta_1} = r_1 + \delta_1$; see Fig. 1(*a*).

For constant fluid properties and irrotational flow between the

[1] Numbers in brackets designate References at end of paper.

Contributed by the Heat Transfer Division and presented at the Fluids Engineering, Heat Transfer, and Lubrication Conference, Detroit, Mich., May 24–27, 1970, of The American Society of Mechanical Engineers. Manuscript received by ASME Heat Transfer Division, November 1, 1968; revised manuscript received, June 25, 1969; final revision received, September 22, 1969. Paper No. 70-HT-9.

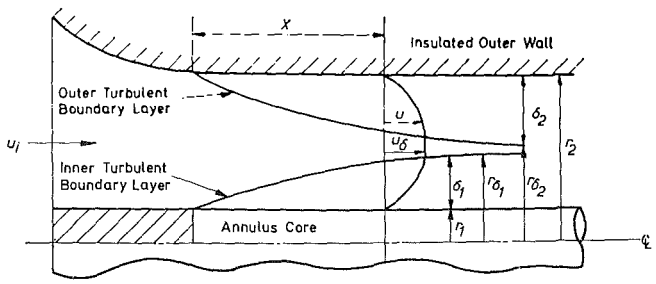

Fig. 1(a) Idealized model of developing hydrodynamic boundary layers in an annulus

inner and outer developing boundary layers

$$\frac{dp}{dx} = -\rho u_\delta \frac{du_\delta}{dx} \tag{2}$$

Since

$$\frac{d}{dx}\left\{u_\delta \int_{r_1}^{r_{\delta_1}} urdr\right\} = u_\delta \frac{d}{dx}\left\{\int_{r_1}^{r_{\delta_1}} urdr\right\} + \left\{\int_{r_1}^{r_{\delta_1}} urdr\right\} \frac{du_\delta}{dx} \tag{3}$$

and substituting equation (2) into equation (1) then the following expression is obtained:

$$\frac{d}{dx}\left\{\int_{r_1}^{r_{\delta_1}} (u_\delta - u)urdr\right\} + \left\{\frac{u_\delta(r_{\delta_1}^2 - r_1^2)}{2} - \int_{r_1}^{r_{\delta_1}} urdr\right\} \frac{du_\delta}{dx} = \frac{\tau_{01} r_1}{\rho} \tag{4}$$

The corresponding equation for the outer wall boundary layer is

$$\frac{d}{dx}\left\{\int_{r_{\delta_2}}^{r_2} (u_\delta - u)urdr\right\} + \left\{\frac{u_\delta(r_2^2 - r_{\delta_2}^2)}{2} - \int_{r_{\delta_2}}^{r_2} urdr\right\} \frac{du_\delta}{dx} = \frac{\tau_{02} r_2}{\rho} \tag{5}$$

where $r_{\delta_2} = r_2 - \delta_2$.

Equation (4) may be rewritten as

$$d\left(\frac{x}{r_1}\right) = \frac{1}{\frac{\tau_{01} r_1^2}{\rho}} d\left\{\int_{r_1}^{r_{\delta_1}} (u_\delta - u)urdr\right\} + \frac{1}{\frac{\tau_{01}}{\rho}} \left\{\frac{u_\delta(r_{\delta_1}^2 - r_1^2)}{2r_1^3} - \frac{1}{r_1^3}\int_{r_1}^{r_{\delta_1}} urdr\right\} d(u_\delta r_1) \tag{6}$$

By making use of the dimensionless variables as defined in the Nomenclature this expression becomes

$$d\left(\frac{x}{r_1}\right) = \frac{1}{r_1{}^{+2}} d\left\{\int_{r_1{}^+}^{r_{\delta_1}{}^+} (u_{\delta_1}{}^+ - u^+)u^+ r^+ dr^+\right\} + \left\{\frac{u_{\delta_1}{}^+(r_{\delta_1}{}^{+2} - r_1{}^{+2})}{2r_1{}^{+3}} - \frac{1}{r_1{}^{+3}}\int_{r_1{}^+}^{r_{\delta_1}{}^+} u^+ r^+ dr^+\right\} d(u_{\delta_1}{}^+ r_1{}^+) \tag{7}$$

Similarly, for the boundary layer on the outer wall

Nomenclature

A^+ = damping constant
b = constant, equation (16)
c = specific heat at constant pressure
D_e = equivalent diameter of annulus
h = local convective heat transfer coefficient
k = thermal conductivity
K = universal mixing constant
p = static pressure
q = local radial heat flux
q_1 = heat flux at inner wall
r = radial distance
r_1 = radius of core
r_2 = radius of outer wall
r_m = radius at which maximum velocity occurs
r^+ = dimensionless radius $\begin{cases} ru_1^*/\nu \text{ for inner boundary layer} \\ ru_2^*/\nu \text{ for outer boundary layer} \end{cases}$
$r_1{}^+$ = dimensionless radius of core $\frac{r_1 u_1^*}{\nu}$
$r_2{}^+$ = dimensionless radius of outer wall $\frac{r_2 u_2^*}{\nu}$
r_{δ_1} = radius at edge of inner boundary layer $r_1 + \delta_1$
r_{δ_2} = radius at edge of outer boundary layer $r_2 - \delta_2$
r_{δ_T} = radius at edge of thermal boundary layer
$r_{\delta_T}{}^+$ = dimensionless radius at edge of thermal boundary layer $\frac{r_{\delta_T} u_1^*}{\nu}$
s = radius ratio r_1/r_2
T = temperature
T_1 = temperature of inner wall
T_{δ_T} = temperature at edge of thermal boundary layer
T^+ = dimensionless temperature parameter $\frac{(T_1 - T)c\tau_{01}}{q_1 u_1^*}$
$T_B{}^+$ = dimensionless bulk temperature, equation (26)
$T_{\delta_T}{}^+$ = dimensionless temperature at edge of thermal boundary layer $\frac{(T_1 - T_{\delta_T})c\tau_{01}}{q_1 u_1^*}$
u = velocity
u_1^* = local friction velocity at inner wall $\sqrt{\tau_{01}/\rho}$
u_2^* = local friction velocity at outer wall $\sqrt{\tau_{02}/\rho}$
u^+ = dimensionless velocity $\begin{cases} u/u_1^* \text{ for inner boundary layer} \\ u/u_2^* \text{ for outer boundary layer} \end{cases}$
u_δ = velocity at edge of inner and outer boundary layers
$u_{\delta_1}{}^+$ = dimensionless velocity at edge of inner boundary layer u_δ/u_1^*
$u_{\delta_2}{}^+$ = dimensionless velocity at edge of outer boundary layer u_δ/u_2^*
u_i = velocity at annulus inlet
x = axial distance from annulus inlet
y = distance from inner or outer walls
y^+ = dimensionless distance $\begin{cases} yu_1^*/\nu \text{ for inner boundary layer} \\ yu_2^*/\nu \text{ for outer boundary layer} \end{cases}$
Nu = local Nusselt number $\frac{2h(r_2 - r_1)}{k}$
Pr = Prandtl number $\mu c/k$
Re = Reynolds number $\frac{2u_i(r_2 - r_1)}{\nu}$
δ_1 = thickness of inner boundary layer
δ_2 = thickness of outer boundary layer
$\delta_1{}^+$ = dimensionless thickness of inner boundary layer $\delta_1 u_1^*/\nu$
$\delta_2{}^+$ = dimensionless thickness of outer boundary layer $\delta_2 u_2^*/\nu$
δ_T = thickness of thermal boundary layer
$\delta_T{}^+$ = dimensionless thickness of thermal boundary layer $\delta_T u_1^*/\nu$
ϵ_H = thermal eddy diffusivity
ϵ_M = momentum eddy diffusivity
μ = absolute viscosity
ν = kinematic viscosity
ρ = density
τ = shear stress
τ_0 = wall shear stress
τ_{01} = inner wall shear stress
τ_{02} = outer wall shear stress

$$d\left(\frac{x}{r_2}\right) = \frac{1}{r_2{}^{+2}}\, d\left\{\int_{r_{\delta 2}{}^+}^{r_2{}^+} (u_{\delta_2}{}^+ - u^+)u^+r^+dr^+\right\}$$

$$+ \left\{\frac{u_{\delta_2}{}^+(r_2{}^{+2} - r_{\delta_2}{}^{+2})}{2r_2{}^{+3}} - \frac{1}{r_2{}^{+3}}\int_{r_{\delta_2}{}^+}^{r_2{}^+} u^+r^+dr^+\right\} d(u_{\delta_2}{}^+r_2{}^+) \quad (8)$$

At the inlet

$$u_{\delta_1}{}^+r_1{}^+ = \frac{u_i r_1}{\nu} = \frac{\mathrm{Re}}{2}\,\frac{s}{1-s}$$

and (9)

$$u_{\delta_2}{}^+r_2{}^+ = \frac{u_i r_2}{\nu} = \frac{\mathrm{Re}}{2}\,\frac{1}{1-s}$$

where the Reynolds number is based on the equivalent diameter of the annulus.

Thus, integrating equations (7) and (8) yields

$$\frac{x}{r_1} = \int_0^{\{\}} \frac{1}{r_1{}^{+2}}\, d\left\{\int_{r_1{}^+}^{r_{\delta_1}{}^+} (u_{\delta_1}{}^+ - u^+)u^+r^+dr^+\right\}$$

$$+ \int_{\frac{\mathrm{Re}}{2}\frac{s}{1-s}}^{u_{\delta_1}{}^+r_1{}^+} \left\{\frac{u_{\delta_1}{}^+(r_{\delta_1}{}^{+2} - r_1{}^{+2})}{2r_1{}^{+3}}\right.$$

$$\left. - \frac{1}{r_1{}^{+3}}\int_{r_1{}^+}^{r_{\delta_1}{}^+} u^+r^+dr^+\right\} d(u_{\delta_1}{}^+r_1{}^+) \quad (10)$$

and

$$\frac{x}{r_2} = \int_0^{\{\}} \frac{1}{r_2{}^{+2}}\, d\left\{\int_{r_{\delta_2}{}^+}^{r_2{}^+} (u_{\delta_2}{}^+ - u^+)u^+r^+dr^+\right\}$$

$$+ \int_{\frac{\mathrm{Re}}{2}\frac{1}{1-s}}^{u_{\delta_2}{}^+r_2{}^+} \left\{\frac{u_{\delta_2}{}^+(r_2{}^{+2} - r_{\delta_2}{}^{+2})}{2r_2{}^{+3}}\right.$$

$$\left. - \frac{1}{r_2{}^{+3}}\int_{r_{\delta_2}{}^+}^{r_2{}^+} u^+r^+dr^+\right\} d(u_{\delta_2}{}^+r_2{}^+) \quad (11)$$

where the upper limits of the first integrals are the variables of the differentials inside those integrals. The Reynolds number may be obtained by using the continuity equation expressed in the form

$$u_i(r_2{}^2 - r_1{}^2) = u_\delta(r_{\delta_2}{}^2 - r_{\delta_1}{}^2) + 2\int_{r_1}^{r_{\delta_1}} urdr + 2\int_{r_{\delta 2}}^{r_2} urdr \quad (12)$$

Hence

$$\mathrm{Re} = 2\left\{\frac{r_{\delta_2}{}^{+2}u_{\delta_2}{}^+}{r_2{}^+(1+s)} - \frac{sr_{\delta_1}{}^{+2}u_{\delta_1}{}^+}{r_1{}^+(1+s)}\right\}$$

$$+ \frac{4}{1+s}\left\{\frac{s}{r_1{}^+}\int_{r_1{}^+}^{r_{\delta_1}{}^+} u^+r^+dr^+ + \frac{1}{r_2{}^+}\int_{r_{\delta_2}{}^+}^{r_2{}^+} u^+r^+dr^+\right\} \quad (13)$$

averaged shear stress and the velocity gradient within the boundary layers.

In dimensionless form

$$\frac{\tau}{\tau_0} = \left(1 + \frac{\epsilon_M}{\nu}\right)\frac{du^+}{dy^+} \quad (14)$$

The integration of equation (14) may be accomplished by making some reasonable assumption for the distribution of τ/τ_0 and ϵ_M/ν.

The shear stress variation in the boundary layer is assumed to be linear while the ϵ_M/ν distribution suggested by Levy [12] for fully developed annular flow is utilized. Levy applied the expression for the eddy diffusivity of momentum for turbulent pipe flow proposed by Reichardt to the inner and outer portions of the annulus and assumed that at the radius of maximum velocities the diffusivities calculated for each boundary layer should be equal. Thus

$$\frac{\epsilon_M}{\nu} = \frac{K}{6}(r_2 - r_m)\frac{\sqrt{\tau_{02}/\rho}}{\nu}\left[1 - \left(\frac{r - r_m}{r_{1\text{ or }2} - r_m}\right)^2\right]$$

$$\times\left[1 + 2\left(\frac{r - r_m}{r_{1\text{ or }2} - r_m}\right)^2\right] \quad (15)$$

If, in developing flow, a similar distribution is applied across the boundary layers, then replacing r_m by r_{δ_1} or r_{δ_2} and using dimensionless variables

$$\frac{\epsilon_M}{\nu} = \frac{K}{6}\delta_2{}^+\left[1 - \left(\frac{r^+ - r_{\delta_1 \text{ or } \delta_2}{}^+}{r_{1\text{ or }2}{}^+ - r_{\delta_1 \text{ or } \delta_2}{}^+}\right)^2\right]$$

$$\times\left[1 + b\left(\frac{r^+ - r_{\delta_1 \text{ or } \delta_2}{}^+}{r_{1\text{ or }2}{}^+ - r_{\delta_1 \text{ or } \delta_2}{}^+}\right)^2\right] \quad (16)$$

where $b = 2$ in the inner portion of annulus and $b = 2.5$ in the outer portion.

The foregoing expression for eddy diffusivity is valid only for regions away from the wall. However, the influence of the walls may be taken into account by multiplying equation (16) by the van Driest [18] damping factor $[1 - \exp - (y^+/A^+)]$. Hence, on further rearrangement, the expressions for the eddy diffusivities of momentum become

$$\frac{\epsilon_M}{\nu} = \frac{K}{6}\delta_2{}^+\left[1 - \left(\frac{y^+ - \delta^+}{\delta^+}\right)^2_{1\text{ or }2}\right]$$

$$\times\left[1 + b\left(\frac{y^+ - \delta^+}{\delta^+}\right)^2_{1\text{ or }2}\right]\left[1 - \exp - \left(\frac{y^+}{A^+}\right)_{1\text{ or }2}\right] \quad (17)$$

Substituting equation (17) into equation (14) and integrating yields the following velocity distributions for the inner and outer boundary layers, respectively,

$$u^+ = \int_0^{y^+} \frac{\left(1 - \frac{y^+}{\delta_1{}^+}\right) dy^+}{\left\{1 + \frac{K}{6}\delta_2{}^+\left[1 - \left(\frac{y^+ - \delta_1{}^+}{\delta_1{}^+}\right)^2\right]\left[1 + 2\left(\frac{y^+ - \delta_1{}^+}{\delta_1{}^+}\right)^2\right]\left[1 - \exp - \left(\frac{y^+}{A^+}\right)\right]\right\}} \quad (18a)$$

$$u^+ = \int_0^{y^+} \frac{\left(1 - \frac{y^+}{\delta_2{}^+}\right) dy^+}{\left\{1 + \frac{K}{6}\delta_2{}^+\left[1 - \left(\frac{y^+ - \delta_2{}^+}{\delta_2{}^+}\right)^2\right]\left[1 + 2.5\left(\frac{y^+ - \delta_2{}^+}{\delta_2{}^+}\right)^2\right]\left[1 - \exp - \left(\frac{y^+}{A^+}\right)\right]\right\}} \quad (18b)$$

In order that the foregoing equations may be integrated it is obviously necessary to select suitable velocity distributions to describe the velocity fields in the inner and outer boundary layers. This begins with the expression relating the time-

The foregoing equations may be solved numerically for particular values of radius ratio and Reynolds number using the following procedure:

1 A value for $\delta_1{}^+$ is specified. However, it is not yet known

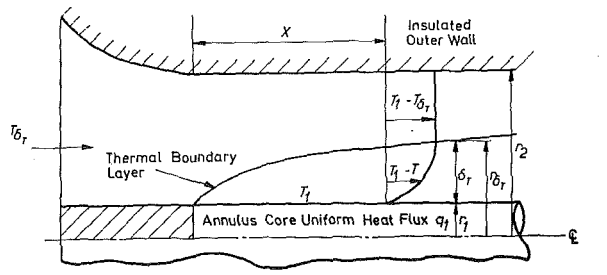

Fig. 1(b) Idealized model of developing thermal boundary layers in an annulus

at which axial position from the inlet this dimensionless boundary layer thickness occurs.

2 Values for δ_2^+ and r_1^+ are arbitrarily chosen.

3 The dimensionless values of the velocity at the edges of the boundary layers $u_{\delta_1}^+$ and $u_{\delta_2}^+$ are calculated from equations (18*a*) and (18*b*).

4 By noting that $s = \dfrac{r_1^+ u_{\delta_1}^+}{r_2^+ u_{\delta_2}^+}$ (equation (9)) then r_2^+ is calculated.

5 The corresponding Reynolds number is obtained from equation (13). For the first attempt, this value of the Reynolds number usually does not agree with the initial specified value. The anomaly may be corrected by changing the value of r_1^+ in a trial and error manner until agreement is obtained.

6 Equations (*10*) and (*11*) are integrated numerically to obtain values of x/r_1 and x/r_2 corresponding to the specified δ_1^+ and the assumed δ_2^+.

7 By dividing x/r_1 into x/r_2 a value of s is determined and this may be made equal to the initial specified value of s by changing δ_2^+.

8 The procedure is then repeated until the correct δ_2^+, r_1^+, and r_2^+ are found.

9 Hence the dimensionless axial distance from the entrance of the annulus x/D_e is found for the specified δ_1^+ since

$$\frac{x}{D_e} = \frac{0.5}{\dfrac{1}{x/r_2} - \dfrac{1}{x/r_1}} \tag{19}$$

By varying δ_1^+ and carrying out the whole of the process, the growth of the hydrodynamic boundary layers may be predicted up to the position of fully developed flow. This is taken as occurring when $r_{\delta_1} = r_{\delta_2}$ or in the calculation procedure when $(r_1^+ + \delta_1^+)u_{\delta_1}^+ = (r_2^+ - \delta_2^+)u_{\delta_2}^+$.

Growth of the Thermal Boundary Layer. The energy-integral equation for the thermal boundary layer that builds up on the heated core of a concentric annulus in which the outer surface is insulated (see Fig. 1(*b*)) may be written as

$$\frac{d}{dx}\left\{\int_{r_1}^{r_{\delta T}} T\rho c u r dr\right\} - T_{\delta_T}\frac{d}{dx}\left\{\int_{r_1}^{r_{\delta T}} \rho c u r dr\right\} = r_1 q_1 \tag{20}$$

or for uniform wall heat flux

$$d\left(\frac{x}{r_1}\right) = \frac{1}{r_1^2}\, d\left\{\int_{r_1}^{r_{\delta T}} \left(\frac{(T - T_{\delta T})}{q_1}\right)\rho c u r dr\right\} \tag{21}$$

Following the assumption of constant fluid properties and uniform wall heat flux, equation (21) may be reduced in dimensionless form to

$$\frac{x}{D_e} = \frac{s}{2(1-s)r_1^{+2}} \int_{r_1^+}^{r_{\delta T}^+} (T_{\delta T}^+ - T^+)u^+ r^+ dr^+ \tag{22}$$

In the foregoing equation the inner wall shear velocity alone has been used to render the local velocities, temperatures, and radii dimensionless. Thus, when the thermal boundary layer extends into the outer hydrodynamic boundary layer, the values of u^+ and r^+, which were calculated previously, must now be multiplied by $u_{\delta_1}^+/u_{\delta_2}^+$ and $u_{\delta_2}^+/u_{\delta_1}^+$, respectively.

In order that equation (22) may be evaluated, a suitable temperature distribution must be selected. An expression relating the radial heat flux to the temperature gradient may be written in dimensionless form as

$$\frac{q}{q_1} = \left(\frac{1}{\mathrm{Pr}} + \frac{\epsilon_H}{\nu}\right)\frac{dT^+}{dy^+} \tag{23}$$

If it is assumed that the heat flux variation through the thermal boundary layer varies in the manner postulated by Lee [20], viz.,

$$\frac{q}{q_1} = \frac{r_1^+}{r^+}\left(\frac{r_{\delta T}^{+2} - r^{+2}}{r_{\delta T}^{+2} - r_1^{+2}}\right) \tag{24}$$

then equation (23) becomes

$$T^+ = \int_0^{\delta_T^+} \frac{r_1^+}{r_1^+ + y^+} \frac{\left(\dfrac{\delta_T^+ - y^+}{\delta_T^+}\right)\left(\dfrac{2r_1^+ + \delta_T^+ + y^+}{2r_1^+ + \delta_T^+}\right) dy^+}{\left(\dfrac{1}{\mathrm{Pr}} + \dfrac{\epsilon_H}{\nu}\right)} \tag{25}$$

For the purpose of the present analysis, it is assumed that the eddy diffusivities of heat and momentum are identical and, hence, the variation of ϵ_H/ν is given by equation (17).

It is now possible to incorporate the information calculated for the hydrodynamic boundary layers at a particular axial station to determine the local dimensionless thickness of the thermal boundary layer. The first case to be considered is that in which fully developed hydrodynamic flow has not been reached. The calculation procedure is as follows:

1 A value of δ_T^+ is chosen and the temperature distribution calculated by means of equation (25).

2 Hence a value for x/D_e is determined from the integration of equation (22) and compared with the value that may be obtained from equation (19).

3 If the values are different δ_T^+ is changed until agreement is achieved.

If the flow is hydrodynamically fully developed the calculation procedure is as follows.

A value of δ_T^+ is selected and using the fully developed velocity distributions the temperature profiles and x/D_e may be calculated directly from equations (25) and (22).

Nusselt Number Parameters. The local Nusselt number at any given x/D_e may be determined using the correct δ_T^+ and by finding the local bulk temperature of the fluid. In dimensionless form the local mixed mean or bulk temperature may be defined by

$$T_B^+ = \frac{\displaystyle\int_{r_1^+}^{\frac{u_{\delta_2}^+}{u_{\delta_1}^+} r_2^+} T^+ u^+ r^+ dr^+}{\displaystyle\int_{r_1^+}^{\frac{u_{\delta_2}^+}{u_{\delta_1}^+} r_2^+} u^+ r^+ dr^+} \tag{26}$$

It can then be readily shown that

$$T_B^+ = T_{\delta_T}^+ - \frac{x}{D_e}\frac{8r_1^+}{\mathrm{Re}}\left(\frac{1-s}{1+s}\right) \tag{27}$$

The local Nusselt number, based on the equivalent diameter of the annulus, may be written as

$$\mathrm{Nu} = \frac{2\left(\dfrac{1-s}{s}\right)r_1^+ \mathrm{Pr}}{T_B^+} \tag{28}$$

Combining equation (28) with equation (27) thus yields the following expression for the local Nusselt number:

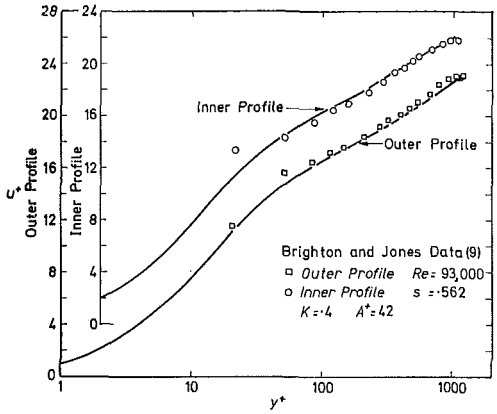

Fig. 2 Comparison of predicted fully developed velocity distributions with experimental data

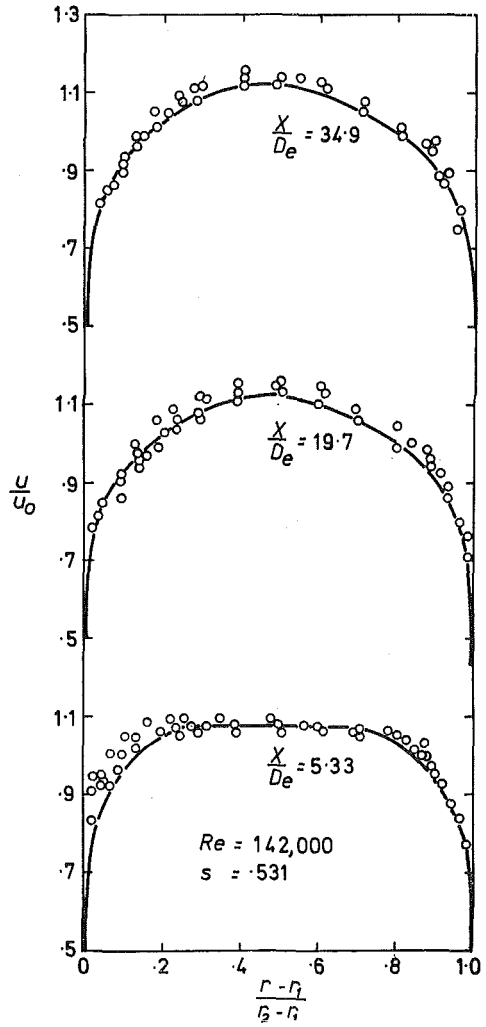

Fig. 3(a) Comparison of predicted developing velocity distributions with experimental data of Okiishi and Serovy [16]

$$\mathrm{Nu} = \frac{2\left(\frac{1-s}{s}\right) r_1^+ \mathrm{Pr}}{T_{\delta T}^+ - \frac{x}{D_e}\frac{8r_1^+}{\mathrm{Re}}\left(\frac{1-s}{1+s}\right)} \tag{29}$$

Results and Discussion

It is apparent from the foregoing analysis that the success of the proposed method depends on the choice of the damping constant A^+ which characterizes the influence of the wall and the universal mixing length constant K. Before the development of the hydrodynamic layers is considered therefore, it is of interest at this stage to discuss the effect that varying A^+ and K has on the fully developed velocity distributions. The damping constant A^+ controls the thickness of the laminar sublayer and increasing A^+ causes a thickening of the sublayer. This has an overall effect of raising the turbulent core portion of the velocity distribution. On the other hand, the universal mixing length constant K controls the slope of the turbulent core and an increase in K produces a decrease in the slope of the curve in this region. Thus, by choosing a suitable combination of A^+ and K, it is possible to predict velocity distributions which are in good agreement with experimental data. This is demonstrated in Fig. 2 in which velocity distributions calculated from equations (18*a*) and (18*b*), assuming $A^+ = 42$ and $K = 0.4$, are compared with the data of Brighton and Jones [9]. It is found, however, that the excellent agreement exists only at annuli radius ratios above 0.2 and below this value the experimental velocity profiles deviate from the curves shown in Fig. 2. However, since as far as the authors are aware all of the reported work on fluid flow and heat transfer in the entrance regions of annuli has been carried out for radius ratios greater than 0.2, the foregoing values of A^+ and K are used in the subsequent examination of the developing hydrodynamic boundary layers.

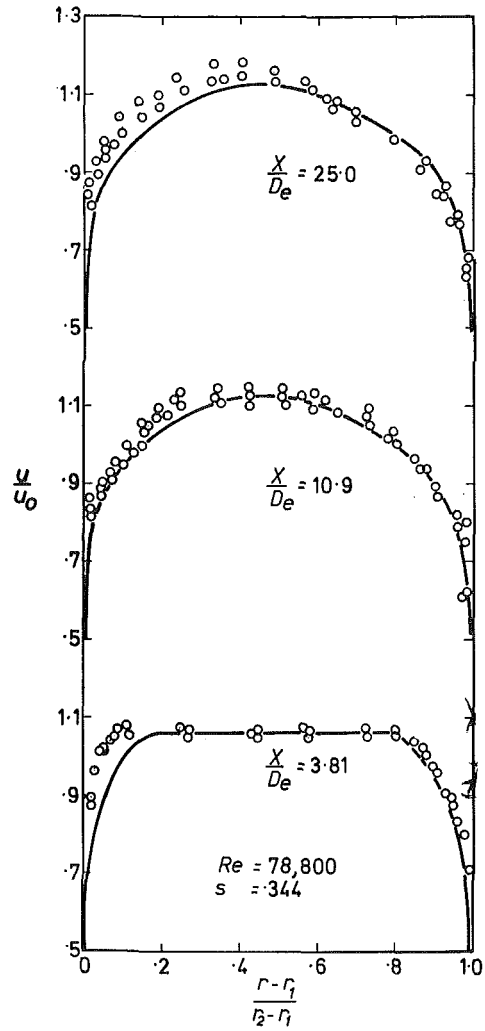

Fig. 3(b) Comparison of predicted developing velocity distributions with experimental data of Okiishi and Serovy [16]

The velocity profiles in the entrance region are calculated by determining x/D_e and δ_2^+ for a chosen δ_1^+ and using the values of δ_1^+ and δ_2^+ as the upper limits in equations (18*a*) and (18*b*). The predicted profiles are made dimensionless with respect to the inlet velocity using equation (9) and are compared with the experimental data of Okiishi and Serovy in Figs. 3(*a*) and (*b*). The data presented were obtained using a rounded inlet and, al-

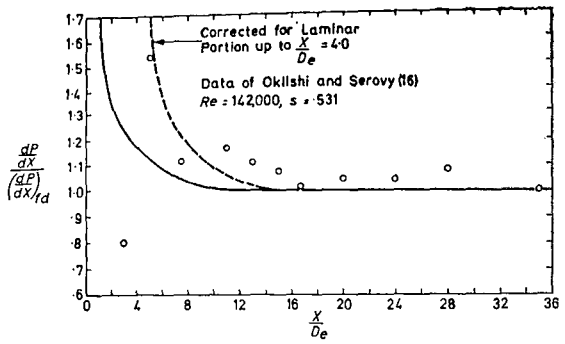

Fig. 4 Comparison of predicted normalized pressure gradient with experimental data

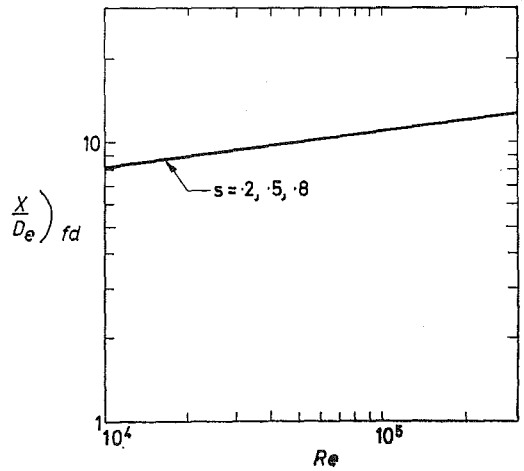

Fig. 5 Variation of predicted hydrodynamic development length with Reynolds number and radius ratio

though Okiishi and Serovy do not mention the use of tripping devices, they did use plastic tube flow straighteners in front of the nozzle. It does appear, therefore, that if laminar boundary layers were present, as indicated by Okiishi and Serovy, they were confined to regions very close to the inlet and have little effect on the developing velocity profiles.

The axial distribution of pressure gradient normalized by the corresponding fully developed value is considered next. The predicted pressure gradient is evaluated from equation (2) using the variation of u_δ with x/D_e which has already been found in the calculation of the developing velocity profiles just discussed. Following the procedure of Jonsson [19], du_δ/dx is determined by fitting a second-degree, least-squares polynomial through five points; this is differentiated and the derivative evaluated at the midpoint. At fully developed flow (i.e., where $r_{\delta 1} = r_{\delta 2}$) the value of the derivative at the end point was used to calculate $(dp/dx)_{fd}$. Two normalized pressure gradients are shown in Fig. 4, one assuming that the boundary layers are fully turbulent from the annulus inlet and the other calculated assuming that the turbulent boundary layers are initiated from an axial position of $x/D_e = 4.0$. The latter curve is included since an examination of the experimental data indicates a reversal of pressure gradient in the inlet regions which is thought to be due to the transition from laminar to turbulent boundary layer flow. Fig. 4 shows, therefore, that provided the transition point is known, the present analysis can be used to predict accurate normalized pressure gradient distributions.

The results of the analysis on the hydrodynamic boundary layers are summarized in Fig. 5. The values of x/D_e at the position where the two boundary layers meet are plotted for three radius ratios against the annulus Reynolds number, assuming the layers to be fully turbulent from the inlet. Fig. 5 shows that the hydrodynamic development is independent of radius ratio and that, over the range considered, fully developed flow is achieved

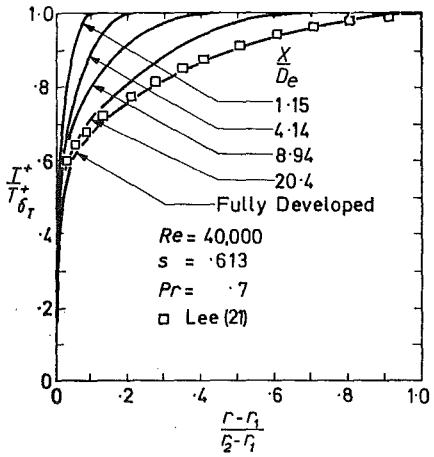

Fig. 6 Developing temperature profiles and comparison with experimental data for fully developed conditions

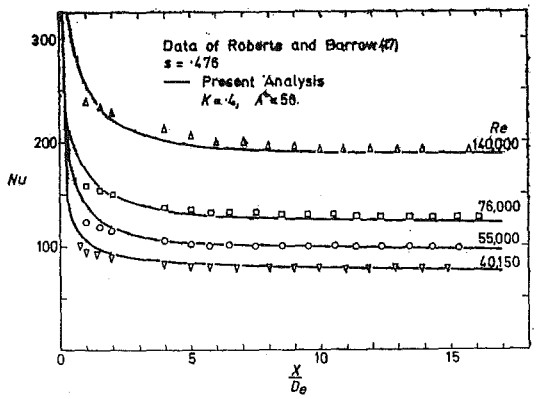

Fig. 7 Comparison of predicted local Nusselt numbers with experimental data; (Pr = 0.7)

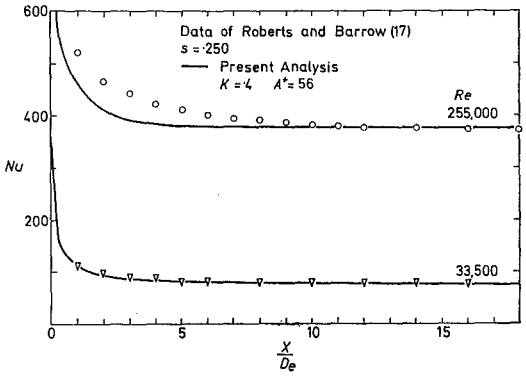

Fig. 8 Comparison of predicted local Nusselt numbers with experimental data; (Pr = 0.7)

in about 10 equivalent diameters. This is less than is usually allowed for in practice, but as just stressed, no account has been taken of any laminar layers at the entry.

The thermal boundary layer is considered to be fully developed when an axial position in the annulus is reached where the temperature profile has no straight-line portion normal to the fluid flow axis. It was found necessary to increase the value of A^+ from 42 to 56 throughout the analysis to obtain good agreement with the experimental data for heat transfer of Lee [21] and Roberts and Barrow. This alteration in A^+ is felt justified since the value used earlier was obtained by comparison with experimental velocity profiles measured only under isothermal conditions.

Using values of $A^+ = 56$ and $K = 0.4$, the developing tem-

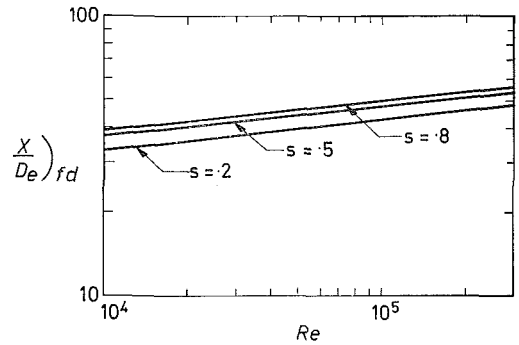

Fig. 9 Variation of predicted thermal development length with Reynolds numbers and radius ratio for air (Pr = 0.7)

perature profiles are evaluated from equation (25) where the dimensionless temperature at the edge of the thermal boundary layer has been calculated using the appropriate value of $\delta_T{}^+$ at the predetermined value of x/D_e. Fig. 6 shows the developing temperature profiles as a function of x/D_e with the fully developed profile compared with the data of Lee referred to earlier.

The temperature profiles may be integrated to obtain the dimensionless bulk temperature (cf. equation (26)) and hence the local Nusselt number variation with x/D_e is determined from equation (29). For the two radius ratios considered, generally excellent agreement is found between prediction and the experimental data gathered by Roberts and Barrow for air, as shown in Figs. 7 and 8. The small discrepancies that do appear at the high values of Reynolds number are, as pointed out by Roberts and Barrow, due to the trip wires being larger than necessary, thus enhancing the heat transfer rates in that region. Nevertheless, it is felt that the agreement achieved by the analysis in the developing thermal boundary layer is attributed to the fact that tripping wires were used in the experiments. This insured that the boundary layers were fully turbulent from the entry point as postulated in the analysis. Unfortunately, they did not present any developing pressure gradient data in their paper which might have afforded a more realistic test of the analysis in the developing hydrodynamic boundary layers.

Finally, the variation of the thermal development length as a function of radius ratio and Reynolds number is shown in Fig. 9. The general trends of these curves are in accordance with those predicted by Lee [20] who analyzed the developing thermal boundary layer in hydrodynamically fully developed flow in an annulus. In the case analyzed here, a slightly greater development length is required.

Conclusions

An analytical investigation, using integral techniques, has been made of the local flow and heat transfer characteristics of a fluid in turbulent motion in the entry region of a concentric annulus which has a uniformly heated core and an insulated outer wall. The important conclusions are:

1 Fully developed hydrodynamic flow is attained in an entrance length of approximately 10 equivalent diameters in the range of Reynolds number studied. The radius ratio range investigated was found to have no influence on x/D_e.

2 Fully developed turbulent heat transfer is obtained within a further 30 equivalent diameters. Increasing the Reynolds number and radius ratio leads to an increase in the required x/D_e.

References

1 Rothfus, R. R., Monrad, C. C., and Senecal, V. E., "Velocity Distribution and Fluid Friction in Smooth Concentric Annuli," *Industrial and Engineering Chemistry*, Vol. 42, No. 2, 1950, p. 2511.

2 Rothfus, R. R., et al., "Isothermal Skin Friction in Flow Through Annular Sections," *Industrial and Engineering Chemistry*, Vol. 47, 1955, p. 913.

3 Barrow, H., "Fluid Flow and Heat Transfer in an Annulus With a Heated Core Tube," *Proceedings, Institution of Mechanical Engineers*, Vol. 196, 1955, p. 1113.

4 Barrow, H., "A Semitheoretical Solution of Asymmetric Heat Transfer in Annular Flow," *Journal of Mechanical Engineering Science*, Vol. 4, 1960, p. 331.

5 Kays, W. M., and Leung, E. Y., "Heat Transfer in Annular Passages—Hydrodynamically Developed Turbulent Flow With Arbitrarily Prescribed Heat Fux," *International Journal of Heat and Mass Transfer*, Vol. 6, 1963, pp. 537–557.

6 Olson, R. M., and Sparrow, E. M., "Measurements of Turbulent Flow Development in Tubes and Annuli With Square or Rounded Entrances," *AIChE Journal*, Vol. 9, 1963, p. 766.

7 Lee, Y., and Barrow, H., "Turbulent Flow and Heat Transfer in Concentric and Eccentric Annuli," Paper 12, Thermodynamics and Fluid Mechanics Convention, Cambridge, 1964.

8 Barrow, H., and Lee, Y., "Heat Transfer With Unsymmetrical Thermal Boundary Conditions," *International Journal of Heat and Mass Transfer*, Vol. 7, 1964, p. 580.

9 Brighton, J. A., and Jones, J. B., "Fully Developed Turbulent Flow in Annuli," *Journal of Basic Engineering*, TRANS. ASME, Series D, Vol. 86, 1964, pp. 835–844.

10 Barrow, H., Lee, Y., and Roberts, A., "The Similarity Hypothesis Applied to Turbulent Flow in an Annulus," *International Journal of Heat and Mass Transfer*, Vol. 8, 1965, p. 1499.

11 Jonsson, V. K., and Sparrow, E. M., "Experiments on Turbulent Flow-Phenomena in Eccentric Annular Ducts," *Journal of Fluid Mechanics*, Vol. 25, 1966, pp. 65–86.

12 Levy, S., "Turbulent Flow in an Annulus," JOURNAL OF HEAT TRANSFER, TRANS. ASME, Series C, Vol. 89, 1967, pp. 25–31.

13 Quarmby, A., "An Experimental Study of Turbulent Flow Through Concentric Annuli," *International Journal of Mechanical Science*, Vol. 9, 1967, pp. 205–221.

14 Wilson, N. W., and Medwell, J. O., "An Analysis of Heat Transfer for Fully Developed Turbulent Flow in Concentric Annuli," JOURNAL OF HEAT TRANSFER, TRANS. ASME, Series C, Vol. 90, 1968, pp. 43–50.

15 Diessler, R. G., and Taylor, M. F., "Analysis of Fully Developed Turbulent Heat Transfer and Flow in an Annulus With Various Eccentricities," NACA-TN-3451, Mar. 1955.

16 Okiishi, T. H., and Serovy, G. K., "An Experimental Study of the Turbulent-Flow Boundary-Layer Development in Smooth Annuli," *Journal of Basic Engineering*, TRANS. ASME, Series D, Vol. 89, 1967, pp 823–836.

17 Roberts, A., and Barrow, H., "Turbulent Heat Transfer to Air in the Vicinity of the Entry of an Internally Heated Annulus," Paper 23, Thermodynamics and Fluid Mechanics Convention, Bristol, 1968.

18 van Driest, E. R., "On Turbulent Flow Near a Wall," Paper 12, Heat Transfer and Fluid Mechanics Institute Symposium, University of California, Los Angeles, Calif., 1955.

19 Jonsson, V. K., "Experimental Studies of Turbulent Flow Phenomena in Eccentric Annuli," PhD thesis, University of Minnesota, 1965.

20 Lee, Y., "Turbulent Heat Transfer From the Core Tube in Thermal Entrance Regions of Concentric Annuli," *International Journal of Heat and Mass Transfer*, Vol. 11, 1968, pp. 509–521.

21 Lee, Y., "Turbulent Flow and Heat Transfer in Concentric and Eccentric Annuli," PhD thesis, University of Liverpool, 1964.

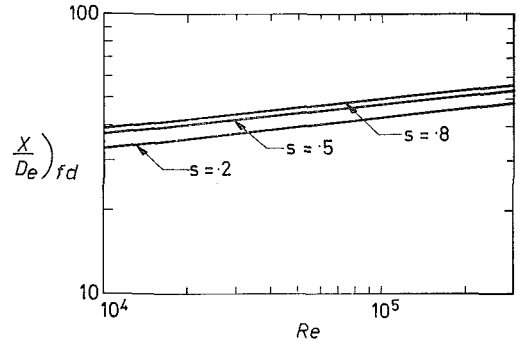

Fig. 9 Variation of predicted thermal development length with Reynolds numbers and radius ratio for air (Pr = 0.7)

perature profiles are evaluated from equation (25) where the dimensionless temperature at the edge of the thermal boundary layer has been calculated using the appropriate value of $\delta_T{}^+$ at the predetermined value of x/D_e. Fig. 6 shows the developing temperature profiles as a function of x/D_e with the fully developed profile compared with the data of Lee referred to earlier.

The temperature profiles may be integrated to obtain the dimensionless bulk temperature (cf. equation (26)) and hence the local Nusselt number variation with x/D_e is determined from equation (29). For the two radius ratios considered, generally excellent agreement is found between prediction and the experimental data gathered by Roberts and Barrow for air, as shown in Figs. 7 and 8. The small discrepancies that do appear at the high values of Reynolds number are, as pointed out by Roberts and Barrow, due to the trip wires being larger than necessary, thus enhancing the heat transfer rates in that region. Nevertheless, it is felt that the agreement achieved by the analysis in the developing thermal boundary layer is attributed to the fact that tripping wires were used in the experiments. This insured that the boundary layers were fully turbulent from the entry point as postulated in the analysis. Unfortunately, they did not present any developing pressure gradient data in their paper which might have afforded a more realistic test of the analysis in the developing hydrodynamic boundary layers.

Finally, the variation of the thermal development length as a function of radius ratio and Reynolds number is shown in Fig. 9. The general trends of these curves are in accordance with those predicted by Lee [20] who analyzed the developing thermal boundary layer in hydrodynamically fully developed flow in an annulus. In the case analyzed here, a slightly greater development length is required.

Conclusions

An analytical investigation, using integral techniques, has been made of the local flow and heat transfer characteristics of a fluid in turbulent motion in the entry region of a concentric annulus which has a uniformly heated core and an insulated outer wall. The important conclusions are:

1 Fully developed hydrodynamic flow is attained in an entrance length of approximately 10 equivalent diameters in the range of Reynolds number studied. The radius ratio range investigated was found to have no influence on x/D_e.

2 Fully developed turbulent heat transfer is obtained within a further 30 equivalent diameters. Increasing the Reynolds number and radius ratio leads to an increase in the required x/D_e.

References

1 Rothfus, R. R., Monrad, C. C., and Senecal, V. E., "Velocity Distribution and Fluid Friction in Smooth Concentric Annuli," *Industrial and Engineering Chemistry*, Vol. 42, No. 2, 1950, p. 2511.

2 Rothfus, R. R., et al., "Isothermal Skin Friction in Flow Through Annular Sections," *Industrial and Engineering Chemistry*, Vol. 47, 1955, p. 913.

3 Barrow, H., "Fluid Flow and Heat Transfer in an Annulus With a Heated Core Tube," *Proceedings, Institution of Mechanical Engineers*, Vol. 196, 1955, p. 1113.

4 Barrow, H., "A Semitheoretical Solution of Asymmetric Heat Transfer in Annular Flow," *Journal of Mechanical Engineering Science*, Vol. 4, 1960, p. 331.

5 Kays, W. M., and Leung, E. Y., "Heat Transfer in Annular Passages—Hydrodynamically Developed Turbulent Flow With Arbitrarily Prescribed Heat Fux," *International Journal of Heat and Mass Transfer*, Vol. 6, 1963, pp. 537–557.

6 Olson, R. M., and Sparrow, E. M., "Measurements of Turbulent Flow Development in Tubes and Annuli With Square or Rounded Entrances," *AIChE Journal*, Vol. 9, 1963, p. 766.

7 Lee, Y., and Barrow, H., "Turbulent Flow and Heat Transfer in Concentric and Eccentric Annuli," Paper 12, Thermodynamics and Fluid Mechanics Convention, Cambridge, 1964.

8 Barrow, H., and Lee, Y., "Heat Transfer With Unsymmetrical Thermal Boundary Conditions," *International Journal of Heat and Mass Transfer*, Vol. 7, 1964, p. 580.

9 Brighton, J. A., and Jones, J. B., "Fully Developed Turbulent Flow in Annuli," *Journal of Basic Engineering*, TRANS. ASME, Series D, Vol. 86, 1964, pp. 835–844.

10 Barrow, H., Lee, Y., and Roberts, A., "The Similarity Hypothesis Applied to Turbulent Flow in an Annulus," *International Journal of Heat and Mass Transfer*, Vol. 8, 1965, p. 1499.

11 Jonsson, V. K., and Sparrow, E. M., "Experiments on Turbulent Flow-Phenomena in Eccentric Annular Ducts," *Journal of Fluid Mechanics*, Vol. 25, 1966, pp. 65–86.

12 Levy, S., "Turbulent Flow in an Annulus," JOURNAL OF HEAT TRANSFER, TRANS. ASME, Series C, Vol. 89, 1967, pp. 25–31.

13 Quarmby, A., "An Experimental Study of Turbulent Flow Through Concentric Annuli," *International Journal of Mechanical Science*, Vol. 9, 1967, pp. 205–221.

14 Wilson, N. W., and Medwell, J. O., "An Analysis of Heat Transfer for Fully Developed Turbulent Flow in Concentric Annuli," JOURNAL OF HEAT TRANSFER, TRANS. ASME, Series C, Vol. 90, 1968, pp. 43–50.

15 Diessler, R. G., and Taylor, M. F., "Analysis of Fully Developed Turbulent Heat Transfer and Flow in an Annulus With Various Eccentricities," NACA-TN-3451, Mar. 1955.

16 Okiishi, T. H., and Serovy, G. K., "An Experimental Study of the Turbulent-Flow Boundary-Layer Development in Smooth Annuli," *Journal of Basic Engineering*, TRANS. ASME, Series D, Vol. 89, 1967, pp 823–836.

17 Roberts, A., and Barrow, H., "Turbulent Heat Transfer to Air in the Vicinity of the Entry of an Internally Heated Annulus," Paper 23, Thermodynamics and Fluid Mechanics Convention, Bristol, 1968.

18 van Driest, E. R., "On Turbulent Flow Near a Wall," Paper 12, Heat Transfer and Fluid Mechanics Institute Symposium, University of California, Los Angeles, Calif., 1955.

19 Jonsson, V. K., "Experimental Studies of Turbulent Flow Phenomena in Eccentric Annuli," PhD thesis, University of Minnesota, 1965.

20 Lee, Y., "Turbulent Heat Transfer From the Core Tube in Thermal Entrance Regions of Concentric Annuli," *International Journal of Heat and Mass Transfer*, Vol. 11, 1968, pp. 509–521.

21 Lee, Y., "Turbulent Flow and Heat Transfer in Concentric and Eccentric Annuli," PhD thesis, University of Liverpool, 1964.

DISCUSSION

E. M. Sparrow[2]

Since the fluid flow and heat transfer results depend on the choice of a turbulent transport model, it is relevant to compare the ϵ_M representation, equation (15), with available data. To this end, the authors may wish to numerically evaluate equation (15) and compare the resulting ϵ_M with experimentally determined ϵ_M profiles measured by Jonsson and Sparrow.[3] The experiments covered the Reynolds number range from approximately 30,000 to 180,000 and encompassed radius ratios from 0.28 to 0.75. These ranges are relevant to those investigated in the present paper.

[2] Department of Mechanical Engineering, University of Minnesota, Minneapolis, Minn. Mem. ASME.

[3] Jonsson, V. K., and Sparrow, E. M., "Turbulent Diffusivity for Momentum Transfer in Concentric Annuli," *Journal of Basic Engineering*, TRANS. ASME, Series D, Vol. 88, 1966, pp. 550–552.

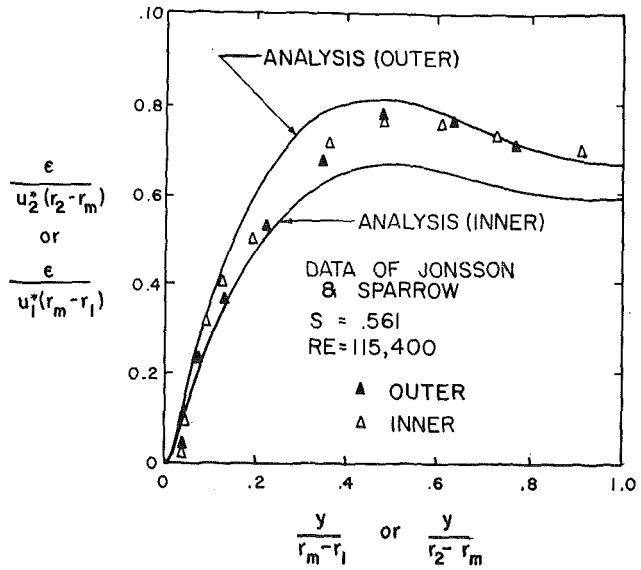

Fig. 10 Comparison of the assumed eddy diffusivity distribution to experimental data

Authors' Closure

We thank Professor Sparrow for his contribution, and we wish to point out that in the preparation of the paper, comparisons were made to available data although this is not specifically mentioned in the paper.

ϵ_M was in fact calculated using equation (17) which was derived from equation (15) as is explained in the text. For fully developed flow, $\delta_1{}^+ = (r_m - r_1)u_1{}^*/\nu$, $\delta_2{}^+ = (r_2 - r_m)u_2{}^*/\nu$, and for regions away from the wall $[1 - \exp(-y^+/A^+)]$ approaches unity. Thus the statement of equation (17) reduces essentially to the form of equation (15) with the exception that $b = 2$ in the inner region of the annulus and $b = 2.5$ in the outer region. A comparison with the data of Brighton [22] is made in the thesis [23] from which the present paper has arisen and the agreement is good within about 10 percent. For the sake of comparison Fig. 10 shows a similar sort of agreement with Jonsson and Sparrow's results.

Additional References

22 Brighton, J. A., "The Structure of Fully Developed Turbulent Flow in Annuli," PhD thesis, Purdue University, August 1963.

23 Wilson, N. W., "Turbulent Flow and Heat Transfer in Concentric and Eccentric Annuli," PhD thesis, University of Wales, March 1970.

R. P. BOBCO
Senior Staff Engineer,
Hughes Aircraft Company,
Space Systems Division,
Los Angeles, Calif.
Mem. ASME

A Script-F Matrix Formulation for Enclosures With Arbitrary Surface Emission and Reflection Characteristics

A design-oriented matrix formulation is derived for computing script-F radiative interchange factors in an enclosure of arbitrary geometrical and emissive-reflective complexity. Algorithms are presented for enclosures containing surfaces which emit either diffusely or directionally and reflect diffusely, specularly, or bidirectionally. Inputs to the transfer matrix are bidirectional and diffuse reflectances, conventional shape factors, and exchange factors which account for specular reflections. Rules are given to identify the various elements of the transfer matrix so that it may be constructed mechanically without writing complete equations for emergent directional and hemispherical fluxes. The formulation is illustrated with a closed-form solution and numerical results for a three-surface enclosure consisting of a bidirectionally reflecting area, a perfectly specular reflector, and a perfectly diffuse reflector.

Introduction

Problems of radiative transfer in nonabsorbing media are described by a Fredholm integral equation of the second kind. Solutions of the integral equation yield either the emergent intensity field or the radiosity at all surface locations in an enclosure. Ordinarily, such solutions are of secondary interest to thermal designers because of both the considerable difficulty or expense in obtaining results in a geometrically complicated enclosure and an instinctive preference for temperature or net heat flux as a primary design parameter. In a typical design situation, a thermal designer will use a nodal model of some structure of interest, and radiative transfer will represent only one of several modes of energy transport. The analytical model will require various coefficients coupling appropriate nodes, and the solution will represent the mean value of a node temperature or net heat flux.

This paper presents a design-oriented formulation for computing radiation interchange factors in enclosures of arbitrary emissive-reflective and geometrical complexity. The formulation is "design-oriented" insofar as finite nodal areas are considered rather than differential areas. The nodal areas include those with real-life characteristics such as directional emittance and bidirectional reflectance, as well as ideal characteristics such as diffuse emission and diffuse, specular, or diffuse-plus-specular reflection. Geometrical complexity is accommodated through the use of conventional shape and exchange factors to account for specular reflections. The derivation starts with Bevans and Edwards' [1][1] third approximation for the emergent intensity of a nodal area in an arbitrary enclosure and leads to an explicit formulation for a gray radiant interchange factor, Hottel's script-F, $\mathfrak{F}_{ki}$ [2].

Problem Statement

Consider an enclosure containing M nodal surfaces. The surfaces $k = 1, 2, \ldots, N$ are assumed to absorb and emit with a directional character and to have bidirectional reflectances. The surfaces $k = N + 1, N + 2, \ldots, M$ absorb and emit diffusely and have diffuse-plus-specular components ($\rho_k = \rho_k{}^d + \rho_k{}^m$) of reflectance. Black space at absolute zero temperature is designated $k = M + 1$. The enclosure is shown schematically in Fig. 1. The problem at hand is to derive coefficients $\mathfrak{F}_{ki}$ which account for the direct and reflected radiative energy exchange in the thermal waveband. The coefficients will be used to express net heat flux at a surface as

$$q_{k,\text{net}} = \sum_{i=1}^{M+1} \sigma \mathfrak{F}_{k,i}(T_k{}^4 - T_i{}^4), \text{ Btu/hr-ft}^2$$

The node-to-node interchange factors, $\mathfrak{F}_{k,i}$, will be formulated in

Contributed by the Heat Transfer Division and presented at the Space Technology and Heat Transfer Conference, Los Angeles, Calif., June 21–24, 1970, of The American Society of Mechanical Engineers. Manuscript received at ASME Headquarters, March 16, 1970. Paper No. 70-HT/SpT-3.

[1] Numbers in brackets designate References at end of paper.

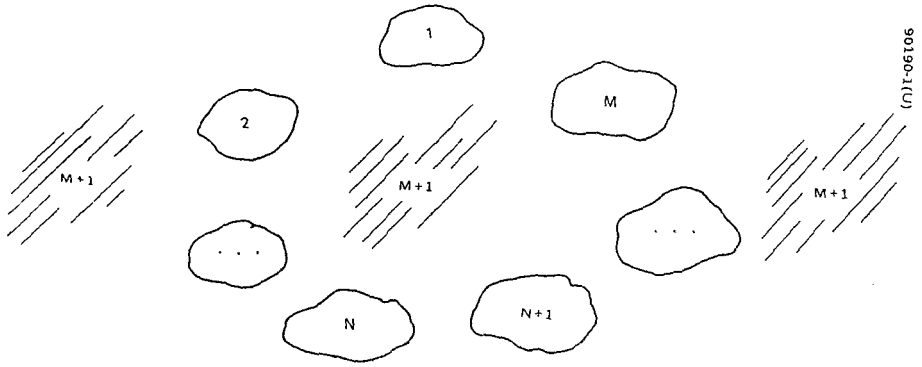

Fig. 1 General enclosure

terms of matrix elements obtained by inverting a matrix of size $[(M+1)(N+1)-N] \times [(M+1)(N+1)-N]$.

Intensity and Radiosity Equations

The approach to the problem used here is based on Bevans and Edwards [1] and is generalized to permit both real (directional/bidirectional) and ideal (diffuse/specular) surfaces in an enclosure. They derived a set of N^2 equations for mean directional intensity of a surface A_k in a directional/bidirectional enclosure:

$$\bar{I}_{kw} = \bar{\epsilon}_{kw} \frac{E_k}{\pi} + \sum_{j=1}^{N} \bar{r}_{jkw} \bar{I}_{jk} \bar{F}_{kj} \qquad (1)$$

Equation (1) describes an enclosure in which each surface "sees" itself ($\bar{I}_{kk}$), and it is assumed that the node representing black space may be treated as a bidirectional surface. Despite its generality, (1) is not suitable for an enclosure containing specularly (or diffuse-plus-specular) reflecting surfaces, except within the framework of Bevans and Edwards' "one-bounce approximation" [1]. The image method [3–5] will be used below to develop a more general form of (1). Additional insight to the "one-bounce" and image formulations is given in [6]. If diffuse emitters and diffuse-plus-specular reflectors are introduced in an enclosure, it is necessary to write only a single intensity equation for each surface based on diffuse emission and diffuse reflection. The concept of radiosity and specular exchange factors may be used in place of intensity.

In the fully mixed enclosure, it is necessary to modify (1) to account for the intensity directed at a specular reflector which arrives at another surface. The mean directional intensity is

Nomenclature

A_k = kth nodal surface area

$D_{\substack{kw \\ jp}}, D_{\substack{k' \\ j'}}$, etc. = elements of transfer matrix occupying (kw)th row (jp)th column and (k')th row, (j') column, respectively

E_k = blackbody thermal excitation of (k)th node, σT_k^4

F_{kj} = conventional shape factor between nodes A_k and A_j

$\mathfrak{F}_{ki}$ = thermal radiation interchange factor accounting for radiant energy emitted by node A_i and absorbed at A_k

G_k = irradiation (i.e., incident flux density) at A_k

$\bar{I}_{kw}$ = total intensity of A_k directed toward A_w, units of power per unit area per steradian

J_k = radiosity of A_k (i.e., diffuse emergent flux density)

$\mathcal{J}_{kw}$ = pseudoradiosity of node A_k, $\pi \bar{I}_{kw}$ (i.e., directional emergent flux density of A_k toward A_w)

k, j, i, p, b, w = indices for summation and subscripts for identifying nodal areas

M = total number of nodal areas in an enclosure

N = total number of directionally emitting, bidirectionally reflecting nodal areas in an enclosure

$q_{k,\text{net}}$ = net heat flux at A_k

$\bar{r}_{jkw}$ = nondimensional bidirectional reflectance of A_k for radiation arriving from A_j and directed toward A_w

T = absolute temperature

α_k, α_k^* = hemispherical thermal and solar absorptance, respectively, of diffusely emitting node A_k

$\beta_{\substack{kw \\ jp}}$ = element of inverted transfer matrix occupying (kw)th row, (jp)th column

δ_k^i = Kronecker delta

$\hat{\delta}_{\substack{kw \\ j}}, \hat{\delta}_{\substack{k' \\ j}}$ = influence coefficients

$\epsilon_k, \bar{\epsilon}_k$ = hemispherical emittance of diffusely emitting and directionally emitting surfaces, respectively

$\bar{\epsilon}_{kw}$ = directional emittance of A_k toward A_w

ρ_k = reflectance of kth node

ρ_k^d, ρ_k^m = diffuse and specular components of reflectance, respectively

$\bar{\rho}_{kj}, \bar{\rho}_{kj}(k)$ = hemispherical-directional semigray reflectance of A_k in the direction of A_j

σ = Stefan-Boltzmann constant

φ_{kj} = complete exchange factor; fraction of diffuse (or pseudodiffuse) energy that leaves A_k and arrives at A_j both directly and by all possible intervening specular reflections

$\varphi_{kj(p)}$ = specular component of φ_{kj} accounting for energy leaving A_k and directed toward all possible images of A_j appearing "behind" A_p

$\varphi_{kj(p,b)}$ = specular component of φ_{kj} accounting for pseudodiffuse radiation leaving A_k and directed toward secondary image of bidirectional surface A_j which appears "behind" both real specular surface A_p and specular image of A_b (in A_p)

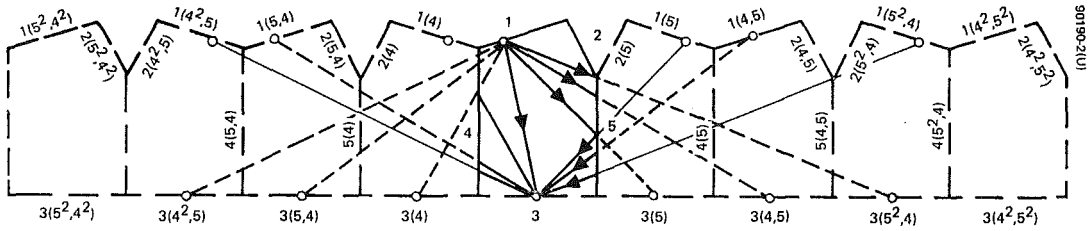

Fig. 2 Mixed enclosure

replaced by a directional flux called pseudoradiosity, and is defined as

$$\mathcal{J}_{kw} = \pi \bar{I}_{kw} \tag{2}$$

The script-J and double subscript are used to distinguish this directional flux from the diffuse flux of true radiosity. A general expression for pseudoradiosity is

$$\mathcal{J}_{kw} = \bar{\epsilon}_{kw}E_k + \sum_{j=1}^{N} \times \left(\bar{r}_{jkw}F_{kj}\mathcal{J}_{jk} + \sum_{p=N+1}^{M} \mathcal{J}_{jp} \sum_{b=N+1}^{M} \bar{r}_{j(b)kw}\varphi_{kj(p,b)} \right) + \sum_{j=N+1}^{M} \left(\bar{r}_{jkw}F_{kj} + \sum_{p=N+1}^{M} \bar{r}_{j(p)kw}\varphi_{kj(p)} \right) J_j \tag{3}$$

The corresponding radiosity expression for a diffuse-plus-specular surface is

$$J_k = \epsilon_k E_k + \rho_k{}^d \left[\sum_{j=1}^{N} \left(\mathcal{J}_{jk}F_{kj} + \sum_{p=N+1}^{M} \mathcal{J}_{jp}\varphi_{kj(p)} \right) + \sum_{j=N+1}^{M} J_j\varphi_{kj} \right] \tag{4}$$

The bar indicating an area mean value is used in the pseudoradiosity expression (3). It is omitted from the radiosity in (4) because the diffuse and specular properties are assumed to be uniform over a nodal surface and independent of directions of incidence and emergence. The use of "wrong way" shape and exchange factors is based on the reciprocity relation. Equations (3) and (4) represent a linear set of $[NM + M - N]$ algebraic equations which must be solved for the radiosities and pseudoradiosities. The shape factors, exchange factors, emittances, reflectances, and emissive powers are assumed known; the product ϵE represents the excitation, or forcing function, at each surface. The term $\mathcal{J}_{jp}\varphi_{kj(p)}$ represents the radiant flux leaving a directional surface A_j, which is specularly reflected from A_p. The notation on the exchange factor $\varphi_{kj(p)}$ denotes that the energy appears to reach A_k from the images of A_j lying behind A_p.

The solution of (3) and (4) by matrix algebra follows the discussion of geometrical factors and surface properties below.

Geometrical Factors

The construction of (3) and (4) may be explained by considering a specific enclosure. Fig. 2 shows an enclosure of five surfaces; three of these ($k = 1, 2, 3$) are directional/bidirectional; the other two ($k = 4, 5$) are diffuse-plus-specular. The image technique is used for this illustration, but alternative procedures may be used to construct the exchange factors, e.g., measurement or Monte Carlo calculations.

The pseudoradiosity from A_3 to A_2 may be expressed as

$$\mathcal{J}_{32} = \bar{\epsilon}_{32}E_3 + \sum_{j=1}^{3} \left(\bar{r}_{j32}F_{3j}\mathcal{J}_{j3} + \sum_{p=4}^{5} \mathcal{J}_{jp} \sum_{b=4}^{5} \bar{r}_{j(b)32}\varphi_{3j(p,b)} \right) + \sum_{j=4}^{5} \left(\bar{r}_{j32}F_{3j} + \sum_{p=4}^{5} \bar{r}_{j(p)32}\varphi_{3j(p)} \right) J_j \tag{5}$$

The first summation will be expanded for $j = 1$:

$$\bar{r}_{132}F_{31}\mathcal{J}_{13} + \mathcal{J}_{14}[\bar{r}_{1(4)32}\varphi_{31(4,4)} + \bar{r}_{1(5)32}\varphi_{31(4,5)}] + \mathcal{J}_{15}[\bar{r}_{1(4)32}\varphi_{31(5,4)} + \bar{r}_{1(5)32}\varphi_{31(5,5)}] \tag{6}$$

The first term, $\bar{r}_{132}F_{31}\mathcal{J}_{13}$, accounts for energy that originates at A_1, goes directly to A_3, and is redirected to A_2. The pseudoradiosity $\mathcal{J}_{13}$ is shown in Fig. 2 as a vector from A_1 to A_3. The second term in (6) accounts for the pseudoradiosity of A_1 which is initially directed toward A_4.

$$\mathcal{J}_{14}[\bar{r}_{1(4)32}\varphi_{31(4,4)} + \bar{r}_{1(5)32}\varphi_{31(4,5)}]$$

Part of this energy arrives at A_3 after one or more specular reflections from the direction of A_4, $\mathcal{J}_{14}\bar{r}_{1(4)32}\varphi_{31(4,4)}$, and the remainder from the direction of A_5, $\mathcal{J}_{14}\bar{r}_{1(5)32}\varphi_{31(4,5)}$. In the general case, the bidirectional reflectances $\bar{r}_{1(4),3,2}$ ($\approx \bar{r}_{432}$) and $\bar{r}_{1(5),3,2}$ ($\approx \bar{r}_{532}$) are different so that they cannot be combined. This distribution of the pseudoradiosity $\mathcal{J}_{14}$ is shown in Fig. 2 as three vectors from A_1 to A_4; two of these vectors account for the first and third images of A_1 lying behind A_4 and comprise the first two terms of $\varphi_{3,1(4,4)}$

$$\varphi_{31(4,4)} = \rho_4{}^m\{F_{31(4)} + \rho_4{}^m\rho_5{}^m[F_{31(4^2,5)} + \ldots]\}$$

The third vector of $\mathcal{J}_{14}$ "arrives" at A_3 from the second image of A_1 behind A_5 and is accounted in the first term of $\varphi_{3,1(4,5)}$:

$$\varphi_{31(4,5)} = \rho_4{}^m\rho_5{}^m\{F_{31(4,5)} + \rho_4{}^m\rho_5{}^m[F_{31(4^2,5^2)} + \ldots]\}$$

Similarly, the second term in (6) accounts for the pseudoradiosity $\mathcal{J}_{15}$ which arrives at A_3 from images behind both A_4 and A_5.

The first summation in (5) for $j = 2$ is similar to that of $j = 1$. The case for $j = 3$ is also similar except that ($\bar{r}_{332}F_{33}\mathcal{J}_{33}$) may appear if A_3 is concave; however, if A_3 is plane or convex, then $\bar{r}_{332} = 0$, $F_{33} = 0$, and $\mathcal{J}_{33} = 0$.

The second summation in (5) contains the diffuse contribution of the diffuse-plus-specular surfaces. The expansion for $j = 4$ is

$$(\bar{r}_{432}F_{34} + \bar{r}_{4(4)32}\varphi_{34(4)} + \bar{r}_{4(5)32}\varphi_{34(5)})J_4 \tag{7}$$

The first term $\bar{r}_{432}F_{34}J_4$, accounts for diffuse energy leaving A_4 which is reflected at A_3 toward A_2. The second term in (7) accounts for diffuse energy which appears to originate at images of A_4 lying behind A_4. For example,

$$\varphi_{34(4)} = \rho_4{}^m\rho_5{}^m[F_{34(5,4)} + \rho_4{}^m \cdot \rho_5{}^m(F_{34(5^2,4^2)} + \ldots)] \tag{8}$$

The last term accounts for images of A_4 lying behind A_5:

$$\varphi_{34(5)} = \rho_5{}^m[F_{34(5)} + \rho_5{}^m\rho_4{}^m(F_{34(5^2,4)} + \ldots)] \tag{9}$$

The exchange factors $\varphi_{34(4)}$ and $\varphi_{34(5)}$ are once removed from conventional exchange factors insofar as they do not include the direct shape factor F_{34}. The conventional shape factor, φ_{34}, would occur in (7) only if $\bar{r}_{432} = \bar{r}_{4(4)32} = \bar{r}_{4(5)35}$ and would be

$$\varphi_{34} = F_{34} + \varphi_{34(4)} + \varphi_{34(5)} \tag{10}$$

The radiosity of surface A_4 follows from (4) as

$$J_4 = \epsilon_4 E_4 + \rho_4{}^d \left[\sum_{j=1}^{3} \left(\mathcal{J}_{j4}F_{4j} + \sum_{p=4}^{5} \mathcal{J}_{jp}\varphi_{4j(p)} \right) + \sum_{j=4}^{5} J_j\varphi_{4j} \right] \tag{11}$$

The expansion of the first summation for $j = 1$ is

$$\mathcal{J}_{14}F_{41} + \mathcal{J}_{14}\varphi_{41(4)} + \mathcal{J}_{15}\varphi_{41(5)} \tag{12}$$

The shape factor $\varphi_{41(4)}$ will be nonzero if A_4 is concave or if A_4 can "see" the image $A_{1(4,5)}$. In the case at hand, A_4 is plane and sees $A_{1(4,5)}$; then,

$$\varphi_{41(4)} = \rho_4{}^m\rho_5{}^m[F_{41(4,5)} + \rho_4{}^m\rho_5{}^m(F_{41(4^2,5^2)} + \ldots)] \tag{13}$$

The remaining exchange factors appearing in (11) are

$$\varphi_{41(5)} = \rho_5{}^m[F_{41(5)} + \rho_5{}^m\rho_4{}^m(F_{41(5^2,4)} + \ldots)] \tag{14}$$

$$\varphi_{44} = \rho_5{}^m[F_{44(5)} + \rho_5{}^m\rho_4{}^m(F_{44(5^2,4)} + \ldots)] \tag{15}$$

$$\varphi_{45} = F_{45} + \rho_4{}^m\rho_5{}^m[F_{45(4,5)} + \rho_5{}^m\rho_4{}^m(F_{44(4^2,5^2)} + \ldots)] \tag{16}$$

All other exchange factors for the enclosure of Fig. 2 may be generated in a manner comparable to those described in the foregoing. It should be remarked that many of the shape factors from real surfaces to images are partial view factors insofar as nonspecular surfaces occlude a complete view.

Surface Properties: Bidirectional, Directional, Specular, and Diffuse. Radiative surface properties are measured parameters whose proper use in thermal analysis requires some discussion. The tutorial paper of Edwards [7] provides excellent insight into the measurement and interpretation of radiative transfer data. Love [8] devotes a chapter to the description of radiative characteristics of surfaces and shows the relationships between bidirectional reflectance and other surface properties. The graphical clarity of Siegel and Howell [9] provides considerable insight into the significance of surface properties and their measurement. The discussion which follows is intended to complement the information in [7–9] by showing how surface property data may be applied to the computation of radiation interchange factors.

The use of mean values of bidirectional and directional properties for nodal surface analysis is postulated in [1]. The bidirectional reflectance $\bar{r}_{jkw}$ denotes a derived property of nodal surface A_k which accounts for the redistribution of radiant energy originating at nodal area A_j and subsequently directed to nodal area A_w. The measured bidirectional reflectance is designated without the bar simply as r_{jkw} and denotes an intrinsic property of dA_k which accounts for the redistribution of radiant energy originating at dA_j and subsequently redirected to dA_w. The mean value $\bar{r}_{jkw}$ must be computed from knowledge of the geometries and orientation of A_j, A_k, and A_w and a catalog of measured data of r_{jkw}. The fundamental relationship defining area mean bidirectional reflectance is given as a multiple integral in [1],

$$\pi A_w F_{wk}F_{kj}\bar{r}_{jkw} = \int_{A_k}\int_{A_j}\frac{1}{A_\kappa}\int_{A_\kappa}\int_{A_w} r_{j\kappa w}K_{wk}K_{\kappa j} \times dA_w dA_\kappa dA_j dA_k \tag{17}$$

where

$$K_{ab}dA_a = \pi F_{dA_b - dA_a}$$

κ = dummy variable for k

Equation (17) may be cast in a form suitable for digital computation by subdividing each nodal area (e.g., A_j) into a number of elemental areas ($\Delta A_{j'}$):

$$A_j = \sum_{j'=1}^{M_j}\Delta A_{j'},\ A_k = \sum_{k'=1}^{M_k}\Delta A_{k'},\ \text{etc.}$$

The quadruple integral of (17) may be approximated by a quadruple summation as

$$\bar{r}_{jkw}F_{kj} = \frac{\sum_{w'=1}^{M_w}\left\{\sum_{k'=1}^{M_k}\left[\sum_{k''=1}^{M_k}\left(\sum_{j'=1}^{M_j} r_{j'k''w'}F_{k''j'}\right)\Delta A_{k''}\right]F_{w'k'}\right\}\Delta A_{w'}}{A_k[A_wF_{wk}]} \tag{18}$$

The element-to-element shape factors, $F_{w'k'}$, and the node-to-node factors, F_{wk}, may be found from closed-form expressions, computed or measured. The local or triple element bidirectional reflectance $r_{j'k''w'}$ must be stored as input data.

The algorithm for mean directional emittance is

$$\bar{\epsilon}_{kw} = \frac{\sum_{k'=1}^{M_k}\sum_{w'=1}^{M_w}\epsilon_{k'w'}F_{k'w'}\Delta A_{k'}}{A_kF_{kw}} \tag{19}$$

The equivalence of directional-hemispherical and hemispherical-directional reflectances [7], together with the complementary relationship between emittance and reflectance, provides a simple evaluation of directional reflectance from (19). Alternatively, directional-hemispherical reflectance of A_k may be computed as

$$\bar{\rho}_{jk}(k) = \sum_{w=1}^{M+1}\bar{r}_{jkw}F_{kw} \tag{20a}$$

while hemispherical-directional reflectance of A_k is

$$\bar{\rho}_{kw}(k) = \sum_{j=1}^{M+1}\bar{r}_{jkw}F_{kj} \tag{20b}$$

The functional notation is used to designate a property of A_k. Hemispherical reflectance follows from (20) as

$$\bar{\rho}_k = \sum_{j=1}^{M+1}\sum_{w=1}^{M+1}\bar{r}_{jkw}F_{kw}F_{kj} \tag{21}$$

The last equation is presented in the interest of completeness rather than in the belief that a hemispherical reflectance will be computed in preference to being measured.

Equations (20) and (21) may be used to obtain values of $\rho_{k\to(\text{space})}$ and $\bar{r}_{j,k,(\text{space})}$ when the space node $k = M + 1$ is arbitrarily distributed in an enclosure (see Fig. 1). That is, if all $\bar{\rho}_{kw}$ and F_{kw} ($w \neq M + 1$) are known and $\bar{\rho}_k$ is known, then

$$\bar{\rho}_{k,M+1} = \frac{\bar{\rho}_k - \sum_{w=1}^{M}\bar{\rho}_{kw}F_{kw}}{1 - \sum_{w=1}^{M}F_{kw}} = \bar{\rho}_{M+1,k} \tag{22}$$

and

$$\bar{r}_{j,k,M+1} = \frac{\bar{\rho}_{jk}(k) - \sum_{w=1}^{M}\bar{r}_{jkw}F_{kw}}{1 - \sum_{w=1}^{M}F_{kw}} \tag{23}$$

Matrix Formulation of Nodal Equations

The design equation for net heat flux appearing in the Problem Statement presented earlier is derived from a more fundamental relationship:

$$q_{k,\text{net}} = \frac{Q_{k,\text{net}}}{A_k} = \begin{pmatrix}\text{radiant flux}\\ \text{emerging at } A_k\end{pmatrix} - \begin{pmatrix}\text{radiant flux}\\ \text{incident at } A_k\end{pmatrix} \tag{24}$$

or, equivalently,

$$q_{k,\text{net}} = \begin{pmatrix}\text{hemispherical radiant}\\ \text{flux emitted at } A_k\end{pmatrix} - \begin{pmatrix}\text{radiant flux}\\ \text{absorbed at } A_k\end{pmatrix} \tag{25}$$

From [1], it follows that when A_k is a directional/bidirectional surface, (24) becomes

$$q_{k,\text{net}} = \sum_{j=1}^{M+1} \mathcal{J}_{kj}F_{kj} - G_k, \quad 1 \leq k \leq N \tag{26}$$

For the diffuse-plus-specular surfaces, (24) reduces to

$$q_{k,\text{net}} = J_k - G_k, \; N+1 \leq k \leq M \tag{27}$$

The most general expression for net heat flux follows from (25)

$$q_{k,\text{net}} = \bar{\epsilon}_k E_k - \overline{\alpha_k G_k} \tag{28}$$

where the product $\overline{\alpha_k G_k}$ is separable only when k represents a diffuse-plus-specular surface. In the case of surfaces which are both gray and emit diffusely, it is possible to let $\epsilon = \alpha$; but in the present analysis of gray surfaces which emit and absorb with a directional dependence, the hemispherical values of emittance and absorptance may be different. The two symbols ϵ and α will be retained in this discussion although they refer to the same spectral interval.

When A_k is in the bidirectional set, the absorbed flux must take account of directional absorptance:

$$\overline{\alpha_k G_k} = \sum_{j=1}^{N}\left[\mathcal{J}_{jk}\bar{\alpha}_{kj}F_{kj} + \sum_{p=N+1}^{M}\mathcal{J}_{jp}\left(\sum_{b=N+1}^{M}\bar{\alpha}_{kj(b)}\varphi_{kj(p,b)}\right)\right] + \sum_{j=N+1}^{M}J_i\left[\bar{\alpha}_{kj}F_{kj} + \sum_{p=N+1}^{M}\bar{\alpha}_{kj(p)}\varphi_{kj(p)}\right] \tag{29a}$$

When A_k is in the diffuse-plus-specular set,

$$\alpha_k G_k = \alpha_k\left\{\sum_{j=1}^{N}\left[\mathcal{J}_{jk}F_{kj} + \sum_{p=N+1}^{N}\mathcal{J}_{jp}\varphi_{kj(p)}\right] + \sum_{j=N+1}^{M}J_j\varphi_{kj}\right\} \tag{29b}$$

The summation over all surfaces may include space, $j = M+1$; but insofar as $J_{M+1} = 0$, there is no space contribution to absorbed flux. The irradiation G_k of a surface may be obtained from (29) by deleting absorptances from the expressions.

The net heat flux equations are general within the framework of nodal analysis and are not constrained to further elucidation by any specific method of solving for the radiosities and pseudoradiosities. In theory, the $\mathcal{J}$'s and J's may be found by (a) solving a linear set of integral equations, (b) using Monte Carlo procedures for ray tracing, or (c) inverting a matrix implied by (3) and (4). The matrix solution is described in the remainder of this paper.

Explicit Solutions for $\mathcal{J}_{kj}$ and J_k. Matrix solutions for diffuse or diffuse-plus-specular surfaces are well documented in the literature of engineering radiation analysis [10–12]. In an enclosure of M surfaces, a transfer matrix, $\hat{D}$, contains M^2 elements of the forms $(\delta_k{}^j - \rho_k{}^d\varphi_{kj})$. The elements of the inverted transfer matrix, $[\hat{D}]^{-1}$, are β_{kj}, and the solutions for radiosity may be expressed explicitly as

$$J_k = \sum_{j=1}^{M}\epsilon_j E_j \beta_{kj}$$

The only real problem in this conceptually simple formulation is that of evaluating the β_{jk} elements in $[\hat{D}]^{-1}$. This last aspect of matrix algebra is not discussed in this paper.

The matrix solution for radiosities and pseudoradiosites in a mixed enclosure containing both bidirectional and diffuse-plus-specular surfaces is also conceptually simple. However, the notation is more cumbersome because up to four indices are required to identify an element of the transfer matrix and, correspondingly, the inverted transfer matrix. Submatrices associated with the bidirectional set are identified with plain indices:

$$\left.\begin{matrix} j \\ k \\ p \\ w \end{matrix}\right\} = 1, 2, \ldots, N$$

Primed indices b', k', etc., refer to nodes in the diffuse-plus-specular set and black space:

$$\left.\begin{matrix} b' \\ j' \\ k' \\ p' \end{matrix}\right\} = N+1, N+2, \ldots, M, M+1$$

This "plain or primed" convention is used in describing the matrix elements only and discontinued when there is no sacrifice in clarity. A matrix equation based on (3) and (4) may be written as

$$\underbrace{\begin{vmatrix} \hat{D}_{jp} & \hat{D}_{jj'} \\ \hat{D}_{k'p} & \hat{D}_{k'j'} \end{vmatrix}}_{\text{Transfer matrix}} \underbrace{\begin{vmatrix} \hat{\mathcal{J}}_{kw} \\ \hat{J}_{k'} \end{vmatrix}}_{\text{Response matrix}} = \underbrace{\begin{vmatrix} \widehat{\bar{\epsilon}_{kw}E_k} \\ \widehat{\epsilon_{k'}E_{k'}} \end{vmatrix}}_{\text{Excitation vector}} \tag{30}$$

The column matrices comprising the response and excitation vectors are shown in the following:

$$\hat{\mathcal{J}}_{kw} = [\mathcal{J}_{11}, \mathcal{J}_{12}, \ldots, \mathcal{J}_{1,M+1} \ldots \ldots \mathcal{J}_{N1}, \ldots, \mathcal{J}_{N,M+1}]^T \text{ order } 1 \times N(M+1) \tag{31a}$$

$$\hat{J}_{k'} = [J_{N+1}, J_{N+2}, \ldots J_M]^T \text{ order } 1 \times (M+1-N) \tag{31b}$$

$$\widehat{\bar{\epsilon}_{kj}E_k} = [\bar{\epsilon}_{11}E_1, \bar{\epsilon}_{12}E_1, \ldots, \bar{\epsilon}_{1,M+1}E_1, \ldots \ldots \bar{\epsilon}_{N1}E_N, \ldots, \bar{\epsilon}_{N,M+1}E_N]^T \text{ order } 1 \times N(M+1) \tag{32a}$$

$$\widehat{\epsilon_{k'}E_{k'}} = [\epsilon_{N+1}E_{N+1}, \epsilon_{N+2}E_{N+2}, \ldots \epsilon_{M+1}E_{M+1}]^T \text{ order } 1 \times (M+1-N) \tag{32b}$$

The elements of the transfer matrix have been partially generalized and are given below. The notation requires some clarification:

$D_{\substack{kw \\ jp}}$ — Row: A_k toward A_w or $A_{w'}$; Column: A_j toward A_p or $A_{p'}$

$D_{\substack{kw \\ j'}}$ — Row: A_k toward A_w or $A_{w'}$; Column: $A_{j'}$

$D_{\substack{k' \\ jp}}$ — Row: $A_{k'}$; Column: A_j toward A_p or $A_{p'}$

$D_{\substack{k' \\ j'}}$ — Row: $A_{k'}$; Column: $A_{j'}$

Elements of $\hat{D}_{jp}^{kw}$ (order $N(M+1) \times N(M+1)$):

$$D_{jp}^{kw} = \delta_k{}^j\delta_w{}^p - \delta_k{}^p(\bar{r}_{jkw}F_{kj}) \tag{33a}$$

$$D_{jp'}^{kw} = \delta_k{}^j\delta_w{}^{p'} - \sum_{b'=N+1}^{M}\bar{r}_{j(b')kw}\varphi_{kj(p',b')} \tag{33b}$$

Elements of $\hat{D}_{j'}^{kw}$ (order $N(M+1) \times (M+1-N)$):

$$D_{j'}^{kw} = -\left[\bar{r}_{j'kw}F_{kj} + \sum_{p'=N+1}^{M}\bar{r}_{j'(p')kw}\varphi_{kj'(p')}\right] \tag{33c}$$

Elements of $D_{jp}^{k'}$ (order $(M+1-N) \times N(M+1)$):

$$D_{\underset{jp}{k'}} = 0 \tag{33d}$$

$$D_{\underset{jp'}{k'}} = -\rho_{k'}{}^{d}\left[\delta_{k'}{}^{p'}\varphi_{k'j} + (1 - \delta_{k'}{}^{p'})\sum_{p'=N+1}^{M}\varphi_{k'j(p')}\right] \tag{33e}$$

Elements of $\hat{D}_{\underset{j'}{k'}}$ (order $(M + 1 - N) \times (M + 1 - N)$):

$$D_{\underset{j'}{k'}} = \delta_{k'}{}^{j'} - \rho_{k'}{}^{d}\varphi_{k'j'} \tag{33f}$$

The transfer matrix contains $[(M + 1)(N + 1) - N]^2$ elements. Inversion of the transfer matrix leads to elements

$$\beta_{\underset{jp}{kw}};\ \beta_{\underset{j'}{kw}};\ \beta_{\underset{jp}{k'}};\ \beta_{\underset{j'}{k'}};\ \text{etc.}$$

corresponding to the D's of (33*a–f*). Straightforward matrix algebra leads to solutions for pseudoradiosity and radiosity in the form

$$\mathcal{J}_{kw} = \sum_{j=1}^{M+1}\hat{\delta}_{\underset{j}{kw}}E_j, \qquad \begin{cases}1 \le k \le N\\ 1 \le w \le M + 1\end{cases} \tag{34a}$$

$$J_k = \sum_{j=1}^{M+1}\hat{\delta}_{\underset{j}{k}}E_j, \qquad N + 1 \le k \le M \tag{34b}$$

The influence coefficients $\hat{\delta}_{\underset{j}{kw}}$ and $\hat{\delta}_{\underset{j}{k}}$ are designated as matrices and may be formed by multiplication of submatrices or obtained explicitly as

$$\hat{\delta}_{\underset{j}{kw}} = \sum_{p=1}^{M+1}\bar{\epsilon}_{jp}\beta_{\underset{jp}{kw}} \tag{35a}$$

$$\hat{\delta}_{\underset{j}{k'}} = \sum_{p=1}^{M+1}\bar{\epsilon}_{jp}\beta_{\underset{jp}{k'}} \tag{35b}$$

$$\hat{\delta}_{\underset{j'}{kw}} = \epsilon_{j'}\beta_{\underset{j'}{kw}} \tag{35c}$$

$$\hat{\delta}_{\underset{j'}{k'}} = \epsilon_{j'}\beta_{\underset{j'}{k'}} \tag{35d}$$

The "plain or primed" convention is suppressed in (34) and in the remaining discussion in the interest of conciseness.

Script-F, Hottel's Interchange Factor. The radiosity and pseudoradiosity solutions of (34) may be used with any of the appropriate expressions for net heat flux to obtain a formulation for a radiation interchange factor. The derivation proceeds by combining (29) and (34) to obtain the absorbed flux at a surface in terms of the nodal emissive powers, geometrical factors, and $\hat{\delta}$ coefficients. The resulting expressions may be used in (28) with the argument of zero net heat flux in an isothermal enclosure [5] to obtain expressions for the radiative interchange factor, $\mathcal{F}_{ki}$:

A_k Bidirectional: $1 \le k \le N$

$$\mathcal{F}_{ki} = \sum_{j=1}^{N}\left[\bar{\alpha}_{kj}F_{kj}\hat{\delta}_{\underset{i}{jk}} + \sum_{p=N+1}^{M}\hat{\delta}_{\underset{i}{jp}}\left(\sum_{b=N+1}^{M}\alpha_{kj(b)}\varphi_{kj(p,b)}\right)\right] + \sum_{j=N+1}^{M}\hat{\delta}_{\underset{i}{j}}\left[\bar{\alpha}_{kj}F_{kj} + \sum_{p=N+1}^{M}\bar{\alpha}_{kj(p)}\varphi_{kj(p)}\right] \tag{36}$$

A_k Diffuse-Plus-Specular: $N + 1 \le k \le M$

$$\mathcal{F}_{ki} = \alpha_k\left\{\sum_{j=1}^{N}\left[F_{kj}\hat{\delta}_{\underset{i}{jk}} + \sum_{p=N+1}^{M}\varphi_{kj(p)}\hat{\delta}_{\underset{i}{jp}}\right] + \sum_{j=N+1}^{M}\varphi_{kj}\hat{\delta}_{\underset{i}{j}}\right\} \tag{37}$$

In both (36) and (37), node A_i is arbitrary and may refer to a bidirectional, diffuse-plus-specular, or space node. Thermodynamic arguments [2] may be invoked to show that reciprocity applies:

$$A_k\mathcal{F}_{ki} = A_i\mathcal{F}_{ik} \tag{38}$$

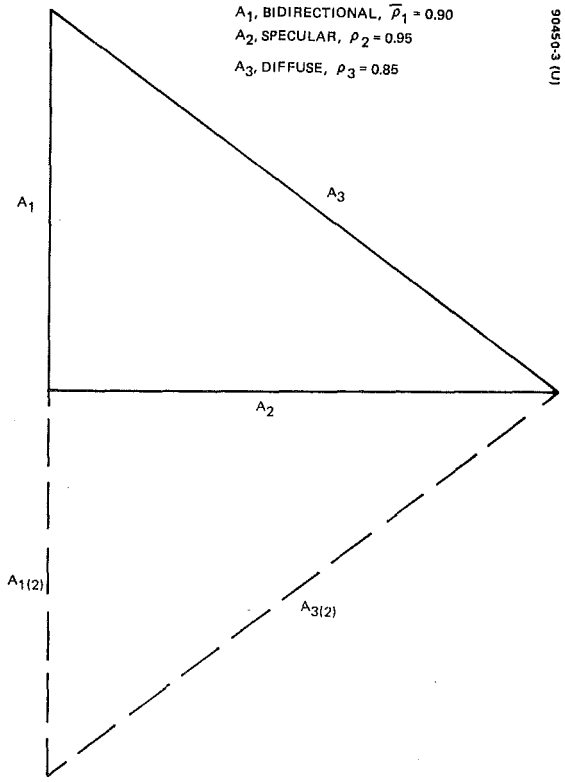

Fig. 3 Hypothetical enclosure showing real surfaces and images

A summation relationship follows from (28) as

$$\sum_{i=1}^{M+1}\mathcal{F}_{ki} = \bar{\epsilon}_k \tag{39}$$

Considerable computational convenience may be achieved from an alternate formulation

$$J_k = \epsilon_k E_k + \rho_k{}^{d}G_k \tag{40}$$

which can be rearranged as

$$G_k = (J_k - \epsilon_k E_k)/\rho_k{}^{d} \tag{41}$$

The net heat flux expression (25) may be used with (34*b*) and (41) and the usual thermodynamic argument invoked to obtain

$$\mathcal{F}_{ki} = \frac{\alpha_k}{\rho_k{}^{d}}\hat{\delta}_{\underset{i}{k}}, \qquad \begin{cases}N + 1 \le k \le M\\ 1 \le i \le M + 1\end{cases} \tag{42}$$

The computational advantage of using (42) instead of (37) is apparent; a computational, but not conceptual, disadvantage occurs when $\rho_k{}^{d} = 0$. The difficulty is not conceptual because $\hat{\delta}_{\underset{i}{k}}$ is directly proportional to $\rho_k{}^{d}$ (when $k \neq i$), so that reflectance is eliminated from the expression. However, it is troublesome to account for this elimination in a computer program. The reciprocity relation remains unchanged, but the summation rule becomes

$$\sum_{i=1}^{M+1}\mathcal{F}_{ki} = \frac{\epsilon_k}{\rho_k{}^{d}}(1 - \rho_k{}^{m}), \qquad N + 1 \le k \le M \tag{43}$$

The radiant interchange factors formulated in (37) and (42) are numerically identical except for $\mathcal{F}_{kk}$. The two different self-absorption factors are related as

$$\underset{\text{Equation (37)}}{\mathcal{F}_{kk}} = \underset{\text{Equation (42)}}{\mathcal{F}_{kk}} - \frac{\epsilon_k{}^{2}}{\rho_k{}^{d}} \tag{44}$$

These two factors have been observed previously and are discussed briefly in [5] and a "Comment," to [11].

Equations (36) through (39), and (42) through (44) represent the relationships which account for radiative interchange in a gray, mixed enclosure in which excitation is provided by surface temperature. All these equations reduce to conventional expressions [2 and 5] when there are no directional emitting/bidirectional reflecting surfaces in an enclosure.

Sample Problem

A simple enclosure is shown in Fig. 3 with three plane surfaces which reflect bidirectionally (A_1), specularly (A_2), and diffusely (A_3). This arrangement of surfaces and properties contains all of the features necessary to illustrate the formulation while allowing an immediate closed-form solution for all interchange factors. The transfer matrix may be constructed using (33) and is shown below with the (1, 1) row and (1, 1) column deleted because A_1 is plane:

$$D = \begin{array}{c|cccc} \text{col} \rightarrow & (1,2) & (1,3) & (2) & (3) \\ \text{row} \downarrow & & & & \\ (1,2) & 1 & 0 & -\bar{r}_{212}F_{12} & -(\bar{r}_{312}F_{13} + \bar{r}_{3(2)12}\varphi_{13(2)}) \\ (1,3) & 0 & 1 & -\bar{r}_{213}F_{12} & -(\bar{r}_{313}F_{13} + \bar{r}_{3(2)13}\varphi_{13(2)}) \\ (2) & 0 & 0 & 1 & 0 \\ (3) & -\rho_3\varphi_{31(2)} & -\rho_3F_{31} & -\rho_3F_{32} & (1 - \rho_3\varphi_{33}) \end{array} \quad (45a)$$

This transfer matrix is readily expanded to obtain

$$D = 1 - \rho_3\varphi_{33} - \rho_3\varphi_{31(2)}(\bar{r}_{312}F_{13} + \bar{r}_{3(2)12}\varphi_{13(2)}) - \rho_3F_{31}(\bar{r}_{313}F_{13} + \bar{r}_{3(2)13}\varphi_{13(2)}) \quad (45b)$$

The exchange factors appearing in (45) may be obtained from image analysis as

$$\varphi_{13(2)} = \rho_2{}^mF_{13(2)};\ \varphi_{31(2)} = \rho_2{}^mF_{31(2)};\ \varphi_{33} = \rho_2{}^mF_{33(2)} \quad (46)$$

The matrix may be inverted using Cramer's Rule, and the result in terms of β elements is

$$[\hat{D}]^{-1} = \begin{array}{c|cccc} & (1,2) & (1,3) & (2) & (3) \\ (1,2) & 1 - \rho_3\varphi_{33} - \rho_3F_{31}(\bar{r}_{313}F_{13} + \bar{r}_{3(2)13}\varphi_{13(2)}) & \rho_3F_{31}(\bar{r}_{312}F_{13} + \bar{r}_{3(2)12}\varphi_{13(2)}) & \bar{r}_{212}F_{12}[1 - \rho_3\varphi_{33} - \rho_3F_{31} \times (\bar{r}_{313}F_{13} + \bar{r}_{3(2)13}\varphi_{1,3(2)})] + [\rho_3F_{32} + \rho_3F_{31}(\bar{r}_{213}F_{12})] \times [\bar{r}_{312}F_{13} + \bar{r}_{3(2)12}\varphi_{13(2)}] & \bar{r}_{312}F_{13} + \bar{r}_{3(2)12}\varphi_{13(2)} \\ (1,3) & \rho_3\varphi_{31(2)}(\bar{r}_{313}F_{13} + \bar{r}_{3(2)13}\varphi_{13(2)}) & 1 - \rho_3\varphi_{33} - \rho_3\varphi_{31(2)} \times (\bar{r}_{312}F_{13} + \bar{r}_{3(2)12}\varphi_{13(2)}) & \bar{r}_{213}F_{12}[1 - \rho_3\varphi_{33} - \rho_3\varphi_{31(2)} \times (\bar{r}_{312}F_{13} + \bar{r}_{3(2)12}\varphi_{13(2)})] + [\rho_3F_{32} + \rho_3\varphi_{31(2)}(\bar{r}_{212}F_{12})] \times [\bar{r}_{313}F_{13} + \bar{r}_{3(2)13}\varphi_{13(2)}] & \bar{r}_{313}F_{13} + \bar{r}_{3(2)13}\varphi_{13(2)} \\ (2) & 0 & 0 & D & 0 \\ (3) & \rho_3\varphi_{31(2)} & \rho_3F_{31} & \rho_3F_{23} + \rho_3F_{31}(\bar{r}_{213}F_{12}) + \rho_3\varphi_{31(2)}(\bar{r}_{212}F_{12}) & 1 \end{array} \div D \quad (47)$$

Script-F factors for this enclosure may be found with the use of (35) and (36) or (37). For example,

$$\mathfrak{F}_{12} = \frac{\epsilon_2}{D}\{\alpha_{12}F_{12} + \rho_3[\alpha_{13}F_{13} + \alpha_{13(2)}\varphi_{13(2)}]\ [F_{23} + F_{31}(\bar{r}_{213}F_{12}) + \varphi_{31(2)}(\bar{r}_{212}F_{12})]\}$$

and

$$\mathfrak{F}_{23} = \frac{\epsilon_3\alpha_2}{D}\{F_{23} + F_{21}[\bar{r}_{312}F_{13} + \bar{r}_{3(2)12}\varphi_{13(2)}]\}$$

For the sake of numerical results, the surface areas were taken in the ratio $A_1:A_2:A_3 = 3:4:5$, and all surfaces were assumed to emit and absorb diffusely; specific properties are shown in Table 1.

Shape factors were evaluated using the "string rule." The transfer matrix corresponding to (45a) is

$$D = \begin{vmatrix} 1 & 0 & -0.1000 & -0.8950 \\ 0 & 1 & -0.4000 & -0.8800 \\ 0 & 0 & 1 & 0 \\ -0.1615 & -0.3400 & -0.5100 & 0.6770 \end{vmatrix}$$

and the inverted matrix is

$$[D]^{-1} = \begin{vmatrix} 1.6197 & 1.3046 & 2.6406 & 3.8370 \\ 0.6093 & 2.2827 & 2.8981 & 3.7727 \\ 0 & 0 & 1 & 0 \\ 0.6924 & 1.4576 & 2.8387 & 4.2871 \end{vmatrix}$$

The interchange factors for the enclosure are

$$A_1\mathfrak{F}_{1,2} = A_2\mathfrak{F}_{2,1} = 0.04686$$

$$A_1\mathfrak{F}_{1,3} = A_3\mathfrak{F}_{3,1} = 0.1897$$

$$A_2\mathfrak{F}_{2,3} = A_3\mathfrak{F}_{3,2} = 0.1253$$

By way of comparison, when A_1 is treated either as a perfectly diffuse or perfectly specular reflector, the $A\mathfrak{F}$ values remain virtually unchanged with differences of less than 2 percent for all cases.

Summary

A general matrix formulation has been derived for calculating script-F radiative interchange factors in enclosures of arbitrary geometrical and reflective complexity. The algorithm is suitable for any combination of surface emission and reflection characteristics. The inputs to the transfer matrix are bidirectional reflectances, the diffuse component of reflectance for diffuse-plus-specular reflecting surfaces, conventional shape factors between surfaces, and exchange factors which account for specular reflections. Matrix inversion yields influence coefficients (i.e., interreflection kernels) which depict the exchange between a pair of surfaces. This formulation is most suitable for enclosure design analysis based on a nodal model of some structure of interest.

Table 1 Surface properties for enclosure of Fig. 3

j	ϵ_j	$\rho_j{}^m$	$\rho_j{}^d$	$\bar{r}_{w,1,j}$ $w = 2$	$w = 3$	$w = 3(2)$
1	0.10	...	...	0	0	0
2	0.05	0.95	0	0.30	1.20	0.30
3	0.15	0	0.85	1.20	0.75	1.20

The derivation and discussion included the development of a general equation for directional radiant flux (pseudoradiosity) including guidelines for constructing modified exchange factors (e.g., $\varphi_{i,j(k)}$) necessary in fully mixed enclosures. A half dozen rules identify the various elements of the transfer matrix so that it may be constructed mechanically without first writing several directional or hemispherical emergent flux equations. Finally, a simple enclosure was examined to illustrate the use of the matrix formulation. A two-dimensional, fully mixed enclosure of three surfaces was postulated to have sides that reflect bidirectionally, specularly, and diffusely. This arrangement allowed a succinct closed-form inversion to show the nature of a typical script-F factor. Some numerical results were included to complete the presentation.

Acknowledgment

This study was conducted as one phase of NASA Contract NAS9-7980, sponsored by the Manned Spacecraft Center, Houston, Texas. The author gratefully acknowledges the assistance of Prof. P. F. O'Brien, UCLA, who reviewed the analysis and eliminated several inconsistencies in notation and formulation.

References

1 Bevans, J. T., and Edwards, D. K., "Radiation Exchange in an Enclosure With Directional Wall Properties," JOURNAL OF HEAT TRANSFER, TRANS. ASME, Series C, Vol. 87, No. 3, Aug. 1965, pp. 388–396.

2 Hottel, H. C., "Radiant Heat Transmission," in W. H. McAdams, *Heat Transmission*, 3rd ed., McGraw-Hill, 1954, pp. 55–81.

3 Eckert, E. R. G., and Sparrow, E. M., "Radiative Heat Exchange Between Surfaces With Specular Reflection," *International Journal of Heat and Mass Transfer*, Vol. 3, No. 1, 1961, pp. 42–54.

4 Sparrow, E. M., Eckert, E. R. G., and Jonssen, V. K., "An Enclosure Theory for Radiative Exchange Between Specularly and Diffusely Reflecting Surfaces, JOURNAL OF HEAT TRANSFER, TRANS. ASME, Series C, Vol. 84, No. 4, Nov. 1962, pp. 294–300.

5 Bobco, R. P., "Radiation Heat Transfer in Semigray Enclosures With Specularly and Diffusely Reflecting Surfaces," JOURNAL HEAT TRANSFER, TRANS. ASME, Series C, Vol. 86, No. 1, Feb. 1964, pp. 123–130.

6 Bobco, R. P., "Analytical Determination of Radiation Interchange Factors," NASA CR 99683, June 1969.

7 Edwards, D. K., "Radiative Transfer Characteristics of Materials," JOURNAL OF HEAT TRANSFER, TRANS. ASME, Series C, Vol. 91, No. 1, Feb. 1969, pp. 1–15.

8 Love, T. J., *Radiative Heat Transfer*, Chas. E. Merrill Publishing Co., 1968.

9 Siegel, R., and Howell, J. R., "Thermal Radiation Heat Transfer, NASA SP-164, U. S. Government Printing Office, Washington, D. C., 1968.

10 Ishimoto, T., and Bevans, J. T., "Method of Evaluating Script-F for Radiant Exchange Within Enclosure," *AIAA Journal*, Vol. 1, No. 6, June 1963, pp. 1428–1429.

11 Sarofim, A. F., and Hottel, H. C., "Radiative Exchange Among Non-Lambert Surfaces," JOURNAL OF HEAT TRANSFER, TRANS. ASME, Series C, Vol. 88, No. 1, Feb. 1966, pp. 37–44.

12 Sparrow, E. M., and Cess, R. D., *Radiation Heat Transfer*, Brooks/Cole Publishing Co., 1966.

R. C. DONOVAN
Engineering Research Center,
Western Electric Co.,
Princeton, N. J.
Formerly Assistant Professor,
Mechanical Engineering Department,
University of Pittsburgh,
Pittsburgh, Pa.

W. M. ROHRER
Associate Professor,
Mechanical Engineering Department,
University of Pittsburgh,
Pittsburgh, Pa.

Radiative and Convective Conducting Fins on a Plane Wall, Including Mutual Irradiation[1]

The radiative and convective heat transfer from a fin array consisting of longitudinal rectangular fins on a plane surface has been theoretically investigated by mathematically describing the interaction among the heat conduction in the fin, the convective heat transfer to the fluid medium, and the radiant exchange of the fin with the neighboring elements. Solutions for the fin temperature distribution, the local radiative heat fluxes over the fin and base surfaces, the total radiative heat transfer, the total convective heat transfer, and the effectiveness of the fins were found. In the primary range of physical interest, the fins usually cause a considerable increase in the convective component of the heat transfer but either cause decreases or only slight increases in the radiative component. Thus convection is generally the more effective mode of heat transfer in fin arrays, and the effectiveness of the fins decreases as the radiative component increases.

Introduction

In the past few years, several studies have attempted to approximate more closely the radiative contribution in extended surfaces cooled or heated by convection and thermal radiation. Most [1–6][2] of these analyses, however, have not considered the mutual irradiation between adjacent fins and the base surface, while one [7] includes irradiation from the base but neglects the effect of the neighboring fins.

This study theoretically investigates the radiative and convective heat-transfer characteristics of the heat-conducting fin array shown in Fig. 1 to achieve the following primary objectives: (1) the evaluation of the total heat transfer from the fin ensemble to determine the effectiveness of the extended surfaces, (2) the evaluation of the individual contributions of radiation and convection to determine the effectiveness of each, and (3) the influence of the important parameters on the thermal performance of the fin array.

The thermal performance of these radiative and convective extended surfaces is determined by the interactions among the heat conduction in the fin, the convective heat transfer to the fluid medium, and the radiant exchange of the fin with the base, the neighboring fins, and the environment. The mathematics is complicated by the nonlinearity of thermal radiation, the complexity of the convective flow, the large number of parameters involved, and the necessity of solving coupled systems of integrodifferential equations.

Analysis

The mathematical model of the physical situation is based on:

1 One-dimensional, steady-state heat conduction through homogeneous isotropic fins.

2 Gray, diffuse surfaces and a radiatively nonparticipating convective fluid.

3 A convective heat-transfer process described by Newton's law of cooling.

4 A constant ambient fluid temperature, T_∞, which is equa-

[1] This paper is based on a dissertation submitted by Dr. Donovan in partial fulfillment of the requirements for a PhD at the University of Pittsburgh.

[2] Numbers in brackets designate References at end of paper.

Contributed by the Heat Transfer Division for publication (without presentation) in the Journal of Heat Transfer. Manuscript received by the Heat Transfer Division, August 20, 1969; revised manuscript received, October 13, 1969. Paper No. 70-HT-F.

Nomenclature

b = fin spacing
B = fin radiosity
B^* = dimensionless fin radiosity, $B/\sigma T_b^4$
$\bar{B}$ = base radiosity
$\bar{B}^*$ = dimensionless base radiosity, $\bar{B}/\sigma T_b^4$
F = shape factor
h_c = convective coefficient
h_c^* = dimensionless convective coefficient, $h_c L^2/kw$
H = fin irradiation
H^* = dimensionless fin irradiation, $H/\sigma T_b^4$
$\bar{H}$ = base irradiation
$\bar{H}^*$ = dimensionless base irradiation, $\bar{H}/\sigma T_b^4$
k = fin thermal conductivity
l = fin width
L = fin length
N_c = conduction parameter, $L^2\sigma T_b^3/kw$
q = heat-transfer rate per unit area
Q = heat-transfer rate
Q_T = heat-transfer rate from the fin system

(*Continued on next page*)

to the radiative environmental temperature, T_0.

The governing equations of the energy transport process are obtained by applying the conservation of energy principle to an infinitesimal element in an arbitrary fin and using the radiant flux balances between two adjacent fins, the included base surface, and the environment. The resulting dimensionless equations [8] are nonlinear and integrodifferential:

$$\frac{d^2T^*}{dx^{*2}} = N_c(B^* - H^*) + h_c^*(T^* - T_\infty^*) \tag{1}$$

$$B^*(x^*) = \epsilon T^{*4}(x^*) + (1 - \epsilon)H^*(x^*) \tag{2}$$

$$H^*(x^*) = \int_0^1 B'^*(x'^*)dF_{dx^*-dx'^*} + \int_0^1 \bar{B}^*(z^*)dF_{dx^*-dz^*} + F_{dx^*-0}(x^*)T_0^{*4} \tag{3}$$

$$\bar{B}^*(z^*) = \epsilon + (1 - \epsilon)\bar{H}^*(z^*) \tag{4}$$

$$\bar{H}^*(z^*) = \int_0^1 B^*(x^*)dF_{dz^*-dx^*} + \int_0^1 B'^*(x'^*)dF_{dz^*-dx'^*} + F_{dz^*-0}(z^*)T_0^{*4} \tag{5}$$

The dimensionless boundary conditions are formulated from the fixed temperature at the root of the fin and the balance of energy at the tip of the fin.

$$T^*(x^*) = 1.0 \quad \text{at} \quad x^* = 0 \tag{6}$$

$$-\frac{dT^*}{dx^*} = \epsilon\frac{w}{L}N_c(T^{*4} - T_0^{*4}) + \frac{w}{L}h_c^*(T^* - T_\infty^*) \quad \text{at} \quad x^* = 1.0 \tag{7}$$

In the above relations, the following dimensionless quantities are used.

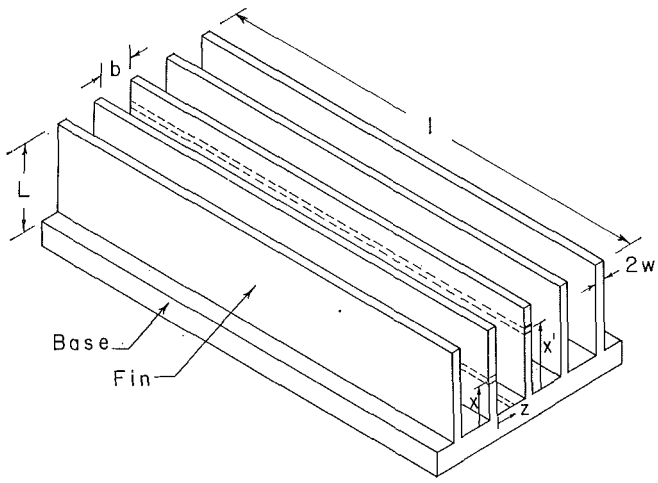

Fig. 1 Fin system configuration

$$x^* = \frac{x}{L}, \quad z^* = \frac{z}{b}, \quad T^* = \frac{T}{T_b}, \quad T^*_\infty = \frac{T_\infty}{T_b}$$

$$B^* = \frac{B}{\sigma T_b^4}, \quad H^* = \frac{H}{\sigma T_b^4}, \quad \bar{B}^* = \frac{\bar{B}}{\sigma T_b^4}, \quad \bar{H}^* = \frac{H}{\sigma T_b^4} \tag{8}$$

$$T_0^* = \frac{T_0}{T_b}, \quad N_c = \frac{L^2\sigma T_b^3}{kw}, \quad h_c^* = \frac{h_c L^2}{kw}$$

The heat-transfer relations are made dimensionless by dividing by the heat transfer Q_0 from the base surface when fins are not present:

$$Q_0 = Q_{0_R} + Q_{0_c} = (b + 2w)l[\epsilon\sigma(T_b^4 - T_0^4) + h_c(T_b - T_\infty)] \tag{9}$$

If Q_T is the total heat transfer from the fin array, the fin system effectiveness Q_T^* is found from

$$Q_T^* = Q_T/Q_0 = \frac{Q_R + Q_c}{Q_0} = Q_R^* + Q_c^* \tag{10}$$

and it can provide a measure of the gain or loss due to finning. The effectiveness of each mode of heat transfer is determined by evaluating the radiative and convective contributions separately.

The interpretation that Q_T^* measures the improvement in heat flow due to finning is valid only if the value of the average convective coefficient h_c is not appreciably altered by the presence of the fins. If h_c is changed significantly, as occurs in many practical fin designs, Q_T^* can only be interpreted as a dimensionless form of the heat transfer, and the proper effectiveness must be determined by use of the appropriate convective coefficients for the finned and nonfinned situations.

The mathematical complexity of the governing equations necessitated a numerical method of solution. The system of equations (1)–(5) becomes a finite system of nonlinear algebraic equations for the values of the unknown functions at discrete points along the fin and base. A numerical iterative procedure, called Steffensen's method [9], which combines the method of successive approximations and the Aitken Δ^2-process, was used to solve the system of nonlinear algebraic equations [8]. The algorithmic procedures were programmed and executed on a digital computer system.

Results

Parametric Values. There are essentially five independent dimensionless parameters, ϵ, $\frac{b}{L}$, N_c, h_c^*, and T_0^* ($\frac{w}{L}$ is not important as a separate independent parameter [8]), and a representative number of values were selected as listed in Table 1.

Table 1 Parametric values

ϵ	0.5, 1.0
h_c^*	0.1, 1.0, 5.0
T_0^*	0.4, 0.8
N_c	0.0, ...
$\frac{b}{L}$	0.25, 0.50, 1.0
$\frac{w}{L}$	0.025

Nomenclature

Q_0 = heat-transfer rate from the unfinned base surface
Q_T^* = fin system effectiveness, Q_T/Q_0
Q^{**} = dimensionless fin system heat flux
T = fin absolute temperature
T_b = base temperature
T_0 = radiative environmental temperature
T_∞ = convective ambient temperature
w = fin half-thickness
x = fin coordinate
x' = adjacent fin coordinate
z = base coordinate
ϵ = emittance
σ = Stefan-Boltzmann constant

Subscripts

c = convection
R = radiation
T = total (radiation and convection)

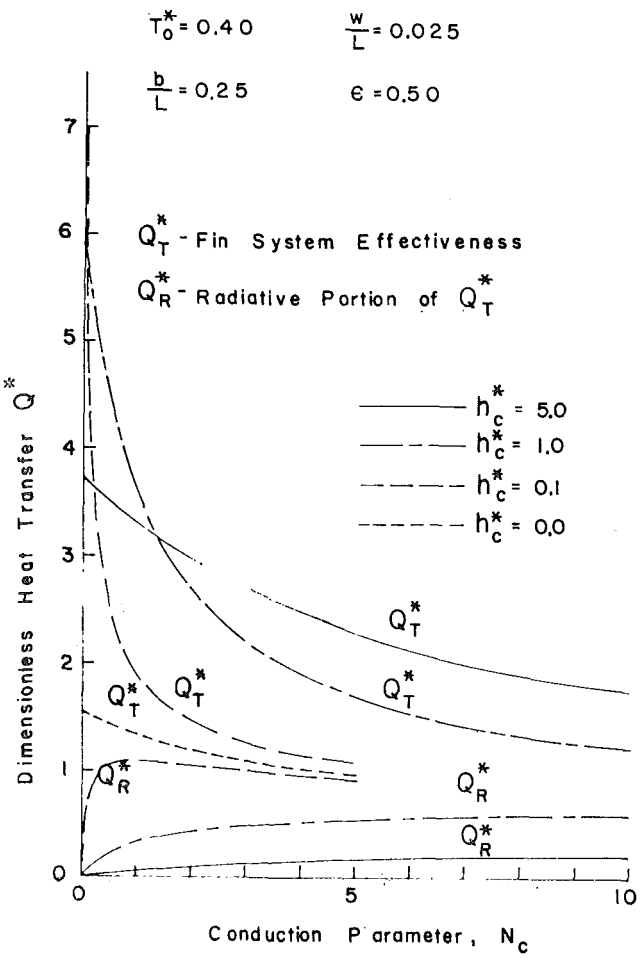

Fig. 2 Dimensionless heat-transfer results

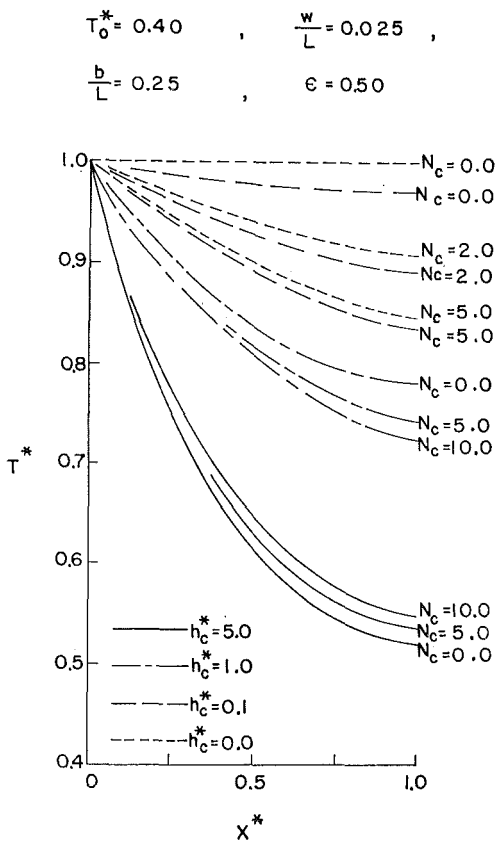

Fig. 3 Fin temperature distributions

A Typical Case. To illustrate the heat-transfer results, a typical set of cases, identified in Fig. 2, is discussed first.

Numerical solutions for the dimensionless heat transfer from the fin array are presented in Fig. 2 and the percentages of the radiative and convective components are clearly illustrated. For example, at $N_c = 2.0$ the radiative percentage of the heat transfer is about 70 percent for $h_c^* = 0.1$ but it is only about 3 percent for $h_c^* = 5.0$.

As the radiative contribution increases (i.e., N_c increases) the effectiveness Q_T^* of the fin ensemble decreases, and the fin ensemble becomes an insulator if N_c is large enough. For small values of h_c^* (e.g., $h_c^* = 0.1$), a large radiation contribution exists even for relatively low values of N_c (i.e., low temperature T_b') and Q_T^* decreases rapidly as N_c increases. For larger h_c^*, Q_T^* does not decrease as rapidly with N_c. These results suggest that maximum effectiveness of the fins occurs in situations where the thermal radiation is small.

Near $N_c = 0.0$, the radiative component is negligible and the effectiveness is largest for the lowest h_c^* value. This is attributed to the smaller fin temperature drops involved with the low h_c^* value, which results in more effective use of the fin surface area.

The fin temperature distributions are given in Fig. 3. For small h_c^*, N_c has a large influence on the temperature distribution, but the effect is less pronounced as h_c^* increases. At $h_c^* = 5.0$, it exhibits the remarkable characteristic that T^* increases as N_c increases, indicating that the fin is radiatively heated.

The local dimensionless fin radiative heat flux is given by $N_c q_R^*$ where

$$q_R^* = B^* - H^* = \epsilon(T^{*4} - H^*) \tag{11}$$

As shown in Fig. 4 the outer portion of the fin is more effective

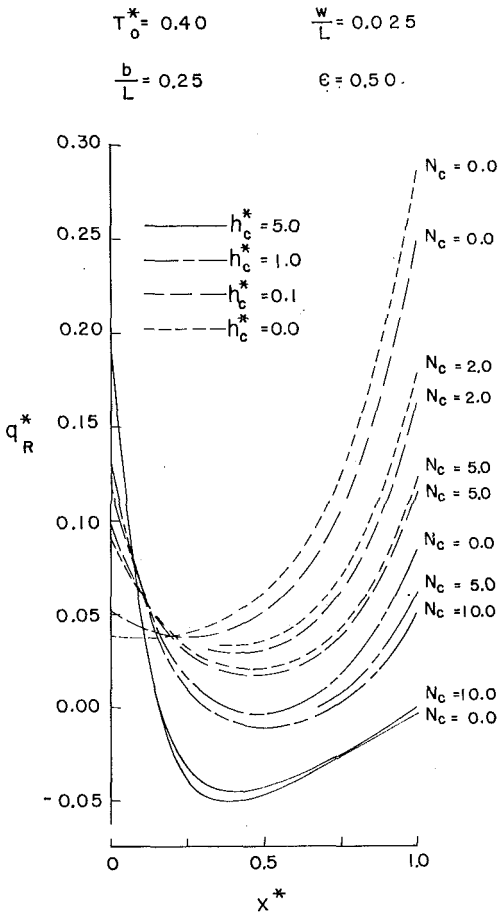

Fig. 4 Dimensionless fin radiative heat transfer

for dissipating radiant energy when h_c^* is small, but for large h_c^* the region near the fin root becomes more effective. The central portion of the fin is the least effective part except at very low values of h_c^* and N_c.

An interesting result is that for large values of h_c^*, at particular locations, the fin is being radiatively heated while being convectively cooled. The convection has caused such a large temperature drop through the fin that the combination of the low emitted energy and the relatively large irradiation from the high-temperature base and surfaces near the fin root provides a negative net radiative heat flux. From the foregoing it is clear that q_R^* cannot be accurately described by constant radiative coefficients h_R or predicted accurately by "isolated fin" radiation analyses. Both of these approaches predict local heat flux distributions considerably different from those in Fig. 4.

A comparison between the local fin convective heat flux and the local fin radiative heat flux can be made with the information in Figs. 3 and 4. Generally, the convective heat fluxes are larger when h_c^* is large or N_c is small. The radiative heat fluxes are larger when h_c^* is small and N_c is large.

The convective heat flux monotonically decreases from the fin root to the fin tip while the radiative heat flux may increase or decrease along the fin surface. If the case of $h_c^* = 1.0$ and $N_c = 5.0$ is examined, Fig. 3 reveals that the convective heat flux decreases monotonically from 0.6 at the fin root to 0.34 at the fin tip, while Fig. 4 reveals that the radiative heat flux has a maximum of 0.62 at the fin root, a minimum of -0.04 near the center of the fin surface, and a value of 0.3 at the fin tip. The integrated results show that the total convective heat transfer from the fin is greater than the total radiative heat transfer.

The local dimensionless base radiative heat flux is given by $N_c\bar{q}_R^*$ where

$$\bar{q}_R^* = \bar{B}^* - \bar{H}^* = \epsilon(1 - \bar{H}^*) \tag{12}$$

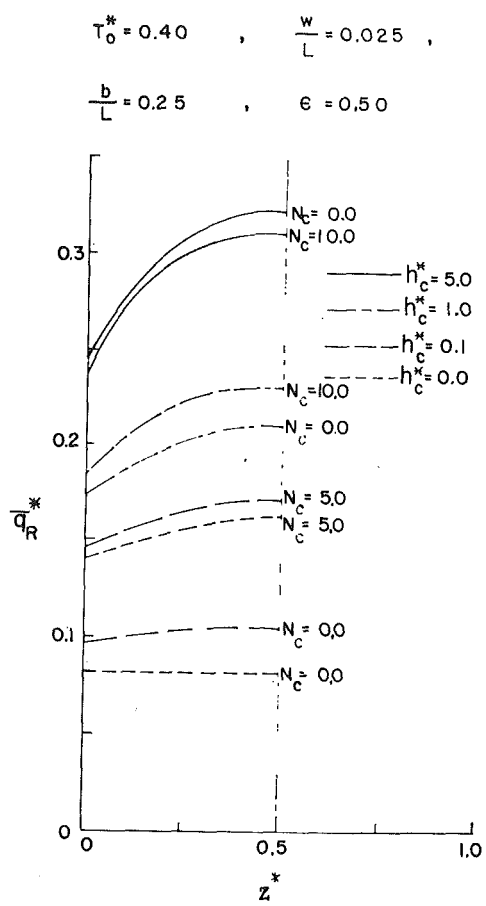

Fig. 5 Dimensionless base radiative heat transfer

and results are presented in Fig. 5. It is seen that $\bar{q}_R^*$ increases from the corners to the center of the base due to the irradiative effects. This variation of $\bar{q}_R^*$ over the base surface can be signifi-

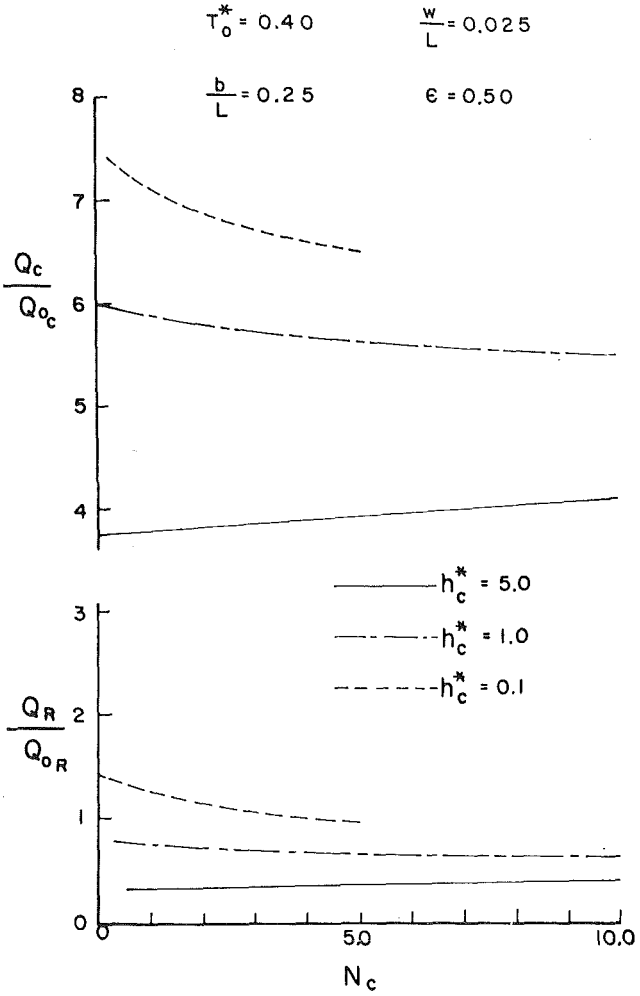

Fig. 6 Effectivenesses of the radiative and convective components

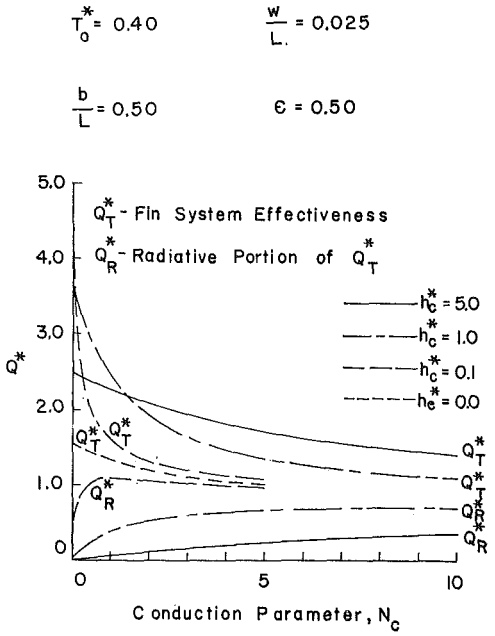

Fig. 7 Dimensionless heat-transfer results

cant, especially for large values of h_c^* or N_c. This effect is even more pronounced at larger spacings and emittances [8], thus illustrating that an isothermal surface can have a large variation in radiative heat flux.

A comparison between the effectiveness of the radiative and convection modes of heat flow is given in Fig. 6, where Q_{0c} and Q_{0R} are defined as the convective and radiative portions, respectively, of the heat flow from the nonfinned plane wall. The results show that the improvement due to addition of fins in the convective heat flow is generally much greater than the radiative improvement.

Fin System Effectiveness. A selection of the numerical solutions for the fin system effectiveness Q_T^* for the cases listed in Table 1 are given in Figs. 7–9 and further results can be found in reference [8]. The information in these figures can be used to: (1) determine the effectiveness of the extended surfaces, (2) calculate the total heat transfer from the fin ensemble, (3) determine the individual contributions of radiation and convection, and (4) evaluate the effects of the independent dimensionless parameters.

Since the effects of N_c and h_c^* were previously described, the following demonstrates only the influences of $\frac{b}{L}$, ϵ, T_0^*.

The emittance affects Q_T^* in a similar qualitative fashion for each $\frac{b}{L}$ and T_0^*. A comparison between Fig. 2 ($\epsilon = 0.5$) and Fig. 8 ($\epsilon = 1.0$) reveals lower values of Q_T^* at the higher emittance. This is attributed to the cavity effect associated with $\epsilon = 0.5$.

Fig. 2 and Fig. 9 can be compared to observe the effect of T_0^*. At a given N_c and h_c^*, the radiative percentage of the heat transfer is larger for the larger T_0^*; thus, for a given base temperature, T_b, radiation plays a more important role in the heat exchange when the temperature difference between the plane wall and the environment is small. This same phenomenon occurs for a nonfinned plane wall since $(1 - T_0^*)$ decreases faster than $(1 - T_0^{*4})$ when T_0^* is increased from 0.4 to 0.8. As a result, the convection tends to decrease faster than the radiation. Since the percentage of the radiation is larger at the larger T_0^*, the overall effectiveness of the fins is smaller.

In contrast to the case of radiative conducting fins, the fin spacing plays an important role when radiation and convection are present. With $N_c = 0.0$, a comparison of Figs. 2 and 7 shows, as is well known, that this purely convective effectiveness increases considerably as $\frac{b}{L}$ decreases. For small $\frac{b}{L}$, a large number of fins is placed on a given base area resulting in a large heat-transfer area available for convection. When N_c is not zero, the thermal radiation contributes to the heat exchange, but the radiation varies only slightly as $\frac{b}{L}$ changes [8]. As $\frac{b}{L}$ increases, the convective heat transfer decreases considerably while the radiative portion is not strongly affected, resulting in an increase in the radiative percentage. Thus Q_T^* still increases as $\frac{b}{L}$ decreases but not as rapidly. When the thermal radiation is predominant, the effect of $\frac{b}{L}$ is diminished. At $h_c^* = 0.1$ and $N_c = 5.0$, for example, Figs. 2 and 7 provide almost identical values for Q_T^*.

It should be recognized that the comparisons made here do not necessarily correspond with the comparisons that a designer should make. As one illustration, changes in $\frac{b}{L}$ may alter h_c^* significantly in a particular design, and comparisons should not be based on a fixed h_c^*.

Total Heat Transfer. An alternate dimensionless heat-transfer quantity, Q_T^{**}, better illustrates the effects of the independent dimensionless parameters on the total heat transfer.

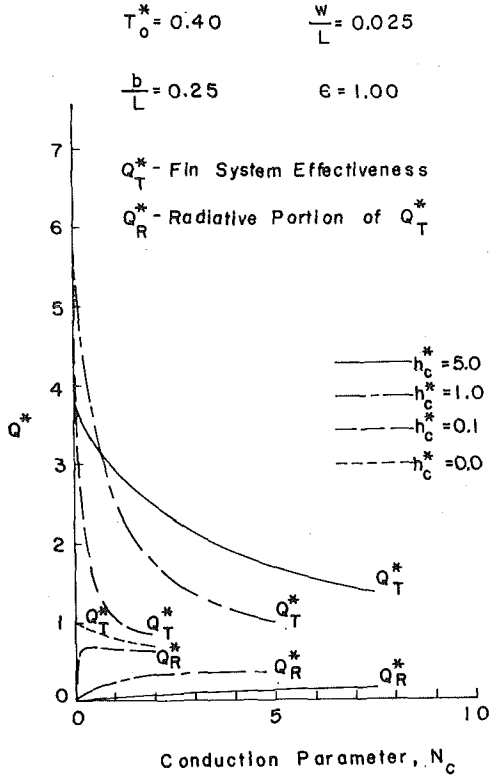

Fig. 8 Dimensionless heat-transfer results

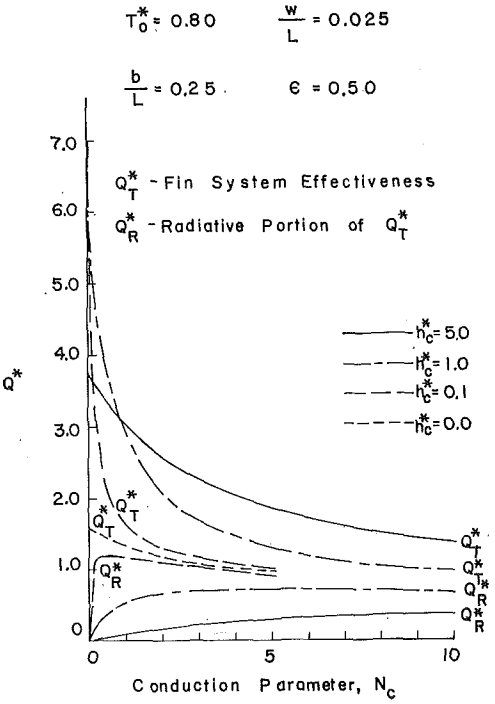

Fig. 9 Dimensionless heat-transfer results

$$Q_T^{**} = \frac{Q_T}{\left(\frac{b}{L} + 2\frac{w}{L}\right) lkT_b \frac{w}{L}} = \frac{Q_R + Q_c}{\left(\frac{b}{L} + 2\frac{w}{L}\right) lkT_b \frac{w}{L}}$$

$$= Q_R^{**} + Q_c^{**}$$

The heat-transfer quantity Q^{**} is called the dimensionless fin system heat flux, and numerical results for Q^{**} are plotted in Figs. 10–11. It is interesting to note that for $h_c^* = 5.0$, the emittance

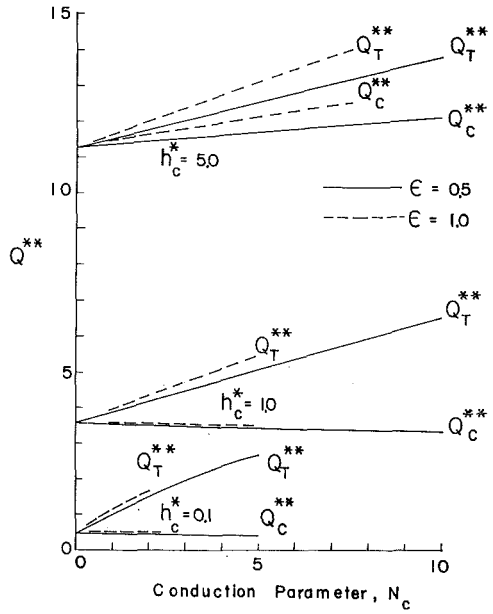

Fig. 10 Dimensionless fin system heat flux

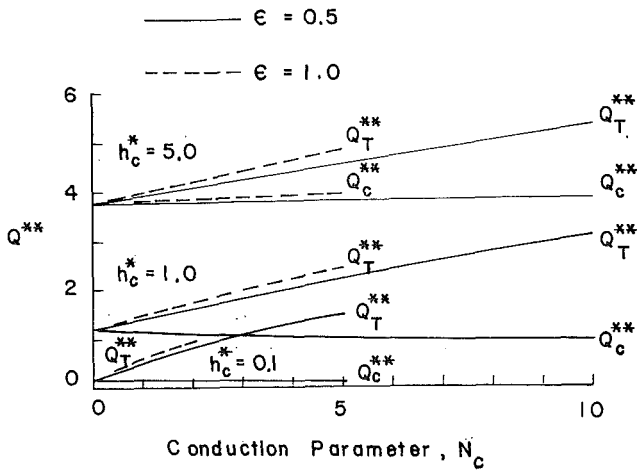

Fig. 11 Dimensionless fin system heat flux

has the unusual effect of increasing the convective heat transfer more than the radiative. The radiative heating of the fin is more pronounced when $\epsilon = 1.0$, causing a smaller temperature drop through the fin and an increase in the convective heat transfer.

For purely convective cases ($N_c = 0.0$), the heat-transfer results are proportional to $(1 - T_0^*)$. For the purely radiative cases in reference [8], the heat flow appears to be, to a reasonable approximation, proportional to $(1 - T_0^{*4})$. However, because of the coupling between the 2 modes of heat transfer, these proportionalities are not valid in the combined radiative and convective case.

Conclusions

A summary of the important results is:

1 When convection is predominant, finning can provide a considerable augmentation in the heat flow. The fins are most effective when h_c^* is small and the fins are closely spaced.

2 When radiation is predominant, the fins may either increase or decrease the heat flow. The fins are most effective when the emittance and the conduction parameter are small. Thus short fins of high thermal conductivity provide the best performance. Also, relatively large spacings are preferred.

3 When both radiation and convection are significant, the fins generally increase the convective component of the heat transfer considerably but either increase slightly or decrease the radiative component. Thus convection is the more effective mode of heat transfer, and the effectiveness of the fins decreases as the radiative component increases.

4 When the thermal radiation is significant, the radiant interaction of the extended surfaces with adjacent fins, the base, and the external environment has an important effect on the heat exchange. Simplifying concepts such as uniform radiative coefficients and isolated fins do not describe the performance of the fin array properly.

Acknowledgment

The computations presented in this paper were performed at the University of Pittsburgh's Computer Center, which is partially supported by the National Science Foundation through Grant No. G11309.

References

1 West, W. E., Jr., and Westwater, J. W., "Radiation-Conduction Correction for Temperature Measurements in Hot Gases," *Industrial and Engineering Chemistry*, Vol. 45, 1953, pp. 2152–2154.

2 Cobble, M. H., "Nonlinear Fin Heat Transfer," *Franklin Institute Journal*, Vol. 277, No. 3, 1964, pp. 206–216.

3 Collicott, H. E., Fontaine, W. E., and Grosh, R. H., "Free Convection and Radiation Heat Transfer From Cylindrical Fins," *ASHRAE Transactions*, Vol. 71, Part II, 1965, pp. 148–151.

4 Okamoto, Y., "Temperature Distribution and Efficiency of a Single Sheet of Radiative and Convective Fin Accompanied by Internal Heat Source," *Bulletin of JSME*, Vol. 7, No. 28, 1964, pp. 751–758.

5 Bernard, J. J., and Genot, J., "Heat Transfer of a Radiator Fin Subject to Small Frictional Heating" (in French), *International Journal of Heat and Mass Transfer*, Vol. 8, No. 3, 1965, pp. 449–453.

6 Sparrow, E. M., and Niewerth, E. R., "Radiating, Convecting and Conducting Fins: Numerical and Linearized Solutions," *International Journal of Heat and Mass Transfer*, Vol. 11, 1968, pp. 377–379.

7 Edwards, J. A., and Chaddock, J. B., "Free Convection and Radiation Heat Transfer From Fin-on-Tube Heat Exchanges," ASME Paper No. 62-WA-205, 1962.

8 Donovan, R. C., "Radiation and Convection From Extended Surfaces," PhD dissertation, University of Pittsburgh, 1967.

9 Henrici, P., *Elements of Numerical Analysis*, Wiley, New York, 1964.

G. L. WEDEKIND
Associate Professor of Engineering,
Oakland University,
Rochester, Mich.
Mem. ASME

An Experimental Investigation Into the Oscillatory Motion of the Mixture-Vapor Transition Point in Horizontal Evaporating Flow

A horizontal tube evaporator in which complete vaporization takes place can be divided into two distinct regions: a two-phase region and a superheat region. The mixture-vapor transition point refers to the boundary between these two regions. Experimental evidence indicates that, during steady as well as transient flow conditions, the motion of the mixture-vapor transition point is of an oscillatory nature. This study is concerned with the statistical characteristics of these oscillations, the physical mechanisms causing them, and the influence of various evaporator parameters. Experimental data are presented which indicate that the statistical characteristics of the transition point oscillations can be described by a transformed Rayleigh distribution, and that the inlet flow quality and evaporator heat flux have a considerable influence on this distribution.

Introduction

Horizontal tube evaporators in which complete vaporization takes place are used quite extensively in the refrigeration industry, and are a major component for many of the Rankine-cycle engines currently receiving considerable attention. Such an evaporator can be divided into two distinct regions: a two-phase region and a superheat region. The two-phase region consists of a mixture of a liquid and its vapor, while the superheat region consists of pure vapor. The mixture-vapor transition point is defined as the axial position in the evaporator where the last of the apparent liquid is vaporized. Therefore, for all practical purposes,[1] it represents the boundary between the two-phase region and the superheat region. Fig. 1 schematically depicts the two regions of such an evaporator. Although the schematic indicates an annular flow configuration in the two-phase region, this is for schematic simplicity only, and does not mean to imply in any way that an annular flow configuration always exists. Experimental evidence [1, 2][2] indicates that the motion of the transition point is of an oscillatory nature, even for steady flow conditions. Furthermore, it appears that this oscillatory motion is an inherent characteristic of two-phase evaporating flow.

The behavior of the mixture-vapor transition point is an important and necessary consideration in any attempt to analyze theoretically the overall dynamic characteristics of a tube-type evaporator in which complete vaporization takes place. The reason for this is that the coefficient of heat transfer between the tube wall and the fluid is in general at least an order of magnitude higher on the two-phase side of the transition point than what it is on the superheat side.

The oscillatory motion of the mixture-vapor transition point is a phenomenon encountered by Wedekind and Stoecker [1, 3] in an earlier experimental study of horizontal evaporating flow. It appears that the only other literature reference to the phenomenon is that reported by Zahn [2]. Zahn reported qualitative observations with respect to the oscillations but no quantitative data.

Experimental observations indicate that it is reasonable to assume that the oscillations of the mixture-vapor transition point can be superimposed upon some apparent *mean* or average motion during steady and transient flow conditions. A theoretical model has been formulated and verified [4] for predicting the transient response of the *mean* motion of the transition point.

In the aforementioned reference, experimental evidence is presented which indicates that there is a degree of randomness

[1] *Justification for this statement is presented at the end of the next section.*

[2] Numbers in brackets designate References at end of paper.

Contributed by the Heat Transfer Division for publication (without presentation) in the Journal of Heat Transfer. Manuscript received by the Heat Transfer Division, April 30, 1970; revised manuscript received, July 28, 1970. Paper No. 70-HT-G.

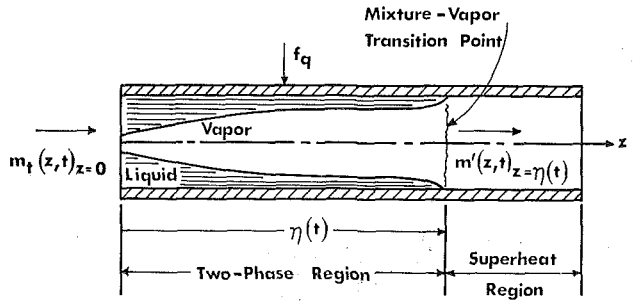

Fig. 1 Regions of a horizontal tube evaporator

present in the transition point oscillations. The purposes of the present study are to investigate the statistical characteristics of the random oscillations and to determine the effects of various evaporator parameters on these characteristics. Such results would seem to have considerable influence on an understanding of the complex mechanisms associated with two-phase evaporating flow phenomena. They will also yield information concerning the amplitude of the transition point oscillations, which in turn will provide important input to stability considerations for this type of an evaporator.

Experimental Apparatus

As a result of the nature of the study, special-purpose experimental equipment had to be designed and constructed. Although the principal component of interest in the experimental apparatus is the evaporator test section, a considerable amount of secondary equipment is required. The function of this secondary equipment is to process the fluid leaving the evaporator test section, and to feed it back into the test-section inlet at the desired thermodynamic conditions.

Basically, the secondary equipment can be divided into two subsystems, a refrigerant system and a water system. The refrigerant system processes the refrigerant used as the evaporating fluid, while the water system is required for proper operation of

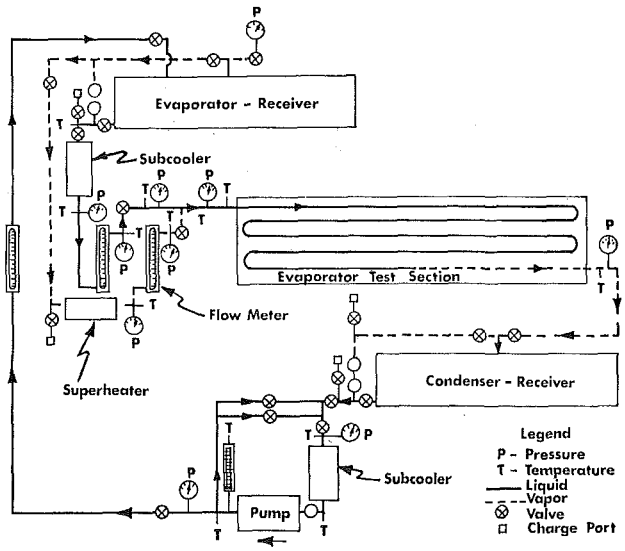

Fig. 2 Schematic of refrigerant system

the refrigerant system. Fig. 2 is a schematic of the refrigerant system.

Evaporating pressures are controlled by the pressures maintained in the condenser-receiver. These pressures can be varied by modulating the temperature of the condenser cooling water. Variation in refrigerant flow rates as well as the thermodynamic properties of the refrigerant entering the test section are controlled by an evaporator-receiver, a subcooler, and a specially designed expansion valve, all of which are located just upstream of the test section. The working fluid used is Refrigerant-12, since its thermodynamic properties are well known, and since the magnitudes of the saturated pressures in a desirable temperature range are convenient from the standpoint of equipment design.

The evaporator test section consists of five horizontal borosilicate glass tubes arranged in a serpentine configuration. Each tube is 6 ft long, has an inside diameter of $^1/_4$ in., and is connected to its adjoining tubes by means of glass U-bends. It is capable

Nomenclature

a = arbitrary distance from the mean position of the transition point, in.

$E\{\ \}$ = expected value of the random variable appearing in the brackets; definition given in equation (6)

$f(\ )$ = probability density function of the random variable appearing in the parentheses; if the random variable is discrete, then the symbol represents the frequency of occurrence

$F(\ )$ = distribution function of the random variable appearing in the parentheses; if the random variable is discrete, then the symbol represents the cumulative frequency of occurrence

f_q = linear heat flux along the evaporator, Btu/min-ft

h = specific enthalpy of saturated liquid, Btu/lb_m

h' = specific enthalpy of saturated vapor, Btu/lb_m

m_t = total mass flow rate of refrigerant, lb_m/min

m' = mass flow rate of vapor, lb_m/min

n = number of frames of experimental data in a particular sample

$N(\ )$ = number of times the particular transition point which appears in the parentheses occurred in the sample

p = mean absolute pressure within the evaporator, $lb_f/in.^2$

Δp = pressure drop across the evaporator, $lb_f/in.^2$

x = arbitrary random variable in a Rayleigh distribution

$\bar{x}$ = mean or expected value of arbitrary random variable x

x_0 = inlet flow quality, ratio of mass flow rate of vapor to total mass flow rate of refrigerant at inlet of evaporator; $x_0 = m'/m_t$

α = principal characteristic parameter in the Rayleigh distribution; can be expressed in terms of the statistically measured standard deviation σ_η; see equation (19)

β = transformation constant, in.; see equation (20)

η = instantaneous position of the transition point measured from the evaporator inlet, in.

η_i = position of transition point for the i-th frame of experimental data, in.

$\bar{\eta}$ = mean or expected value of the transition point, η, in.; estimated from experimental data by equation (1)

ξ = dummy variable

ρ = density of saturated liquid, lb_m/ft^3

ρ' = density of saturated vapor, lb_m/ft^3

σ_x = standard deviation of the random variable x about its mean

σ_η = standard deviation of the transition point η about its mean, in.; estimated from experimental data by equation (2)

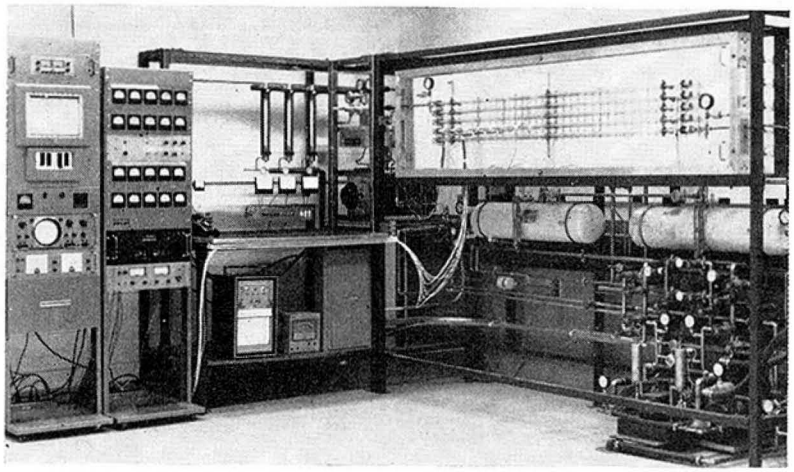

Fig. 3 Experimental apparatus

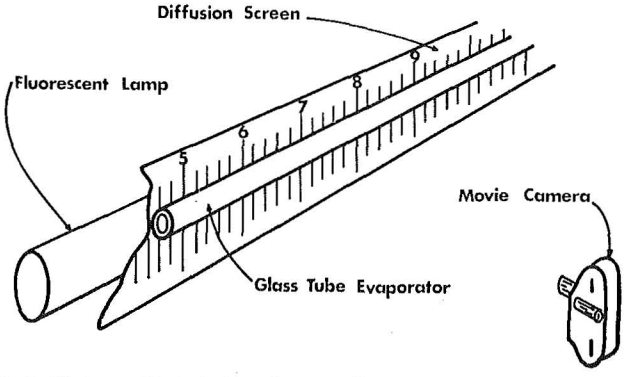

Fig. 4 Photographic technique for recording motion of mixture-vapor transition point

of handling evaporating pressures of up to 100 psig. The heat flux is applied to the tube electrically by means of a pressure-sensitive heating tape which is wound in a double helix around the outside periphery of the tube. The linear heat flux capability ranges up to 700 Btu/hr-ft. Temperature and pressure transducers are located on either end of the test section for measuring inlet and outlet thermodynamic conditions. Fig. 3 is a photograph of the experimental apparatus and some of the associated instrumentation.

The possibility that the oscillatory phenomenon under study here is inherently coupled to the hydrodynamic stability of the experimental apparatus is a legitimate concern. However, for several reasons, it does not appear to be a problem here. Density-wave oscillations of the type reported by Stenning and Veziroglu [5] do not appear to be present in the apparatus, because no flow oscillations have been detected. Also, the apparatus design for the present study is considerably different from the apparatus used for the initial investigation [1]. This change in apparatus configuration does not seem to have had any effect on the oscillatory behavior of the transition point.

A technique has been developed for obtaining a photographic record of the position of the transition point as a function of time. The basic principle behind the technique is the utilization of the light-scattering properties of a liquid-vapor mixture. As shown in Fig. 4, a glass-fiber diffusion screen is located between a light source and the glass test section. A series of opaque vertical lines are placed on the face of this diffusion screen. To an observer, looking through the glass test section at the face of the diffusion screen, the vertical lines are not visible through that portion of the test section occupied by the liquid-vapor mixture, but are visible through that portion of the test section occupied by pure vapor. Fig. 5 is an actual photograph obtained by utilizing this technique. The boundary between the two regions is identified as the interface where the vertical lines become visible. The interface is seen to have a slight taper, the length of which varies during a given test. However, the average taper length is 4.0 in., and appears to be rather insensitive to heat flux or inlet flow quality. The position of the mixture-vapor transition point is defined as the midpoint of the interface taper.

It should be emphasized that this photographic detection scheme indicates the position in the tube where the last of the apparent liquid is vaporized. This means that the tube wall is dry, and that no droplets of suspended liquid are visible. This does not rule out the possibility that there might be some liquid present in the form of microscopic droplets entrained as an invisible mist. However, if these microscopic droplets of liquid do exist beyond the transition point detected by the photographic technique, the literature indicates that the amount of liquid so entrained will be very small.

Further justification exists for stating that for all practical purposes, the transition point represents the boundary between

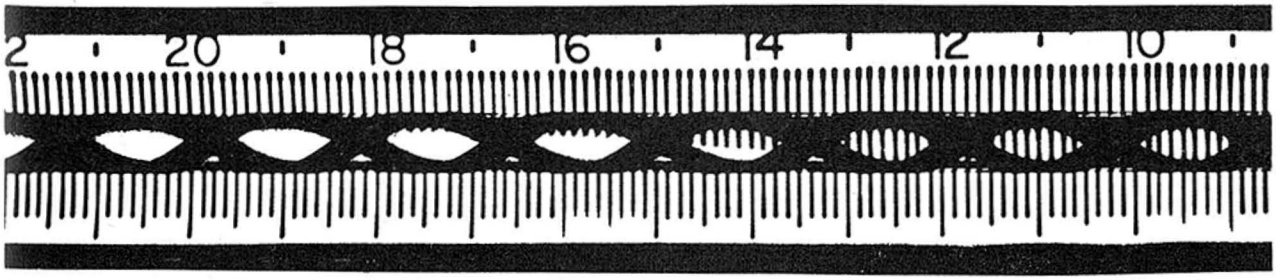

Fig. 5 Actual photograph of mixture-vapor transition point

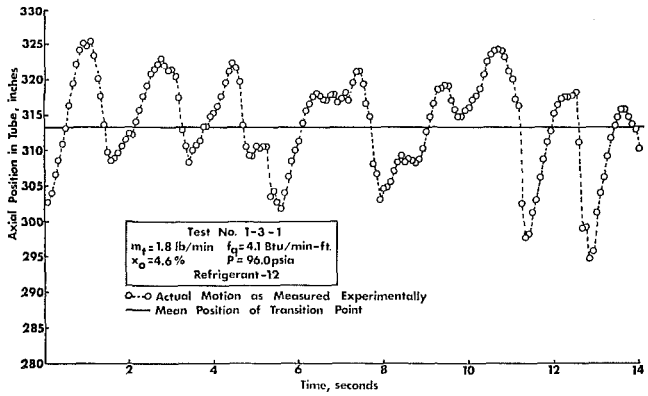

Fig. 6 Motion of mixture-vapor transition point for steady flow conditions

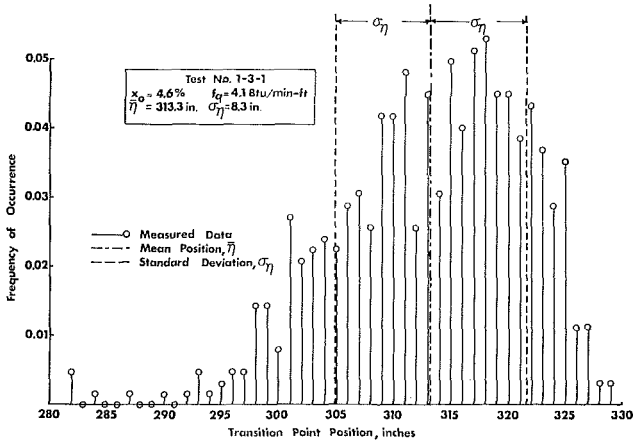

Fig. 7 Statistical characteristics of transition point motion

the two-phase and the superheat region. For steady flow conditions, the mean position of the transition point as measured by the photographic technique can be predicted by means of an energy balance. The amount of error in such a prediction falls within the expected error due to inherent errors in basic instrumentation for the measurement of physical parameters such as mass flow rate, inlet quality, heat flux, etc. The measured mean transition point position was always downstream of the theoretical position; the prediction error ranging from 1.0 to 10.0 percent, with a mean of 6.0 percent.

In addition, thermocouples located on the glass tube indicate a sharp rise in the tube temperature downstream of the mean position of the transition point. Since the heat flux along the tube is uniform, the temperature increase suggests a decrease in the convective heat transfer coefficient downstream of the transition point. More accurate and quantitative temperature measurements could be made if the tube were metal; however, then the transition point could not be observed simultaneously.

Transition Point as a Random Variable

Using the photographic technique in conjunction with a motion picture camera, the position of the mixture-vapor transition point, η, can be measured as a function of time. Naturally, this method yields discrete rather than continuous data. An example of the motion of the transition point which is typical for steady flow conditions is shown in Fig. 6. As was mentioned earlier, a study of these and similar data leads to the conclusion that there is an element of randomness present in the motion of the transition point. This conclusion suggests that the position of the transition point can be considered to be a random variable.

Statistical Characteristics. The behavior of a random variable can be characterized by various statistical parameters which are estimated from experimental measurements. For the transition point, these statistical parameters include the mean value, $\bar{\eta}$, and the standard deviation of the transition point about its mean, σ_η. Also of interest is the probability density function, $f(\eta)$, and the distribution function, $F(\eta)$. For discrete data, these functions are sometimes referred to as frequency of occurrence and cumulative frequency of occurrence, respectively.

If for some particular set of steady flow conditions, a sample of the transition point's motion consists of n frames of data, then an unbiased estimate of the mean value of the transition point is provided by the following summation:

$$\bar{\eta} = \frac{1}{n} \sum_{i=1}^{n} \eta_i \tag{1}$$

where η_i represents the position of the transition point for the i-th frame of experimental data. Similarly, the standard deviation of the transition point about its mean can be estimated by

$$\sigma_\eta = \left\{ \frac{1}{n-1} \sum_{i=1}^{n} (\eta_i - \bar{\eta})^2 \right\}^{1/2} \tag{2}$$

The frequency of occurrence represents the number of times, $N(\eta_j)$, a particular transition point, η_j, occurred, divided by the sample size, n; therefore

$$f(\eta_j) = \frac{1}{n} N(\eta_j) \tag{3}$$

The integer $N(\eta_j)$ is determined by dividing the domain of transition points into equal intervals with η_j located in the center of each interval. The integer $N(\eta_j)$ represents the number of times the transition point fell into that particular interval.

As for the cumulative frequency of occurrence, it represents the summation of the frequency of occurrence, that is,

$$F(\eta_j) = \sum_{i=1}^{j} f(\eta_i) = \frac{1}{n} \sum_{i=1}^{j} N(\eta_i) \tag{4}$$

Plots of the frequency of occurrence and cumulative frequency of occurrence for a typical sample of transition point data are shown in Figs. 7 and 8, respectively.

Similarity to Rayleigh Distribution. An examination of the frequency of occurrence as depicted in Fig. 7 reveals some similarities to the Rayleigh distribution [6]. They are both nonsymmetrical, and their slopes tend toward zero at one end of the distribution and appear to be finite at the other end. The most obvious difference, however, is that they are reversed.

The density function, $f(x)$, of a Rayleigh distribution is given by the expression

$$f(x) = \frac{2}{\alpha} x \exp\{-x^2/\alpha\}; x \geq 0 \tag{5}$$

where $\alpha > 0$ is the characteristic parameter of the function.

The mean value, $\bar{x} \equiv E\{x\}$, (or expected value) of the random variable x is defined as

$$\bar{x} \equiv E\{x\} = \int_{x=0}^{\infty} x f(x) dx$$

$$= \frac{2}{\alpha} \int_{x=0}^{\infty} x^2 \exp\{-x^2/\alpha\}\, dx = \frac{1}{2} (\pi\alpha)^{1/2} \tag{6}$$

Also, the variance, σ_x^2, of the random variable x is equal to the expected value of $(x - \bar{x})^2$, that is,

$$\sigma_x^2 = E\{(x - \bar{x})^2\} = E\{x^2\} - \bar{x}^2 \tag{7}$$

Now,

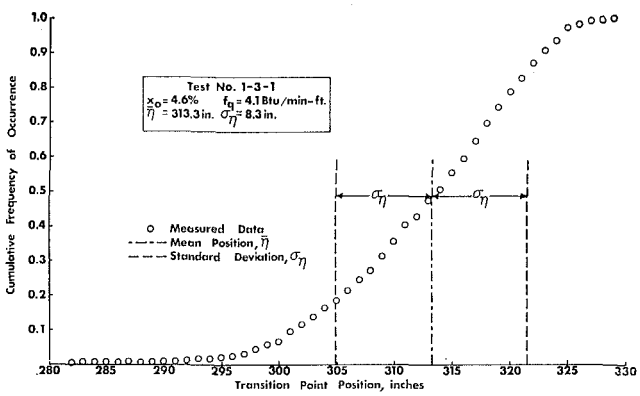

Fig. 8 Statistical characteristics of transition point motion

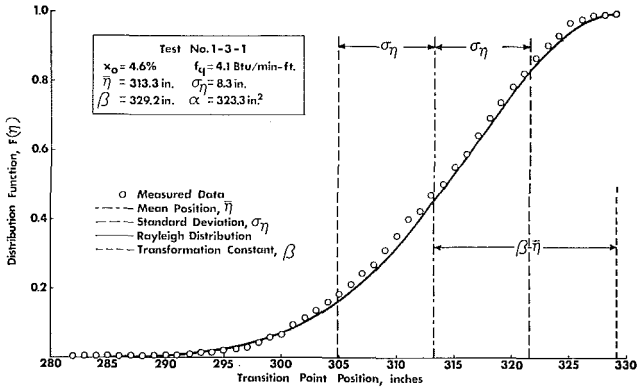

Fig. 10 Comparison of statistical characteristics with those predicted by Rayleigh distribution

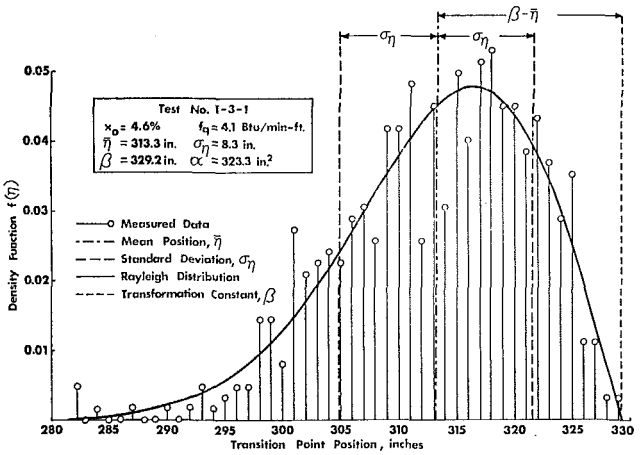

Fig. 9 *Comparison of statistical characteristics with those predicted by Rayleigh distribution*

$$E\{x^2\} = \int_{x=0}^{\infty} x^2 f(x)dx = \frac{2}{\alpha}\int_{x=0}^{\infty} x^3 \exp\{-x^2/\alpha\}dx = \alpha \quad (8)$$

Combining equations (6) and (8) with equation (7) yields

$$\sigma_x^2 = \alpha\left(1 - \frac{\pi}{4}\right) \quad (9)$$

A probability density function for the mixture-vapor transition point can be approximated by a Rayleigh density function if the following linear transformation is made:

$$x = \beta - \eta \quad (10)$$

where β is a transformation constant to be determined. Taking the expected value of equation (10) yields

$$E\{x\} = E\{(\beta - \eta)\} = \beta - E\{\eta\} = \beta - \bar{\eta} \quad (11)$$

Therefore, the substitution of equation (6) into equation (11) yields the following expression for the transformation constant, β, in terms of the characteristic parameter, α, and the mean value of the transition point, $\bar{\eta}$:

$$\beta = \frac{1}{2}(\pi\alpha)^{1/2} + \bar{\eta} \quad (12)$$

It is necessary to be able to determine an expression for the characteristic Rayleigh parameter, α, in terms of statistically measurable parameters. This can be accomplished by substituting the linear transformation given by equation (10) into equation (7); thus,

$$\sigma_x^2 = E\{(x - \bar{x})^2\} = E\{[(\beta - \eta) - \overline{(\beta - \eta)}]^2\} \quad (13)$$

Now,

$$\overline{(\beta - \eta)} = \beta - \bar{\eta} \quad (14)$$

Substituting equations (9) and (14) into equation (13) yields

$$\alpha\left(1 - \frac{\pi}{4}\right) = E\{[(\beta - \eta) - (\beta - \bar{\eta})]^2\} = E\{(\eta - \bar{\eta})^2\} \quad (15)$$

Since the expected value of $(\eta - \bar{\eta})^2$ is the variance, σ_η^2, then equation (15) yields

$$\alpha = \frac{4\sigma_\eta^2}{(4 - \pi)} \quad (16)$$

Thus, the characteristic Rayleigh parameter, α, can be expressed in terms of the standard deviation of the transition point about its mean, σ_η.

The probability density function and the distribution function for the transition point can be approximated respectively by the expressions

$$f(\beta - \eta) = \frac{2}{\alpha}(\beta - \eta)\exp\{-(\beta - \eta)^2/\alpha\} \quad (17)$$

and

$$F(\beta - \eta) = \int_{\xi=0}^{(\beta-\eta)} \frac{2}{\alpha}\xi \exp\{-\xi^2/\alpha\}d\xi = 1 - \exp\{-(\beta - \eta)^2/\alpha\} \quad (18)$$

where

$$\alpha = \frac{4\sigma^2}{(4 - \pi)} \quad (19)$$

and

$$\beta = \frac{1}{2}(\pi\alpha)^{1/2} + \bar{\eta} \quad (20)$$

The capability of this transformed Rayleigh distribution to predict the statistical behavior of the transition point is demonstrated in Figs. 9 and 10 where the predictions of equations (17) and (18) are compared with the frequency of occurrence and cumulative frequency of occurrence, respectively, for a typical sample of experimental data.

An important implication of the ability of the transformed Rayleigh distribution to predict the statistical behavior of the transition point motion, is that only two statistical parameters, $\bar{\eta}$ and σ_η, are needed to completely specify this behavior. These

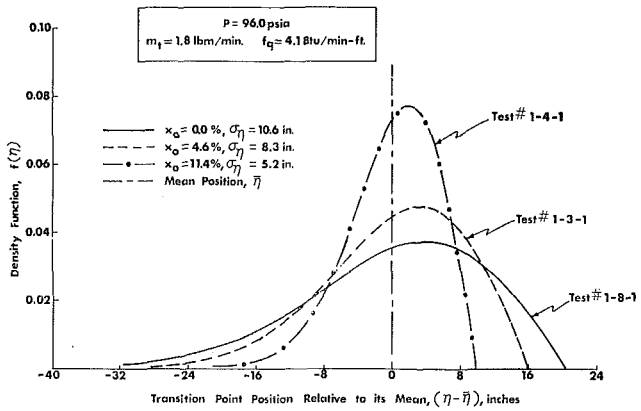

Fig. 11 Influence of inlet flow quality on transition point distribution

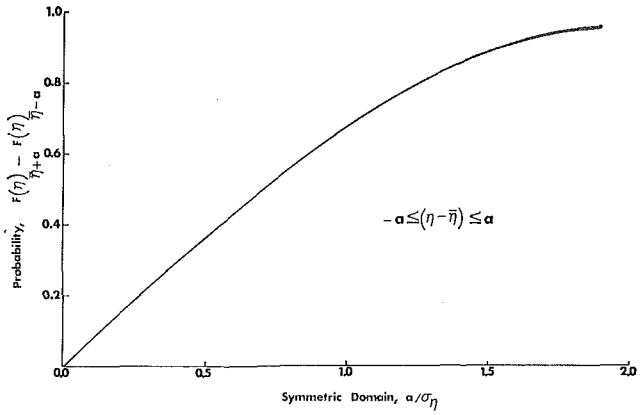

Fig. 12 Probability of transition point being within symmetric domain

two parameters, for which unbiased estimates are provided by equations (1) and (2), respectively, can be determined from experimental measurements of the mixture-vapor transition point during steady flow conditions.

Results of Parametric Study

As was mentioned earlier, one of the purposes of this study was to investigate the effects of various evaporator parameters on the statistical characteristics of the transition point oscillations. Some of the parameters which might influence the oscillatory behavior of the transition point are inlet flow quality, heat flux, flow rate, fluid properties, and evaporator geometry. Of the particular parameters which have been studied thus far, the inlet flow quality and the heat flux appear to exert the greatest influence.

Influence of Inlet Flow Quality. The influence which the inlet flow quality, x_0, has on the oscillatory motion of the transition point was determined by running a series of steady-state tests holding all of the parameters constant with the exception of the inlet flow quality. The mean value of the transition point, $\bar{\eta}$, and the standard deviation of the transition point about its mean, σ_η, were then estimated from photographic data of the transition point's motion. Using these two statistical parameters, the two characteristic parameters of the transformed Rayleigh distribution, α and β, were calculated. Experimental data were taken for inlet flow qualities ranging from a slightly subcooled liquid to a quality of just under 30.0 percent.

The effects which the inlet flow quality has on the statistical characteristics of the transition point oscillations can best be demonstrated by referring to Fig. 11, where the probability density function, $f(\eta)$, is plotted versus the transition point position relative to its mean, $(\eta - \bar{\eta})$, for three different inlet flow qualities. Several interesting facts become evident. The area under a segment of the density function can be viewed as the probability of finding the transition point within the domain represented by the segment. Therefore, considering a domain which is symmetrical about the mean position, for example $-a \leq (\eta - \bar{\eta}) \leq a$, it is seen that the probability of finding the transition point in the portion of the domain downstream of its mean position is greater than the probability of finding it in the portion of the domain upstream of its mean. For the same type of symmetrical domain, it is clear that the probability of finding the transition point within the domain increases as the inlet flow quality increases. Thus, the transition point spends more of its time closer to its mean position when the inlet flow quality is high than it does for a lower inlet quality. This means that the average amplitude of the oscillations decreases as the inlet flow quality increases. The foregoing can be expressed quantitatively by integrating the probability density function, $f(\eta)$, over the domain $-a \leq (\eta - \bar{\eta}) \leq a$. After considerable rearrangement, equations (17) through (20) can be combined to yield

$$\int_{\eta=\bar{\eta}-a}^{\bar{\eta}+a} f(\eta)d\eta = \exp\left\{-\left[\frac{\pi}{4} + \left(1 - \frac{\pi}{4}\right)\left(\frac{a}{\sigma_\eta}\right)^2\right]\right\} \times \left\{\exp\left\{\left[\pi\left(1 - \frac{\pi}{4}\right)\right]^{1/2}\left(\frac{a}{\sigma_\eta}\right)\right\} - \exp\left\{-\left[\pi\left(1 - \frac{\pi}{4}\right)\right]^{1/2}\left(\frac{a}{\sigma_\eta}\right)\right\}\right\} \quad (21)$$

This expression is plotted in Fig. 12 as a function of the dimensionless ratio, (a/σ_η). Because of the nonsymmetry of the density function, the maximum value of the symmetric domain which has any physical meaning is when

$$a = (\beta - \bar{\eta}) \quad (22)$$

This corresponds to a symmetric domain which extends downstream of the mean position to the position reached by the largest oscillation. Therefore, the maximum value of the dimensionless ratio, (a/σ_η), corresponding to this domain can be determined by the use of equations (19) and (20) as follows:

$$\frac{(\beta - \bar{\eta})}{\sigma_\eta} = \frac{(\pi\alpha)^{1/2}}{2\sigma_\eta} = \left\{\frac{\pi}{(4 - \pi)}\right\}^{1/2} = 1.91 \quad (23)$$

It is of interest to note that out of the more than seventeen thousand frames of experimental data which have been analyzed, less than a half dozen frames of the data indicated that the transition point oscillated beyond the value $(\beta - \bar{\eta})$ predicted by the above expression.

Referring to Fig. 12, it can be shown that the probability of finding the transition point within one standard deviation of its mean, $(a/\sigma_\eta) = 1.0$, is equal to 0.674, while the probability of finding it within 1.91 standard deviations of its mean, $(a/\sigma_\eta) = 1.91$, is equal to 0.956.

The standard deviation, σ_η, has been shown to be an important statistical parameter in the description of the oscillatory characteristics of the transition point. Fig. 13 depicts the influence which the inlet flow quality, x_0, has on the standard deviation. The standard deviation is seen to range from about 10.5 in. to 4.5 in. as the inlet flow quality varies from 0.0 to 0.29, respectively. This represents a considerable effect on the average amplitude of the transition point oscillations. The greatest effect appears to exist as the inlet flow quality varies from 0.0 to 0.15. Beyond that point, the standard deviation appears to become a comparatively weak function of the inlet flow quality.

The effect which the inlet flow quality has on the oscillatory motion can be expressed in terms of a probability, and in terms of a maximum oscillation, $(\beta - \bar{\eta})$, by making use of Fig. 12. For an inlet flow quality of 0.0, the average standard deviation obtained from the experimental data was 10.75 in. Therefore, the

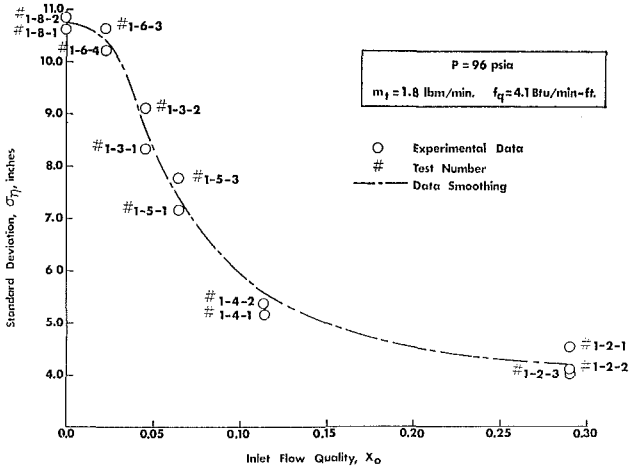

Fig. 13 Influence of inlet quality on transition point oscillations

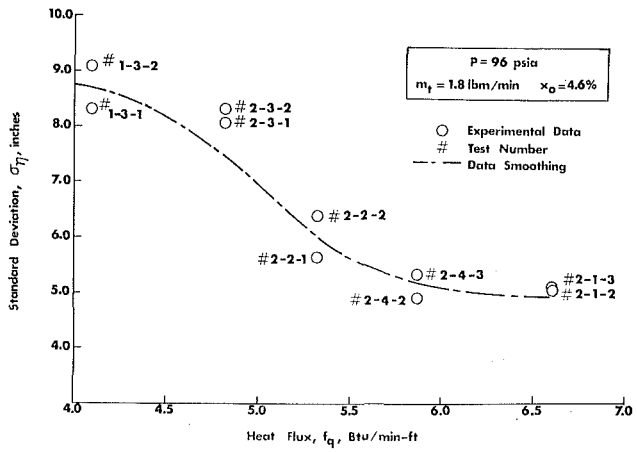

Fig. 15 Influence of heat flux on transition point oscillations

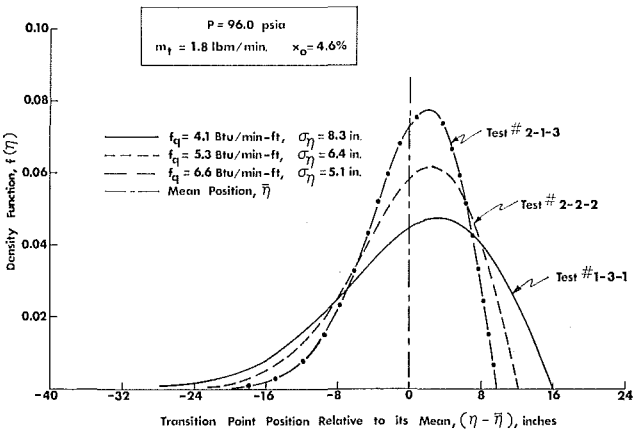

Fig. 14 Influence of heat flux on transition point distribution

transition point stayed within ± 10.75 in. of its mean position 67.4 percent of the time, while the maximum oscillation which occurred, $(\beta - \bar{\eta})$, was 20.6 in. For an inlet flow quality of 0.29, the average standard deviation was 4.25 in. Therefore, the transition point stayed within ±4.25 in. of its mean position 67.4 percent of the time, while the maximum oscillation which occurred, $(\beta - \bar{\eta})$, was 8.1 in. This represents a considerable change in the average amplitude of the oscillations.

Influence of Heat Flux. The influence which the linear heat flux, f_q, had on the oscillatory motion of the transition point was obtained in a similar manner as that for the inlet flow quality. A set of steady flow tests were performed holding all of the evaporator parameters constant except for heat flux. The heat flux was varied from about 4.0 Btu/min-ft up to 7.0 Btu/min-ft. Its effects on the statistical characteristics of the transition point oscillations can be demonstrated in a manner similar to the manner in which the effects of inlet flow quality were demonstrated. Referring to Fig. 14, the probability density function, $f(\eta)$, is plotted versus $(\eta - \bar{\eta})$ for three different heat fluxes.

The results and implications for the heat flux are similar to those of the inlet flow quality; that is, the higher the heat flux, the smaller the oscillation. This is also depicted in Fig. 15 where the standard deviation is plotted as a function of heat flux. Expressed in terms of a probability, and in terms of a maximum oscillation, for a heat flux of 4.1 Btu/min-ft, the average standard deviation was about 9.6 in. Therefore, the transition point stayed within ±9.6 in. of its mean position 67.4 percent of the time, while the maximum oscillation which occurred, $(\beta - \bar{\eta})$, was 18.3 in. For a heat flux of 6.6 Btu/min-ft, the average standard deviation was 5.2 in. Therefore, the transition point stayed within ±5.2 in. of its mean position 67.4 percent of the time, while the maximum oscillation which occurred, $(\beta - \bar{\eta})$, was 9.9 in. This, too, represents a considerable change in the average amplitude of the oscillations. The effect is slightly less but of the same order of magnitude as that of the inlet flow quality.

Summary and Conclusions

Experimental evidence indicates that the motion of the mixture-vapor transition point for steady flow conditions is of an oscillatory nature, where oscillations appear to be sufficiently random to warrant the consideration of the transition point as a random variable. An analysis of the statistical characteristics of the transition point indicates that the random variable can be described quite accurately by a transformed Rayleigh distribution. An important consequence of this discovery is that only two statistical parameters are needed to completely describe the random process; the mean position of the transition point, $\bar{\eta}$, and the standard deviation of the transition point about its mean, σ_η. Another consequence is that because of the nonsymmetrical nature of the transformed Rayleigh distribution, the probability of finding the transition point within some interval immediately downstream of its mean position is greater than that of finding it within the same interval immediately upstream of its mean position. Also, there appears to be a position downstream of the mean position which represents the limiting amplitude for the largest oscillation.

The evaporator parameters which appear to exert the greatest influence on the transition point oscillations are the inlet flow quality, x_0, and the linear heat flux, f_q. An increase in the inlet flow quality causes a decrease in the standard deviation of the transition point about its mean. This corresponds to a decrease in the average amplitude of the oscillations. A similar situation exists for the heat flux, f_q, with the actual effect being slightly less but of the same order of magnitude as for the inlet flow quality over the ranges in which the two parameters were tested.

Since the test section was transparent, the entire evaporation process could be observed. Qualitatively, all indications are that the transition point oscillations are actually caused by liquid waves which propagate along the liquid annulus in the annular flow regime. Those waves which reach the superheat region appear to "wash up" on and "recede" from the dry tube wall much like surface waves on a lake interact with the beach. The liquid waves which propagate within the liquid annulus appear to be caused by the waves and slugs which exist near the inlet of the evaporator where the wavy and slug flow regimes exist.

Experimental observations indicate that the largest waves and slugs exist when the inlet flow quality is the lowest. Thus, since the transition point oscillations are the largest for low inlet

Table 1 Experimental data for inlet flow quality study, Refrigerant-12

Test Number	x_o	σ_η	$\bar{\eta}$	α	β	n	f_q	m_t	p	Δp	ρ	ρ'	$(h'-h)$
1-8-1	0.000	10.62	329.7	526.03	350.0	609	4.12	1.78	94.8	5.9	81.81	2.33	59.32
1-8-2		10.86	330.0	549.35	350.8	592							
1-6-3	0.023	10.21	325.2	486.07	344.8	639	4.12	1.81	95.3	4.8	81.76	2.34	59.26
1-6-4		10.64	325.0	528.00	345.3	603							
1-3-1	0.046	8.33	313.3	323.34	329.2	622	4.11	1.81	96.1	5.5	81.70	2.36	59.20
1-3-2		9.11	311.6	386.32	329.0	610							
1-5-1	0.065	7.15	310.3	238.42	324.0	614	4.12	1.80	96.5	5.5	81.66	2.37	59.15
1-5-3		7.77	312.4	281.38	327.3	605							
1-4-1	0.114	5.15	267.9	123.55	277.8	604	4.10	1.74	96.9	4.5	81.61	2.39	59.10
1-4-2		5.35	267.4	133.38	277.6	600							
1-2-1	0.29	4.54	241.2	95.95	249.8	387	4.08	1.81	95.2	4.8	81.76	2.34	59.26
1-2-2		4.11	241.6	78.84	249.5	568							
1-2-3		4.00	238.5	74.38	246.1	600							

Table 2 Experimental data for heat flux study, Refrigerant-12

Test Number	x_o	σ_η	$\bar{\eta}$	α	β	n	f_q	m_t	p	Δp	ρ	ρ'	$(h'-h)$
1-3-1	0.046	8.33	313.3	323.34	329.2	622	4.11	1.81	96.1	5.5	81.70	2.36	59.20
1-3-2		9.11	311.6	386.32	329.0	610							
2-3-1	0.045	8.09	259.2	304.66	274.7	621	4.83	1.80	95.2	5.0	81.77	2.34	59.27
2-3-2		8.34	261.5	324.46	277.5	587							
2-2-1	0.046	5.66	238.3	149.05	249.1	605	5.33	1.81	96.1	5.5	81.70	2.36	59.20
2-2-2		6.42	240.5	192.33	252.8	603							
2-4-2	0.045	4.95	227.8	114.16	237.3	603	5.88	1.87	96.7	6.0	81.64	2.38	59.13
2-4-3		5.37	227.7	134.52	237.9	613							
2-1-2	0.046	5.11	197.7	121.54	207.5	607	6.61	1.81	96.1	5.5	81.70	2.36	59.20
2-1-3		5.13	197.7	122.41	207.5	596							

flow qualities, this would suggest that the sizes of the liquid waves which propagate along the liquid annulus and cause the transition point oscillations are related to the size of the waves and slugs which exist in the early stages of the evaporator. This would explain the influence which the inlet flow quality has on the oscillations. As the inlet flow quality increases, the slug and wavy flow regimes which exist in the early stages of the evaporator gradually diminish. In fact, an annular flow configuration exists at the entrance of the evaporator when the inlet flow quality approaches 20 to 25 percent.

The apparent mechanism for how the heat flux affects the transition point oscillations can be explained as follows: As a liquid wave in the annulus "washes up" on the dry tube wall in the superheat region, it is evaporated. From an energy consideration, the time which is required and hence the distance along the dry wall which the wave advances will be directly proportional to the amount of liquid present in the wave and inversely proportional to the heat flux. Therefore, with waves of comparable volume, the distance along the dry wall which the wave will advance would be expected to decrease as the heat flux increases. This is seen to be consistent with the statistical data which has been presented.

The experimental study is continuing in an effort to establish the effects on the transition point oscillations of some of the other evaporator parameters, including the evaporator tube configuration and inlet geometry. An attempt is also being made to formulate some type of theoretical model which would provide further insight into the physical mechanisms by which these evaporator parameters influence the statistical parameters associated with the transformed Rayleigh distribution.

Acknowledgments

Acknowledgments are due to Mr. F. H. Phillips, a graduate student, who has contributed significantly and continually during the design, construction, and experimental phases of this research program; to Mr. S. E. Rollins, an undergraduate student, for his contribution with respect to data reduction and associated computer programming; to Mr. B. T. Beck, an undergraduate student, for his efforts with respect to equipment design and data analysis; to my colleagues in the School of Engineering for the many helpful discussions; and to the National Science Foundation for their financial support of the research under Grant GK-1575.

References

1 Wedekind, G. L., and Stoecker, W. F., "Transient Response of the Mixture-Vapor Transition Point in Horizontal Evaporating Flow," *ASHRAE Transactions*, Vol. 72, Part 1, 1966.

2 Zahn, W. R., "A Visual Study of Two-Phase Flow While Evaporating in Horizontal Tubes," ASME Paper No. 63-WA-166, 1963.

3 Wedekind, G. L., "Transient Response of the Mixture-Vapor Transition Point in Two-Phase Horizontal Evaporating Flow," PhD thesis, University of Illinois, 1965.

4 Wedekind, G. L., and Stoecker, W. F., "Theoretical Model for Predicting the Transient Response of the Mixture-Vapor Transition Point in Horizontal Evaporating Flow," JOURNAL OF HEAT TRANSFER, TRANS. ASME, Series C, Vol. 90, No. 1, Feb. 1968, pp. 165–174.

5 Stenning, A. H., and Veziroglu, T. N., "Density-Wave Oscillations in Boiling Freon-11 Flow," ASME paper No. 66-WA/HT-49, 1966.

6 Beckman, P., *Elements of Applied Probability Theory*, Harcourt, Brace and World, 1968, pp. 49–50.

APPENDIX

Some of the physical parameters, refrigerant properties, and statistical measurements pertinent to the experimental study of the effect of inlet flow quality and linear heat flux are contained in Tables 1 and 2, respectively.

LEONARD Y. COOPER
Bell Telephone Laboratories,
Whippany, N. J.
Assoc. Mem. ASME

Constant Temperature at the Surface of an Initially Uniform Temperature, Variable Conductivity Half Space[1]

The transient temperature distribution resulting from a constant and uniform temperature being imposed on the surface of an initially uniform temperature, variable conductivity half space is studied. Various solution expansion ideas are discussed. These are utilized in the solution of an example problem, and the resulting approximate analytic solutions representations are compared to exact numerical results. One of these approximations is found to be superior to the others, and, in fact, it is shown to yield useful results over a range of variables where the nonlinearities of the problem are significant.

1 Introduction

THIS WORK treats the solution to a problem where heat is transferred to or from an initially constant-temperature, T_0^*, half space as a result of a temperature $T_s^* \neq T_0^*$ being imposed at the surface for all time greater than zero. We consider the material properties of density, ρ^*, and specific heat, C^*, to be such that $\rho^* C^*$ is constant, while the thermal conductivity, k^*, is taken as a (single valued) function of temperature. For the sake of being definite we introduce the following dimensionless dependent variables:

$$V = \lambda(T^* - T_0^*)/T_0^*, \qquad \phi = k^*(T^*)/k^*(T_0^*) = \phi(V), \quad (1)$$

where λ is an arbitrary constant, and the temperature, T^*, is a function of time, t^*, and depth into the half space, x^*. We choose independent dimensionless variables as

$$x = x^*(T_0^* C^{*3})^{1/2}\rho^*/k^*(T_0^*), \qquad t = t^* T_0^* C^{*2}\rho^*/k^*(T_0^*). \quad (2)$$

We will eventually assume a particular form for $k^*(T^*)$, but prior to such specifications a few remarks are appropriate.

The boundary value problem which describes the above diffusion phenomenon is, generally,

$$\frac{\partial V}{\partial t} = \frac{\partial}{\partial x}\left[\phi(V)\frac{\partial V}{\partial x}\right], \quad (3)$$

$$\phi = 1 \quad \text{or} \quad V = 0, \quad x > 0, t = 0, \quad (4)$$

$$\phi = \phi_s = k^*(T_s^*)/k^*(T_0^*) \quad \text{or} \quad V = V_s = \lambda(T_s^* - T_0^*)/T_0^*, \quad x = 0, t > 0. \quad (5)$$

It is well known that, independent of the functional dependence of k^* on T^* (or ϕ on V), the above problem admits a similarity variable $\eta \sim xt^{-1/2}$ [1].[2] Thus selecting, for example,

$$\eta = x(2t)^{-1/2}, \quad (6)$$

the problem becomes

$$[\phi(V)V']' + \eta V' = 0, \quad (7)$$

$$V = V_s \quad \text{or} \quad \phi = \phi_s = \phi(V_s), \qquad \eta = 0, \quad (8)$$

$$\lim_{\eta\to\infty} V = 0 \quad \text{or} \quad \lim_{\eta\to\infty} \phi = 1, \quad (9)$$

where primes denote differentiations with respect to η.

There are, of course, any number of alternate, but equivalent, means of describing the original boundary conditions, equation (5), of our problem. For the purpose of discussing a heat transfer phenomenon the most appropriate alternate surface requirement is that of heat transfer rate. Thus we ask: what surface heat transfer rate, $H^*(t^*) = -k^*(T_s^*)\partial T^*/\partial x^*|_{x^*=0}$, will yield the constant temperature T_s^* at the surface of our half space? Alternatively we might ask: what time dependency is required of the surface heat transfer rate, H^*, so as to allow for η to be a valid similarity variable? As it happens, it is a simple matter to deduce the presumably unique answer to these questions. Namely, the heat transfer rates which are equivalent to the constant surface temperature boundary condition discussed above

[1] This work was supported by the U. S. Army under Contract DA-30-069-AMC-333(Y).

Contributed by the Heat Transfer Division for publication (without presentation) in the JOURNAL OF HEAT TRANSFER. Manuscript received by the Heat Transfer Division, August 27, 1969; revised manuscript received, May 22, 1970. Paper No. 70-HT-H.

[2] Numbers in brackets designate References at end of paper.

are proportional to $t^{*-1/2}$. For the purpose of posing our problem in terms of a surface heat transfer rate, H^*, we therefore define a dimensional parameter h^* and corresponding dimensionless parameters such that

$$H^*(t^*) = h^* t^{*-1/2}, \qquad \zeta = -\lambda h^* [\rho^* k^* (T_0{}^*) C^*/2]^{-1/2} / T_0{}^*. \tag{10}$$

A careful look at the governing equations reveals that the problem described above and explicitly stated in equations (7)–(9) could be equivalently stated by equations (7), (9), and the boundary condition

$$\phi(V)V' = \zeta, \qquad \eta = 0. \tag{11}$$

Similar to the role of V_s in equations (7)–(9), ζ is now a parameter in the problem of equations (7), (9), and (11). Moreover, in view of the equivalence of the two problem statements, there must be an equivalence between ζ and V_s.

It is worthwhile pointing out that the half space problem discussed here is also equivalent to an infinite space problem where, initially, the separate half spaces $x < 0$ and $x > 0$, both having identical k^* and $\rho^* C^*$ (as per our earlier restrictions on these properties), are at different temperatures.

A discussion of solution techniques for the above problem along with extensive results for specific variable conductivities (diffusivities) are presented in the treatise by Crank [2]. Generally applicable solution methods treated there include iterative and numerical integrations. Phillip [3] has established and cataloged a large class of $\phi(V)$ for which the boundary value problem previously discussed admits an exact (closed form) solution. The present investigation studies direct techniques for solving the class of problem under consideration. In particular, various perturbation solution ideas are presented and discussed in section 2. In section 3 these ideas are applied to a specific example problem (which does not admit a closed form solution) and results are compared. It is concluded that a prudent choice of expansion parameter can yield an approximate analytic result which is useful over a range of parameter where corresponding physics and mathematics exhibit significant nonlinear behavior.

2 Some Solution Ideas

If an exact solution to our problem is not available for a given $\phi(V)$ of interest, approximations might be sought by expanding the solution about zero values of one of several possible parameters, that is, by expanding the solution, in some sense, about the initial uniform temperature state, $V = 0$, or uniform conductivity state, $\phi = 1$. Thus a suggested solution form for $V(\eta; V_s)$ might be, for example,

$$V(\eta; V_s) = \sum_{n=1}^{\infty} V_s{}^n V_n{}^{(1)}(\eta). \tag{12}$$

This kind of solution treatment has been used recently by Andre-Talamon [4] and by others to whom he refers. In theory the expectation would be that V is an analytic function of the complex variable V_s, in some neighborhood of $V_s = 0$, and, should singular points exist, that V can be analytically continued along the real V_s axis to whatever V_s is required. In practice the hope would be that the above series would converge rapidly enough so that the few early V_n, which might be practically obtained, would yield an accurate solution for the particular V_s range of interest. It is, of course, possible that the function $\phi(V)$ may introduce singularities into our solution through the governing equation, and thereby limit the radius of convergence of the previously suggested expansion. Thus, for example, if we approximate a dimensionless conductivity of interest according to

$$\phi = 1 + V, \tag{13}$$

and a standard perturbation procedure is carried out using the expansion of equation (12) in our differential equation and boundary conditions, we would expect that the validity of our expansion may be limited to $|V_s| < 1$. As we will see, a possible remedy is to introduce a secondary expansion parameter, a function of V_s, which transforms the potential problem point, $V_s = -1$, out of the finite plane and retains all other real V_s on the finite real axis. Thus, for example, we can introduce

$$W = V_s/(1 + V_s),$$

$$V_s = W/(1 - W) = \sum_{n=1}^{\infty} W^n \quad \text{for} \quad |W| < 1, \tag{14}$$

and consider a solution expansion in the form

$$V(\eta; W) = \sum_{n=1}^{\infty} W^n V_n{}^{(2)}(\eta). \tag{15}$$

Then according to equations (14), we would hope that the new expansion would be valid for all $|W| < 1$, which includes all real V_s in the range $-1/2 < V_s < \infty$.

The transformation from V_s to W suggested in equation (14) is a form of the Euler transformation [5]. The introduction of the new expansion of equation (15) is a form of analytic continuation of our solution, considered as a function of V_s and as represented by equation (12), onto a domain which includes all positive real values of V_s.

Before attempting to test the utility of the transformation idea on an example problem, we will introduce a solution expansion based on one more parameter.

With the problem form of equations (7), (9), and (11), a solution expansion in terms of ζ about $\zeta = 0$ is in consonance with the direction of our reasoning. Thus we might assume the solution form

$$V(\eta; \zeta) = \sum_{n=1}^{\infty} \zeta^n V_n{}^{(3)}(\eta), \tag{16}$$

Nomenclature

b = $\phi_s - 1$, an expansion parameter
C^* = specific heat
g = a parameter defined in [6][2]
H^* = surface heat transfer rate
h^* = dimensional parameter defined in equation (10)
k^* = conductivity
k = a parameter defined in [2]
T^* = temperature
$T_0{}^*$ = initial temperature
$T_s{}^*$ = surface temperature
t^* = time
t = dimensionless t^* defined in equation (2)
V = dimensionless T^* defined in equation (1)
$V_n{}^{(1)}(\eta), V_n{}^{(2)}(\eta), V_n{}^{(3)}(\eta), n$ = 1, 2, . . . functions generated in three different parameter expansions of V
V_s = surface value of V
W = $V_s/(1 + V_s)$, an expansion parameter
x^* = depth into half space
x = dimensionless x^* defined in equation (2)
β = $b/(1 + b)$, an expansion parameter
ζ = dimensionless h^* as defined in equation (10)
η = similarity variable defined in equation (6)
λ = arbitrary dimensionless constant
ρ^* = density
ϕ = dimensionless k^* defined in equation (1)
$\phi_n{}^{(1)}(\eta), \phi_n{}^{(2)}(\eta), \phi_n{}^{(3)}(\eta), n$ = 1, 2, . . . functions generated in three different parameter expansions of ϕ
ϕ_s = surface value of V

and carry through the equations with the usual perturbation procedure. There are no apparent ζ singular points in our differential equation, and it would appear that the earlier potential problem of a limited radius of convergence would be abated in the expansion of equation (16).

The next section treats a specific problem of the type discussed above. We will select a particular $k^*(T^*)$ and make use of the above ideas in seeking a solution to the resulting nonlinear boundary value problem. Our result will be compared to existing numerical results given in the literature.

3 Example

Consider a particular case of the general boundary value problem discussed in section 1 where the thermal conductivity of interest can accurately be represented by

$$\phi \equiv k^*(T^*)/k^*(T_0^*) = \exp\,[\lambda(T^* - T_0^*)/T_0^*] \equiv \exp V, \quad (17)$$

and where λ is arbitrary in both sign and magnitude. This conductivity representation has been used in previous studies of both molecular diffusion [2, 6] and heat conduction [7]. Using equation (17), the governing equation (7) can be neatly written in terms of the dependent variable ϕ. Thus

$$\phi\phi'' + \eta\phi' = 0. \quad (18)$$

The boundary conditions of equations (8) and (9) are rewritten as

$$\phi(0) = \phi_s \quad \text{and} \quad \phi(\infty) = 1, \quad (19)$$

whereas those of equations (9) and (11) become

$$\phi'(0) = \zeta \quad \text{and} \quad \phi(\infty) = 1. \quad (20)$$

The general solution ideas introduced in the previous section were couched in terms of V as the dependent variable. In our present problem we will use such ideas in seeking a solution for ϕ. Once such a solution is available the function V can easily be obtained according to our definition of equation (17).

Let us consider the problem of equations (18) and (19). Then in the spirit of our expansion suggestion of equation (13) we introduce a parameter, b, defined by

$$\phi_s = 1 + b, \quad (21)$$

and expand our unknown function about $b = 0$. Thus we assume

$$\phi(\eta; b) = 1 + \sum_{n=1}^{\infty} b^n \phi_n^{(1)}(\eta). \quad (22)$$

We are, of course, interested in ϕ for all real b such that $-1 < b < \infty$. The present expansion, however, is expected to yield values for only $|b| < 1$. Using this expansion in equations (18) and (19) results in the following problems for the $\phi_n^{(1)}$'s:

$$\phi_1^{(1)\prime\prime} + \eta\phi_1^{(1)\prime} = 0, \qquad \phi_1^{(1)}(0) = 1, \qquad \phi_1^{(1)}(\infty) = 0, \quad (23)$$

$$\phi_n^{(1)\prime\prime} + \eta\phi_n^{(1)\prime} = -\sum_{m=1}^{n-1} \phi_m^{(1)}\phi_{n-m}^{(1)\prime\prime} \equiv h_n^{(1)}(\eta), \qquad n > 1, \quad (24)$$

$$\phi_n^{(1)}(0) = \phi_n^{(1)}(\infty) = 0.$$

The solution to equations (23) is given by

$$\phi_1^{(1)}(\eta) = \operatorname{erfc}\,(2^{-1/2}\eta), \quad (25)$$

where the complementary error function, erfc (x), is defined in terms of the error function, erf (x), as

$$\operatorname{erfc}\,(x) = 1 - \operatorname{erf}\,(x) = 1 - 2\pi^{-1/2}\int_0^x \exp\,(-t^2)dt. \quad (26)$$

The solution to equation (24) can generally be represented in the quadrature form

$$\phi_n^{(1)}(\eta) = -(\pi/2)^{1/2}\left\{\int_\eta^\infty \exp\,(\xi^2/2)\operatorname{erfc}\,(2^{-1/2}\xi)h_n^{(1)}(\xi)d\xi - \operatorname{erfc}\,(2^{-1/2}\eta)\left[\int_0^\infty \exp\,(\xi^2/2)\operatorname{erfc}\,(2^{-1/2}\xi)h_n^{(1)}(\xi)d\xi - \int_0^\eta \exp\,(\xi^2/2)h_n^{(1)}(\xi)d\xi\right]\right\}, \qquad n > 1. \quad (27)$$

Specific results for $n = 2$ and 3 have been obtained from this solution. They are

$$\phi_2^{(1)}(\eta) = (1/\pi)[\operatorname{erfc}\,(2^{-1/2}\eta) - \exp\,(-\eta^2)] + [(2/\pi)^{1/2}/2]\eta\exp\,(-\eta^2/2)\operatorname{erfc}\,(2^{-1/2}\eta), \quad (28)$$

$$\phi_3^{(1)}(\eta) = [(2/\pi)^2/2][\operatorname{erfc}\,(2^{-1/2}\eta) - \exp\,(-\eta^2)] + [(2/\pi)^{3/2}/2]\eta\exp\,(-\eta^2/2)\operatorname{erfc}\,(2^{-1/2}\eta) + [1/(4\pi)]\{[(3^{1/2} - 4) - 2(\eta^2 - 2)\exp\,(-\eta^2)]\operatorname{erfc}\,(2^{-1/2}\eta) - 3^{1/2}\operatorname{erfc}\,[\eta(3/2)^{1/2}]\} + [(2/\pi)^{1/2}/8]\eta(\eta^2 - 3)\exp\,(-\eta^2/2)\operatorname{erfc}^2\,(2^{-1/2}\eta). \quad (29)$$

In order to analytically continue our solution as represented by the expansion of equation (22) onto a domain that includes all real $b > 1$, we introduce a new parameter, β, which is the Euler transformation of b. Thus

$$\beta = b/(1 + b), \qquad b = \beta/(1 - \beta) = \sum_{n=1}^{\infty} \beta^n \quad \text{for} \quad |\beta| < 1. \quad (30)$$

Using the expansion of equation (30) in equation (22) we find a new solution form for ϕ, considered as a function of β, and expanded about $\beta = 0$. Thus

$$\phi(\eta; \beta) = 1 + \sum_{n=1}^{\infty} \beta^n \phi_n^{(2)}(\eta) \quad (31)$$

where [4]

$$\phi_n^{(2)}(\eta) = \sum_{m=0}^{n-1} \{(n-1)!/[m!(n-m-1)!]\}\phi_{m+1}^{(1)}(\eta).$$

We expect that this latter expansion would be valid for $|\beta| < 1$ which, according to equation (30), includes all real b in the range $-1/2 < b < \infty$.

Theoretically we would expect that, together, the expansions of equations (22) and (31) would yield solution results for the entire range of physically interesting b or ϕ_s. In fact, the utility of our two expansions should overlap in the range of real ϕ_s such that $-1/2 < \phi_s < 2$ or, according to equation (17), $-\ln(2) < V_s < \ln 2 = 0.6932$.

Before studying the above results in terms of available three term approximations of our two expansions, we will investigate the ζ expansion idea of section 2.

Let us consider the problem of Eqs. (18) and (20). Then, since ζ is the only parameter, we expand our solution about $\zeta = 0$,

$$\phi(\eta; \zeta) = 1 + \sum_{n=1}^{\infty} \zeta_n \phi_n^{(3)}(\eta). \quad (32)$$

Presumably this expansion is valid in the entire ζ-plane. Using the above expansion in equations (18) and (20) results in specific problems for the $\phi_n^{(3)}$'s. For a given n, these are identical to the problems of equations (23) and (24) once all superscripts (1) have been changed to (3) except that the conditions required of $\phi_n^{(1)}(0)$ in equations (23) or (24) are now required of $\phi_n^{(3)\prime}(0)$. The solution for $\phi_1^{(3)}(\eta)$ is given by

$$\phi_1^{(3)}(\eta) = -(\pi/2)^{1/2} \operatorname{erfc}(2^{-1/2}\eta). \quad (33)$$

The solution of all other $\phi_n^{(3)}$ can be represented in the quadrature form

$$\phi_n^{(3)}(\eta) = -(\pi/2)^{1/2}\left[\int_\eta^\infty \exp(\xi^2/2)\operatorname{erfc}(2^{-1/2}\xi)h_n^{(3)}(\xi)d\xi + \operatorname{erfc}(2^{-1/2}\eta)\int_0^\eta \exp(\xi^2/2)h_n^{(3)}(\xi)d\xi\right], \quad n > 1. \quad (34)$$

Specific results for $n = 2$ and 3 have been obtained from this solution. They are

$$\phi_2^{(3)}(\eta) = -\exp(-\eta^2)/2 + (\pi/2)^{1/2}\eta \times \exp(-\eta^2/2)\operatorname{erfc}(2^{-1/2}\eta)/2 + (\pi/4)\operatorname{erfc}(2^{-1/2}\eta), \quad (35)$$

$$\begin{aligned}\phi_3^{(3)}(\eta) = {} & -\eta\exp(-3\eta^2/2)/8 + (\pi/2)^{1/2}\{\exp(-\eta^2)/2 \\ & + (3^{1/2}/8)\operatorname{erfc}[(3/2)^{1/2}\eta] \\ & + (\eta^2/4 - 1/2)\exp(-\eta^2)\operatorname{erfc}(2^{-1/2}\eta)\} \\ & - (\pi/2)[(\eta^3 - 3\eta)\exp(-\eta^2/2)\operatorname{erfc}^2(2^{-1/2}\eta)/8 \\ & + \eta\exp(-\eta^2/2)\operatorname{erfc}(2^{-1/2}\eta)/2] \\ & - (\pi/2)^{3/2}\operatorname{erfc}(2^{-1/2}\eta)/8.\end{aligned} \quad (36)$$

All of the above leads us to three different approximate solutions to our problem, the accuracy of which we would like to determine. These are

$$e^{V(\eta)} = \phi(\eta) = \begin{cases} \phi(\eta; b) \simeq 1 + \sum_{n=1}^{3} b^n\phi_n^{(1)}(\eta) & (37a) \\ \phi(\eta; \beta) \simeq 1 + \sum_{n=1}^{3} \beta^n\phi_n^{(2)}(\eta) & (37b) \\ \phi(\eta; \zeta) \simeq 1 + \sum_{n=1}^{3} \zeta^n\phi_n^{(3)}(\eta) & (37c) \end{cases}$$

We will seek answers to the following two questions:

1 Fixing a value of $\zeta = \phi'(0)$, that is, given a specified heat transfer rate of the type considered in equation (10), and requiring all solution approximations to satisfy this boundary condition, how accurately does each of these solution representations estimate $V(\eta)$?

2 Fixing a value of $V_s = V(0)$, and requiring all solution approximations to satisfy this temperature boundary condition, how accurate are the estimates of $V(\eta)$?

There are two sources of numerical solutions in the literature to which our approximate solutions of equations (37) can be compared. Wagner [6] presents results in tabular form. A given g in his work is related to a specific ϕ_s, V_s, and ζ, the values of which can be explicitly determined. Crank [2] (pp. 270–271) presents results in graphical form, each curve being labeled by a value of exp (k) (in his notation) from which the corresponding V_s and ϕ_s can be explicitly determined. Besides the use of graphical means to determine initial curve slopes, however, there is no way to obtain the explicit ζ value which is associated with each curve of this latter data. We will have use for both of the above references in answering the above questions.

In Fig. 1 we have plotted data which are computed directly from the results of Table II of [6] for a selected number of g values. The selected data encompass the entire tabulated range of g. Plots of the approximate solutions of equations (37) are also presented in this figure. The choices of the b, β, and ζ values of these are such that the values of the dimensionless heat transfer rate, $\phi'(0)$, computed from each approximation curve under a given letter grouping are identical to the value of $\phi'(0)$ for the exact solution of the pertinent constant g curve. We can compute from [6], for example, that $g = -1.2$, which is labeled under D, is equivalent to $\phi'(0) = \zeta = -1.6340$. Thus the constant b curve of D is a plot of $V(\eta; b_D) = \ln \phi(\eta; b_D) = \ln [1 + b_D\phi_1^{(1)}(\eta) + b_D^2\phi_2^{(1)}(\eta) + b_D^3\phi_3^{(1)}(\eta)]$, where b_D is a solution of $\phi'(0) = -1.6340 = \phi'(0; b_D) = b_D\phi_1^{(1)\prime}(0) + b_D^2\phi_2^{(1)\prime}(0) + b_D^3\phi_3^{(1)\prime}(0)$. Thus $b_D = 1.7529$.

From our presentation of Fig. 1 the first question below equations (37) is now answered from the following conclusions:

1a. Of the three approximate solutions of equations (37), the ζ expansion is useful over the largest range of $\phi'(0) = \zeta$. In

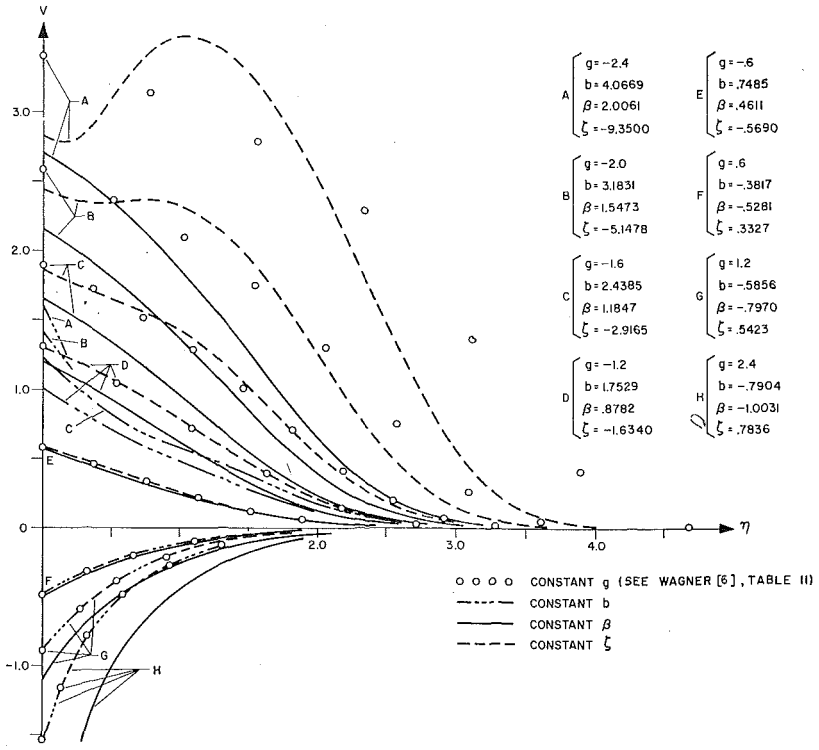

Fig. 1 Plots of $V(\eta)$ as per [6] and equations (37) with $\phi'(0)$ specified

fact, for $\zeta > 0$ the useful range of this approximate solution exceeds that of the available numerical data. As far as can be determined, the errors in the V values resulting from this expansion, when ζ is specified, will be less than 10 percent for $-2.92 < \zeta < \zeta_P$ where $\zeta_P > 0.78$ and less than 3 percent for $-1.63 < \zeta < \zeta_P$.

1*b*. In the present comparison the approximation of the β expansion, equation (37*b*), is qualitatively correct for $\zeta < 0.55$, while the b expansion approximation of equation (37*a*) is qualitatively correct for $-1.63 < \zeta$. Thus the overlap range of validity of these two expansions that we might have expected even in the present problem description has been exhibited. It should finally be noted that in the range $0.55 < \zeta$, the b expansion is in no way inferior to the ζ expansion.

In Fig. 2 we have reproduced the data which were computed

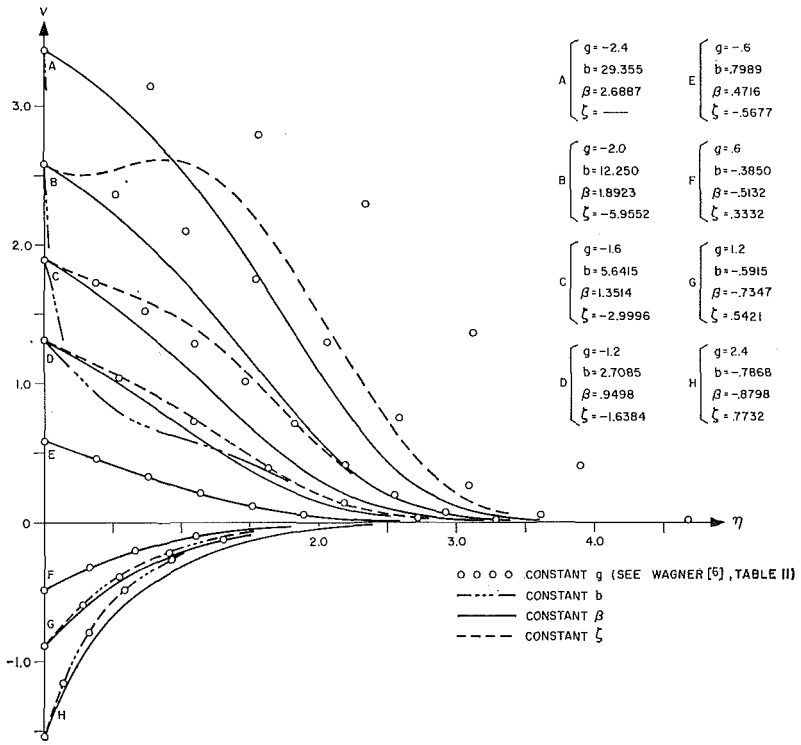

Fig. 2 Plot of $V(\eta)$ as per [6] and equations (37) with V_s specified

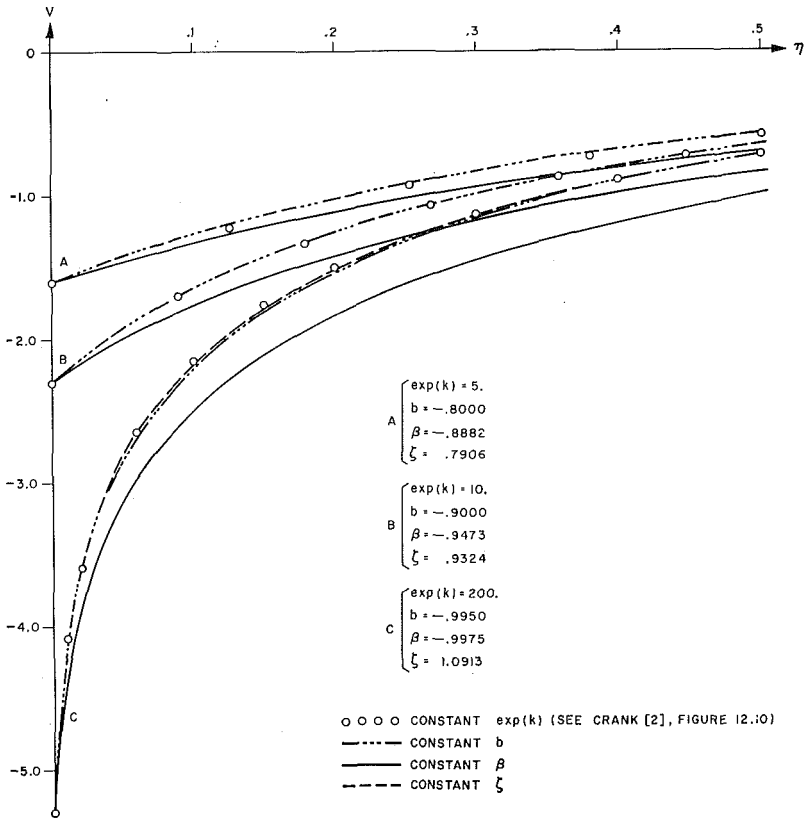

Fig. 3 Plot of $V(\eta)$ as per [2] and equations (37) for V_s specified

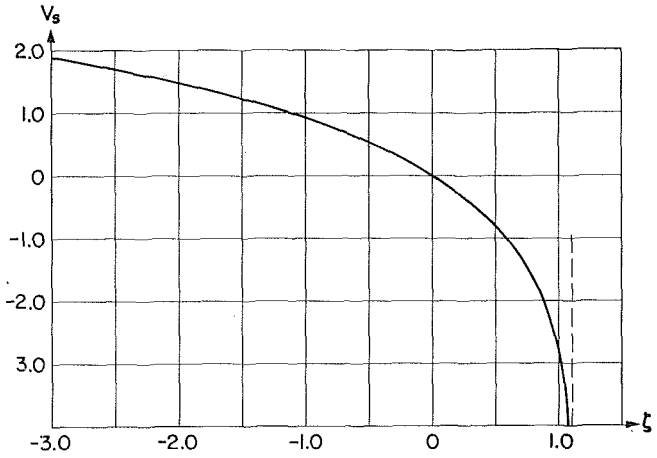

Fig. 4 Plot of $V_s(\zeta)$ as per equation (38)

from [6] and plotted in Fig. 1. Plots of the three approximate solutions of equations (37) are also presented in Fig. 2. The b, β, and ζ values of these are such that the values of the dimensionless surface temperature $V_s = V(0) = \ln \phi(0)$ computed from each approximation curve under a given letter grouping are identical to the value of V_s for the exact solution of the pertinent constant g curve. We can compute from [6], for example, that $g = -1.2$, which is labeled under D, is equivalent to $V_s = 1.3106$. Thus the constant b curve of D is a plot of $V(\eta; b_D) = \ln \phi(\eta; b_D)$ as per equation (37a), where b_D is now a solution of $V_s = 1.3106 = \ln \phi(0; b_D) = \ln [1 + b_D\phi_1^{(1)}(0) + b_D{}^2\phi_2^{(1)}(0) + b_D{}^3\phi_3^{(1)}(0)] = \ln [1 + b_D]$, that is, $b_D = \exp (1.3106) - 1 = 2.7085$.

We can study the present comparison further by using Fig. 12.10 of [2]. (That presentation of graphical data is useful over a larger range of $V_s > 0$ than the tabulated data of [6].) Data points have been taken off curves of this graph and replotted in Fig. 3 for different cases of constant exp (k) (in the notation of [2]). In a manner similar to that described above for our Fig. 2 we have plotted the three approximate solutions of equations (37) which correspond to each of the constant exp (k) curves considered.

From our presentation of Figs. (2) and (3), the second question below equations (37) is now answered from the following conclusions:

2a. Of the three approximate solutions of equations (37), the ζ expansion is useful over the largest range of $V_s = V(0)$. In fact, even with the extended range of data from [2] which was available in the case of the present comparison, we conclude that for $V_s < 0$ the useful range of this approximate solution exceeds that of the existing numerical data. As far as can be determined, the errors in the V values resulting from this expansion, when V_s is specified, will be less than 8 percent for $v_s < V_s < 1.89$ where $v_s < -5.30$ and less than 3 percent for $v_s < V_s < 1.31$.

2b. In the present comparison of the approximation of the b expansion, equation (37a) yields V values with errors less than 3 percent when $V_s \leq 0.6$, while the β expansion approximation of equation (37b) has some utility for positive values of V_s in a range where the b expansion is useless. Thus the overlap range of validity of these two expansions as predicted below equation (30) is exhibited. We note, finally, that in the range $V_s < 0.6$ the b expansion is in no apparent way inferior to the ζ expansion.

As concluded in 1a and 2a, the approximation of our expansion solution, equation (37c), is generally superior to the b and β expansion approximations of equations (37a) and (37b). It is a useful solution representation for positive V_s and negative $\phi'(0)$, but within a range of these variables that is smaller than existing numerical data. It is a useful solution representation for negative V_s and positive $\phi'(0)$ within a range of variable that exceeds all available numerical data. The use of this expansion for a fixed $\phi'(0)$ problem is a simple matter, namely, one chooses $\zeta = \phi'(0)$ and plots V from equation (37a). For a fixed V_s problem the use of this expansion for computing V requires one to find the proper ζ solution to the algebraic equation

$$\exp (V_s) = 1 + \zeta\phi_1^{(3)}(0) + \zeta^2\phi_2^{(3)}(0) + \zeta^3\phi_3^{(3)}(0). \quad (38)$$

In order to allow for easy use of the ζ expansion in this latter type of problem, a working plot of V_s as a function of ζ as per equation (38) is presented in Fig. 4.

References

1 Carslaw, H. S., and Jaeger, J. C., *Conduction of Heat in Solids*, Oxford Press, 1959.

2 Crank, J., *Mathematics of Diffusion*, Oxford Press, 1957.

3 Phillip, J. R., "General Method of Exact Solution of the Concentration-Dependent Diffusion Equation," *Australian F. Physics*, Vol. 13, 1960, p. 1.

4 Andre-Talamon, T., "Sur la diffusion non-lineare de la chaleur," *International Journal of Heat and Mass Transfer*, Vol. 11, 1968, p. 1351.

5 Meksyn, D., *New Methods in Laminar Boundary Layer Theory*, Pergamon Press, London, 1961.

6 Wagner, C., "On the Solution to Diffusion Problems Involving Concentration-Dependent Diffusion Coefficients," *Journal of Metal Trans.*, Vol. 4, 1952, p. 91.

7 Cooper, L. Y., "Constant Surface Heating of a Variable Conductivity Half-Space," *Quart. Appl. Math.*, Vol. 27, 1969, p. 173.

E. ARANOVITCH
Euratom—C.C.R.,
Department of Engineering,
Ispra, Italy

A Method for the Determination of the Local Turbulent Friction Factor and Heat Transfer Coefficient in Generalized Geometries

A method is presented for the determination of the distributions of velocity, local friction, and heat transfer coefficients in a forced axial turbulent flow with an arbitrary cross section. The method uses as basis the characteristics of the laminar flow. A comparison is made with some experimental results concerning different geometries.

Introduction and General Principles of the Method

A METHOD is proposed for the determination of the velocity distribution of the local heat transfer and friction factor for fully developed turbulent flows of fluids of constant properties through ducts of arbitrary cross section with a prescribed heat flux distribution at the wall.

A field of application concerns the design of nuclear fuel elements. In the case of compact fuel element geometries such as clusters, local variations of the heat transfer coefficient, even of the order of 20 percent, can have important consequences on their thermal and thermomechanical behavior (hot spots, bowing phenomena, stability, etc.).

The method can be divided into three parts. The first part concerns the distribution of the velocity near the wall. The velocity profile on a line normal to the wall is represented by equations of the same type as those used for the circular geometry, with the reduced velocity u^+ as a function of the reduced distance n^+ to the wall. Only the friction velocity u^* varies. When the distribution of the local friction velocity is known, the velocity profile in each point is known. This approach is supposed to be valid as long as the local radius curvature of the wall is not too small compared to the average hydraulic diameter.

The second part concerns the velocity distribution in the core. In this region it is assumed that the flow can be represented by a gradient-diffusion type of equation. This assumption, from a theoretical point of view, can be questioned since it neglects completely the existence of secondary flows. From a practical point of view, little is known of the influence of these secondary flows on the local heat transfer coefficient and friction factor. In the core it is supposed that the eddy diffusivities of momentum and of heat are constant. From different models concerning the circular geometry such as Prandtl's or von Karman's, it can be noted that the eddy diffusivity of momentum can take many different forms without appreciably affecting the velocity distribution. If we apply this remark to a generalized geometry, one is led to take the simplest form of the eddy diffusivity function, that is, a constant. With this simplification the turbulent velocity distribution in the core is represented by a Poisson's equation, such as in the laminar flow. Furthermore, if we suppose that the

Contributed by the Heat Transfer Division for publication (without presentation) in the JOURNAL OF HEAT TRANSFER. Manuscript received by the Heat Transfer Division, October 30, 1969; revised manuscript received, March 1970. Paper No. 70-HT-M.

Nomenclature

C_p = specific heat of fluid

d_h = hydraulic diameter, $d_h = \frac{4s}{p_w}$

f_l = average laminar friction factor

f_{ol} = laminar friction factor for the circular geometry

F_l = reduced laminar velocity: $F_l = \frac{u}{u_l}$

f_{ot} = turbulent friction factor for the circular geometry

f_t = average turbulent friction factor

F_t = reduced turbulent velocity: $F_t = \frac{u}{u}$

$g(i)$ = dimensionless function of (i)

$g_{\max}$ = maximum value of $g(i)$

$G(i), G(io), G(\theta)$ = reduced friction velocity, $G = \frac{u^*}{u_{\max}{}^*}$, functions of (i), (io), or (θ)

$\bar{G}, \bar{G}^2$ = average values of G or G^2

$h(i), h(\theta)$ = local heat transfer coefficient, functions of (i) or (θ)

(*Continued on next page*)

solution has a constant value when extrapolated to the wall, we obtain a solution similar in form (not identical) to the solution of the laminar flow.

This crucial assumption which can only be justified by subsequent comparison with experimental results, gives the possibility of using the laminar flow, in a generalized geometry, as basis for the study of the turbulent flow. In this text a generalized geometry is defined as a cylindrical configuration with an arbitrary cross section.

One feels intuitively that there are similarities between the turbulent and the laminar flows. The points or the curves of maximum velocities are never very far apart in the two cases (a property which has been used extensively in the study of the annular flow). The distribution along the wall of the local heat transfer coefficient presents the same general variations, only more attenuated in the case of the turbulent flow. The problem is to find an acceptable law of attenuation.

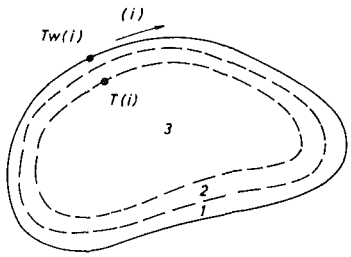

1 Laminar and buffer layers

2 Turbulent layer near the wall

3 Turbulent core

Fig. 1 Generalized geometry

The third part concerns the linking together of the velocity function near the wall with the velocity function in the core. In order to do so, we write that along a certain equal velocity line separating the two velocity zones, the distribution of the normal derivative of the velocity is the same for the two functions. By joining the two velocity profiles, the distribution of the local friction velocity can be determined. Then it is assumed that the distributions of the local heat transfer coefficient and of the friction velocity are identical. After a mathematical presentation of the model, a certain number of applications concerning various geometries are presented.

Velocity Distributions

The flow in a given geometry (Fig. 1) can be divided into two parts: a zone near the wall, made up successively of a laminar, buffer, and turbulent layers; and the turbulent core.

Steady state conditions are assumed.

Velocity Profile in the Layer Zone. It is assumed that in the vicinity of the wall, where distances are small compared to the mean hydraulic diameter, the velocity distribution can be represented by functions identical in form to those used for the circular geometry. Among different available expressions, we have retained Deissler's formulas [1][1]

[1] Numbers in brackets designate References at end of paper.

Nomenclature

h_0 = heat transfer coefficient for the circular geometry
$h_{\max}$ = maximum value of h
(i) = arc coordinate of the wall
(io) = arc coordinate where the value of the normal derivative of the velocity is equal, in laminar flow, to that of the circular geometry at the same hydraulic diameter and average velocity
m = coefficient
n_i = distance along the normal to the equal velocity curves from a point of the wall defined by the arc coordinate (i)
n^+ = reduced distance from the wall, $n^+ = \frac{n_i u^*(i)}{\nu}$
Nu_o = Nusselt number for the circular geometry
Pr = Prandtl number
p_w = wetted perimeter
Re = Reynolds number
s = flow cross-section area
T = fluid temperature
$T(i)$ = turbulent fluid temperature at the limit of the turbulent core, facing point at the wall defined by (i)
$T_w(i)$ = wall temperature at point (i)
u = laminar or turbulent velocity
u_i = velocity, function of n_i
u_l = average laminar velocity
u_t = average turbulent velocity
$u^*(i)$ = local friction velocity, function of (i)
$u_{\max}{}^*$ = maximum value of the friction velocity
$u^*(io)$ = friction velocity at point (io)
u^+ = reduced velocity $u^+ = \frac{u_i}{u^*(i)}$
$W(i), W(\theta), W(y)$ = reduced functions of the normal derivative of the laminar velocity at the wall. $W = \left[\frac{dF_l}{dn}\right] \Big/ \left[\frac{dF_l}{dn}\right]_{\max}$
$W(io)$ = value of the function W at the point (io)
$\bar{W}$ = average value of the function W
x, y = rectangular coordinates
$\frac{dF_l}{dn}, \frac{dF_t}{dn}$ = normal derivative of the function F_l and F_t
$\left[\frac{dF_l}{dn}\right]_{\max}, \left[\frac{dF_t}{dn}\right]_{\max}$ = maximum values of $\frac{dF_l}{dn}$ and $\frac{dF_t}{dn}$
$\frac{dp}{dz}$ = axial pressure drop per unit length
α = molecular diffusivity of heat
$\epsilon_{hx}, \epsilon_{hy}$ = eddy diffusivities of heat, in the x or y direction
ϵ_h = eddy diffusivity of heat, constant
$\epsilon_{mx}, \epsilon_{my}$ = eddy diffusivities of momentum, in the x or y direction
ϵ_m = eddy diffusivity of momentum, constant
θ = polar coordinate
κ_l = laminar form coefficient, $\kappa_l = \frac{f_l}{f_{ol}}$
κ_t = turbulent form coefficient, $\kappa_t = \frac{f_t}{f_{ot}}$
λ = thermal conductivity
ν = kinematic viscosity
ξ = coefficient
ρ = density
$\tau(i)$ = local shear stress, function of (i)
$\Phi(i)$ = wall flux, function of (i)
η = coefficient
β, γ = coefficient
$\int^c$ = integration along the wetted perimeter
$\iint^s$ = integration over the flow cross-section area

$$n^+ = \frac{1}{a}\frac{\int_0^{au^+} e^{-(au^+)^2/2} d(au^+)}{e^{-(au^+)^2/2}} \qquad \text{with } 0 < n^+ < 26 \quad (1)$$

$a = 0.109$

$$u^+ = 3.80 + 2.78 \ln n^+ \qquad \text{with } n^+ > 26 \quad (2)$$

The local characteristic of this function appears through the local friction velocity $u^*(i)$ where (i) is the wall arc coordinate

$$n^+ = \frac{n_i u^*(i)}{\nu} \quad (3)$$

$$u^+ = \frac{u_i}{u^*(i)} \quad (4)$$

The local friction velocity $u^*(i)$ is defined by

$$u^*(i) = u_t \sqrt{f_t/2} \cdot g(i) \quad (5)$$

The local shear stress $\tau(i)$ is

$$\tau(i) = \rho u^{*2}(i) \quad (6)$$

when $g(i)$, which is a dimensionless function of (i) and f_t, which is the average friction factor for the considered geometry, are known, the velocity distribution in the layer zone is fully determined.

The Turbulent Core. In an arbitrary geometry, at greater distances from the wall, there is no reason to believe that the velocity distribution, on a line normal to the equal velocity curves, could be represented in all points by a logarithmic function (consider for instance a rectangular geometry where the ratio of the two sides is very great).

In a general form, the velocity distribution is given by the equation:

$$\frac{1}{\rho}\frac{dp}{dz} = \frac{\partial}{\partial x}\left[(\nu + \epsilon_{mx})\frac{\partial u}{\partial x}\right] + \frac{\partial}{\partial y}\left[(\nu + \epsilon_{my})\frac{\partial u}{\partial y}\right] \quad (7)$$

According to different authors, the anisotropy of the eddy diffusivity of momentum function ϵ_m is not negligible, especially near the wall. Nevertheless experimental results on this subject are scarce and difficult to inject into general formulation. In our present case, the kinematic viscosity ν is neglected, and it is supposed that the eddy diffusivity of momentum is constant in the turbulent core and equal to

$$\frac{\epsilon_m}{\nu} = 0.033 \text{ Re } \sqrt{f_t/2} \quad (8)$$

This value has been derived from Cess's formula after simplification. The equation (7) becomes a Poisson's equation

$$\frac{1}{\rho}\frac{dp}{dz} = -2u_t^2 \cdot f_t \cdot \frac{1}{d_h} = \epsilon_m\left[\frac{\partial^2 u}{\partial x^2} + \frac{\partial^2 u}{\partial y^2}\right] \quad (9)$$

of which the boundary conditions are defined in the next paragraph.

Similarities Between the Laminar and Turbulent Velocity Distributions. The laminar velocity distribution in the steady state is given by

$$\frac{1}{\rho}\frac{dp}{dz} = \nu\left[\frac{\partial^2 u}{\partial x^2} + \frac{\partial^2 u}{\partial y^2}\right] = -2u_l^2 \cdot f_l \cdot \frac{1}{d_h} \quad (10)$$

with $u = 0$ at the wall.

The equations (9) and (10) can be written in the following form for the turbulent flow

$$\frac{\partial^2 F_t}{\partial x^2} + \frac{\partial^2 F_t}{\partial x^2} = -120\sqrt{f_t/2} \cdot \frac{1}{d_h^2} \quad (11)$$

for the laminar flow

$$\frac{\partial^2 F_l}{\partial x^2} + \frac{\partial^2 F_l}{\partial y^2} = -32\kappa_l \cdot \frac{1}{d_h^2} \quad (12)$$

F_t and F_l are reduced turbulent and laminar velocity functions, κ_l is a form coefficient which is defined by

$$\kappa_l = \frac{f_l}{f_{ol}} = \frac{d_h}{8} \cdot \left[\frac{\overline{dF_l}}{dn}\right]_{\text{wall}} \qquad \text{where } f_{ol} = \frac{16}{\text{Re}} \quad (13)$$

f_{ol} is the laminar friction factor for the circular geometry with the same Reynolds number and same hydraulic diameter.

$\left[\frac{\overline{dF_l}}{d_n}\right]_{\text{wall}}$ is the mean normal derivative of the function F_l at the wall.

If it is assumed that the factor F_t, defined for the turbulent core, has a constant value ξ when extrapolated to the wall, there exists a simple relation between F_t and F_l.

$$F_t = \xi + \eta \cdot F_l \quad (14)$$

where ξ and η are two coefficients. From equations (11) and (12) it can be seen that

$$\eta = \frac{3.75}{\kappa_l} \cdot \sqrt{f_t/2} \quad (15)$$

As was said in the Introduction, this boundary condition can only be justified by a satisfactory comparison of calculated friction factors and velocity distributions with experimental results.

The coefficient η varies little with the Reynolds number, approximately as $\text{Re}^{-0.1}$. The coefficient ξ, which determines the boundary condition for equation (11), is calculated by iteration, considering that the average value of the velocity is equal to u_t. If one considers only the reduced velocity function F_t for the turbulent core, but averaged over the whole cross section, a value slightly greater than 1 will be found (from the different numerical applications which have been made, a value of 1.05 can be taken as a first approximation).

$$\frac{1}{s}\iint^s F_t \, ds = \frac{1}{s}\iint^s (\xi + \eta \cdot F_l) ds = \xi + \eta \simeq 1.05 \quad (16)$$

then

$$\xi \simeq 1.05 - \eta \quad (17)$$

Determination of the Friction Velocity Distribution $u^*(i)$. In order to determine the friction velocity distribution $u^*(i)$ we write that the normal reduced velocity derivative $\left[\frac{dF_t}{dn}\right]_i \Big/ \left[\frac{dF_t}{dn}\right]_{\max}$ along a certain equal velocity line, defined by F_{tk}, near the wall, is the same for equations (2) and (11). (The maximum value $\left[\frac{dF_t}{dn}\right]_{\max}$ along this line is being taken as reference.)

For equation (11) it is assumed that this normal derivative function near the wall can be taken equal to the same function at the wall.

$$\underbrace{\left[\frac{dF_t}{dn}\right]_i \Big/ \left[\frac{dF_t}{dn}\right]_{\max}}_{\text{along } F_{tk}\text{, near the wall}} \simeq \underbrace{\left[\frac{dF_t}{dn}\right]_i \Big/ \left[\frac{dF_t}{dn}\right]_{\max}}_{\text{at the wall}} \quad (18)$$

which is the same in the laminar flow, and we introduce the function $W(i)$. At the wall

$$\left[\frac{dF_t}{dn}\right]_i \Big/ \left[\frac{dF_t}{dn}\right]_{\max} = \left[\frac{dF_l}{dn}\right]_i \Big/ \left[\frac{dF_l}{dn}\right]_{\max} = W(i) \quad (19)$$

Coming back, near the wall, to a logarithmic velocity profile of the form

$$u^+ = \beta + \gamma \ln u^+ \tag{20}$$

which in our reduced system can be written:

$$F_t = \frac{u^*(i)}{u_t}\left[\beta + \gamma \ln \frac{n_i u^*(i)}{\nu}\right] \tag{21}$$

The normal derivative is:

$$\left[\frac{dF_t}{dn}\right]_i = \gamma \frac{u^*(i)}{u_t}\cdot\frac{1}{n_i} \tag{22}$$

Along the equal velocity line F_{tk}, n_i is eliminated between the equations (21) and (22)

$$F_{tk} = \frac{u^*(i)}{u_t}\left[\beta + \gamma \ln \frac{\gamma}{\nu}\cdot\frac{u^{*2}(i)}{u_t}\cdot\frac{1}{\left[\frac{dF_t}{dn}\right]_i}\right] \tag{23}$$

In the same manner, at the reference point, where u^* and $\frac{dF_t}{dn}$ are maximum.

$$F_{tk} = \frac{u_{\max}{}^*}{u_t}\left[\beta + \gamma \ln \frac{\gamma}{\nu}\frac{u_{\max}{}^{*2}}{u_t}\cdot\frac{1}{\left[\frac{dF_t}{dn}\right]_{\max}}\right] \tag{24}$$

By combination of equations (23) and (24), we obtain, along the equal velocity line F_{tk}

$$\left[\frac{dF_t}{dn}\right]_i \Big/ \left[\frac{dF_t}{dn}\right]_{\max} = \left[\frac{u^*(i)}{u_{\max}{}^*}\right]^2 \cdot e^{-m\left[\frac{u_{\max}{}^*}{u^*(i)}-1\right]} \tag{25}$$

where

$$m = \frac{1}{\gamma}\cdot F_{tk}\cdot\frac{u_t}{u_{\max}{}^*} \tag{26}$$

We introduce the function $G(i) = \frac{u^*(i)}{u_{\max}{}^*}$, and according to the assumption represented by equation (19), we can write

$$W(i) = G^2(i) e^{-m\left[\frac{1}{G(i)}-1\right]} \tag{27}$$

This formula, which links the turbulent friction velocity distribution to the normal derivative at the wall of the laminar velocity distribution, represents the fundamental relation of the method presented here. The value of the coefficient m will be determined from experimental results.

The interest of this formula lies in the fact that the value of the coefficient m seems to vary very little with the geometry and the Reynolds number. From the experimental results which have been analysed, a value of the order of 4 is proposed in the range of $10^4 < \mathrm{Re} < 10^5$.

The formula (27) is a relation between two relative distributions which have their maximum values as references (it is assumed that these maxima occur at the same point in the turbulent and in the laminar flows). In order to obtain the absolute values, we define the point (io) at the wall, where the normal derivative of the laminar velocity is equal to the value it would have in the circular geometry with the same hydraulic diameter and same mean velocity. This point (io) is given by

$$W(io) = \frac{1}{\kappa_t}\cdot\int^c \frac{W(i)di}{p_w} = \frac{\overline{W}}{\kappa_t} \tag{28}$$

The assumption is made that at this point, (io), the friction velocity $u^*(io)$ is also equal to the value it would have in the circular geometry with the same hydraulic diameter and same mean velocity, that is,

$$u^*(io) = u_t\sqrt{f_{ot}/2} \tag{29}$$

For the circular friction factor f_{ot}, Blasius's formula can be proposed

$$f_{ot} = 0.079\ \mathrm{Re}^{-0.25} \tag{30}$$

If $G(io)$ is the transform at the point (io) of the function $W(io)$, the local friction velocity $u^*(i)$ is

$$u^*(i) = u^*(io)\cdot\frac{G(i)}{G(io)} \tag{31}$$

Determination of the Turbulent Friction Factor f_t. The average turbulent friction factor f_t can be obtained from the pressure drop formula or from the shear stress $\tau(i)$, defined by equation (6). By using also equations (31) and (29), one can write

$$-\frac{dp}{dz} = 2\rho u_t{}^2\frac{1}{d_h}\cdot f_t = 4\rho u^{*2}(io)\cdot\frac{1}{d_h}\cdot\frac{f_t}{f_{ot}} \tag{32}$$

$$-\frac{dp}{dz} = \frac{1}{s}\int^c \tau(i)di = \frac{\rho}{s}\int^c u^{*2}(i)di = \frac{\rho}{s}\cdot\frac{u^{*2}(io)}{G^2(io)}\cdot p_w\cdot\bar{G}^2 \tag{33}$$

where

$$\overline{G^2} = \frac{1}{p_w}\int^c G^2(i)di \tag{34}$$

Then by combination of equations (32) and (33)

$$\frac{f_t}{f_{ot}} = \kappa_t = \frac{\overline{G^2}}{G^2(io)} \tag{35}$$

As in the case of the laminar flow, a turbulent form coefficient κ_t is introduced.

The function $g(i)$ in equation (5) is given by

$$g(i) = \frac{G(i)}{\sqrt{\bar{G}^2}} \tag{36}$$

All the elements for a formal determination of the turbulent flow are available.

Temperature Distributions and Local Heat Transfer Coefficients

The heat flux at the wall is defined by the function $\Phi(i)$, and the wall temperature distribution is defined by the function $T_w(i)$. It is assumed that the Prandtl number is high enough ($\mathrm{Pr} > 1$) so that the temperature drops in the film are predominant compared to the temperature variations in the bulk.

The influence of temperature on the fluid characteristics has been neglected. Steady state conditions are assumed. The average fluid temperature in a given cross section is taken as reference.

Temperature Distribution in the Turbulent Core and at the Wall. In a general form the fluid temperature is represented by the equation (37).

$$\frac{\partial}{\partial x}\left[(\alpha + \epsilon_{hx})\frac{\partial T}{\partial x}\right] + \frac{\partial}{\partial y}\left[(\alpha + \epsilon_{hy})\frac{\partial T}{\partial y}\right] = u\frac{dT}{dz} \tag{37}$$

This equation shows similarities with the equation (7). The same remarks made previously on the anisotropy of the eddy diffusivity of momentum ϵ_m apply here as far as the eddy diffusivity of heat ϵ_h is concerned. Simplifications identical to those made for equation (7) are carried out. The thermal diffusivity α is neglected. It is assumed that ϵ_h is isotropic and constant. The equation (37) becomes

$$\epsilon_h \left[\frac{\partial^2 T}{\partial x^2} + \frac{\partial^2 T}{\partial y^2} \right] = u \frac{dT}{dz} \tag{38}$$

The boundary conditions are different from those of equation (7)

$$\epsilon_h \cdot \rho \cdot C_P \cdot \frac{dT}{dn} = \Phi(i) \text{ at the wall} \tag{39}$$

with

$$\iint^s T ds = 0 \tag{40}$$

To perform these calculations the limits of the turbulent flow are extrapolated to the wall. The boundary condition (39) means that in effect the transversal diffusion of heat near the wall in the laminar and buffer layers is neglected. It should not be forgotten that as far as the wall temperature distribution is concerned, the variations in the bulk temperature will generally represent a small influence which justifies the simplifications, and in most cases the equation (38) could be further simplified by supposing that the turbulent velocity u is constant and equal to the average velocity u_t. The solution of the equation (38) will give the fluid temperature distribution $T(i)$ at the boundary of the turbulent core, identified here with the wall. The value of ϵ_h is obtained by supposing that the ratio ϵ_h/ϵ_m is constant. Some authors take this ratio equal to one. Some experimental results seem to indicate that the ratio is greater than one and probably not constant over the whole cross section.

Determination of the Turbulent Local Heat Transfer Coefficient. The local heat transfer coefficient $h(i)$ is defined by the relation

$$h(i) = \frac{\Phi(i)}{T_w(i) - T(i)} \tag{41}$$

where $T(i)$ is the local fluid turbulent temperature near the wall. We have chosen that definition in order that the local heat transfer coefficient be expressed solely in terms of local parameters, and to underline that the wall temperature variations are not only dependent upon the variations of the heat transfer coefficient but also upon the variations of the temperature in the bulk, which in turn are influenced by the heat flux function $\Phi(i)$. It is assumed that the distribution of the local heat transfer coefficient $h(i)$ is identical to the distribution of the friction velocity $u^*(i)$.

$$\frac{h(i)}{h_o} = \frac{u^*(i)}{u^*(io)} \tag{42}$$

h_o, which is the heat transfer coefficient for the circular geometry at the same hydraulic diameter, same Reynolds number, and same Prandtl number, can be determined, for instance, from the formula of Dittus and Boettler

$$\mathrm{Nu}_o = 0.023\ \mathrm{Re}^{0.8}\ \mathrm{Pr}^{0.4} \tag{43}$$

Applications of the Method

A few examples of applications of the method and comparisons with experimental results are given. The experimental coefficient m of formula (27) has been taken equal to 4 in all cases.

Friction Factor and Heat Transfer Coefficient in an Equilateral Triangle. As an example, let us consider an equilateral triangle. Fig. 2, for which the reduced laminar velocity function F_l is

$$F_l = \frac{30}{a^3} \cdot x[(a - x)^2 - 3y^2] \tag{44}$$

The laminar form coefficient κ_l is determined by equation (13) and found equal to 0.833. By reason of symmetry, it is sufficient to consider the normal derivative on the side corresponding to $x = 0$ where

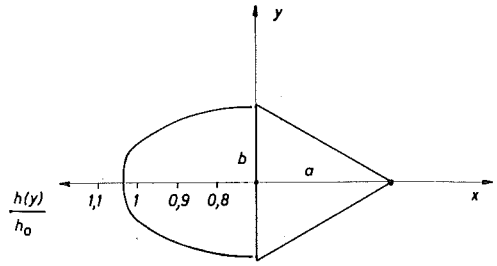

Fig. 2 Local heat transfer coefficient in an equilateral triangle (up to 0.95 b)

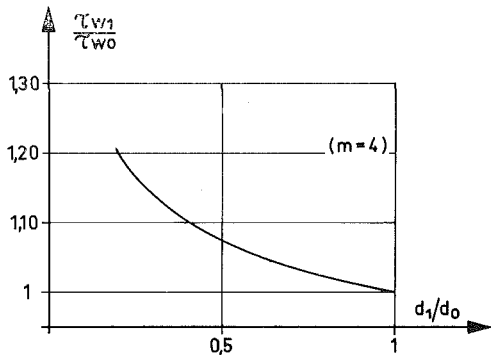

Fig. 3 Ratio of wall shear stresses in annular geometry

$$W(y) = 1 - 3\left[\frac{y}{a}\right]^2 \tag{45}$$

The function $G(y)$ is given by equation (27). The turbulent form coefficient κ_t can then be calculated by equation (35) and is found equal to 0.92. By this method it is found that the turbulent friction factor for the equilateral triangle is 8 percent smaller than the friction factor for the circular geometry with the same hydraulic diameter and Reynolds number. The distribution of the local turbulent heat transfer coefficient is calculated by equation (42). See Fig. 2. A similar procedure can be applied to other geometries for which there exists an analytical solution of the laminar flow, such as the right isosceles triangle, the ellipse, or the symmetrical annular geometry, etc.

Ratio of Inside and Outside Shear Stresses and Friction Factor for an Annular Geometry. The annular geometry would seem the most convenient one to check the validity of the method. However, this symmetrical configuration does not present local variations of the friction velocity, but it is interesting to see how the ratio τ_{w1}/τ_{w0} of the inside wall shear stress over the outside wall shear stress varies when calculated by the proposed method. The procedure is similar to the one used in the preceding section. The results are shown in Fig. 3.

In Fig. 4, the average friction factor is represented versus the ratio d_1/d_o of the internal diameter over the external diameter for both laminar and turbulent flows. For values of this ratio between 0.2 and 1, the friction factor for both types of flows is fairly constant. The laminar friction factor is about 50 percent, and the turbulent friction factor is about 13 percent higher than the respective same friction factors for the circular geometry.

A survey of experimental data shows an important scattering of results between different authors [1–3, etc.]. Turbulent friction factors for the annular geometry have been found to be 10 percent to 15 percent larger than the circular geometry friction

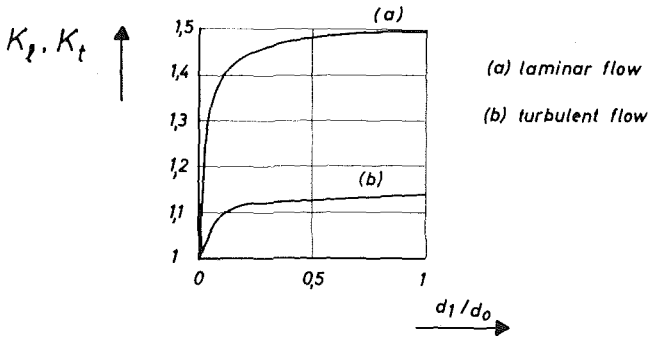

Fig. 4 Average friction factor for the annular geometry

factor; however, most recent works seem to indicate values not exceeding by more than 5 percent to 7 percent the circular geometry values.

The rather high value found here is due to the fact that the laminar form coefficient is high for the annular geometry. It also could be that the assumption represented by equation (28) is too simplified.

The Cluster Geometry. The cluster geometry is quite frequent in the nuclear field, and when the distance between adjacent rods is small, it is of special importance to know the distribution of the local heat transfer coefficient.

Average Friction Factor and Velocity Distributions. A comparison is made in Fig. 5 with the experimental results of Eifler and Nijsing [4] concerning the geometry shown in Fig. 6, where the pitch p could be made to vary. The curve was calculated by the procedure shown in the paragraph entitled "Friction Factor and Heat Transfer Coefficient in an Equilateral Triangle." The functions W were established by electrical analogy methods. The curve is compared with experimental points of two sorts; the first ones were obtained by direct pressure drop measurements, and the second ones were determined from the experimental velocity distributions according to a method expounded by the mentioned authors.

In Fig. 7, a comparison is made between the calculated velocity distributions and the experimental points obtained by Eifler and Nijsing in the same geometry, at a Reynolds number of 30,000 and at two values of the pitch, for three different angular

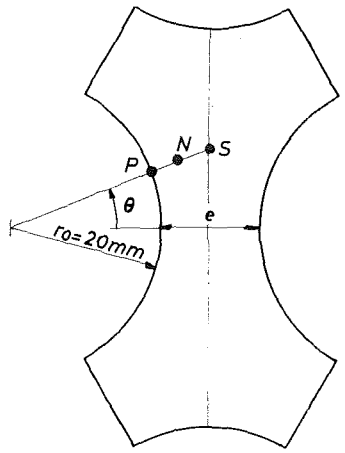

$$\text{pitch } p = 1 + \frac{e}{2r_0}$$

$$PN = n$$

$$PS = n_1$$

Fig. 6 Cluster type geometry

positions. There seems to be a rather satisfactory agreement between the experimental points and the calculated curves. In these curves, the velocity profile in the turbulent core has been limited to a distance from the wall equal to 10 percent of the mean hydraulic diameter. Near the wall the velocity profile is given by equation (2). The fitting between these two profiles can show small discrepancies which are represented by small vertical lines in Fig. 7. As the two velocity distributions are very near one another in that zone, the choice of the exact boundary between them is of no fundamental importance.

Local Heat Transfer Coefficient. The local heat transfer coefficient was studied experimentally by the author in the geometry represented in Fig. 8. Only a brief description of the experimental method used will be given here as a paper is being prepared on the

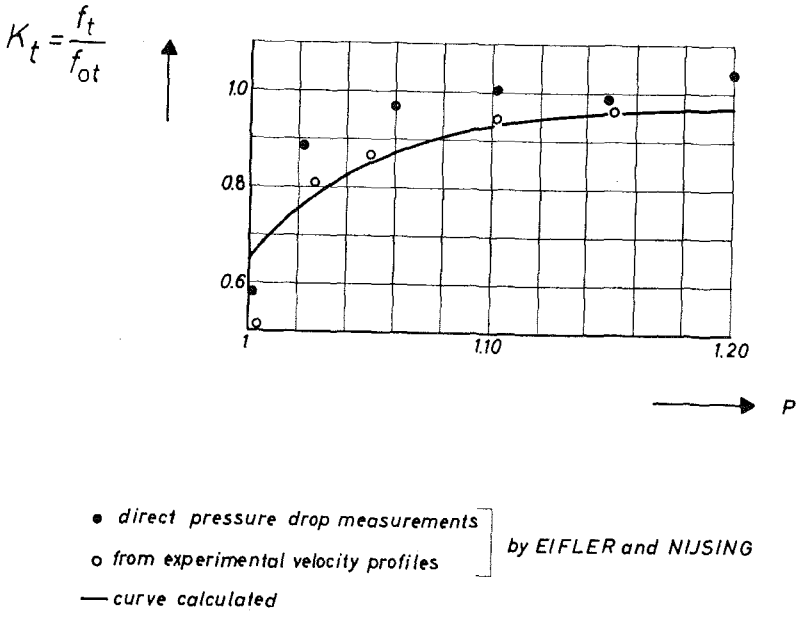

Fig. 5 Experimental and calculated average friction factor for a cluster geometry

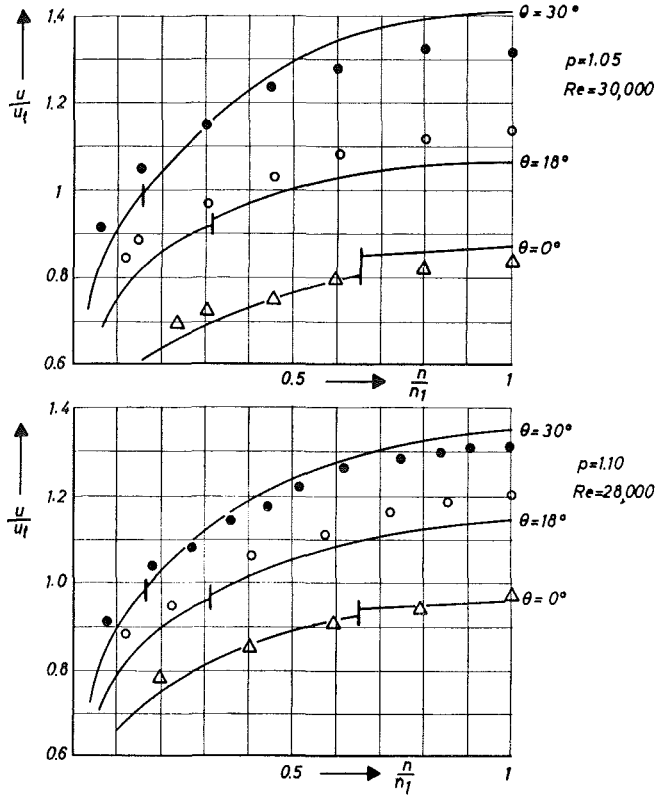

● ○ △ : experimental points from EIFLER and NIJSING

——— : calculated curves

Fig. 7 Calculated and experimental velocity distributions

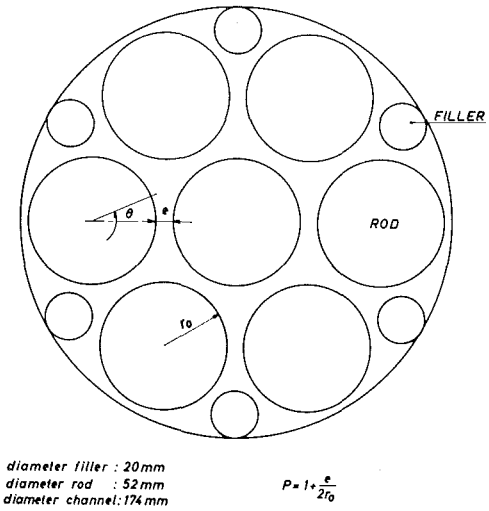

diameter filler : 20mm
diameter rod : 52mm
diameter channel: 174mm

$P = 1 + \frac{e}{2r_0}$

Fig. 8 Seven rod cluster geometry

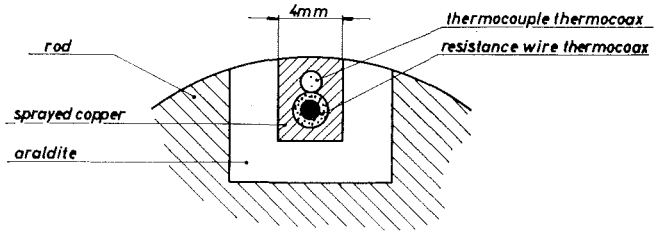

Fig. 9 Schematic design of detector

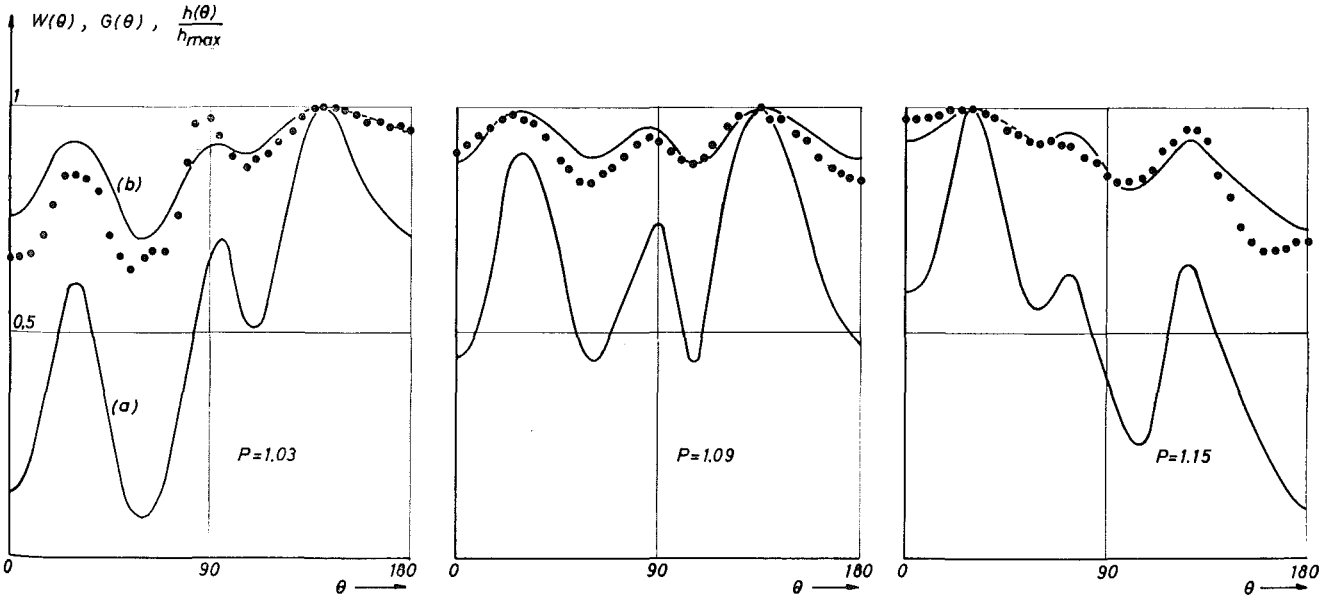

(a) : W(θ) (b): G(θ)

⊙ experimental points : $\frac{h(\theta)}{h_{max}}$ concerning a peripheral rod (Re = 30,000)

Fig. 10 Comparison between calculated and experimental values of the local heat transfer coefficient

subject. The distributions of the local heat transfer coefficient were determined by the rotation of the central rod and of one peripheral rod on which the detectors were mounted in the test model represented in Fig. 8.

A schematic design of a detector is shown in Fig. 9. It consists principally of a 200-mm-long insulated resistance wire "thermocoax" on which has been fixed an insulated thermocouple. They are copper sprayed together and machined into a bar (200 × 5 × 4 mm) and then placed into a groove in the test rods from which they are thermally insulated by araldite. The main functions of the device are to produce a local heat flux and indicate a wall temperature while limiting as much as possible the lateral heat losses at the boundaries.

In the test model, the distance between the central rod and each peripheral rod could vary independently. In Fig. 10, the local heat transfer distributions were plotted versus the angular position for three different values of the pitch. For these three different geometries, the functions W were determined by electrical analogy methods. The corresponding functions G were then obtained through the equation (27), and it was supposed that the local heat transfer coefficient distribution was related to the function G by

$$\frac{h(\theta)}{h_{\max}} = G(\theta) \tag{46}$$

Conclusions

The comparison of the method with a certain number of experimental results shows a rather satisfactory agreement, which is the more encouraging because these results concern three different fields of experimentation (velocity distribution, average friction factor, local heat transfer coefficient), but it is clear that comparisons with more experimental results must be made.

What are the limits of validity of the model? One limit is surely reached where the local wall curvature becomes too small compared to the average hydraulic diameter or in the vicinity of tangent surfaces. The existence of secondary flows has been neglected. Steady state conditions have been assumed, although from a practical point of view the entrance effect can be important for complicated geometries.

The use of the laminar characteristics for the determination of the turbulent flows has already been proposed either implicitly or explicitly by different authors such as Gelin [5, 6].

Before passing to more complicated models, an experimental and theoretical effort should be made on the study of the anisotropy of the eddy diffusivities of momentum and heat.

Acknowledgment

The author wishes to express his thanks to Mr. Geoffrion who performed the studies by electrical analogy methods and the numerical treatments.

References

1 Knudsen, and Katz, *Fluid Dynamics and Heat Transfer*, McGraw-Hill, p. 162.

2 Rothfus, R. R., Monrad, C. C., and Senecal, V. E., "Velocity Distribution and Fluid Friction in Smooth Concentric Annuli," *Industrial and Engineering Chemistry*, *42*, 12.

3 Monrad, C. C., and Pelton, J. F., "Heat Transfer by Convection in Annular Spaces," Symposium of the Heat Transfer Division of the American Society of Mechanical Engineers, 1942.

4 Eifler, W., and Nijsing, R., "Fundamental Studies of Fluid Flow and Heat Transfer in Fuel Element Geometries," EUR 2193.e, 1964.

5 Gelin, P., "Détermination théorique des coefficients locaux de frottement et d'échange de chaleur dans un canal cylindrique á section droite quelconque," *Compte-rendus de l'Académie des Sciences*, 1957, p. 2190.

6 Gelin, P., "Détermination expérimentale des coefficients de frottement locaux dans un canal cylindrique á section droite quelconque," *Rapport CEA* n. 598.

7 Reynolds, W. C., "Turbulent Heat Transfer in a Circular Tube With Variable Circumferential Heat Flux," *International Journal of Heat and Mass Transfer*, June 1963.

8 Deissler, R. G., and Taylor, M. F., "Analysis of Axial Turbulent Flow and Heat Transfer Through Banks of Rods," Reactor Heat Transfer Conference, 1956.

9 Ibragimov, Kh., Isupov, I. A., Kobzar, L. L., and Subbotin, V. I., "Calcul des coefficients de résistance hydraulique dans l'écoulement turbulent d'un liquide dans des canaux non-circulaires," *Atomia Energia*, Oct. 1967.

CLINTON E. BROWN
Chief Scientist,
HYDRONAUTICS, Inc.,
Laurel, Md.

SHAIKH A. MATIN
Assistant Professor,
Weapons Department,
U. S. Naval Academy,
Annapolis, Md.
Assoc. Mem. ASME

The Effect of Finite Metal Conductivity on the Condensation Heat Transfer to Falling Water Rivulets on Vertical Heat-Transfer Surfaces

An analytical study has been made of the condensation of vapor onto falling rivulets of liquid which are constrained in lateral width by vertical non-wetting Teflon stripes on a flat metal heat-transfer surface. Under the condition studied it is shown that finite metal conduction plays a primary role in limiting the overall heat-transfer coefficient because in any system (drops or rivulets) where a triple point of metal, vapor, and liquid exists, the zero water path at the triple point would provide an unlimited conductance of heat were it not for finite metal conductivity or interfacial resistance. In the present paper, the temperature field and heat flow in a liquid rivulet and the underlying metal are computed using finite-difference methods. The metal plate is of constant thickness but the liquid rivulet is bounded by an arc of a circle as dictated by surface tension. The system involves two connected regions of different conductivity and shape, and the entire network is solved by an over-relaxation process taking into account the discontinuity in temperature gradient at the liquid-metal junction. Results are related to the practical application of such a system in desalination processes. The work was supported by the Office of Saline Water, Department of the Interior.

Introduction

Nusselt [1][1] analyzed the problem of condensation of vapor on a flat uniform falling film and showed that the main resistance to heat flow was in the water film and was caused by the relatively low thermal conductivity of the water. It was known, however, that great increases in heat-transfer coefficient were obtained when the condensation was "dropwise," i.e., when the condensate balled up on the plate until gravity caused the drop to fall and sweep off other immature droplets. It is now known that the good efficiency of dropwise condensation results from the high heat flux at the drop edges where the water path for heat flux goes to zero length. Calculations made by Umur and Griffith [2] for growing drops included the limiting effect of interfacial resistance but did not include the finite metal conductivity. The interfacial heat-transfer resistance is a fundamental effect which arises from the disturbance of molecular equilibrium at the liquid-vapor interface [3]. Its magnitude depends on the "evaporation coefficient," a measure of the percentage of the incident vapor molecules which are captured by the surface. Hickman [4] has shown that contrary to earlier estimates, the evaporation coefficient is greater than 0.6 and most probably close to unity, its maximum value. The interfacial resistance is also a function of the saturated vapor density or temperature, and using unity for the evaporation coefficient, very low values are obtained. The variation of interfacial heat-transfer coefficient with temperature is plotted in Fig. 1, and for a temperature as low as 100 deg F the value is over 200,000. It is clear then that except in cases of high *local* heat transfer the interfacial resistance should be of secondary importance. However, all cases involving a water film of locally vanishing thickness are indeed special cases where the interfacial resistance or the metallic resistance limits the integral or overall mean heat flux. This is easily seen if we consider any water film edge which makes an angle θ with the metal surface as shown in the sketch: If the metal were of infinite con-

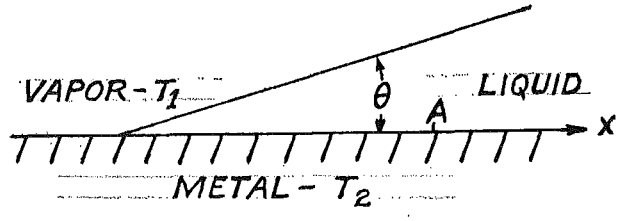

[1] Numbers in brackets designate References at end of paper.

Contributed by the Heat Transfer Division for publication (without presentation) in the Journal of Heat Transfer. Manuscript received by the Heat Transfer Division, November 13, 1969; revised manuscript received, May 11, 1970. Paper No. 70-HT-O.

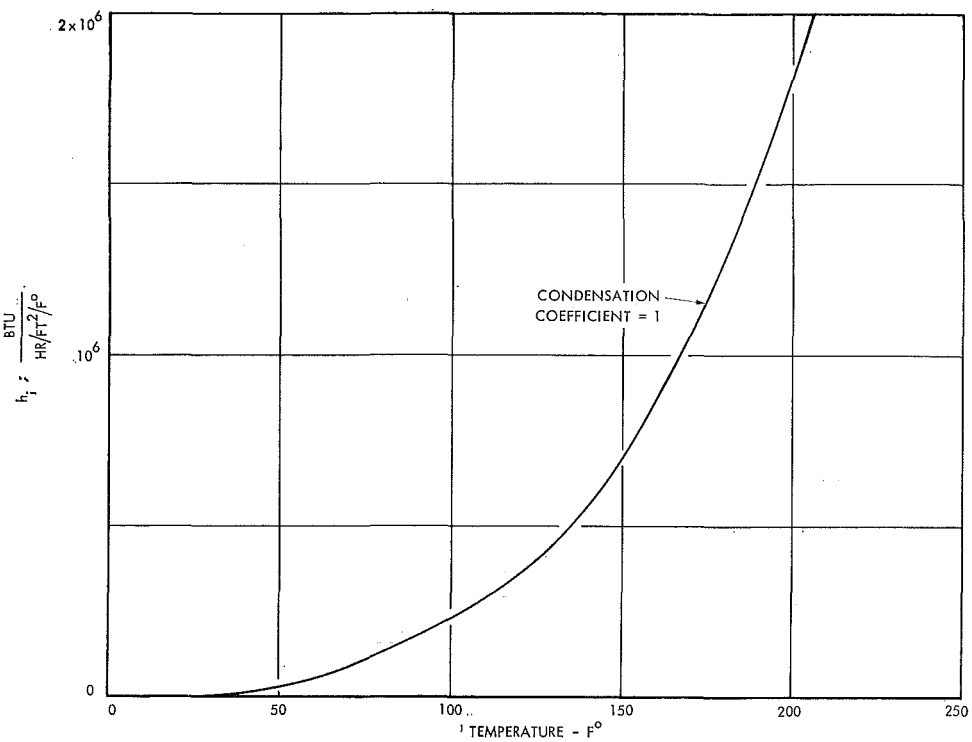

Fig. 1 Variation of interfacial heat-transfer coefficient with temperature

ductivity and the interfacial resistance were zero, the heat flux would be computed by an integral of the local heat flux at the surface which would be

$$q = \int_0^A \frac{K_l(T_2 - T_1)}{x\theta}\, dx$$

where q is the full flux over the small region, 0-A, k is the liquid conductivity, T_2 and T_1 the temperatures as shown in the sketch, and x is the distance along the plate. Since the integral is infinite for any small but finite value of A, it is clear that the mean heat flux value for any such system must be limited by local resistance in the metal or at the interface.

For the case under study vertical stripes of non-wetting material are assumed to provide tracks or bounds on downward-flowing rivulets, that is, the metal in the spaces between the lines is assumed to have a very small capillary angle so that surface tension forces the liquid into a cylindrical rivulet with a surface of constant radius (see Fig. 2). Such a system involves the special triple-point system discussed above and, as shown in Fig. 3, case 1, the region of high heat transfer would be in the corner where the Teflon stripes touch the rivulet. It is of great importance to limit the thickness of the Teflon at the corner, otherwise the situation shown as case 2 would occur. Here the thickness δ is the shortest heat flux pathway, and for values of δ of the order of 1 mil, the local heat-transfer coefficient would be limited to

$$h_l = \frac{k_l \times 12}{(0.001)} \cong \frac{0.4 \times 12}{0.001} = 4800$$

a value which would impair the achievable overall heat transfer considerably.

In the present study, the overall advantages of a "tracked" surface are computed taking into account the limiting effects of finite metal conductivity and interfacial resistance. Comparisons are given with flat film condensation for various combinations of metal thickness and conductivity.

Basic Equations for Condensing-Rivulet Flow

The dynamic and thermal behavior of the falling rivulet with an

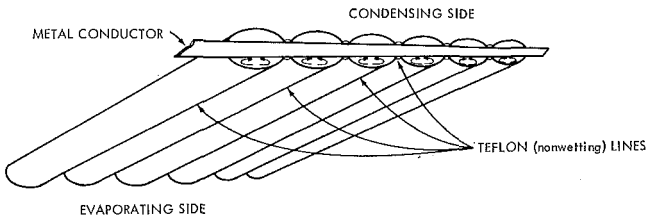

Fig. 2 Rivulet system

Nomenclature

c = half-width of rivulet
g = acceleration of gravity
h_n = heat-transfer coefficient (flat film)
h_i = heat-transfer coefficient (interfacial)
h_r = heat-transfer coefficient (rivulet)
k_l = thermal conductivity (liquid)
k_m = thermal conductivity (metal)
M = (See equation (16))
n = distance measured normal to free surface
q = heat flux per unit area
t = thickness of water film
t_n = thickness of water film (flat film case)
T = temperature
T_0 = temperature of saturated vapor and liquid surface
T_w = temperature of the outer wall boundary
u = downward liquid velocity
x, y, z = cartesian coordinates (see Fig. 4)
Γ = weight flow of liquid per unit breadth
Γ_r = weight flow of liquid in rivulet per unit breadth
ΔT = $(T_0 - T_w)$
δ = metal plate thickness
θ = rivulet corner angle
λ = heat of vaporization
ν = kinematic viscosity
ρ = fluid density

assumed cross-sectional shape of a circular arc as shown in Fig. 4 are mathematically described by the Navier-Stokes equations and the energy equation, respectively. However, for the condensation case the only driving force is the force of gravity acting longitudinally along the length of the rivulet. Hence the only non-zero velocity is along the vertical axis (neglecting the mass flow rate effect across the surface of the rivulet). The other simplifying assumptions are as follows:

1 Constant values of conductivity, viscosity, and density in liquid and metal.
2 Negligible width for the non-wetting lines.
3 Constant temperature on the water surface.
4 Metal-liquid capillary angles are zero.

The first assumption is quite good for the small-temperature-difference systems used in desalination; the second assumption is made to simplify the calculation and should have only a small effect on the final results; the third assumption follows from the requirement that the vapor is pure, and hence the saturated vapor pressure and temperature adjust very quickly on the surface; and the fourth assumption is apparently fufilled in reality by most metals since dropwise condensation is very difficult to maintain on metals without the use of promoters or special treatments [5]. Under these assumptions, two of the three Navier-Stokes equations are satisfied trivially; the third one and the energy equation reduce to:

$$\nu\left(\frac{\partial^2 u}{\partial x^2}+\frac{\partial^2 u}{\partial y^2}+\frac{\partial^2 u}{\partial z^2}\right)=g \tag{1}$$

and

$$\frac{\partial^2 T}{\partial x^2}+\frac{\partial^2 T}{\partial y^2}+\frac{\partial^2 T}{\partial z^2}=0 \tag{2}$$

Since the longitudinal dimension of the rivulet is several orders of magnitude larger than its cross-sectional dimension ($c/L \sim 10^{-3}$), from dimensional considerations the x derivatives of both u and T are negligible as compared to their derivatives in the y and z-directions. Hence equations (1) and (2) reduce to:

$$\nu\left(\frac{\partial^2 u}{\partial y^2}+\frac{\partial^2 u}{\partial z^2}\right)=g \tag{3}$$

and

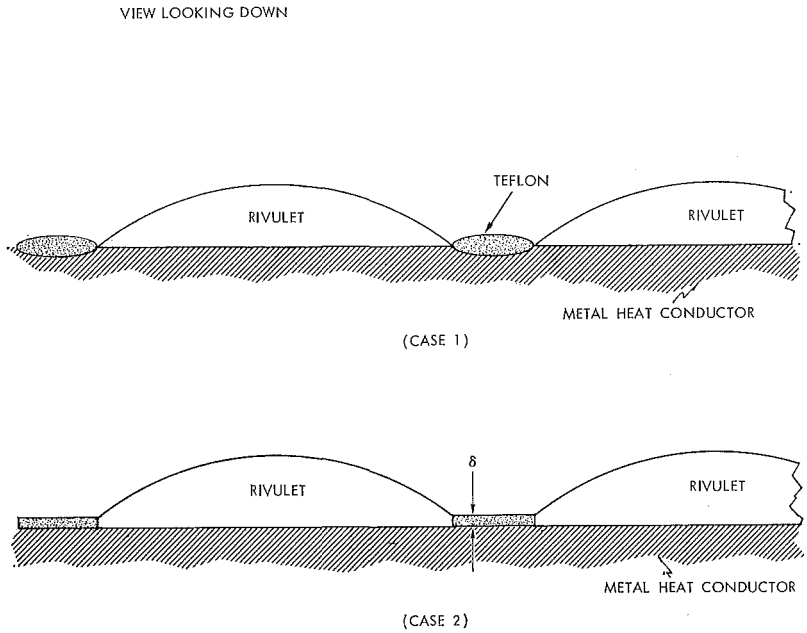

Fig. 3 Condensing rivulets with flush and non-flush Teflon stripes

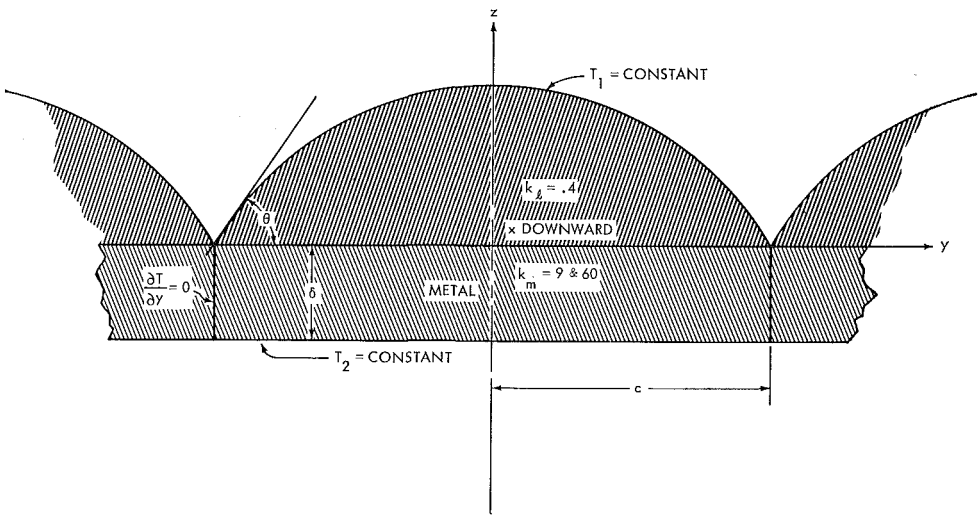

Fig. 4 Rivulet-metal system geometry

$$\frac{\partial^2 T}{\partial y^2} + \frac{\partial^2 T}{\partial z^2} = 0 \tag{4}$$

Equations (3) and (4) represent two-dimensional dynamic and heat conduction problems in the cross-sectional coordinates; and the axial dimension, x, enters only through the variation of the rivulet contact angle, θ, along the vertical axis.

The boundary conditions on equations (3) and (4) are as follows:

1 At the free liquid surface:

$$\frac{\partial u}{\partial n} = 0 \tag{5}$$

$$T = T_0 = \text{constant} \tag{6}$$

2 At the plate face ($z = -\delta$):

$$T = T_{\text{wall}} = \text{constant} \tag{7}$$

3 At the metal-liquid interface:

$$u = 0, \tag{8}$$

$$k_l \left.\frac{\partial T}{\partial z}\right|_{\text{liquid}} = k_m \left.\frac{\partial T}{\partial z}\right|_{\text{metal}} \tag{9}$$

and T is continuous across the interface.

Equation (9) represents the physical requirement that no heat sources or sinks exist along the interface.

Boundary conditions (5)–(9) are sufficient for the problem theoretically; however, for computational convenience the symmetry of the u and T profiles is utilized. This results in an added boundary condition on $y = 0$ as

$$\left.\frac{\partial u}{\partial y}\right|_{y=0} = \left.\frac{\partial T}{\partial y}\right|_{y=0} = 0 \tag{10}$$

To complete this description, the equation of the rivulet liquid surface utilized in describing condition in equation (5) is recorded as:

$$y^2 + z^2 + 2zC \cos\theta = C^2 \sin\theta \tag{11}$$

Equation (11) follows from the physical condition of constant temperature and hence surface tension on the liquid surface.

The velocity and temperature fields are uncoupled and only depend on the geometry of the rivulet; however, to obtain the overall heat transfer for a surface of finite height, the local heat flux must be integrated to take into account the varying geometry and water flow with vertical distance. For this we write

$$\frac{\partial}{\partial x}(\Gamma_r) = \frac{k_l}{\lambda} \int_{-c}^{+c} \left(\frac{\partial T}{\partial z}\right)_{z=0} dy = \frac{h_r \Delta T}{\lambda} \tag{12}$$

which states that the increase in water flow down the rivulet must result from the vapor condensed which is equal to the net heat transfer divided by the latent heat of evaporation, λ.

Solution of equations (1)–(11) has been carried out for various values of θ and δ/c by expressing the equations in finite-difference form and solving them by an "over-relaxation" method. The curved boundary and the type of boundary conditions imposed introduce certain computational difficulties which are discussed in reference [6]. The entire field of points established by a uniform grid is subject to an iteration technique in which values of the temperature are adjusted point by point and the entire area is repeatedly swept through until no further changes occur and the temperatures have relaxed to the proper and final values. At the boundary the computer is instructed to recompute the normal derivatives as it passes from one region to the other. Results have been obtained as plots of isotherms, and for each case the integral of the heat flux is obtained on the boundaries.

An evaluation of the precision of the results is difficult because the closed-form solutions are not available. Estimates of the converged solutions using 300, 400, and 500 iterations indicated accuracy much better than required for engineering analysis. Furthermore, graphical comparisons of exact and computer solutions for similar boundary-value problems were made in reference [4] with very good accuracy.

For cases in which the rivulet is very shallow and the underlying metal very thin, it is probable that a simple theory assuming negligible lateral heat flux would suffice. For this we assume one-dimensional heat flow at each x-wise position on the rivulet so that the local heat transfer is governed by the sum of three resistances: interfacial, liquid, and metal. At any station then the local heat-transfer coefficient can be expressed as

$$h_r'(y) = \frac{1}{\frac{1}{h_i} + \frac{t(y)}{k_l} + \frac{\delta}{k_m}} \tag{13}$$

t is the rivulet thickness, δ the metal thickness, k_l and k_m the liquid and metal conductivity, respectively, and h_i the interfacial heat-transfer coefficient. Values of h_i are plotted in Fig. 1.

The rivulet thickness, t, can be approximated for slender rivulets by

$$t = \frac{\theta c}{2}\left[1 - (y/c)^2\right] \tag{14}$$

Equation (13) may now be integrated to obtain the mean heat-transfer coefficient for the rivulet.

$$h_r = \frac{1}{c}\int_0^c h_r'(y)dy = \frac{2k_l}{c\theta\sqrt{1+M}} \operatorname{ctnh}^{-1}\sqrt{1+M} \tag{15}$$

where

$$M = \frac{2k_l}{c\theta}\left[\frac{1}{h_i} + \frac{\delta}{k_m}\right] \tag{16}$$

and is simply the ratio of heat-transfer coefficient in the water at maximum rivulet thickness to the combined heat-transfer coefficient due to interfacial and metallic resistance. The mean volume of flow per unit rivulet width, Γ_r, may be calculated using the theory of laminar flow as

$$\Gamma_r = \frac{\rho g}{3\nu c}\int_0^c t(y)^3 dy = \frac{2\rho g \theta^3 c^3}{105\,\nu} \tag{17}$$

An exact solution for Γ_r may also be obtained from the numerical solution of equation (1) as

$$\Gamma_r = \frac{1}{2c}\iint_A \rho u dA \tag{18}$$

where A is the rivulet cross-sectional area. Comparison of numerical values of Γ_r from equations (17) and (18) for various values of θ is shown in Table 1. The agreement in the values up to θ equal to 45 deg is quite acceptable and hence warrants the use of approximate formulation, especially for small values of θ.

Table 1 Values of $\Gamma' = \dfrac{\Gamma_r}{(\rho^2 c^3 g/\mu)}$

θ deg	Γ' equation (17)	Γ' equation (18)	percent difference
15	0.000338	0.000336	−0.59
30	0.002740	0.002720	−0.73
45	0.009175	0.010750	+14.7
60	0.021900	0.030500	+28.3
75	0.042600	0.076500	
90	0.074400	0.183	

To obtain an equivalent liquid flux in a flat film (Nusselt flow)

the film would require a thickness t_N obtained by equating Γ_r to the flat film flow or

$$\frac{2\rho g\theta^3 c^3}{105\,\nu} = \frac{\rho g t_N^3}{3\,\nu} \tag{19}$$

from which

$$t_N = 0.77(\theta c/2) \tag{20}$$

The corresponding heat-transfer coefficient would be

$$h_n = \frac{1}{\frac{1}{h_i} + \frac{\delta}{k_m} + \frac{t_N}{k_l}} \tag{21}$$

and substituting equation (20) in (21)

$$h_n = \frac{2k_l}{\theta c(0.77 + M)} \tag{22}$$

Forming now the ratio of rivulet heat-transfer coefficient to flat film of equivalent water flux we obtain

$$\frac{h_r}{h_n} = \frac{(0.77 + M)}{\sqrt{1 + M}} \operatorname{ctnh}^{-1}\sqrt{1 + M} \tag{23}$$

Equation (23) permits comparison of rivulet and flat film heat transfer at a local point; however, for comparison with a complete condensing system, it is necessary to perform an integration taking into account the variation in θ with vertical distance, x. Differentiating equation (17) and substituting the result in equation (12) yields

$$\frac{d\Gamma_r}{dx} = \frac{6\rho g c^3\theta^2}{105\,\nu}\frac{d\theta}{dx} = \frac{h_r \Delta T}{\lambda} \tag{24}$$

and rearranging and integrating both sides

$$\frac{105\,\nu\Delta TL}{6\lambda c^3\rho g} = \int_0^{\theta_{\max}} \frac{d\theta}{h_r(c,\,\theta,\,\delta/c,\,R_l/R_m)} \tag{25}$$

The value of $\theta_{\max}$ is obtained in terms of Γ from equation (17), and values of h_r may be taken from equation (15) or from the more exact numerical calculations. The final heat-transfer coefficient becomes a function of the fluid flow variables viscosity, density, and conductivity which are mainly temperature dependent, the metallic thickness and conductivity, the stripe spacing, and the total mass flow rate per unit breadth, Γ. Writing the relation between the mean overall heat-transfer coefficient and Γ, there is obtained

$$h_m = \frac{\Gamma\lambda}{\Delta TL} \tag{26}$$

Solving for $\Delta TL/\lambda$ and substituting in equation (25) gives finally

$$h_m = \frac{105\,\nu\Gamma}{6\rho g c^3 \int_0^{\theta_{\max}} \frac{d\theta}{h_r(c,\,\theta,\,\delta/c,\,k_l/k_m)}} \tag{27}$$

Solutions were obtained by numerical integration of equation (27), making use of values of h_r obtained from the numerical solutions as well as those from equation (15) for the one-dimensional theory case.

Results of the Analysis

Temperature fields for several illustrative cases are given in Figs. 5–7. It can be seen that there is a large lateral heat flow in the metal, especially near the rivulet edge; for the thinner metal plates the effect is largely confined to this region.

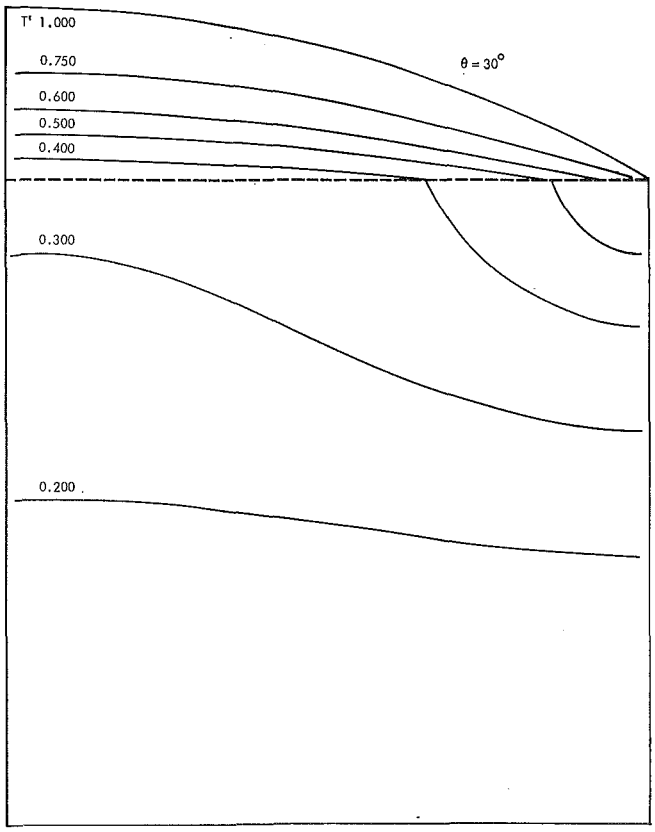

Fig. 5 Isotherms for titanium with $\delta/c = 1$

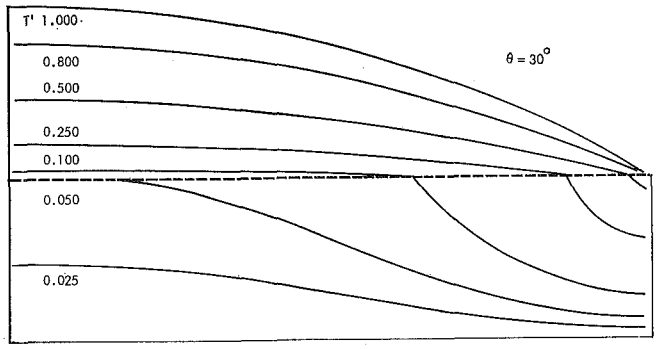

Fig. 6 Isotherms for titanium with $\delta/c = 0.25$

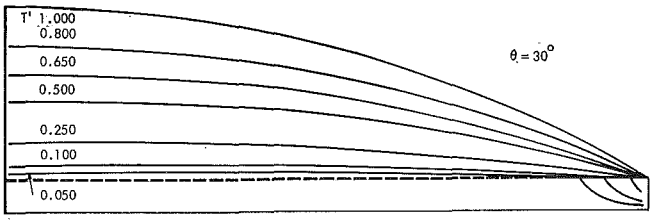

Fig. 7 Isotherms for titanium with $\delta/c = 0.05$

Lines of heat flow are normal to the isotherms, and it can be inferred from the figures that near the rivulet corner the heat flow is approximately radial. The differences between the CuNi and titanium metal plates is not especially noticeable except for temperature level; however, it should be remembered that larger thicknesses are to be associated with CuNi in practical applications because of corrosion and strength considerations.

Temperature profiles along the metal-liquid interface are presented in Figs. 8 and 9. The effect of lateral heat flow in the metal appears to have the effect of raising the interfacial temperatures, especially away from the rivulet edge. Agreement between the one-dimensional theory and the more exact numerical solutions is good for only the thin metal cases.

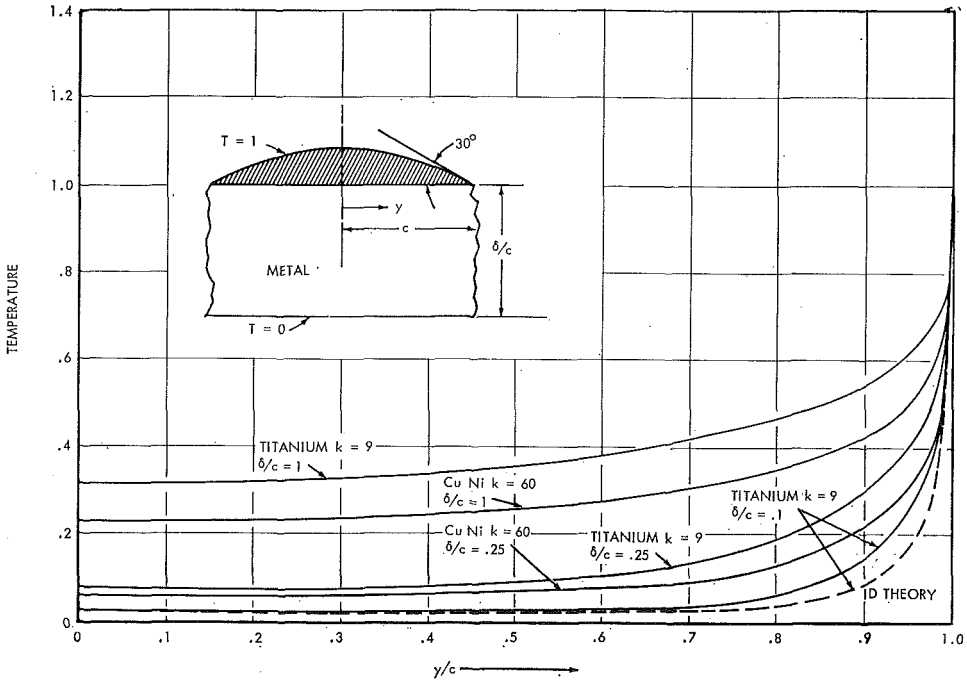

Fig. 8 Temperature distribution along metal-liquid interface

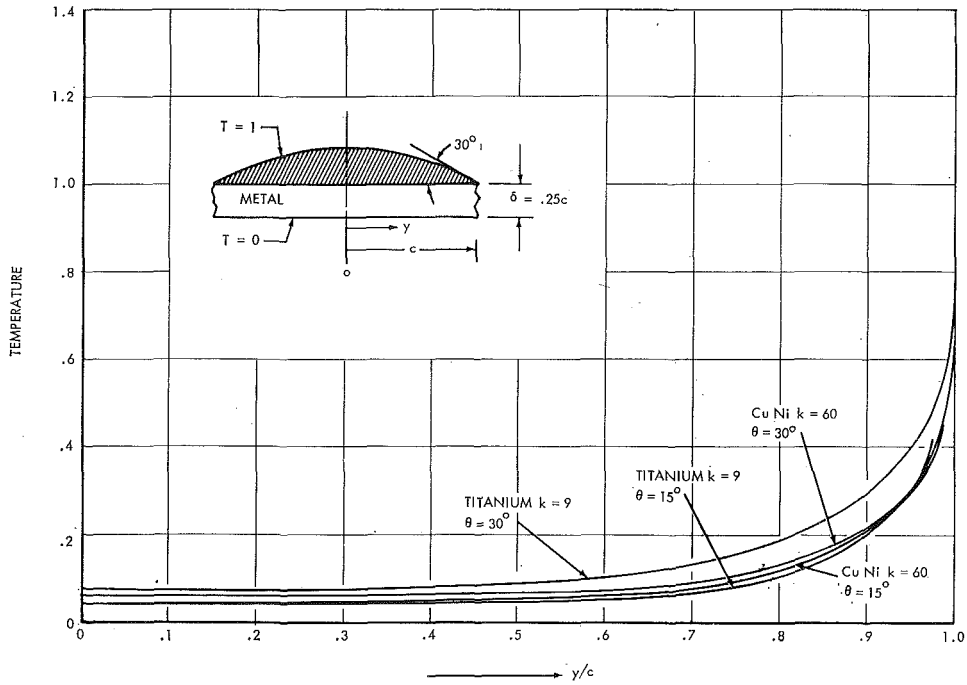

Fig. 9 Temperature distribution on metal-liquid interface

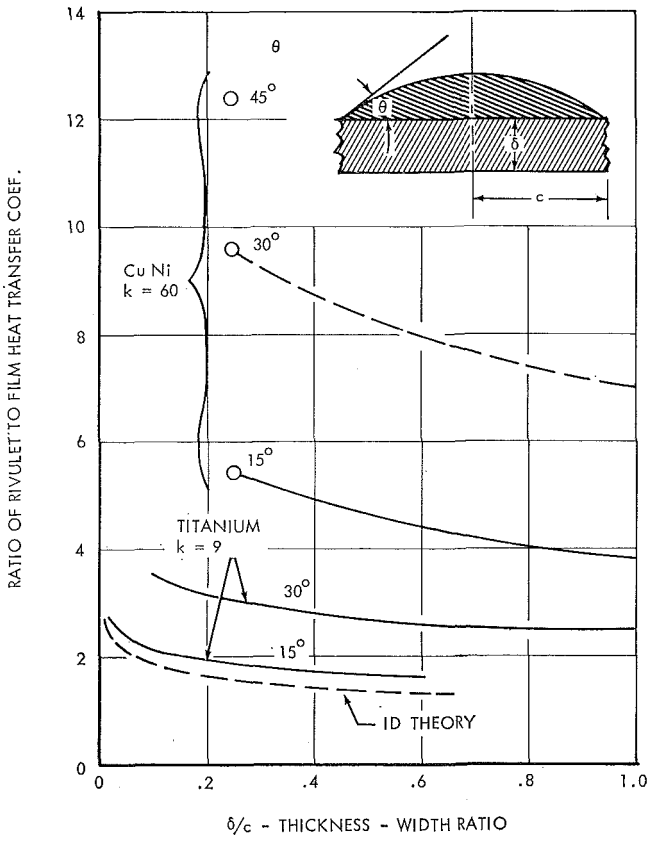

Fig. 10 Heat flux ratios

Plotted in Fig. 10 are the ratios of mean heat-transfer coefficient for the rivulet to that of a flat falling film carrying the same downward water flux as the rivulet. For the slender rivulet with edge angle of 15 deg the computer result is somewhat higher than the one-dimensional theory, and for the larger-angle rivulets the simple theory grossly underestimates the ratio; the value computed for CuNi, δ/c of 0.25, and θ of 15 deg is shown in the figure as 5.41, whereas the simple theory for this case is only 2.2. The comparisons shown illustrate the effects of interest but for practical applications the mean heat-transfer coefficient from top to bottom of the condensing rivulet system is more meaningful. The calculated mean heat-transfer coefficients for a vertical plate or tube 20 ft high are plotted in Figs. 11 and 12 as a function of mean surface heat flux. Thicknesses of practical interest are used, and it is seen that the metal conductivity plays an important role in setting the level of the mean heat-transfer coefficient. Note that even though the local metal heat-transfer coefficient for the CuNi is 24,000 compared with 36,000 for the titanium foil, the CuNi surface permits more than a two-fold increase in the condensative heat-transfer coefficient!

The results of Figs. 11 and 12 may be applied to shorter columns if it is remembered that the coefficients depend on Γ, the flow rate per unit breadth; thus the value of 10,000 Btu/hr·ft² on the 20-ft length would provide the same coefficients on a 10-ft length with a heat flux of 20,000 Btu/hr·ft².

Concluding Remarks

The analysis of constrained rivulet flow with condensing conditions has demonstrated the improved heat-transfer efficiency of triple-point systems in general. The intersection of metal, liquid, and condensing vapor provides a point at which very high local

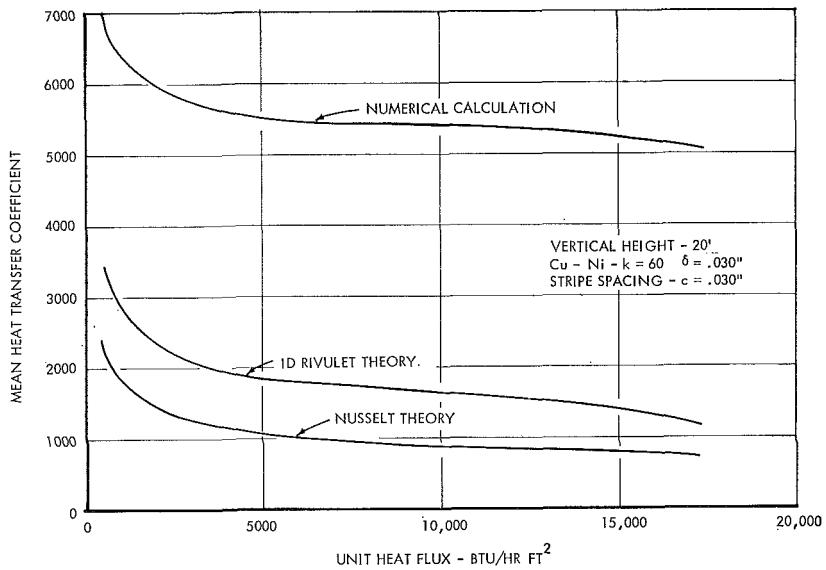

Fig. 11 Effect of finite metal conductivity on condensing heat transfer

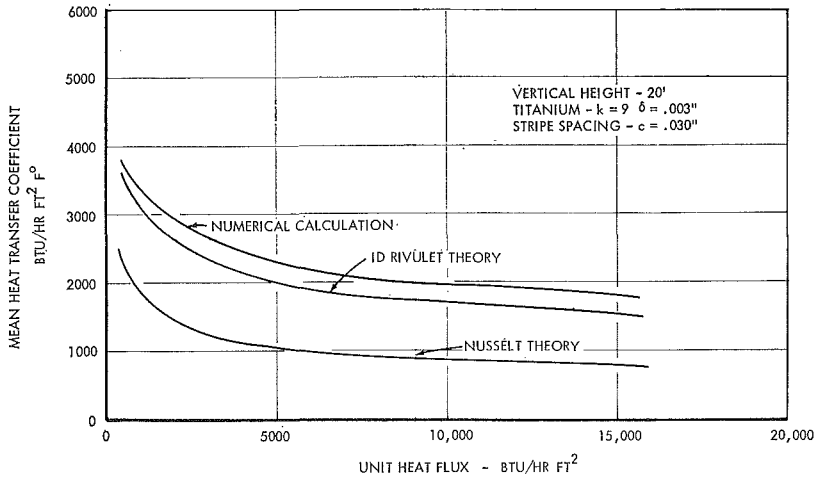

Fig. 12 Effect of finite metal conductivity on condensing heat transfer

heat flux can occur, limited only by finite metal conductivity or interfacial resistance. It has been shown that the high-conductivity metals provide improved lateral flow of heat under the triple point and therefore yield substantial increases in overall heat-transfer coefficients. The scale of the rivulet system is of importance, and the analysis brings out the desirability of very fine spacings.

References

1 Nusselt, W., *Z. Ver deut. Ing.*, Vol. 60, 1916, pp. 541–569.

2 Umur, A., and Griffith, P., "Mechanism of Dropwise Condensation," JOURNAL OF HEAT TRANSFER, TRANS. ASME, Series C, Vol. 87, No. 2, May 1965, pp. 275–282.

3 Baer, E., and McKelvey, J., "Heat Transfer in Film Condensation," *AIChE Journal*, Vol. 4, No. 2, June 1958, pp. 218–222.

4 Hickman, K., "Reviewing the Evaporation Coefficient," *Desalination*, Vol. 1, No. 1, April 1966.

5 Matin, S. A., "Numerical Iteration of an Elliptic Mixed Boundary-Value Problem in a Region with a Curved Boundary," *Journal of Comp. Physics*, Vol. 3, No. 2, Oct. 1968.

6 Matin, S. A., "Numerical Iteration of Simultaneous Semi-Linear Elliptic Partial Differential Equations Over a Non-rectangular Region," *The Punjab University Journal of Mathematics*, Lahore, Pakistan (Submitted July 1969).

NAM P. SUH
Associate Professor,
Department of Mechanical Engineering,
Massachusetts Institute of Technology,
Cambridge, Mass.

C. L. TSAI
Research Assistant,
Carnegie-Mellon University,
Pittsburgh, Pa.

Thermocouple Response Characteristics in Deflagrating Low-Conductivity Materials[1]

The transient thermocouple response characteristics in deflagrating low-conductivity materials with high temperature gradients were investigated theoretically and experimentally. The theoretical model considers the thermocouple bead and lead wires separately, and the two resulting partial differential equations are solved simultaneously by a finite difference technique. The experimental results are obtained by embedding various size thermocouple wires in double-base solid propellants and consequently measuring the temperature profiles and the surface temperatures. The theoretical model is used to predict the experimentally measured temperatures. There is good agreement. The experimentally measured values are smaller than the correct surface temperature, corresponding to the model prediction for zero wire diameter, by at least 20 percent even when 1/2-mil thermocouple wire is used. Both the experimental and theoretical results show a plateau when the thermocouple bead emerges from the solid into the gas phase. The theoretical results also show that there is an optimum ratio of the thermocouple bead diameter to the wire diameter, which is found to be close to three

Introduction

The temperature distribution and the surface temperature of deflagrating insulators and ablating materials are important parameters in the experimental and theoretical investigation of deflagration and ablation phenomena. Without the precise knowledge of these parameters it is difficult to evaluate the validity of mathematical models that are purported to represent the physical phenomena. However, the correct measurement of these parameters is difficult because of the extremely large temperature gradient existing in the insulator and because of the extremely rapid rate of surface deflagration and ablation.

Two types of measurement techniques have been attempted in the past: thermocouples [1, 2][2] and optical sensing of the surface radiation [3]. Although the optical technique seemed to show promise as a surface temperature measuring technique, it was found that in the case of deflagrating solids the high-temperature gas generated at the surface interferes with the surface temperature measurement [4]. Although the thermocouple technique is the most widely used, it presents many difficulties due to the complex response characteristics and lead losses, especially in deflagrating insulators with high temperature gradients. While many papers deal with the thermocouple response characteristics and lead loss, all of them deal with the case in which the size of the thermocouple bead is very small relative to the temperature gradient in the insulator.

However, in a typical temperature measurement of a double-base solid propellant burning at low pressure, the temperature difference across the thermocouple bead is of the order of 70 deg–100 deg C, even when the thermocouple wire is only 1/2 mil in diameter. Beck [5], Nydick [6], Beck and Hurwicz [7], and Johnson, Osterle, and Weinstein [8] considered the problem theoretically, but in all these cases the temperature gradient assumed was such that the temperature difference across the thermocouple bead was neglected. Furthermore, their results were not checked against experimental results.

This paper presents the theoretical and experimental results of the thermocouple response and lead loss in an insulating material with a high temperature gradient. The theoretical model consists of a model for heat transfer around the thermocouple bead and another for the leads. The resulting partial differential equations are numerically solved simultaneously. The experiments were performed by embedding various size thermocouple wires in solid propellants and measuring the temperature profile as the propellant deflagrated. The emergence of the thermocouple through the deflagrating surface was checked by high-speed photography. The measured thermocouple bead temperatures were compared with the theoretically predicted values based on an assumed surface temperature; they were in good agreement. The agreement established confidence in the theoretical surface temperature prediction for the zero wire diameter case. This value corresponds to the assumed surface temperature in the analysis.

This paper shows that the thermocouple bead as well as the lead wires should be considered in a mathematical model for better accuracy, that the emergence of the thermocouple bead from the solid introduces a plateau on the experimentally measured

[1] This work was supported by Picatinny Arsenal through the Army Research Office, Durham, Grant DA-ARO-D-31-124-61029.

[2] Numbers in brackets designate References at end of paper.

Contributed by the Heat Transfer Division and presented at the Fluids Engineering, Heat Transfer, and Lubrication Conference, Detroit, Mich., May 24–27, 1970, of The American Society of Mechanical Engineers. Manuscript received by the Heat Transfer Division, April 28, 1969; revised manuscript received, December 29, 1969. Paper No. 70-HT-7.

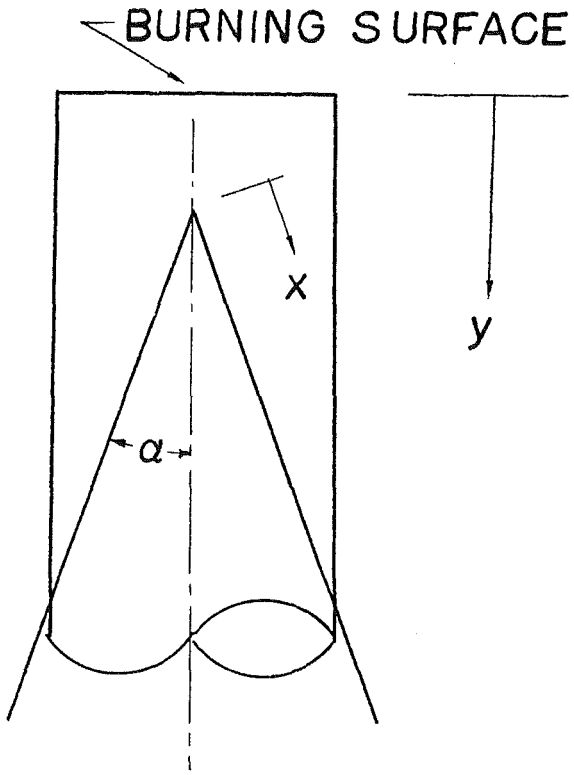

Fig. 1 Schematic representation of the problem

temperature profile, and that thermocouples can be used to measure the temperature profile and the surface temperature if corrections are made for the thermocouple response characteristics. It is also shown that there is an optimum ratio of the bead diameter to wire diameter which gives the best thermocouple response characteristics.

Description of the Problem and Assumptions

The problem is shown in Fig. 1. The thermocouple wire is embedded in a deflagrating insulator with its bead at the center. The lead wires form a V-shape and are straight. The coordinate axis is chosen such that the y-axis is along the axis of the insulator and moves with the burning surface. The burning rate is constant. The burning surface is always perpendicular to the y-axis and is planar. As the insulator deflagrates, the moving surface eventually reaches the thermocouple.

It will be assumed that the temperature in the insulator is one-dimensional, being only a function of y, and that the material properties are constant. The heat transfer coefficient is assumed to remain constant and the radiant heat transfer to the insulator is assumed to be negligible. It will be further assumed that there is no chemical reaction between the thermocouple wire and the insulator.

Any solid-phase reaction in the insulator is neglected. The surface temperature of the insulator is assumed to remain constant, which is the case for steady-state deflagration. The length of the insulator is assumed to be semi-infinite. Under these assumptions the temperature distribution in the insulator can be easily shown to be

$$T_p = T_o + (T_s - T_o) \exp(-\rho cry/k) \tag{1}$$

where T_p is the temperature at any point in the insulator; T_s is the surface temperature; T_o is the initial temperature of the insulator; r is the burning rate; and c, k, and ρ are the specific heat, the thermal conductivity, and the density of the insulator, respectively. It should be noted that the temperature profile is a sensitive function of the burning rate.

Although equation (1) indicates that the temperature gradient of the insulator is so high that there can be a large temperature difference across the thermocouple bead, it will be assumed that the thermocouple bead is at a uniform temperature because of the high thermal diffusivity of the thermocouple material relative to that of the insulator. The actual physical shape of the thermocouple bead is almost spherical, and, therefore, it will be assumed to be a perfect sphere as shown in Fig. 2.

Thermocouples embedded in an insulator disturb the local temperature of the solid. The degree of disturbance is reflected by a heat transfer coefficient which defines the thickness of the disturbed region. In the absence of any other model for the heat transfer coefficient in solids, the expression derived by Nydick [6], which is an extension of the work done by Beck [9], is used without any modification to estimate the heat transfer coefficient in the propellant.

Analysis of Thermocouple Response Characteristics

Under the assumptions made in the preceding section, the energy equation for the bead at a uniform temperature in a rapidly changing temperature field may be written as

$$\rho_w V_B C_w \frac{\partial T_B}{\partial t} = h \int_{A_{y1}}^{A_{y2}} (T - T_B) dA_B - Q_{\text{lead}} \tag{2}$$

where ρ_w and C_w are the density and specific heat of the thermocouple wire, respectively; V_B is the volume of the thermocouple bead; T_B is the bead temperature; A_B is the surface area of the thermocouple bead; h is the heat transfer coefficient between the surrounding and the bead; and Q_{lead} is the heat loss through the thermocouple leads. It should be noted that $T = T_p$ in the insulator. y_1 and y_2 designate the front and rear ends of the thermocouple bead. The physical properties of the bead are assumed to be the same as those of the thermocouple wires since in the experiment platinum–platinum-10-percent-rhodium thermocouples were used.

The initial condition for the thermocouple bead is

$$T_B = T_o \quad \text{at} \quad t = 0 \quad \text{and} \quad y \to \infty \tag{3}$$

The governing equation for the thermocouple lead wires is

$$\frac{\partial^2 T_w}{\partial x^2} + \frac{hP}{k_w A}(T_p - T_w) = \frac{\rho_w C_w}{k_w} \frac{\partial T_w}{\partial t} \tag{4}$$

where T_w is the temperature in the wire; k_w is the thermal conductivity of the wire; x is measured along the axis of the wire; $x = 0$, corresponding to the center of the thermocouple bead; P is wire circumference; and A is the cross-sectional area of the wire. The boundary conditions are:

$$\begin{aligned} T_w &= T_B \quad \text{at} \quad x = 0 \\ T_w &= T_o \quad \text{at} \quad x \to \infty \end{aligned} \tag{5}$$

The initial condition is

$$T_w = T_o \quad \text{for all } x \text{ at } t = 0 \tag{6}$$

The initial condition (6) is valid when the initial condition for the thermocouple bead (3) is valid.

The heat transfer coefficient between insulators and V-shaped thermocouple leads was derived by Nydick [6] for the steady-state case as

$$h = \frac{2k/R}{3 \ln (2L/R)} + \frac{\beta k}{2}(1 + e^{-\beta L \cos \alpha}) \tag{7}$$

where R is the radius of the thermocouple wire; L is the length of the thermocouple wire embedded in the insulator; α is the angle the lead wire makes with the axis of the insulator; and β is $\rho cr/k$ given in equation (1). Equation (7) is based on the assumption that the temperature gradient at the thermocouple–insulator inter-

face may be approximated by the average of temperature gradients in the wire and in the insulator [9]. Although the heat transfer coefficient is strictly true for the steady-state case, it may be a reasonable estimate even for the transient case since the position of the thermocouple is fixed with respect to the propellant in all cases. Furthermore, as the computation results will later show, 100 percent error in estimating the heat transfer coefficient does not affect the results too significantly. The value given by equation (7) is assumed to be valid around the bead in the absence of any better number to use.

Equation (2) may be rewritten as

$$\rho V_B C \frac{\partial T_B}{\partial t} = \pi Dh \int_{y_1}^{y_2} (T_p - T_B)\, dy + 2k_w A_w \frac{\partial T_w}{\partial x}_{x=0} \tag{8}$$

In equation (8), the small difference in the conductivity of platinum–platinum-10-percent-rhodium thermocouple wires is neglected. It should be noted that the integral in equation (8) takes into account the area change at different y-values along the sphere.

Numerical Solutions

Equations (4) and (8) may be written in a finite difference form as:

$$\frac{\theta_{wi+1,j} - 2\theta_{wi,j} + \theta_{wi-1,j}}{(\Delta\bar{x})^2} + C_1(\theta_{pi,j} - \theta_{wi,j}) = \frac{\theta_{wi,j+1} - \theta_{wi,j}}{\Delta\bar{t}} \tag{9}$$

$$C_3 \frac{\theta_{Bj+1} - \theta_{Bj}}{\Delta\bar{t}} = C_4 \sum_{n=1}^{m} (\theta_{pn,j} - \theta_{Bj})\Delta\bar{y}_n + 2\,\frac{\theta_{w2,j} - \theta_{w1,j}}{\Delta\bar{x}} \tag{10}$$

where i and j identifies the location in the $\bar{x} - \bar{t}$ space. The unknowns are $\theta_{wi,j+1}$ and θ_{Bj+1}. The dimensionless parameters are defined as:

$$\bar{x} = \frac{x}{L};\quad \bar{t} = \frac{tk_w}{\rho_w C_w L^2};\quad C_1 = \frac{hP}{k_w A} L^2$$

$$\bar{y} = \frac{y}{L};\quad C_3 = \frac{V_B}{AL};\quad C_4 = \frac{\pi Dh\, L^2}{k_w A} \tag{11}$$

$$\theta = \frac{T_w - T_o}{T_s - T_o};\quad \theta_p = \frac{T_p - T_o}{T_s - T_o};\quad \theta_B = \frac{T_B - T_o}{T_s - T_o}$$

The initial and boundary conditions for equation (9) may also be written as

$$\begin{aligned} \theta_w &= 0 \quad \text{at} \quad \bar{x} = 1 \\ \theta_w &= \theta \quad \text{at} \quad \bar{x} = 0 \\ \theta_w &= 0 \quad \text{at} \quad \bar{t} = 0 \end{aligned} \tag{12}$$

Similarly, for equation (10) the initial condition becomes

$$\theta_B = 0 \quad \text{at} \quad \bar{t} = 0 \tag{13}$$

The computation was done by an iteration method of first evaluating θ_{Bj+1} and then θ_w's, using equations (10) and (9), respectively. The iteration procedure was repeated until the successively calculated values of θ_B were within 0.01 percent. Then the time increment was increased by one step. The initial position of the thermocouple was taken to be where the propellant temperature was one degree higher than the initial temperature of the thermocouple bead.

As the thermocouple bead started emerging from the solid surface, the heat transfer coefficient was assumed to be equal to the laminar gas flow case. Since the thermal conductivity of the gas is not very different from that of the insulator in the case of propellants, the temperature gradient in the gas was assumed to be 2 deg per micron. The temperature gradient in the solid at the surface was 3.5 deg per micron. The experimentally measured surface temperature was assumed to correspond to the theoretical bead temperature T_B when the rate of temperature change is minimum. This always occurs soon after the top of the thermocouple emerges from the surface. The identification of the correct bead temperature is simple since there is a sudden change in the temperature gradient at the surface.

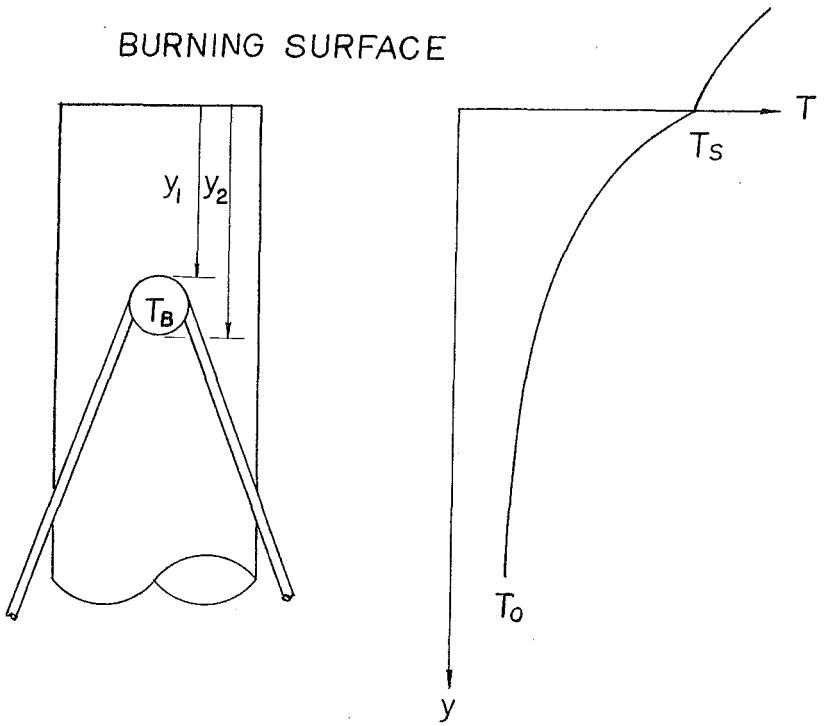

Fig. 2 Thermocouple configuration

The stability of equation (9) was determined by employing the von Neumann criterion [10]. The stability condition becomes

$$\frac{C_1 \cdot \Delta\bar{t}}{4} < M \leq \frac{2 + C_1 \cdot \Delta\bar{t}}{4} \tag{14}$$

where $M = \Delta\bar{t}/\Delta\bar{x}^2$. The criterion on the left defines the maximum $\Delta\bar{x}$. The criterion on the right defines the maximum $\Delta\bar{t}$ corresponding to $\Delta\bar{x}$. The actual values used in the computation were:

$$\Delta\bar{t} = 2.012 \times 10^{-5}; \quad \Delta\bar{x} = 1 \times 10^{-2}$$

Several values have been tried and equation (14) was found to be a reliable criterion. The convergence test was also made, and the mesh size used was shown to yield accurate results.

Numerical Results

Figs. 3, 4, and 5 present the numerical results which show the temperature profile as a function of the dimensionless parameter C_1 for a given value of the ratio $\frac{D}{d}$. It should be noted that as soon as the thermocouple emerges from the solid phase there exists a sharp change in the slope of the temperature profile. The degree of change depends on the assumed value of heat transfer coefficient in the gas phase. However, when the heat transfer coefficient in the gas was varied from 0.01 to 0.1 cal/cm² sec deg C, the temperature profiles were not significantly different.

The lowest curve in each figure was obtained using values which correspond to the experimental conditions employed in this paper. It should be noted that an increase in C_1 increases the response characteristics, i.e., it decreases error. The increase in C_1 can be accomplished by decreasing the thermocouple wire size and thermal conductivity, or by increasing the heat transfer coefficient. The error introduced by doubling the value of C_1 is not as significant as one might expect. Therefore a small error in estimating the heat transfer coefficient may be tolerated in determining the thermocouple response characteristics.

The thermocouple bead temperature profile is plotted as a function of the thermocouple wire diameter in Fig. 6. The bead temperature, which is taken to be the temperature of the bead at the instant the rate of temperature change is at a minimum, is a very sensitive function of the wire diameter. It should be noted that the minimum rate of temperature change occurs soon after the thermocouple emerges from the solid surface. The thermocouple bead temperature will lag more and more as the temperature gradient becomes steeper. This is the case as the deflagration rate increases or as the deflagrating surface temperature increases.

Fig. 7 shows the effect of the bead diameter on the temperature profile. One of the most interesting conclusions of the analysis is that there is an optimum ratio of the bead diameter to the lead wire diameter. It should be emphasized that this analysis assumes the existence of a spherical bead. When the bead size is increased from three times the wire diameter to four and five times the wire diameter, the error in the temperature measurements increases with the bead size. On the other hand, when it is decreased to twice the wire diameter, again the response decreases. This is an important result since there are many papers which claim that their temperature measurements are accurate because of the small bead size used in the experiments. The main reason for the existence of the optimum ratio of the bead diameter to the wire diameter under the assumptions employed here is that the temperature rise in the bead is proportional to the cube of the bead diameter, whereas the heat transfer rates to the bead and the lead wire are directly proportional to the square of radius. It should be noted that for the best response the wire diameter should be as small as possible, maintaining the optimum ratio of the bead diameter to the wire diameter. However, the response characteristics of a thermocouple are more sensitive to changes in the wire diameter than to changes in the bead diameter. Therefore a thermocouple with a higher response may be obtained for a smaller wire diameter away from the optimum ratio than for a larger wire diameter at the optimum ratio.

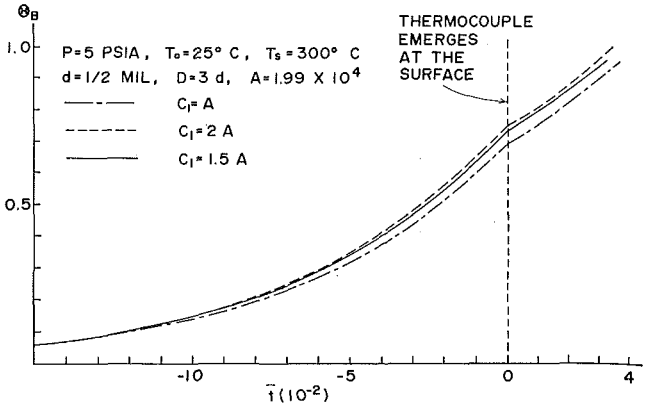

Fig. 3 Temperature profile for various values of C_1 for $D/d = 3$, $d = 1/2$ mil

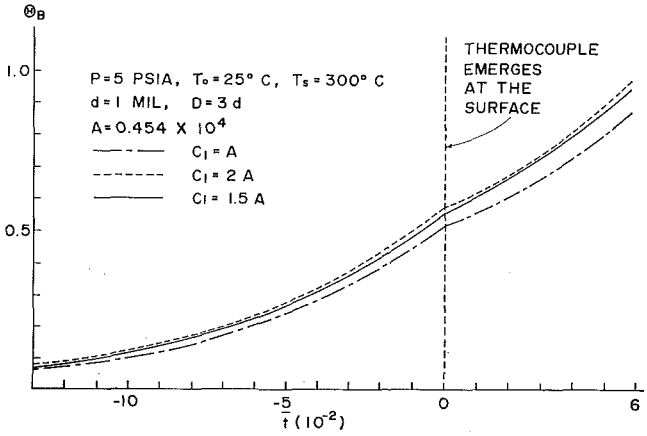

Fig. 4 Temperature profile for various values of C_1 for $D/d = 3$, $d = 1$ mil

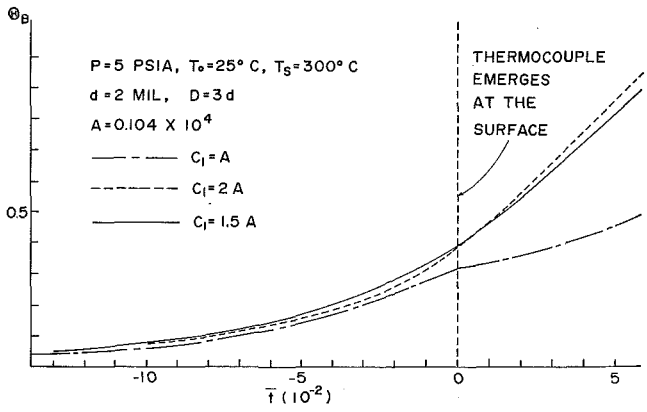

Fig. 5 Temperature profile for various values of C_1 for $D/d = 3$, $d = 2$ mil

Fig. 8 shows the heat loss through the thermocouple leads as a function of the wire size. The heat loss increases with the wire diameter but not directly proportional to the radius squared. In fact it is less than linearly proportional to the radius. Although it is not plotted, the heat loss is also affected by the bead size, but

only slightly. Most of the changes in the heat loss due to the thermocouple bead size variation is on account of the temperature gradient change.

Experimental Arrangement and Procedure

The insulator used in the experiments was a double-base solid propellant. Its physical properties are given in Table 1. It

Table 1 Physical properties of the insulator used

Solid density	= 1.50 − 1.64 gm/cm³
Ratio of specific heats	= 1.191
Thermal conductivity	= $5.0 \times 10^{-4} - 5.5 \times 10^{-4}$ cal/sec cm deg C
Specific heat C_p	= 0.37 cal/gm deg K
Diameter of strand	= 0.175 in.

should be noted that two values of density and thermal conductivity are given since typical physical properties fall between these values. The cylindrical strands of approximately 0.175-in. diameter were cut into pieces 2.5 in. long; then one half of each strand was milled away. A thermocouple was then embedded in one half, and a similar piece was bonded to the other half using acetone. They were then dried in a guide which was clamped in a vise. After drying, the cylinders were coated with a flame inhibitor to insure planar burning. The fuse wires (Indalloy 0.010 in. in dia) were placed a fixed distance apart by drilling small holes perpendicular to the axis of the insulator.

The diameters of the thermocouple wires were 1/2, 1, 2, and 3

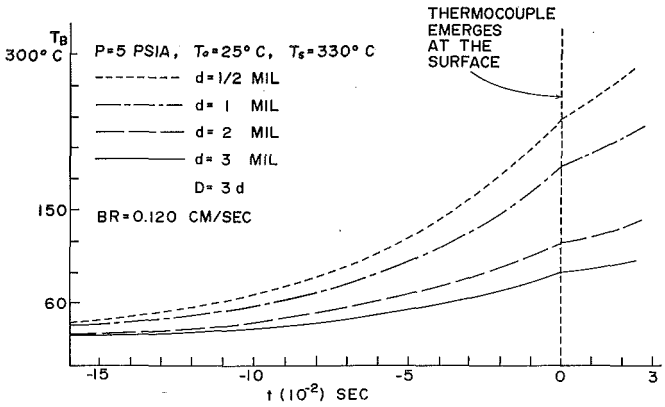

Fig. 6 Temperature profile as a function of wire diameter

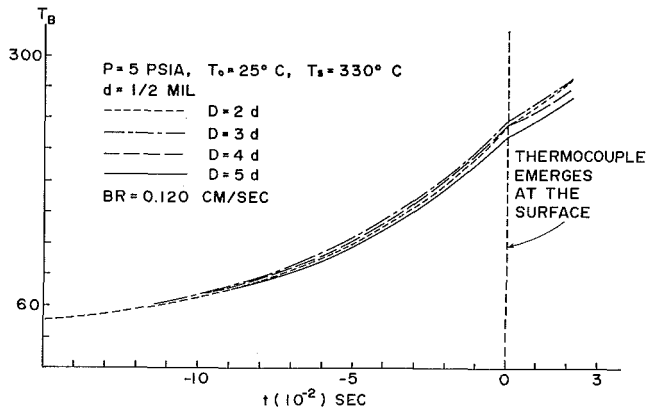

Fig. 7 Temperature profile as a function of bead diameter

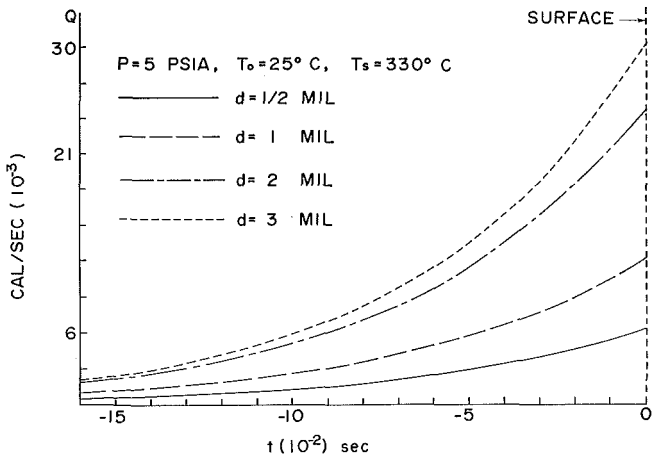

Fig. 8 Heat loss through the thermocouple leads as a function of time and wire diameter

mils. The thermocouples were platinum and platinum with 10 percent rhodium (purchased from Omega Engineering, Inc.). The diameter of the bead was close to three times the diameter of the thermocouple wire. The thermocouple was embedded for continuous contact between the thermocouple and the propellant. The angle between the two lead wires was 40 deg, i.e., $\alpha = 20$ deg. In order to obtain reproducible results, a die block with grooves was used in locating the thermocouples.

The schematic arrangement of the stainless steel combustion chamber is shown in Fig. 9. The propellant was placed vertically in the chamber and ignited at the lower end with an ignitor of resistance-heated platinum wire. The chamber was connected to a large pressure reservoir to insure that the pressure in the chamber did not change significantly. The thermocouple leads and the fuse wires were connected through the walls of the chamber so that the burning rate and temperature could be recorded. A quartz window was placed at one end of the chamber so that the burning process could be observed. It was found that the orientation of the propellant had no appreciable effect either on the burning rate or on the temperature profile. The experiments were run in argon.

The thermocouple output was amplified and measured by a Honeywell Visicorder (fluid-damped M 1650 galvanometer). The Visicorder paper speed was 80 in./sec. The time resolution

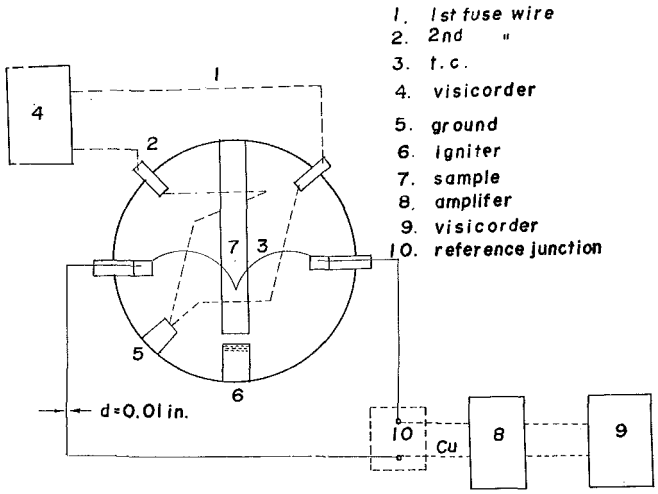

Fig. 9 Schematic representation of the combustion chamber

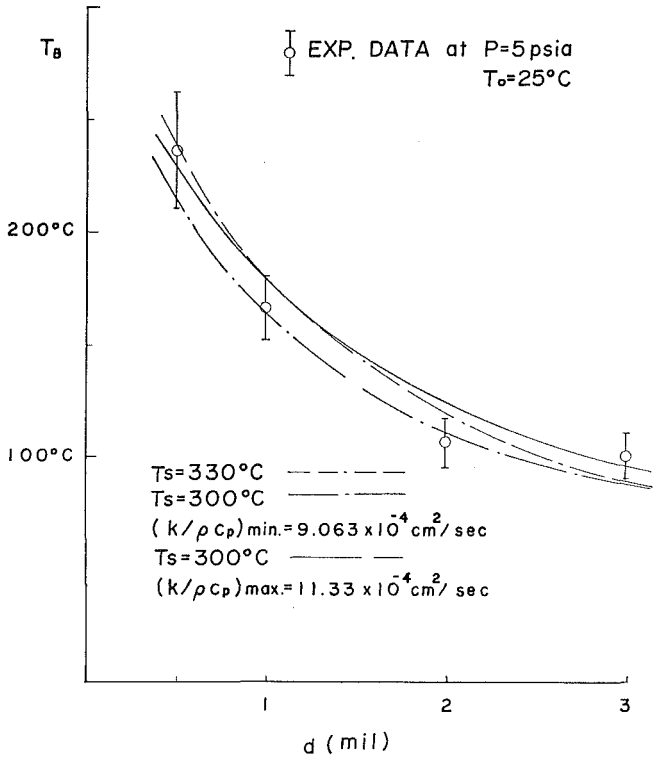

Fig. 10 Theoretically predicted and experimentally obtained surface temperature

was 0.001 sec. Because of the good time resolution available, the details of the profile could be examined and the interesting changes in the profile previously unavailable were noted.

In order to determine the time of the thermocouple emergence from the solid propellant, a high-speed camera (Fastax 16 mm WF-14)—500 to 600 frames per sec—was focused on the thermocouple bead location and synchronized with the thermocouple output by feeding timing pulses on to the film and the Visicorder paper simultaneously. The corresponding temperature and time could consequently be identified later.

Experimental Results

Experimental results showing the temperature profile as a function of time are shown in Fig. 11 for $^1/_2$-mil thermocouple wires. All of the experimental results are shown to illustrate the variation in the experimental measurements. The existence of the plateau should be noted. The plateau length increases with the thermocouple bead size. The temperature curves are reproducible up to the plateau and many of them are superimposable. After the plateau, the curves are not always reproducible, although they are usually similar.

By comparing the high-speed photographic record with the Visicorder record, it was found that the appearance of the thermocouple bead is associated with the existence of the plateau. As shown by the theoretical results, the plateau is caused by the decrease in the heat input to the thermocouple bead when it emerges from the solid phase. This is believed to be due to a low heat transfer coefficient in the gas phase very near the solid surface. Therefore, after the thermocouple bead is partially in the gas phase, the heat loss through the leads is nearly equal to the heat input to the bead. However, once the bead is completely in the gas phase, because of the low temperature gradient in the gas, the lead loss again becomes small relative to the heat input.

The temperature of the thermocouple bead at the surface, as indicated by the plateau, is given in Table 3. The values given in the table are the average of many experimental results as indicated. The standard deviation is also given. The large variations between the experimentally determined temperature profiles shown in Fig. 11 are related to the variations in the thermocouple lead wire size and the bead size. In all cases the temperature is higher when the lead diameter is smaller, especially away from the surface. Although the manufacturer stated that the diameter of the thermocouple wire is 1 mil in one case, careful measurements (see Table 2) indicate that the wire size varies considerably. The bead size also varies significantly, as indicated in the table. The slope of the temperature profile near the burning surface also increases with decrease in the wire diameter. This reemphasizes the fact that the heat loss through the thermocouple leads, which is affected by both the bead size and the wire diameter, is one of the prime controlling factors in the thermocouple response.

Comparison of Theoretical Results With the Experimental Results

The experimentally determined apparent surface temperatures are compared with the theoretically predicted apparent surface temperatures, i.e., the bead temperatures, for various cases in Table 3 and Fig. 10. In view of the fact that the validity of the expression for heat transfer coefficient has not been thoroughly checked heretofore, the prediction of the bead temperature made by analysis is quite good. This may be due to the fact that a small error in the heat transfer coefficient does not affect the results too significantly. The physical properties of propellant samples from the batch vary because of the manufacturing technique. Therefore the theoretical curves are drawn for the maximum and the minimum values of thermal diffusivity provided by the manufacturer. It should be noted that both of them lie within the scatter of the experimental data. Based on the analysis it may be stated that the surface temperature of the propellant is between 300 and 330 deg C.

Table 2 Thermocouple wire size variation*

No.	Wire size d (mil)	Bead size D (mil)	Ratio D/d
111	0.8	2.4	3
115	0.9	2.4	2.93
116	0.95	2.45	2.58
117	0.875	2.45	2.8
118	0.875	2.51	3.0
119	0.8	2.45	3.06
120	1.0	2.8	2.8
141	0.875	2.7	3.09
142	0.8	2.4	3.0

* Nominal diameter 1 mil

Since the heat transfer coefficients in the gas phase were chosen arbitrarily within a reasonable range, several values have been tried, as stated in an earlier section. As shown in Table 3 for the 5-psia cases, this does not affect the experimental results significantly when the thermocouple bead size is small because of the relatively high heat transfer coefficient in the solid compared with that in the gas. The effect, however, becomes quite significant for larger bead sizes, although a further decrease in the coefficient below the values indicated in Table 3 has little effect.

The theoretically predicted temperature profiles of the thermocouple bead, corresponding to the minimum value of thermal diffusivity at T_s = 300 deg C, are plotted in the same figures as those for the experimental results, i.e., Fig. 11. The theoretical curve lies within the experimentally measured curves, although the theoretically predicted bead temperatures tend to be lower than the experimental results away from the burning surface.

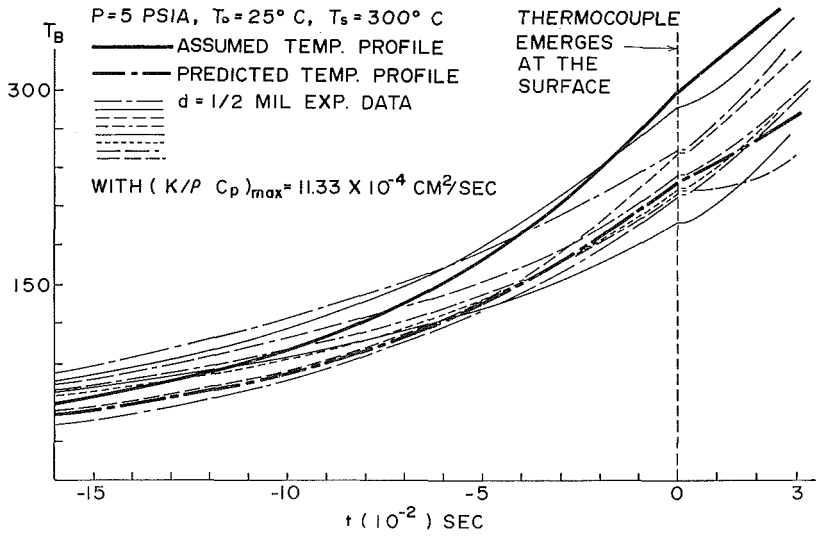

Fig. 11 Experimental temperature profile for $^1/_2$-mil thermocouple wire, the theoretically predicted bead temperature profile (thick line), and assumed theoretical temperature distribution (thick line)

The slope of the experimental curves near the burning surface is close to the theoretically predicted curves.

There are a number of possible reasons that may contribute to the deviations between the experimental and theoretical results. The most obvious reasons are that the heat transfer coefficient of the bead may not be constant and equal to that around the lead wires, that the heat transfer coefficient around the lead wire may vary with temperature, and that the assumed theoretical temperature distribution in the propellant may be incorrect because of the solid-phase reaction and the variation in physical properties as functions of temperature. Other contributing factors are clearly deviations of the physical dimensions and configurations of the actual thermocouples used from those of assumed ones, although extreme care and special die were used in embedding the thermocouples.

The assumption that the thermocouple bead temperature is uniform is reasonable here, since the thermal diffusivity of the propellant is 0.9×10^{-3} cm^2/sec and that of the thermocouple wire is 0.25 cm^2/sec. Because of the significant difference in thermal diffusivity, it is obvious that the temperatures in the thermocouple bead will equalize about 300 times faster than in the propellant. This would be the case for all temperature measurements in insulators such as polymers. In the case of ceramics such as quartz crystals, the thermal diffusivity is only an order of magnitude less, but the assumption should still yield farily accurate values.

The theoretical model can be extended to the case of high conductivity, provided that the temperature distribution in the bead can be analyzed using a realistic boundary condition around the bead. However, since the disturbance created in the presence of

Table 3 Summary of experimental results

Thermocouple wire dia, mil	Average surface temp (Plateau deg C)	Pressure psia	Burning rate cm/sec	Number of experiments	Theoretically predicted temperatures, deg C				
$^1/_2$	237 ± 26.6[6]	5	0.124 ± 0.0049	8	218[1]	216[2]	239[3]	231[4]	232[5]
1	167 ± 14.8	5	0.125 ± 0.006	4	169	165	182	180	184
2	107 ± 12.1	5	0.108 ± 0.0057	5	126	112	120	125	134
3	101 ± 9.1	5	0.124 ± 0.0064	7	128	87	89	96	110
$^1/_2$	245 ± 22.0	10	0.144 ± 0.0046	7		218	229	218	219
1	156 ± 18.0	10	0.147 ± 0.0067	9		162	172	167	171
2	103 ± 14.4	10	0.153 ± 0.0098	8		112	107	113	124
3	103 ± 17.5	10	0.162 ± 0.0079	8		98	80	87	104

The initial temperature T_0 = 25 deg C. The heat coefficient in solid is given by equation (7)

[1] Heat transfer coefficient in gas 0.1 $\frac{\text{cal}}{\text{cm}^2\,\text{sec}^\circ\,\text{C}}$ at T_s = 300° C, $\frac{k}{\rho c} = 9.063 \times 10^{-4}\ \frac{\text{cm}^2}{\text{sec}}$

[2] Heat transfer coefficient in gas 0.01 $\frac{\text{cal}}{\text{cm}^2\,\text{sec}^\circ\,\text{C}}$ at T_s = 300° C, $\frac{k}{\rho c} = 9.063 \times 10^{-4}\ \frac{\text{cm}^2}{\text{sec}}$

[3] Heat transfer coefficient in gas 0.01 $\frac{\text{cal}}{\text{cm}^2\,\text{sec}^\circ\,\text{C}}$ at T_s = 330° C, $\frac{k}{\rho c} = 9.063 \times 10^{-4}\ \frac{\text{cm}^2}{\text{sec}}$

[4] Heat transfer coefficient in gas 0.01 $\frac{\text{cal}}{\text{cm}^2\,\text{sec}^\circ\,\text{C}}$ at T_s = 300° C, $\frac{k}{\rho c} = 11.33 \times 10^{-4}\ \frac{\text{cm}^2}{\text{sec}}$

[5] Heat transfer coefficient in gas 0.1 $\frac{\text{cal}}{\text{cm}^2\,\text{sec}^\circ\,\text{C}}$ at T_s = 300° C, $\frac{k}{\rho c} = 11.33 \times 10^{-4}\ \frac{\text{cm}^2}{\text{sec}}$

[6] Standard deviations

the thermocouple in the medium is less in the case of high-conductivity material because of the similar physical properties, neglecting the bead size may be reasonable.

Conclusions

1 The technique presented in this paper may be used to predict the correct surface temperature in a deflagrating insulator.

2 There is an "optimum" ratio of the thermocouple bead diameter to the lead wire diameter when the thermocouple bead is spherical. However, no matter what the bead size is, correction for the thermocouple response and lead loss must be made. The error is more sensitive to the change in wire diameter.

3 When a part of the thermocouple bead is exposed to a gas stream, especially when the thermocouple bead is large, the measurement can be quite erroneous unless the temperature gradient in the gas and the heat transfer coefficients are known.

4 The surface temperature of deflagrating M-2 double-base propellants is about 300–330 deg C at 5–10 psia.

Acknowledgment

The authors would like to thank Mr. C. L. Thompson and Mr. T. L. Wang for their help in the preparation of this paper. The authors are also grateful to Mr. Charles Lenchitz and Dr. J. Picard of Picatinny Arsenal for their support of the work.

References

1 Klein, R., et al., "Determination of the Thermal Structure of a Combustion Wave by Five Thermocouples," *Journal of Physical Colloidal Chemistry*, Vol. 54, 1950, p. 877.

2 Strittmater, R. C., Holmes, H. E., and Watermeier, L. A., "Measurement of Temperature Profiles in Burning Solid Propellants," Memorandum Report No. 1737, ROTCE Project Nr. 1C222901A211, Ballistics Research Laboratories, Aberdeen Proving Ground, Maryland, 1966.

3 Powling, J., and Smith, W. A. W., "Measurement of the Burning Surface Temperature of Propellant Compositions by Infra-red Emission," *Combustion and Flame*, Vol. 6, 1962, p. 173.

4 Rogers, C. R., and Suh, N. P., "The Ignition and Surface Temperatures of Double Base Propellants II—Comparison of the Optical Technique With the Thermocouple Technique," submitted to *AIAA Journal*.

5 Beck, J. V., "Thermocouple Temperature Disturbances in Low Conductivity Materials," JOURNAL OF HEAT TRANSFER, TRANS. ASME, Series C, Vol. 84, 1962, p. 124.

6 Nydick, S. E., "Thermocouple Errors in Ablation Materials," Instrument Society of America, Preprint No. 16.12-3-66, Oct. 1966.

7 Beck, J. V., and Hurwicz, H., "Effect of Thermocouple Cavity on Heat Sink Temperature," JOURNAL OF HEAT TRANSFER, TRANS. ASME, Series C, Vol. 32, 1960, p. 27.

8 Johnson, N. R., Weinstein, A. S., and Osterle, F., "The Influence of Gradient Temperature Fields on Thermocouple Measurements," ASME paper 57-HT-18, 1957.

9 Beck, J. V., "Study of Thermal Discontinuities and Associated Temperature Disturbances in a Solid Subject to a Surface Heat Flux, Part III. Effect of Sensors in Low Conductivity Material Upon Temperature Distribution and Its Measurement," AVCO Technical Report RAD-TR-9(7)-59-26, Oct. 1959.

10 Garabedian, P. R., *Partial Differential Equations*, Wiley, New York, 1964.

the thermocouple in the medium is less in the case of high-conductivity material because of the similar physical properties, neglecting the bead size may be reasonable.

Conclusions

1 The technique presented in this paper may be used to predict the correct surface temperature in a deflagrating insulator.

2 There is an "optimum" ratio of the thermocouple bead diameter to the lead wire diameter when the thermocouple bead is spherical. However, no matter what the bead size is, correction for the thermocouple response and lead loss must be made. The error is more sensitive to the change in wire diameter.

3 When a part of the thermocouple bead is exposed to a gas stream, especially when the thermocouple bead is large, the measurement can be quite erroneous unless the temperature gradient in the gas and the heat transfer coefficients are known.

4 The surface temperature of deflagrating M-2 double-base propellants is about 300–330 deg C at 5–10 psia.

Acknowledgment

The authors would like to thank Mr. C. L. Thompson and Mr. T. L. Wang for their help in the preparation of this paper. The authors are also grateful to Mr. Charles Lenchitz and Dr. J. Picard of Picatinny Arsenal for their support of the work.

References

1 Klein, R., et al., "Determination of the Thermal Structure of a Combustion Wave by Five Thermocouples," *Journal of Physical Colloidal Chemistry*, Vol. 54, 1950, p. 877.

2 Strittmater, R. C., Holmes, H. E., and Watermeier, L. A., "Measurement of Temperature Profiles in Burning Solid Propellants," Memorandum Report No. 1737, ROTCE Project Nr. 1C222901A211, Ballistics Research Laboratories, Aberdeen Proving Ground, Maryland, 1966.

3 Powling, J., and Smith, W. A. W., "Measurement of the Burning Surface Temperature of Propellant Compositions by Infra-red Emission," *Combustion and Flame*, Vol. 6, 1962, p. 173.

4 Rogers, C. R., and Suh, N. P., "The Ignition and Surface Temperatures of Double Base Propellants II—Comparison of the Optical Technique With the Thermocouple Technique," submitted to *AIAA Journal*.

5 Beck, J. V., "Thermocouple Temperature Disturbances in Low Conductivity Materials," JOURNAL OF HEAT TRANSFER, TRANS. ASME, Series C, Vol. 84, 1962, p. 124.

6 Nydick, S. E., "Thermocouple Errors in Ablation Materials," Instrument Society of America, Preprint No. 16.12-3-66, Oct. 1966.

7 Beck, J. V., and Hurwicz, H., "Effect of Thermocouple Cavity on Heat Sink Temperature," JOURNAL OF HEAT TRANSFER, TRANS. ASME, Series C, Vol. 32, 1960, p. 27.

8 Johnson, N. R., Weinstein, A. S., and Osterle, F., "The Influence of Gradient Temperature Fields on Thermocouple Measurements," ASME paper 57-HT-18, 1957.

9 Beck, J. V., "Study of Thermal Discontinuities and Associated Temperature Disturbances in a Solid Subject to a Surface Heat Flux, Part III. Effect of Sensors in Low Conductivity Material Upon Temperature Distribution and Its Measurement," AVCO Technical Report RAD-TR-9(7)-59-26, Oct. 1959.

10 Garabedian, P. R., *Partial Differential Equations*, Wiley, New York, 1964.

DISCUSSION

Robert C. Pfahl, Jr.[3]

Suh and Tsai have tackled part of a very difficult problem: the study of the response of thermocouples embedded in an ablating or deflagrating material. They have extended the work of Nydick [6] to include the effect of a thermocouple bead. Both Nydick and Suh and Tsai endeavor to model realistically the effect of a surface burning at a constant rate and temperature. Both works have modeled the moving surface by sacrificing a complete transient two-dimensional model of the conduction heat transfer between the material and the thermocouple. Transient conduction between the material and the thermocouple is modeled using heat transfer coefficients.

There are two heat transfer coefficients in Suh and Tsai's model: one to describe heat transfer between the thermocouple wire and the material, and one to describe heat transfer between the thermocouple bead and the material. The coefficients, equation (7), were developed by Nydick [6] from Beck's report [9]. Beck derived his heat transfer coefficient for a steady-state problem, for a linear temperature distribution in the material, and for a thermocouple oriented normal to the heated surface. The equation included an effective length of the thermocouple, l, which was less than the total thermocouple length, L. Beck determined the validity of his approximate method of estimating thermocouple temperature perturbations by comparing his solution with a two-dimensional finite-difference solution to the problem; he concluded that while the results showed substantial agreement, the numerical results would be recommended in general.

Nydick used Beck's formula for the heat transfer coefficient, but changed the effective length to an undefined length, l_2, without indicating the change or offering comment. He applied the formula to a transient rather than steady-state problem in which the temperature distribution was exponential instead of linear. He did not demonstrate the validity of Beck's formula under these new conditions.

Nydick extended Beck's formula to a wire located parallel to the heated surface. In his extension he assumed that the heat transfer coefficient was the sum of two terms: (1) Beck's formula for a wire normal to the heated surface and (2) a term which he described as "the gradient at that point in an undisturbed material." It is not clear to this discusser why this second term should be present. Nydick further modified this model to the case of a wire at an angle to the heated surface; it is this coefficient which appears as equation (7) in Suh and Tsai's article.

The following paragraphs discuss the suitability of equation (7) for describing heat transfer between the thermocouple wire and the material for the two limiting cases:

$\alpha = 0$, the thermocouple oriented normal to the heated surface

$\alpha = \pi/2$, the thermocouple oriented parallel to the heated surface.

For the $\alpha = 0$ case equation (7) should, but does not, reduce to Beck's original form. In addition, the ability of Beck's formula to describe transient conduction in a body with exponential temperature distribution should be demonstrated before it is used to describe this new situation.

The $\alpha = \pi/2$ case has been studied in analytical [11] and experimental [12] papers. The paper by Pfahl and Dropkin [11] models the transient two-dimensional conduction for a step in surface heat flux using finite-differences. The conclusions of the study are that the disturbances can be severe if the sensor is located within four radii of the heated surface, or if the volumetric specific heat, ρc_p, of the thermocouple is greater than twice that of the material. The disturbances are relatively insensitive to the ratio of thermal conductivities in contrast to the $\alpha = 0$ case [5].

The study predicts that there are two transient phases to the temperature disturbance. The thermocouple initially overresponds because the temperature "wave" as it progresses into the material crosses the thermocouple faster than the neighboring material due to the thermocouple's higher diffusivity. After this brief initial transient, the thermocouple begins to lag the undisturbed temperature response. This delay in response is caused by the volumetric specific heat of the thermocouple being greater than that of the material; hence, the thermocouple acts as a heat sink.

[3] Member of Research Staff, Western Electric Engineering Research Center, Princeton, N. J.

The above effects were observed experimentally by Brewer [12]. Brewer instrumented samples with thermocouples oriented both normal and parallel to the heated surface and compared them to a reference thermocouple. He exposed his samples to a plasma arc so that his experimental boundary condition is essentially an isotherm moving at constant velocity. His results support the predictions for the $\alpha = 0$ case [5] and $\alpha = \pi/2$ case [11].

The above discussion indicates that a heat transfer coefficient for the $\alpha = \pi/2$ case should depend on the ratio of volumetric specific heats and on the depth of the thermocouple; equation (7) depends on neither. The transient change in the sign of the perturbation suggest that the coefficient is a strong function of time.

For the heat transfer coefficient between the bead and the material, Suh and Tsai again use equation (7). A possible alternative expression which has been developed to describe transient conduction from a sphere which is suddenly placed in a low-conductivity material at a different temperature [13] is

$$h = 2k/D \tag{15}$$

For a bead diameter three times the wire diameter this alternative expression becomes

$$h = 2k/3R \tag{16}$$

which agrees with the first term of equation (7) except that the $\ln (2L/R)$ term does not appear in the denominator. For Suh and Tsai's experiments with a $^1/_2$-mil wire, $\ln (2L/R) = 6.93$; thus, the new coefficient would be 593 percent larger.

I emphasize that the heat transfer coefficients used by Suh and Tsai were developed by previous authors. Suh and Tsai clearly question the validity of the coefficients which they use; they simply are using the best information available to them. They have demonstrated in Figs. 3 to 5 that an error of 100 percent in the coefficient will not strongly affect their predictions. The purpose of the preceding discussion is to indicate that these coefficients could be in error by more than 500 percent and that they could be strongly time-dependent. Until the accuracy of the coefficients is verified experimentally or by a more complete analytical model, it is premature for Suh and Tsai to use their model to reach conclusions on secondary effects such as the existence of an optimum bead diameter; the effect of changing the bead diameter by a factor of two is approximately the same as that produced by changing the heat transfer coefficient by the same factor.

The effect of bead diameter on temperature measurements from thermocouples embedded in deflagrating materials also has been studied analytically by Strittmater, Holmes, and Watermeier [14]. They develop a model which approximates what they consider to be the dominant mechanisms of heat transfer. They conclude that, "Although some important factors in the complete heat-transfer problem have been neglected in the foregoing analysis, qualitative estimates of these factors lead the writers to believe that the implications (of their results) will remain essentially unchanged in a more complete analysis." Their results do not reveal an optimum bead size, but rather that the ratio of D/d should be as large as possible. This prediction results from only considering the bead's ability to store thermal energy and neglecting the temperature perturbation which the bead causes. An unrealistic prediction from this model is that the disturbance is independent of wire diameter. Suh and Tsai's model, being more complete than that of reference [14], does predict that the disturbance depends primarily on wire diameter.

Brewer [12] indicates that a serious source of error when there is a steep temperature gradient is not knowing the exact location of the sensor. Suh and Tsai's experimental results have been presented in a manner which masks any uncertainties in thermocouple location. This masking occurs because the authors shift the time scale of their curves (time and location relative to the moving surface are linearly related) so that all thermocouples reach the surface at time zero. The experimental results offer no support for the conclusion that there is an optimum bead diameter, but the results do illustrate the severity of temperature perturbations and show the strong dependency on wire diameter. It is to be hoped that these results will serve to point out to the uninitiated the severity of temperature perturbations produced by embedded sensors.

Additional References

11 Pfahl, R. C., Jr., and Dropkin, D., "Thermocouple Temperature Perturbations in Low-Conductivity Materials," ASME Paper No. 66-WA/HT-8, 1966.

12 Brewer, W. D., "Effect of Thermocouple Wire Size and Configuration on Internal Temperature Measurements in a Charring Ablator," NASA TN D-3812, 1967.

13 Melvin, A., "The Transient Behavior of Small Thermocouples in Static Gas Environments," *British Journal of Applied Physics*, Ser. 2, Vol. 2, 1969, pp. 1339–1343.

14 Strittmater, R. C., Holmes, H. E., and Watermeier, L. A., "Lead Loss Problem for a Thermocouple Imbedded in a Burning Propellant," *Journal of Spacecraft and Rockets*, Vol. 3, No. 8, 1966, pp. 1302–1303.

James V. Beck[4]

The authors are to be commended on their choice of a method of analysis which utilizes the concept of a heat transfer coefficient in a solid. This concept was originally proposed in my report for AVCO [9]. While a paper based on this work was never produced, one on the transient, two-dimensional analysis of a thermocouple normal to the heated surface has been published [5].

The concept of a heat transfer coefficient in a solid is valid, but one must be careful to use it properly. An implicit premise in my derivation of h is that it is a *correction* to a measurement that is being sought. Thus, say, a 10 percent error in estimating the correction results in a smaller error in the actual corrected temperature. Average coefficients found by relatively crude approximations may be tolerated. Nevertheless, h can vary an order of magnitude; therefore, one should not use this estimation premise as a license for laxity.

Suh and Tsai's equation (6) has been taken from a paper by Nydick. This author partially based his work upon mine. Mutations or rearrangements which occurred during the two reworkings will be discussed below.

Reference [9] of their paper is an analysis of the *steady-state* problem of a thermocouple in a *nonablating* medium. The thermocouple is *normal* to the heated surface. The equation given for the heat transfer coefficient is

$$h = \frac{2k/R}{3 \ln (2l/R)} \tag{17}$$

where l is *not* the *length* of the wire but a characteristic length depending upon the distance that the wire temperature, compared with the ambient, is depressed. The ambient temperature was considered to decrease linearly with y.

In one of Nydick's cases, the relation

$$h = \frac{2k/R}{3 \ln (2l_2/R)} + k\beta \tag{18}$$

was given for a wire of length L *parallel* to an ablating surface and in a region where the temperature gradient is proportional to β. The first term on the right-hand side is similar to equation (17) and the second is added to account for "the gradient at that point in an undisturbed material." No derivation of equation (18) was given, although Nydick refers to the heat flux

$$\dot{q} = k \left.\frac{dT}{dr}\right|_R \tag{19}$$

[4] Associate Professor, Department of Mechanical Engineering, Michigan State University, East Lansing, Mich.

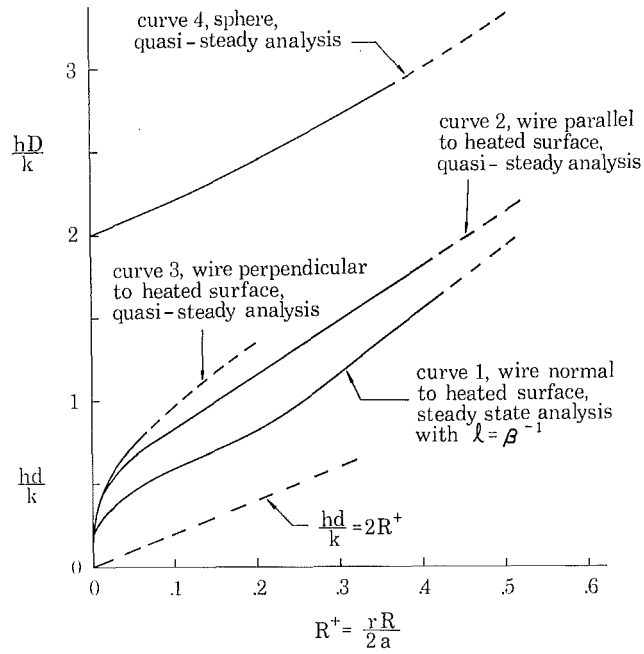

Fig. 12 Heat transfer coefficients in solids for certain cases

which for his orientation varies between $\pm\beta(T_s - T_0)k$ but has the average value of zero. Nydick also modified the $k\beta$ term to a form similar to the last term of equation (7). Note that as α goes to zero this term becomes

$$\frac{\beta k}{2}(1 + e^{-\beta L}) \tag{20}$$

Clearly this value is not zero, yet it should be in order to reduce to equation (17). Nydick accepted equation (17) for the case of a wire normal to the heated surface. I conclude that the second term in equations (7) and (18) should not be present.

Nydick did not give equation (7) exactly as Suh and Tsai wrote it. For example, instead of ln $(2L/R)$, he gave ln $(2l_2/R)$; however, he did not explicitly state what l_2 is. For equation (18) Nydick considered the geometry of the wire to be the shape of an inverted L with the shorter leg parallel to the heated surface. For this case the length of the short leg might possibly be identified with l_2. Nydick also considered the case of a wire at angle α (as shown by Fig. 1) for length L' with the wire then bent normal to the heated surface. Although not specified, Nydick may have intended α to be near 90 deg and L' to be small, in which case l_2 in equation (18) might possibly be represented by L' (but the βk term should be dropped). Suh and Tsai considered an unbent wire but retained the Nydick analysis and let L' become large and equal to L, the length of the thermocouple wire embedded in the insulator. They then set l_2 equal to L. After these modifications, equation (7) becomes incorrect for the use intended.

Rather than this expression, several alternatives are suggested. Instead of $l = L$, the wire length in equation (17) would be better expressed as $l = \beta^{-1} = r/a$ where $a = k/\rho c$. Then equation (17) can be written

$$\frac{hd}{k} = \frac{4}{3 \ln R^+} \tag{21}$$

where

$$d = 2R \qquad R^+ = \frac{rR}{2a} \tag{22}$$

Implicit in the derivation of equation (21) is that R^+ must be small. Equation (21) is shown as curve 1 of Fig. 12.

The above analysis is for steady state. One can obtain quasi-steady h values for a constant ablation velocity. Two cases may be obtained fairly directly from Carslaw and Jaeger [15] using line and point sources in a medium moving at velocity r. An infinite line source perpendicular to the direction of movement (analogous to a wire parallel to the heated surface) produces

$$\frac{hd}{k} = \frac{2}{K_0(R^+)} \tag{23}$$

where $K_0(x)$ is the zero-order modified Bessel function of the second kind. The result is shown as curve 2 in Fig. 12. Again R^+ is assumed to be small.

In the case of an infinite wire normal to the heated surface, the describing equation for transient radial heat transfer outside an infinite cylinder is

$$\frac{k}{r'}\frac{\partial}{\partial r'}\left(r'\frac{\partial T}{\partial r}\right) = \rho c_p \frac{\partial T}{\partial t} \tag{24}$$

The equation for steady-state heat transfer from outside an infinite cylinder to a fluid flowing parallel to its axis is

$$\frac{k}{r'}\frac{\partial}{\partial r'}\left(r'\frac{\partial T}{\partial r}\right) = \rho c_p r \frac{\partial T}{\partial z} \tag{25}$$

where r' is the radial coordinate and r is the axial velocity. Notice that any solution of (24) is also a solution of (25) with t replaced by z/r. For the boundary conditions for $T(r',z)$

$$\begin{aligned} T(R,z) &= T_0 \\ T(\infty,z) &= T_\infty \\ T(r',0) &= T_\infty \end{aligned} \tag{26}$$

one can derive for small R^+

$$\frac{hd}{k} = 2\left\{\frac{-1}{\ln R^+ + \gamma} - \frac{\gamma}{2[\ln R^+ + \gamma]^2} + \ldots\right\} \tag{27}$$

utilizing Carslaw and Jaeger's equation [16] and employing $z = a/r$ as the characteristic length. This result is shown as curve 3 of Fig. 12. In equation (27), $\gamma = 0.57722\ldots$ is Euler's constant.

A heat transfer coefficient for the spherical junction can be obtained by using the moving point source solution [17]. For small R^+ one can derive

$$\frac{hD}{k} = 2e^{R^+} \tag{28}$$

for steady state. This result is the upper curve (curve 4) of Fig. 12. Unlike that of the wire, the sphere value of h has a non-zero value as R^+ approaches zero.

It is not apparent how these results may be compared with those of Suh and Tsai. If there is a sufficiently large value for L/R in equation (7), it reduces to

$$\frac{hD}{k} = 2R^+ \tag{29}$$

which is the lower straight line in Fig. 12. Compared to curves 2 and 3, this can be 100 percent or more in error.

Several other aspects of the paper are worthy of comment, for example, the choice of finite-difference scheme. Other approximations, such as the Crank-Nicolson, are more accurate and stable for any time step. Also, a generalized transient analysis could be developed, together with some correction kernels, for use in other integrals [18]. Further comments will be deferred.

Additional References

15 Carslaw, H. S., and Jaeger, J. C., *Conduction of Heat in Solids*, 2nd ed., Oxford, London, 1959, p. 268.
16 Ibid., p. 336.
17 Ibid., p. 267.
18 Beck, J. V., "Determination of Undisturbed Temperatures from Thermocouple Measurements Using Correction Kernels," Nuclear Engineering and Design, Vol. 7, 1968, p. 9–12.

Authors' Closure

It is indeed gratifying that our paper aroused sufficient interest on the part of Dr. Pfahl and Professor Beck to write such extensive comments. We would like to thank them for the thorough study of the paper. It is rather amusing, in a sense, that what we considered to be the most trivial part of the paper generated more interest than any other aspect of the paper. Since it is clear that the major purpose of the paper has not been conveyed to the readers, the basic purpose of the work will be stated here and our approach to this type of problem will be discussed.

The major purpose of the paper is to convey a *concept* which enables the "measurement" of the surface temperature of a rapidly deflagrating solid. The purpose of the paper *is not* to evaluate various heat transfer coefficients in solids. The method used by others in the past in "measuring" the surface temperature was to use a thermocouple and then through analyses determine the probable error involved in the measurement. Such a method is not reliable since the validity of the analyses cannot be checked. Therefore, we decided to *predict* the surface temperature by measuring its value using several sizes of thermocouples and by extrapolating the results to zero wire diameter based on the most probable temperature profile in the solid.

In order to accomplish the stated purpose, reasonable values for the heat transfer coefficients were going to be assumed in order to by-pass the difficulty of knowing the exact extent of the region disturbed by the presence of the thermocouple. We felt that as long as the temperatures measured by various sized thermocouples could be predicted by a model to the desired accuracy, the exact form of the heat transfer coefficients would not be important for our purpose. Then, we found that the Nydick's expressions were available. We used Nydick's expressions as the first approximation, since the whole question of the heat transfer coefficients in solids has not been verified experimentally to a satisfactory degree, as Dr. Pfahl pointed out in his comments. Our method might not have been a good one if it depended sensitively on the heat transfer coefficient. However, it turned out that the solution does not depend on the coefficient sensitively, as shown in the paper. For our purpose any expression or values for the heat transfer coefficient that correctly predicted the surface temperatures measured by a large number of different sized thermocouple wires would have been acceptable. For example, we could have assumed the heat transfer coefficient to be a polynomial function of pertinent parameters with undetermined coefficients and then varied the coefficients until it fit all the experimental results.

We would like to thank both Dr. Pfahl and Professor Beck for commenting on the numerical scheme. We are certain that the comments will be useful to those who want to refine the concept presented in our paper. However, we think that our solutions are sufficiently accurate. Furthermore, one should realize that the assumed model is an approximation of a complex, real phenomenon. Reasonable solutions, i.e., reasonable both in time, cost, and accuracy, have to be provided to this type of real problem without losing sight of one's objectives. The accuracy of a numerical result cannot, after all, exceed the accuracy within which a model can approximate the actual phenomenon.

Finally, a few comments will be made on the optimum ratio of the bead diameter to the wire diameter. The exact value for the optimum ratio will be subject to the assumptions made in the paper such as the dependence of the heat transfer coefficient on the radius of the thermocouple bead. Therefore, if the expression given by Dr. Pfahl, i.e., equation (15), is used, the optimum ratio will assume a different value. It will be interesting to use the equation suggested by Dr. Pfahl and to determine if it yields a better correlation with the experimental results. When the total heat transfer rate from the surrounding material to the bead does not depend on the size of the thermocouple, obviously the smaller the bead the more accurate will be the result. The purpose of discussing the question of the optimum bead size was to point out that making the bead diameter as small as possible at a great expense does not necessarily guarantee accurate measurements.

R. G. HERING
Professor.

T. F. SMITH
Research Assistant.

Department of Mechanical Engineering, University of Illinois at Urbana-Champaign, Urbana, Ill.

Surface Roughness Effects on Radiant Energy Interchange[1]

Radiant interchange between opaque interacting surfaces is formulated for unequal temperature adjoint plates with a one-dimensional surface roughness profile. Rough surface bidirectional reflectance and directional emittance depend on material emittance, roughness element slope, and roughness element specularity. Numerical solution to simultaneous integral equations governing the dimensionless radiant intensities lead to local and overall absorption factors for selected values of the influencing parameters. Absorption factor results show a strong dependence on surface roughness and indicate that roughness effects are more important in the evaluation of radiant interchange than radiant heat loss. Absorption factor values differing by a factor of two to four are commonly observed for identical emittance materials as a result of roughness. The diffuse emission-diffuse reflection property model employing rough surface apparent hemispherical emittance gave the closest agreement to rough surface absorption factor results. Simple property model results, however, were often significantly in error.

Introduction

Surface roughness is recognized as a characteristic of engineering materials which can significantly influence thermal radiation properties. Roughness may change the magnitude of emittance and reflectance relative to that of the constituent material as well as the directional dependence of emission and reflection properties. Since common engineering methods for evaluating radiant energy interchange rates between interacting surfaces do not account for directional property effects, these techniques may yield large deviations from actual heat transfer rates. All apparent thermal radiation properties necessary to implement radiant transfer studies for rough surfaces were recently reported [1][2] for a one-dimensionally rough surface consisting of V-shaped roughness elements. These properties have been used to evaluate surface roughness effects on radiative heat transfer and equilibrium temperature of isolated surfaces [2, 3] as well as radiative heat transfer for interacting equal temperature surfaces [4, 5] in the absence of external radiation fields. In the cited studies, it was established that surface roughness strongly influenced radiative heat transfer and equilibrium temperature, particularly for materials with low emittance or absorptance, and that common engineering methods of analysis are often grossly in error. It has been suggested [6, 7] that the surface property model employed in radiant transfer analysis is more critical for evaluation of local and overall radiant energy interchange rates than for radiant heat transfer rates. The pur-

[1] This paper presents results of research supported in part by Jet Propulsion Laboratory, California Institute of Technology, Contract 951661.

Contributed by the Heat Transfer Division and presented at the Space Technology and Heat Transfer Conference, Los Angeles, Calif., June 21–24, 1970, of The American Society of Mechanical Engineers. Manuscript received at ASME Headquarters, March 19, 1970. Paper No. 70-HT/SpT-2.

[2] Numbers in brackets designate References at end of paper.

Nomenclature

A = area
a_0 = autocorrelation distance
B_{ij} = overall absorption factor
B_{di-j} = local absorption factor
$\mathcal{F}_{ij}$ = overall interchange factor
$\mathcal{F}_{di-j}$ = local interchange factor
f, g = functions defined in equations (7)
I_b = intensity of black body radiation
I^+, I^- = intensities of emergent and incident radiation
l = plate length
q = local radiant heat transfer rate
$q_{di\rightleftarrows j}$ = local radiant interchange rate
Q = overall radiant heat transfer rate
$Q_{i\rightleftarrows j}$ = overall radiant interchange rate
T = temperature
x, z = coordinates
$\alpha, \alpha_H, \alpha_w$ = apparent directional, hemispherical, and wall absorptance
γ = included angle between plates
$\epsilon, \epsilon_a, \epsilon_H, \epsilon_w$ = apparent directional, apparent hemispherical, hemispherical, and wall emittance
θ, θ' = angles of emergent and incident energy
Θ = limiting angle defined in equation (2)

(*Continued on next page*)

pose of this study is to utilize surface radiation properties developed in [1] to examine surface roughness effects on radiant interchange rates for a simple system of interacting unequal temperature surfaces and to establish the magnitude of error incurred when simple engineering property models are employed in analysis.

The system of interacting surfaces selected for study consists of equal length plates of infinite width sharing a common edge and including angle γ (see Fig. 1). Both surfaces are opaque and have identical uniform temperature-independent radiative properties but unequal uniform temperatures. This simple configuration was chosen primarily because of the availability of extensive radiant heat transfer results evaluated on the basis of simple direction independent property models commonly employed in radiant heat transfer analysis [9, 10, 11] as well as more comprehensive property models [4, 7, 8, 12]. The surface roughness of each plate consists of V-groove elements of identical included angle with axes parallel to that of the adjoint plates. Apparent thermal radiation properties for the roughness profile described have been developed in [1]. External sources of radiant energy are absent, and the intervening medium is radiatively nonparticipating.

Analysis

Unlike analysis for diffusely or specularly reflecting surfaces with direction-independent properties, radiative transfer analysis for the system of rough surfaces is initiated from the fundamental equation governing radiant intensity. Consider differential surface area element $dA_1 (= dx_1 dz_1)$ located distance x_1 from the apex on the plate designated surface 1 in Fig. 1. Let θ_1' and θ_1 denote arbitrary directions of incident and emergent radiant energy, respectively, measured from the mean surface normal in a plane perpendicular to the plate axis. The intensity of radiant energy emerging from the considered plate increment per unit time and per unit area, $I_1^+(x_1, \theta_1)$, which is confined to the solid angle increment, $d\omega_1$, defined by the cylindrical sector subtended by angular increment, $d\theta$, satisfies the following relation [4].

$$I_1^+(x_1, \theta_1) = \epsilon(\theta_1) I_{b,1} + \frac{\pi}{2} \int_{-\pi/2}^{\pi/2} \rho_{bd}(\theta_1', \theta_1) \cdot I_1^-(x_1, \theta_1') \cos \theta_1' d\theta_1' \quad (1)$$

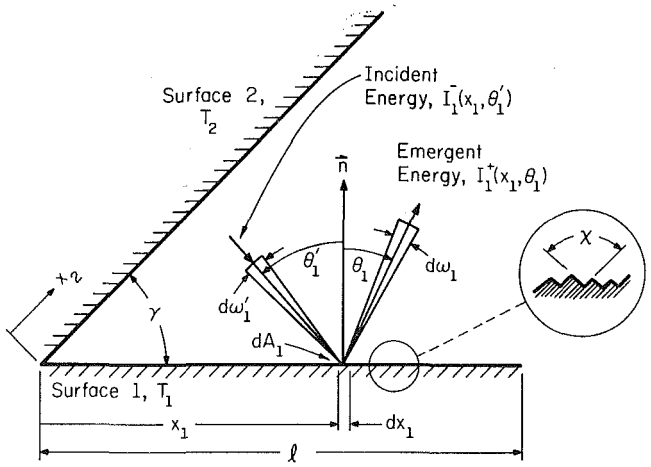

Fig. 1 Schematic diagram of adjoint plate system

The first term to the right in equation (1) is the intensity of emitted energy with $\epsilon(\theta_1)$ and $I_{b,1}$ denoting directional emittance and intensity of a black surface evaluated at temperature T_1, respectively. The remaining term is the contribution of energy incident at dA_1 from all possible directions which after reflection from the surface element emerges within $d\omega_1$. $I_1^-(x_1, \theta_1')$ is the intensity of radiant energy incident at dA_1 from within solid angle increment $d\omega_1'$ defined by angular increment $d\theta'$ about direction θ_1', and $\rho_{bd}(\theta', \theta)$ is the bidirectional reflectance of the rough surface. The solid angle relations $d\omega_1 = 2d\theta_1$ and $d\omega_1' = 2d\theta_1'$ have been employed in the development of equation (1).

For the adjoint plate system in the absence of external radiation fields, the contributing directions of incident energy are limited to a value $\Theta_1(x_1)$ less in absolute value than $\pi/2$ and given by

$$\Theta_1(x_1) = -\tan^{-1}\left[\frac{\cos\gamma - (x_1/l)}{\sin\gamma}\right] \quad (2)$$

Also, since the intervening medium is radiatively transparent, the intensity of incident energy $I_1^-(x_1, \theta_1')$ is identical to the intensity of emergent energy of the adjacent plate evaluated at a suitable location and direction, $I_2^+(x_2, \theta_2)$. From geometry it follows that

$$\left.\begin{aligned} \frac{x_2}{x_1} &= \frac{\cos\theta_1'}{\cos(\theta_1' - \gamma)} \\ \theta_2 &= \theta_1' - \gamma \end{aligned}\right\} \quad (3)$$

Hence, equation (1) may be written

$$I_1^+(x_1, \theta_1) = \epsilon(\theta_1) I_{b,1} + \frac{\pi}{2} \int_{\Theta_1(x_1)}^{\pi/2} \rho_{bd}(\theta_1', \theta_1) \cdot I_2^+[x_2(x_1, \theta_1'), \theta_2(\theta_1')] \cos\theta_1' d\theta_1' \quad (4)$$

A similar development for local emergent intensity in direction θ_2 for surface 2 yields

$$I_2^+(x_2, \theta_2) = \epsilon(\theta_2) I_{b,2} + \frac{\pi}{2} \int_{\Theta_2(x_2)}^{\pi/2} \rho_{bd}(\theta_2', \theta_2) \cdot I_1^+[x_1(x_2, \theta_2'), \theta_1(\theta_2')] \cos\theta_2' d\theta_2' \quad (5)$$

with $\Theta_2(x_2)$, x_1, and θ_1 given by equations (2) and (3) after interchanging subscripts 1 and 2. In equation (5), $I_{b,2}$ is the intensity of a black surface evaluated at temperature T_2.

Equations (4) and (5) constitute a pair of simultaneous linear integral equations for angular dependence of local radiant intensity on each surface. Because of the linearity of the equations, their solution can be constructed by superposing solutions of the following alternate pair of dimensionless integral equations

$$\left.\begin{aligned} f(\xi_1, \theta_1) &= \epsilon(\theta_1) + \frac{\pi}{2} \int_{\Theta_1(\xi_1)}^{\pi/2} \rho_{bd}(\theta_1', \theta_1) \cdot g[\xi_2(\xi_1, \theta_1'), \theta_2(\theta_1')] \cos\theta_1' d\theta_1' \\ g(\xi_2, \theta_2) &= \frac{\pi}{2} \int_{\Theta_2(\xi_2)}^{\pi/2} \rho_{bd}(\theta_2', \theta_2) \cdot f[\xi_1(\xi_2, \theta_2'), \theta_1(\theta_2')] \cos\theta_2' d\theta_2' \end{aligned}\right\} \quad (6)$$

Nomenclature

ξ = dimensionless plate coordinate, x/l
ρ_{bd} = bidirectional reflectance
ρ_H, ρ_w^s, ρ_w^d = hemispherical, specular, and diffuse components of wall reflectance
σ = Stefan-Boltzmann radiation constant
σ_0 = root mean square roughness
χ = roughness included angle
$d\omega$, $d\omega'$ = solid angle increments of emergent and incident energy

Subscripts

1 = surface 1
2 = surface 2

with

$$\left.\begin{aligned}\frac{I_1^+(x_1,\theta_1)}{I_{b,1}} &= f(\xi_1,\theta_1) + rg(\xi_1,\theta_1)\\ \frac{I_2^+(x_2,\theta_2)}{I_{b,2}} &= f(\xi_2,\theta_2) + \frac{1}{r}\,g(\xi_2,\theta_2)\end{aligned}\right\} \tag{7}$$

and

$$\xi_1 = \frac{x_1}{l}, \qquad \xi_2 = \frac{x_2}{l}, \qquad r = \frac{I_{b,2}}{I_{b,1}} = \left(\frac{T_2}{T_1}\right)^4 \tag{8}$$

It may be noted that equations (6) are the governing integral equations for intensity when surface 1 has unit black surface intensity and surface 2 is at a temperature of absolute zero.

Once the radiant intensity functions have been evaluated, local radiant heat transfer follows from the difference between emission rate and rate of absorption of incident energy. For surface 1,

$$q_1(x_1) = \epsilon_a\sigma T_1^4 - \frac{\pi}{2}\int_{\Theta_1(x_1)}^{\pi/2} \alpha(\theta_1')I_1^-(x_1,\theta_1')\cos\theta_1' d\theta_1' \tag{9}$$

where ϵ_a and $\alpha(\theta_1')$ denote the rough surface properties' apparent hemispherical emittance and directional absorptance for energy incident at polar angle θ_1', respectively. Replacing subscript 2 with 1 in equation (9) yields the analogous result for local radiant heat transfer for surface 2. Upon introducing $I_1^-(x_1,\theta_1') = I_2^+(x_2,\theta_2)$ into equation (9), utilizing equation (5) and expressing the resulting relation in terms of the dimensionless intensity functions of equation (7), the following result is obtained

$$q_1(x_1) = \epsilon_a\sigma T_1^4 - \mathfrak{F}_{d1-1}(x_1)\sigma T_1^4 - \mathfrak{F}_{d1-2}(x_1)\sigma T_2^4 \tag{10}$$

where

$$\mathfrak{F}_{d1-1}(x_1) = \tfrac{1}{2}\int_{\Theta_1(x_1)}^{\pi/2} \alpha(\theta_1')g[x_2(x_1,\theta_1'),\theta_2(\theta_1')]\cos\theta_1' d\theta_1' \tag{11}$$

$$\mathfrak{F}_{d1-2}(x_1) = \tfrac{1}{2}\int_{\Theta_1(x_1)}^{\pi/2} \alpha(\theta_1')f[x_2(x_1,\theta_1'),\theta_2(\theta_1')]\cos\theta_1' d\theta_1' \tag{12}$$

The functions $\mathfrak{F}_{d1-1}(x_1)$ and $\mathfrak{F}_{d1-2}(x_1)$ are generalized local radiant interchange factors defined such that $\mathfrak{F}_{d1-1}(x_1)\sigma T_1^4$ and $\mathfrak{F}_{d1-2}(x_1)\sigma T_2^4$ are the rate of absorption by dA_1 per unit area of energy emitted by surfaces 1 and 2, respectively. It is more convenient to use analogous local radiant absorption factors $B_{d1-j}(x_1)$ in the presentation of results, and these are simply related to the interchange factors by

$$B_{d1-1}(x_1) = \frac{\mathfrak{F}_{d1-1}(x_1)}{\epsilon_a}, \qquad B_{d1-2}(x_1) = \frac{\mathfrak{F}_{d1-2}(x_1)}{\epsilon_a} \tag{13}$$

The interchange factors must satisfy reciprocity, that is,

$$\left.\begin{aligned}\mathfrak{F}_{d1-1}(x_1) &= \mathfrak{F}_{1-d1}(x_1)\frac{A_1}{dA_1},\\ \mathfrak{F}_{d1-2}(x_1) &= \mathfrak{F}_{2-d1}(x_1)\frac{A_2}{dA_1}\end{aligned}\right\} \tag{14}$$

Also, since surfaces 1 and 2 form an enclosure with the environment which may be represented by a black surface, say 3, tightly stretched between the plate ends and at a temperature of absolute zero, the following enclosure relation is satisfied.

$$\epsilon_a = \mathfrak{F}_{d1-1}(x_1) + \mathfrak{F}_{d1-2}(x_1) + \mathfrak{F}_{d1-3}(x_1) \tag{15}$$

Using equation (15), the local radiant heat transfer expression of equation (10) may be recast in terms of net radiant interchange rates.

$$q_1(x_1) = \sum_{j=1}^{3} q_{d1\rightleftarrows j} \tag{16}$$

where the interchange rate from dA_1 to A_j is given by

$$q_{d1\rightleftarrows j}(x_1) = \mathfrak{F}_{d1-j}[\sigma T_1^4 - \sigma T_j^4] = \epsilon_a B_{d1-j}(x_1)[\sigma T_1^4 - \sigma T_j^4], \qquad 1 \le j \le 3 \tag{17}$$

Clearly, local radiant interchange rates are completely specified for uniform but arbitrary temperatures of the system surfaces when either the local interchange or absorption factors are available.

Overall or total heat transfer for each of the system surfaces is obtained by integration of local heat transfer over plate length. Thus, for example, overall heat transfer for surface 1 follows from equation (9) as

$$\frac{Q_1}{l} = \epsilon_a\sigma T_1^4 - \frac{\pi}{2l}\int_0^l\int_{\Theta_1(x_1)}^{\pi/2} \alpha(\theta_1')I_1^-(x_1,\theta_1')\cos\theta_1' d\theta_1' dx_1 \tag{18}$$

or equivalently from equation (10) as

$$\frac{Q_1}{l} = \epsilon_a\sigma T_1^4 - \mathfrak{F}_{11}\sigma T_1^4 - \mathfrak{F}_{12}\sigma T_2^4 \tag{19}$$

where

$$\left.\begin{aligned}\mathfrak{F}_{11} &= \frac{1}{l}\int_0^l \mathfrak{F}_{d1-1}(x_1)dx_1\\ \mathfrak{F}_{12} &= \frac{1}{l}\int_0^l \mathfrak{F}_{d1-2}(x_1)dx_1\end{aligned}\right\} \tag{20}$$

$\mathfrak{F}_{11}$ and $\mathfrak{F}_{12}$ are overall interchange factors defined such that $\mathfrak{F}_{11}l\sigma T_1^4$ and $\mathfrak{F}_{12}l\sigma T_2^4$ ($= \mathfrak{F}_{21}l\sigma T_2^4$) are the rate of absorption by surface 1 per unit depth of energy emitted by surfaces 1 and 2, respectively. Again, it is convenient to present results in terms of overall absorption factors B_{1j}, and these factors are related to the interchange factors by the expressions

$$B_{11} = \frac{\mathfrak{F}_{11}}{\epsilon_a}, \qquad B_{12} = \frac{\mathfrak{F}_{12}}{\epsilon_a} \tag{21}$$

Following a procedure similar to that employed in the development of equation (17) yields total radiant heat transfer as the sum of overall radiant interchange rates

$$\frac{Q_1}{l} = \sum_{j=1}^{3}\frac{Q_{1\rightleftarrows j}}{l} \tag{22}$$

where the overall interchange rate from A_1 to A_j is

$$\frac{Q_{1\rightleftarrows j}}{l} = \mathfrak{F}_{1j}[\sigma T_1^4 - \sigma T_j^4] = \epsilon_a B_{1j}[\sigma T_1^4 - \sigma T_j^4], \qquad 1 \le j \le 3 \tag{23}$$

Thus overall radiant interchange rates may be evaluated for arbitrary plate temperatures once either the overall interchange or absorption factors have been determined.

Rough Surface Radiation Properties

All apparent radiation properties for a one-dimensionally rough surface consisting of symmetric V-shaped roughness elements with identical included angle have been reported [1]. In the cited study asperity walls were diffusely emitting with wall emittance ϵ_w equal to wall absorptance α_w. A direction-independent reflectance model with a specular component $\rho_w{}^s$ and a diffuse component $\rho_w{}^d$ was employed to describe reflection within roughness elements. In addition to material properties, apparent radiation properties depend on roughness element included angle χ. Alternatively, the included angle dependence may be viewed as a dependence on surface roughness slope. The influence of the aforementioned parameters on apparent properties was gener-

ally presented in terms of wall absorptance α_w, wall specularity ratio ρ_w^s/ρ_w, and included angle χ. It is not the purpose here to discuss property results at length, but rather to point out important characteristics of rough properties pertinent to the present study. Detailed development and discussion is available elsewhere [1].

Although all rough surface properties significantly differ from those commonly employed in radiant heat transfer analysis, their most striking feature is the concentration of reflected energy in directions at or near the direction of incident energy. In other words, rough surface bidirectional reflectance is dominated by a back-scattering characteristic. Bidirectional reflectance results for rough surfaces with diffusely reflecting asperities presented in Fig. 2 illustrate this characteristic. Although not included on the figure, a diffusely reflecting plane surface would be represented on this figure by a semicircle with radius ρ_w/π. Gross departure of rough surface bidirectional reflectance from that of a diffusely reflecting plane surface is clearly evident. Even more striking phenomena are suggested by the specular reflectance factors used to construct rough surface bidirectional reflectance for specularly reflecting roughness elements [1] and presented in Fig. 3. In this figure, back-scattering occurs when there is a sign reversal between the direction of incident and reflected energy. It may be observed that a back-scattered beam is present for all directions of incident energy and a forward-scattered beam only exists for a limited range of direction for incident energy. For an included angle of 90 deg [1] a forward-scattered beam does not exist for any direction of incidence.

In Fig. 4 apparent directional emittance results are displayed for selected values for the surface roughness parameters. On this figure a diffusely emitting plane surface is represented by a semicircle with the radial $\epsilon(\theta)$ coordinate equal to wall emittance. Although directional emittance for large ϵ_w does not differ greatly from that for a diffusely emitting smooth surface, significant differences are evident at the smallest ϵ_w for which rough surface directional emittance in the normal direction exceeds wall emittance by a factor as large as three. Clearly, directional emittance and absorptance of the rough surface differs substantially from that of a smooth surface.

Rough surface apparent hemispherical emittance values are presented in Table 1 for various combinations of the roughness parameters. Apparent emittance exceeds that of a plane surface of identical material because of the well-known cavity effect.

Method of Solution

Since only numerical results were available for bidirectional reflectance of rough surfaces with diffusely reflecting asperities, numerical techniques were employed to solve the simultaneous integral equations for the f and g functions of equations (6). The fundamentals of the numerical method employed are discussed elsewhere [4]. The resulting solutions were numerically integrated according to equations (11) and (12) to obtain local radiant interchange factors. Numerical integration of local interchange factors gave total interchange factors. Numerical procedures

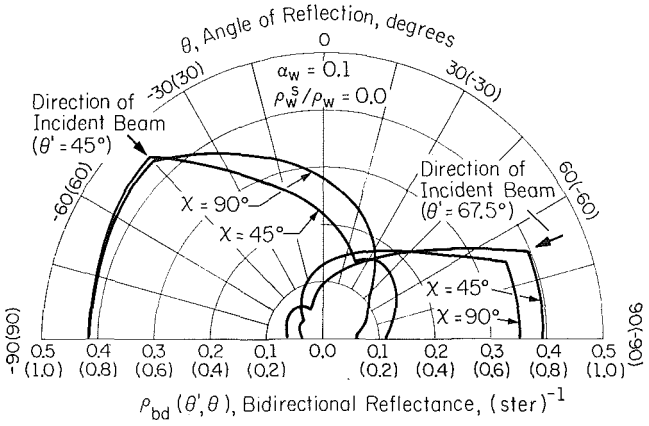

Fig. 2 Bidirectional reflectance for rough surface with diffusely reflecting roughness elements (scales in parenthesis are for $\rho_{bd}(\theta', \theta)$ curves for $\theta' = 67.5$ deg)

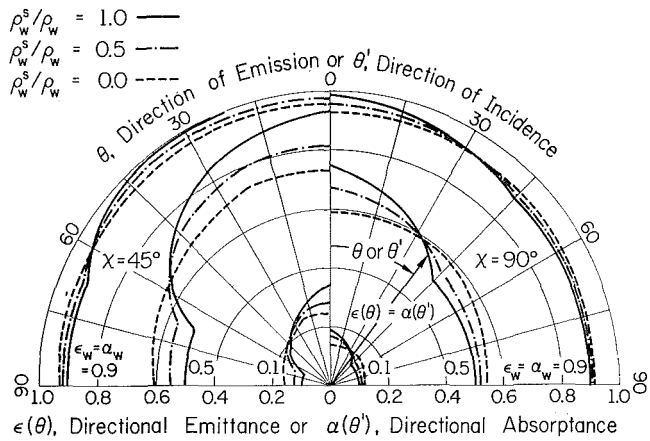

Fig. 4 Apparent directional emittance and absorptance

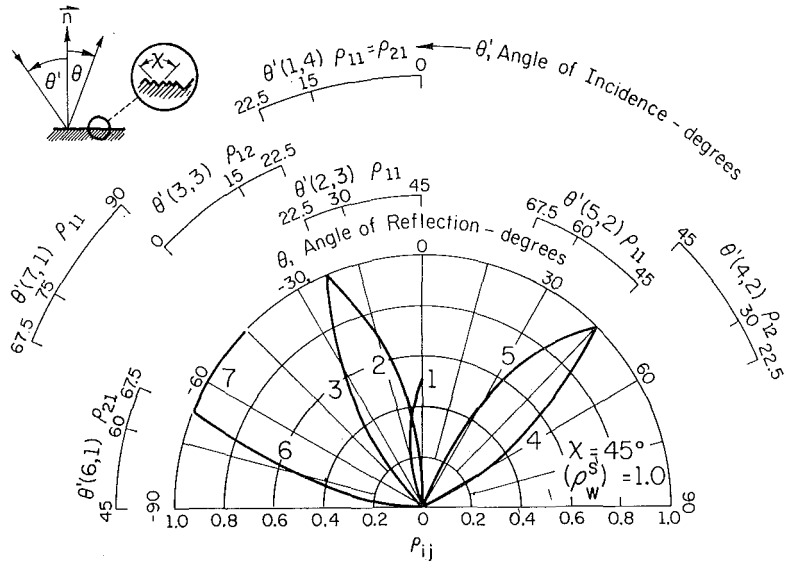

Fig. 3 Specular reflectance factors ($\chi = 45$ deg, $\rho_w^s = 1.0$)

were verified by calculating local and overall heat transfer rates for equal temperature plates from equations (10) and (19) and comparing these results to those reported in an earlier study [4]. In all instances, heat fluxes were within 1 percent of those previously reported. Further verification of the calculation procedure was obtained by comparing overall interchange factor results of this study to those evaluated for diffusely and specularly reflecting surfaces using Monte Carlo techniques [8]. Agreement was within the estimated accuracy of the Monte Carlo results. As a result of these comparisons, it is estimated that the results for local interchange factors are accurate to within 1 percent, and even greater precision was attained for overall interchange factors.

Results and Discussion

Local Absorption Factors. Local radiant absorption factor distributions are illustrated in Figs. 5 and 6 for an included angle of 45 deg between the plates. Material (wall) emittance values of 0.1, 0.5, and 0.9 were considered. Results are presented for rough surfaces with diffusely reflecting ($\rho_w^s/\rho_w = 0.0$) and specularly reflecting ($\rho_w^s/\rho_w = 1.0$) asperities for roughness element included angle (χ) values of 45 and 90 deg. Distributions for B_{d1-2} and B_{d1-1} are shown in Figs. 5 and 6, respectively.

Consider the results for B_{d1-2} shown in Fig. 5. The distributions for the various combinations of roughness parameters χ and ρ_w^s/ρ_w lie in bands which yield larger values for local absorption factor as material emittance increases. Within each band, local absorption factor distributions are generally ordered according to the value for rough surface apparent hemispherical emittance (see Table 1) with the rough surface of greatest apparent emittance yielding the largest value for B_{d1-2}. An exception is the distribution for the low-emittance material with specularly reflecting asperities of smaller roughness slope. Furthermore, the local absorption factor value is generally greater for a surface with specularly reflecting elements than for an identical surface with diffusely reflecting asperities. For high-emittance materials, this trend is mainly attributed to the larger values for directional emittance and absorptance in directions not far removed from the mean surface normal (see Fig. 4) for surfaces with specularly reflecting asperities. On the other hand, for low-emittance materials and particularly for $\chi = 90$ deg, this trend is attributed to the large differences in back-scattering characteristics of rough surface bidirectional reflectance pointed out previously. Although energy reflected from the rough surfaces with diffusely reflecting elements is concentrated in the back-scattering direction, a significant amount of the incident energy exists from the system at each reflection. In contrast, the rough surface with specularly reflecting asperities, particularly for the surface of smaller roughness slope, suffers considerably less energy loss to the environment; hence, it retains emitted energy within the system longer and, thereby, provides greater opportunity for interreflection and, consequently, absorption by the system surfaces. The variation in local absorption factor for the range of values considered for the roughness parameters is less than 5 percent for the high-emittance material. As material emittance decreases, however, the influence of surface roughness increases and yields differences in local absorption factor values of 20–30 percent for materials of intermediate emittance. The variation in B_{d1-2} approaches a factor of two for low-emittance materials. The distributions for the low-emittance material with smaller roughness slope are particularly interesting. Note that according to Table 1, apparent hemispherical emittance for this surface is nearly independent of roughness element specularity. Thus the large differences in local absorption factor values evident in Fig. 5 for surfaces with diffusely and specularly reflecting roughness elements is due almost entirely to differences in the directional dependence of emission and absorption properties as well as the significantly different spatial distribution of reflected energy for the two surfaces.

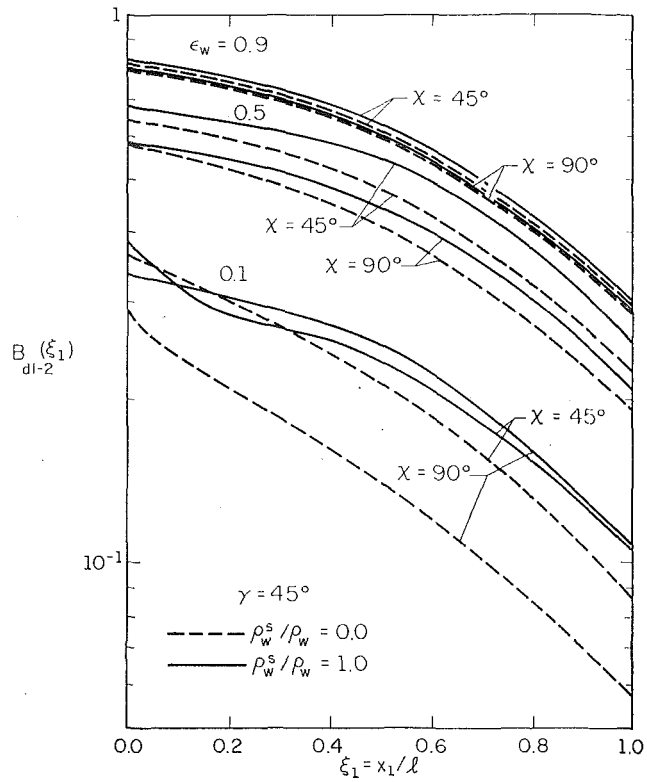

Fig. 5 Surface roughness effects on local absorption factor $B_{d1-2}(\xi_1)$; $\gamma = 45$ deg

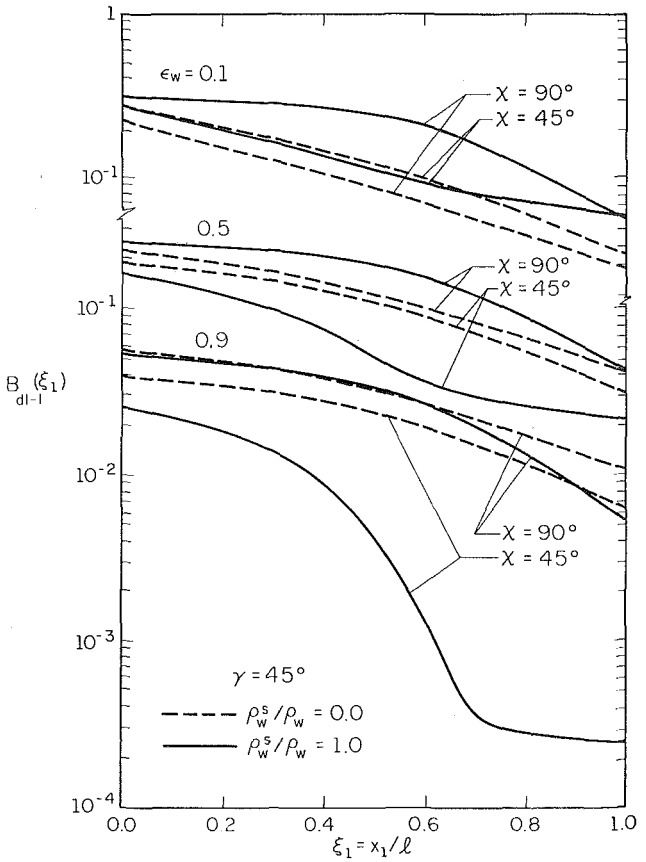

Fig. 6 Surface roughness effects on local absorption factor $B_{d1-1}(\xi_1)$; $\gamma = 45$ deg

The results displayed in Fig. 6 for B_{d1-1} show characteristics which differ from those for B_{d1-2}. Although distributions for different wall emittance remain clustered in bands, those for low and intermediate-emittance materials overlap. Except for one distribution ($\epsilon_w = 0.5$, $\chi = 90$ deg, $\rho_w^s/\rho_w = 0.0$), however, local absorption factor B_{d1-1} diminishes with an increase in material emittance. Furthermore, now local absorption factor generally decreases as apparent hemispherical emittance increases for each material. The back-scattering phenomena particularly dominant for specularly reflecting asperities of 90 deg included angle on the low-emittance surface yields a local absorption factor distribution which exceeds that evaluated for all other combinations of the surface roughness parameters χ and ρ_w^s/ρ_w. Of particular note in Fig. 6 is the large variation in values for B_{d1-1} with the values for roughness element slope and specularity. For low-emittance materials, the variation in B_{d1-1} is commonly of the order of a factor of two to three. This difference increases to almost a factor of five for intermediate-emittance materials. For high-emittance materials, the variation is approximately a factor of two at minimum and attains values close to fifty. In the latter situation, however, it is well to keep in mind that the small energy transfer associated with the low B_{d1-1} values is usually not important in radiant heat transfer calculations.

Of particular interest is a comparison of rough surface local absorption factor results to those evaluated using radiation surface property models commonly employed in engineering analysis. Results were obtained using the diffuse emission model with both a diffuse and a specular reflection model. All directional dependence of surface properties was ignored. One method employed material properties, that is, hemispherical emittance equal to wall emittance $\epsilon_H = \epsilon_w$ with $\epsilon_H = \alpha_H = 1 - \rho_H$. Analysis and results for this model are referred to and denoted as CW—an acronym for constant wall—which is a contraction for constant (direction-independent) property analysis using wall properties. CW analysis completely neglect roughness effects on surface properties, and, therefore, local absorption factors, while employing a direction independent reflection model which assumes reflection, is either diffuse or specular. A second method employed rough surface apparent hemispherical emittance for hemispherical emittance ($\epsilon_H = \epsilon_a$) in the constant property calculation. Analysis and results for this model are referred to and denoted CA—an acronym for constant apparent—which is a contraction for constant property analysis using apparent hemispherical properties of the rough surface. Results from CA analysis account for the influence of surface roughness on the magnitude of energy emitted and reflected but ignore the influence of roughness on the directional character of emission and absorption properties as well as the spatial distribution of reflected energy.

Local absorption factor distributions evaluated from rough surface analysis as well as from the less detailed analysis required for the simpler property models are presented in Fig. 7 for $\epsilon_w = 0.1$. Only a limited number of distributions are illustrated for constant property analysis employing the specular reflection model because these results were always in poorer agreement with rough surface distributions than those evaluated with the diffuse reflection model. Any reference to discrepancy between rough surface and constant property results, therefore, always pertains to constant property analysis employing the diffuse reflection model. Results from CA analysis are keyed to the proper rough surface distribution in Fig. 7 by appending the notation CA with parenthesis which enclose the hemispherical emittance value employed in the computation. Examination of Fig. 7 reveals certain general characteristics. First, CW and CA analysis always yields local absorption factors which are less than those evaluated from rough surface analysis. This should be expected since the back-scattering phenomena dominating reflection from the rough surfaces provides additional opportunity for absorption at the system surfaces. Secondly, engineering analysis generally shows greater error in the calculation of B_{d1-1} than B_{d1-2}. This is attributed to the complete dependence of the former factor on reflected energy and the secondary importance of the latter factor on such energy. In other words, B_{d1-1} is more sensitive to the approximation for the spatial distribution of reflected energy. Thirdly, engineering analysis generally yields better agreement with results for rough surfaces with diffusely reflecting asperities than with results for an identical surface with specularly reflecting roughness elements. This is not surprising in view of the fact that, although the diffuse reflection model

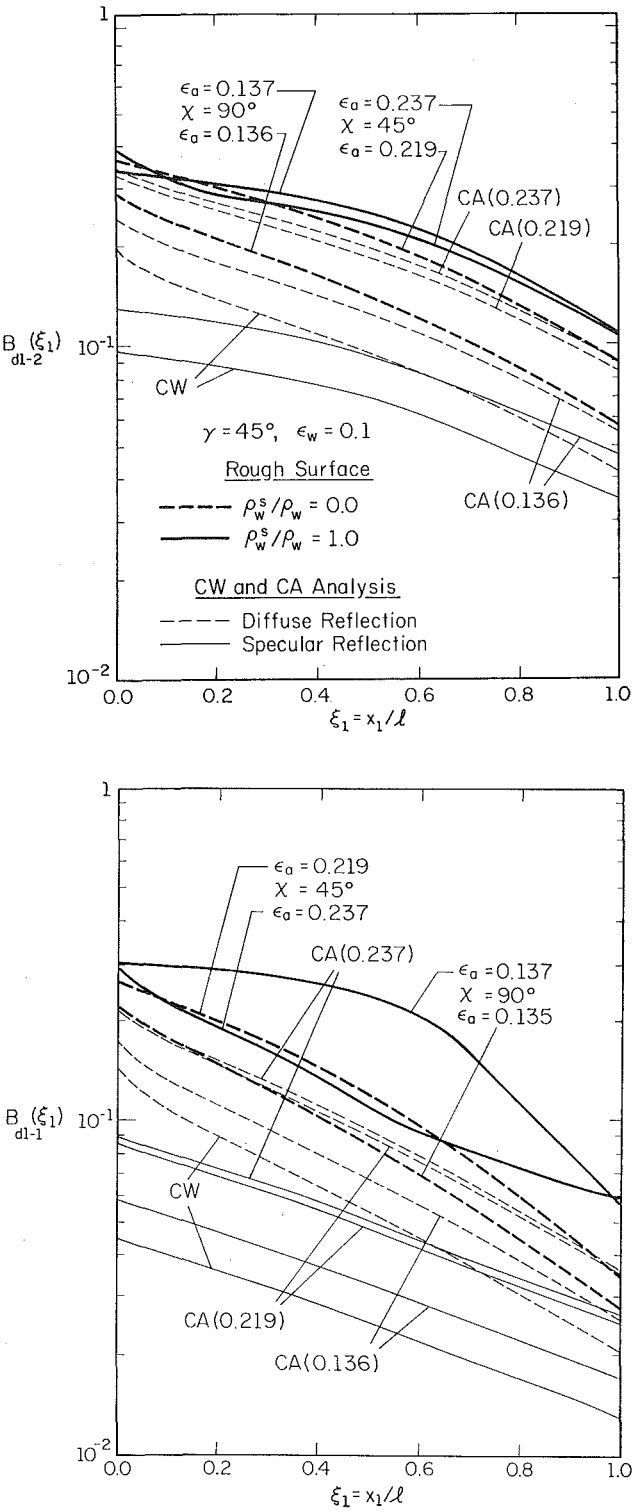

Fig. 7 Comparison of rough surface and approximate results for local absorption factor; $\epsilon_w = 0.1$

does not concentrate reflected energy in the back-scattering direction, it does distribute reflected energy over hemispherical space similar to that of the rough surface with diffusely reflecting roughness elements. On the other hand, the distribution of reflected energy for the diffuse reflection model does not approximate that for the rough surface with specularly reflecting asperities to any significant degree. Finally, complete disregard of the influence of roughness on surface properties such as for CW analysis yields local absorption factor values which are low by as much as a factor of two for B_{d1-2} and a factor of five for B_{d1-1}.

Except for the rough surface with specularly reflecting asperities of larger included angle, the error in results from constant property analysis is markedly reduced when roughness influences on emittance and reflectance are accounted for by utilizing rough surface apparent emittance in the constant property calculation. Although CA analysis with a diffuse reflection model yields the best approximation to the rough surface local absorption factor distributions, discrepancies remain significant. CA analysis yields results which are in error by 10–20 percent for B_{d1-2} and approximately twice these values for B_{d1-1}. In the exceptional case cited previously (χ = 90 deg, ρ_w^s/ρ_w = 1.0), CA analysis is in error by a factor of two to four. This poor agreement is attributed to the unusually large values for B_{d1-1} which occur in this system of rough surfaces because of the large impedance to energy flow to the environment pointed out previously.

Local absorption factor distributions are presented in Fig. 8 for ϵ_w = 0.5. As a consequence of the conclusions drawn from the low wall emittance results, distributions are limited to those from rough surface analysis and CA analysis using a diffuse reflection model. As should be expected in view of the diminished importance of reflected energy to B_{d1-2}, CA analysis yields results for this factor which deviate by less than a maximum of 12 percent from the rough surface values. Some improvement in CA analysis is also observed for B_{d1-1}. CA analysis, however, continues to give values for this factor which are sometimes low by a factor of two.

Although results are not presented here, CA analysis with a diffuse reflection model gave results for B_{d1-2} which differed from the rough surface distributions by less than 2 percent for high-emittance materials. However, CA analysis generally continued to yield poor results for B_{d1-1}.

Overall Absorption Factors. Overall absorption factors are presented in Table 1. Results evaluated from the rough surface and approximate analyses of this study as well as those reported [8] for two other surface property models are tabulated. Values in the column headed DSW employed a directional-emittance model with a direction-dependent specular reflection model. Results contained in the columns with the heading $BP(\sigma_0/\lambda;\ a_0/\lambda)$ were evaluated with a directional-emittance model and a bidirectional-reflectance model for slightly rough surfaces based on diffraction theory. For such surfaces roughness does not effect hemispherical emittance so that $\epsilon_H = \epsilon_a = \epsilon_w$. The diffraction theory bidirectional-reflectance model is generally characterized by a concentration of reflected energy about the specular reflection direction.

Consider first the results obtained in this study. Examination of the values for B_{12} in Table 1 reveals that the rough surface parameters χ and ρ_w^s/ρ_w do not significantly influence this factor for high-emittance materials. As material emittance decreases, however, the influence of the roughness parameters becomes increasingly important. For example, the largest B_{12} value exceeds the smallest value by 60 percent for the low-emittance material. The results for B_{11} show an even stronger dependence on the values for the roughness parameters, and this dependence increases with material emittance. The minimum variation of B_{11} with the roughness parameters is approximately a factor of two for low and intermediate-emittance materials, and this increases to a factor of four for high-emittance materials.

Constant property analysis employing rough surface apparent hemispherical emittance and a diffuse-reflection model yields results in closest agreement with the rough surface values from this study. Comparison of the B_{12} values shows that CA analysis is in error by less than 1 percent for the high-emittance material. Except for χ = 90 deg and ρ_w^s/ρ_w = 1.0, CA analysis is in error by less than 15 percent for the low-emittance material and approximately half this value for the intermediate-emittance material. In the exceptional situation just cited, results from CA analysis are in error by 30 percent for the intermediate-emittance material

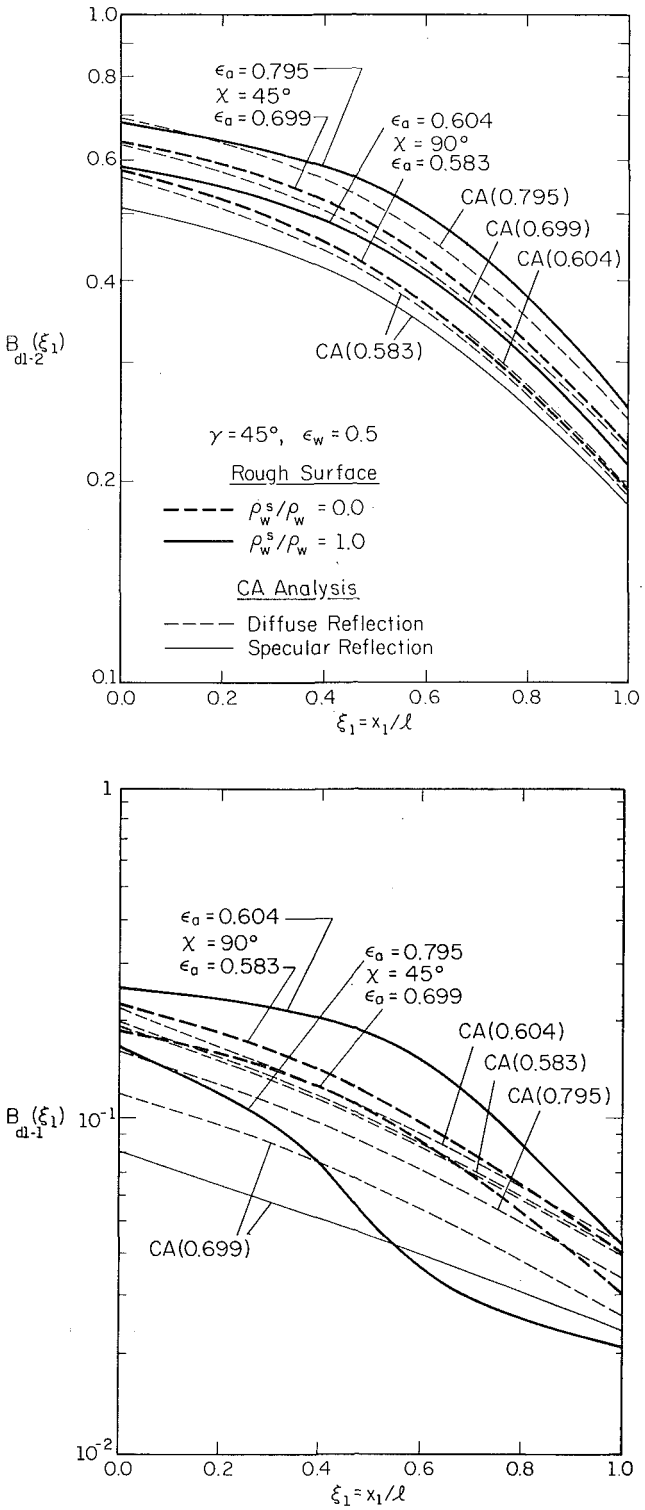

Fig. 8 Comparison of rough surface and approximate results for local absorption factor; ϵ_w = 0.5

and approximately twice this value for the low-emittance material. Results from CA analysis for B_{11} are generally in error by approximately 20 percent for the low-emittance and the discrepancy increases to 30–60 percent for intermediate and high-emittance materials with specularly reflecting roughness elements.

The variation in results for overall interchange factor B_{12} with all surface property models for which values are tabulated is less than 10 percent for high-emittance materials, but this variation sharply increases with decreasing emittance, finally attaining a value of almost a factor of four for low-emittance materials. B_{12} values calculated with the diffraction model always yield low values which do not generally differ significantly from those evaluated with the directional property model (DSW). DSW results, however, are generally in good agreement with CA analysis employing a specular reflection model. In relation to the rough surface results obtained using the diffraction model for bidirectional reflectance, the B_{12} results from this study lie in the intermediate to high ranges of values. As expected, the overall interchange factor, B_{11}, exhibits a stronger dependence on the reflectance model employed in its evaluation. For both high and low-emittance materials, the variation in B_{11} with the various property models used exceeds a factor of eight. The diffraction model for roughness effects yields low values for B_{11} for low-emittance materials, intermediate values for intermediate-emittance materials, and generally high values for high-emittance materials. The roughness model employed here generally yields intermediate to high values for B_{11}.

Conclusion

Radiant energy interchange between interacting one-dimensionally rough surfaces was formulated for a system of simple geometrical character. The direction-dependent apparent thermal radiation properties of the rough surfaces introduced into the analysis include bidirectional reflectance, directional emittance, and directional absorptance. Rough surface properties depend on three surface roughness parameters: constituent material emittance, roughness element specularity, and roughness included angle or slope. Local absorption factor distributions and overall absorption factors were evaluated for a range of values for each roughness parameter. Supplementary absorption factor results were determined from less detailed analysis utilizing the simple property models commonly employed in engineering analysis.

The following conclusions may be drawn from this study. First, from a comparison of the results presented here and those reported previously [4] for radiant heat loss, it is evident that surface roughness influences radiant interchange to a greater degree than radiant heat loss. Secondly, although the dependence of absorption factor values for adjacent surfaces on surface roughness was small for high-emittance materials, this dependence steadily increases as material emittance diminished. For low-emittance materials, differences amounting to a factor of two in local absorption factor and 60 percent in overall absorption factor were observed as the surface roughness parameters were varied over the limited range considered here. Thirdly, interchange factors for self-interchange demonstrated an even stronger dependence on surface roughness, and this dependence increased with increasing material emittance. Finally, of the simple property models considered, the diffuse emission-diffuse reflection model employing rough surface apparent hemispherical emittance gave the closest agreement to rough surface results for local and overall absorption factors. Agreement was significantly better for interchange factors between adjacent surfaces than for a surface to itself. The discrepancy between the simple model results and interchange factors for adjacent surfaces was generally of the order of 20 percent and sharply diminished as material emittance increased. On the other hand, self-absorption factors calculated with the simple property model differed from rough surface values by a factor as large as two to four.

References

1 Hering, R. G., and Smith, T. F., "Apparent Radiation Properties of a Rough Surface," AIAA Paper No. 69-622, to be published in *AIAA Progress Series*, vol. entitled "Thermophysics: Application to Thermal Design of Spacecraft."

2 Hering, R. G., and Smith, T. F., "Surface Roughness Effects on Equilibrium Temperature," *Journal of Spacecraft and Rockets*, Vol. 6, No. 8, 1969, pp. 955–957.

3 Hering, R. G., and Smith, T. F., "Surface Roughness Effects on Radiant Heat Transfer," *Journal of Spacecraft and Rockets*, Vol. 6, No. 12, 1969, pp. 1465–1466.

4 Hering, R. G., and Smith, T. F., "Surface Roughness Effects on Radiant Transfer Between Surfaces," to be published in *International Journal of Heat Mass Transfer*.

5 Hering, R. G., Smith, T. F., and Shaffer, J. T., "Surface Roughness Effects on Radiant Transfer Between Surfaces," to be

Table 1 Overall absorption factors for $\gamma = 45$ deg

				B_{12}								
		ϵ_a		$\chi = 45°$		$\chi = 90°$		BP($\sigma_o/\lambda, a_o/\lambda$)†				
ϵ_w	ρ_w^s/ρ_w	$\chi = 45°$	$\chi = 90°$	Rough Surface	CA Analysis	Rough Surface	CA Analysis	(2/3,10)	(1/6,5/2)	(1/30,1/2)	DSW† Analysis	CW Analysis
0.1	0.0	0.219	0.135	0.216	0.189*	0.149	0.129	0.0753	0.080	0.0742	0.074	0.100*
					0.146**		0.0911					
	1.0	0.237	0.137	0.229	0.201	0.238	0.131					0.0679**
					0.157		0.0924					
0.5	0.0	0.699	0.583	0.462	0.450	0.401	0.391	0.317	0.325	0.318	0.318	0.349
					0.436		0.368					
	1.0	0.795	0.604	0.517	0.500	0.430	0.402					0.318
					0.493		0.380					
0.9	0.0	0.952	0.926	0.590	0.588	0.574	0.573	0.564	0.566	0.559	0.568	0.558
					0.588		0.572					
	1.0	0.982	0.937	0.610	0.606	0.584	0.580					0.557
					0.606		0.579					
				B_{11}								
0.1	0.0	0.219	0.135	0.129	0.100	0.0970	0.0758	0.0548	0.0474	0.0335	0.0314	0.0615
					0.0502		0.0343					
	1.0	0.237	0.137	0.132	0.104	0.210	0.0766					0.0264
					0.0530		0.0350					
0.5	0.0	0.699	0.583	0.108	0.0900	0.126	0.109	0.143	0.120	0.075	0.0773	0.116
					0.0618		0.0714					
	1.0	0.795	0.604	0.0700	0.0681	0.165	0.106					0.0734
					0.0478		0.0702					
0.9	0.0	0.952	0.926	0.0230	0.0187	0.0324	0.0281	0.0442	0.0289	0.0139	0.0142	0.0370
					0.0134		0.0201					
	1.0	0.982	0.937	0.00824	0.00723	0.0310	0.0242					0.0264
					0.00519		0.0173					

*Diffuse Reflection Model. **Specular Reflection Model. †From [8].

published in Proceedings of Fourth International Heat Transfer Conference, Versailles, France, 1970.

6 Schornhorst, J. R., and Viskanta, R., "Effect of Direction and Wavelength Dependent Surface Properties on Radiant Heat Transfer," *AIAA Journal*, Vol. 6, 1968, 1450-1455.

7 Toor, J. S., and Viskanta, R., "A Numerical Experiment of Radiant Heat Interchange by the Monte Carlo Method," *International Journal of Heat Mass Transfer*, Vol. 11, 1968, pp. 883–897.

8 Toor, J. S., "Radiant Heat Transfer Analysis Among Surfaces Having Direction Dependent Properties by the Monte Carlo Method," M.S.M.E. Thesis, Purdue University, Lafayette, Ind., June 1967.

9 Sparrow, E. M., Gregg, J. L., Szel, J. V., and Manos, P., "Analysis, Results and Interpretation for Radiation Between Some Simply Arranged Gray Surfaces," JOURNAL OF HEAT TRANSFER, TRANS. ASME, Vol. 83, No. 2, May 1961, pp. 207-214.

10 Eckert, E. R. G., and Sparrow, E. M., "Radiative Heat Exchange Between Surfaces with Specular Reflection," *International Journal of Heat Mass Transfer*, Vol. 3, 1961, pp. 42–54.

11 Hering, R. G., "Radiative Heat Exchange and Equilibrium Surface Temperature in a Space Environment," *Journal of Spacecraft and Rockets*, Vol. 5, No. 1, 1968, pp. 47-54.

12 Hering, R. G., "Radiative Heat Exchange Between Specularly Reflecting Surfaces With Direction Dependent Properties," Proceedings of the Third International Heat Transfer Conference, AIChE, New York, 1966, Vol. V, pp. 200-206.

VIJAY DHIR
Research Assistant.

JOHN LIENHARD
Professor.
Mem. ASME

Boiling and Phase-Change Laboratory,
Mechanical Engineering Department,
University of Kentucky,
Lexington, Ky.

Laminar Film Condensation on Plane and Axisymmetric Bodies in Nonuniform Gravity[1]

Expressions are developed for the condensate film thickness and the local Nusselt number on arbitrary axisymmetric bodies, including vertical plates and cylinders. The expressions are the same as the Rohsenow-Nusselt expressions except that they are based on an "effective gravity" that corrects both for variable gravity and for the form of the body. The limitations on the expressions are: that radii of curvature greatly exceed the film thickness, that Prandtl numbers are never much less than unity, and that the ratio of sensible to latent heats is not large. These criteria include almost all practical situations. Several applications are developed.

Introduction

Contemporary schemes for augmenting heat transfer frequently call for condensation in nonuniform body force fields, or on various surfaces whose slopes change in a uniform gravity field. This is true, for example, in space applications, in certain heat pipe configurations, and for many bodies at earth-normal gravity. Our own interest in this problem was initially motivated by the need to design a reflux condenser for a centrifuge boiling experiment.

The problem of laminar film condensation on a vertical plate in a constant gravity field was solved by Nusselt in 1916 [1][2] subject to two major assumptions. The first—that the temperature profile in the film is linear—was corrected by Rohsenow in 1956 [2]. Both this and the second assumption—that the inertia terms in the momentum equation could be neglected—were delimited by Sparrow and Gregg in 1959 [3]. The very complete treatment in [3] verified Rohsenow's modification of Nusselt's result[3]

$$\mathrm{Nu} = 0.707 \left[g \frac{\rho_f(\rho_f - \rho_g)h_{fg}'x^3}{\mu k \Delta T} \right]^{1/4} \tag{1}$$

for all Prandtl numbers on the order of unity or greater and for

[1] This work was supported by NASA Grant NGR/18-001-035.
Contributed by the Heat Transfer Division for publication (without presentation) in the Journal of Heat Transfer. Manuscript received by the Heat Transfer Division, May 7, 1970; revised manuscript received, June 30, 1970. Paper No. 70-HT-P.

[2] Numbers in brackets designate References at end of paper.

[3] Symbols not explained in context are defined in the Nomenclature section.

Nomenclature

$A = \mu k \Delta T/(\rho_f - \rho_g)\rho_f h_{fg}'$
C = arbitrary constant
c_p = specific heat of condensate
D = diameter of a horizontal cylinder or sphere
g = gravitational acceleration
g_{eff} = an effective g for use in Nusselt's equations, defined by equation (10)
h = heat transfer coefficient
h_{fg} = latent heat of vaporization
h_{fg}' = h_{fg} corrected to account sensible heat of subcooling in the film; equal to $h_{fg} + 0.68\, c_p \Delta T$
k = thermal conductivity of condensate (or of vapor in the film boiling problem)
Nu = local Nusselt number, hx/k or $h(\mu/\rho_f\omega^2)^{1/2}/k$
Nu_D = Nusselt number for a cylinder or a sphere, $(hD/k)_{\mathrm{average}}$
R = radius of curvature of an axisymmetric body
X = distance from axis of rotation to top of plate in a rotational system
x = distance along plate from leading edge
y = distance normal to plate from surface
Γ_c = rate of mass flow of condensate per unit breadth
α = cone angle
ΔT = difference between saturation temperature and wall temperature
δ = condensate film thickness
μ = viscosity of condensate (or of vapor in the film boiling problem)
ρ_f, ρ_g = densities of liquid and saturated vapor, respectively
ω = angular velocity

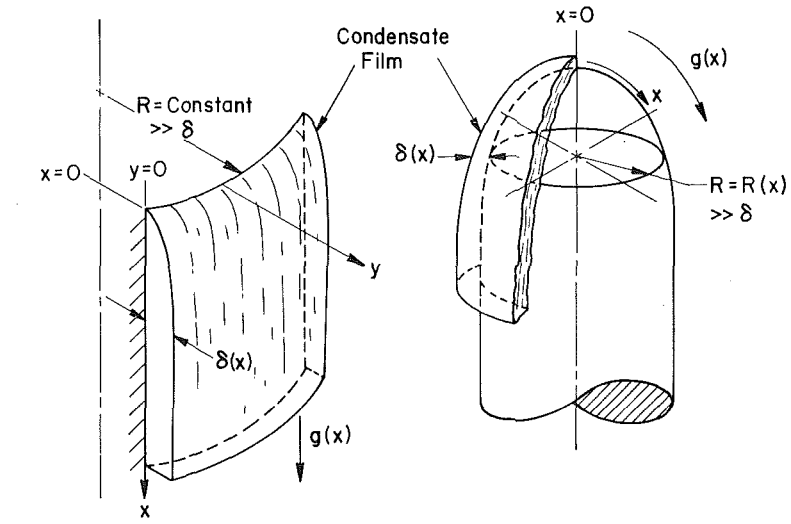

a) vertical plate or vertical cylinder b) axi-symmetric body

Fig. 1 Configurations under present consideration

$c_p\Delta T/h_{fg}$ less than the order of unity. The latent heat of vaporization corrected for sensible heat absorption in the film, h_{fg}', is

$$h_{fg}' = h_{fg}(1 + 0.68\, c_p\Delta T/h_{fg}) \tag{2}$$

which slightly exceeds Nusselt's earlier prediction.

The limitations imposed by [3] only exclude equation (1) from use with liquid metals. It will provide valid predictions of almost all other physically realistic situations. But liquid metal condensation, in turn, introduces grave complications related to accommodation coefficients and possible temperature decrements between the saturation temperature and the liquid-vapor interface. These difficulties exclude liquid metals from the present kind of treatment in any case.

With this limitation in mind we shall redevelop the Nusselt-Rohsenow analysis for a general gravity field, $g(x)$, where x is the distance from the leading edge of a plate, or nose of an axisymmetric body, as shown in Fig. 1. The "gravity" might actually be varying as it would in, say, a centrifugal field; or the slope of the surface might be curved so that the x coordinate is bent and the component of a gravity force might change with x; or both effects might be present. It would be convenient if Sparrow and Gregg's analysis could be adapted for $g = g(x)$; however, their similarity transformation generally breaks down when g varies arbitrarily with x.

We shall also allow the radius of curvature $R(x)$ of the body to vary. The vertical cylinder or plate (Fig. 1*a*, with R = constant or ∞) are special cases of the present situation. Our solution, like all of the previous condensation solutions, will not really be valid unless $x \gg \delta$. It will likewise be invalid unless $R \gg \delta$. Since these conditions are generally met while x and R are still much less than characteristic dimensions, their failure near $x = 0$ will introduce very minor error.

Sparrow and Gregg [4] adapted their method to one case of condensation in a nonuniform body force field on an axisymmetric body. They found that the condensing film on a disk rotating at ω rad/sec was of uniform thickness so that their similarity transformation became trivial. Their limiting value of Nusselt number for negligible inertia was independent of radius:

$$\mathrm{Nu} \equiv \frac{h}{k}\left(\frac{\mu}{\rho_f\omega}\right)^{1/2} = 0.904\left[\frac{(\rho_f - \rho_g)h_{fg}'\mu}{\rho_f k\Delta T}\right]^{1/4} \tag{3}$$

Since there is inherently great outward and Coriolis acceleration, the limitations on this solution are a little more stringent than on equation (1). It is generally accurate only for $c_p\Delta T/h_{fg} \lesssim 0.1$, and accurate for higher $c_p\Delta T/h_{fg}$ only if the Prandtl number stays just a little larger than unity.

Sparrow and Gregg also used their methods to treat a third case [5] which also will be accessible to our method, namely condensation on a horizontal pipe. Their no-inertia limit was

$$\mathrm{Nu}_D = C\left[g\frac{\rho_f(\rho_f - \rho_g)h_{fg}'D^3}{\mu k\Delta T}\right]^{1/4} \tag{4}$$

where C was 0.733. Nusselt had also done this problem in his original paper and obtained $C = 0.725$. Chen [6] subsequently corrected two of Sparrow and Gregg's analyses [3, 5] for vapor drag on the interface and obtained the presently accepted value of $C = 0.728$.

Analysis

Nusselt's local mass flow rate $\Gamma_c \mathrm{lb}_m/\mathrm{ft\text{-}hr}$ is expressible in terms of the film thickness $\delta(x)$ without reference to the history of the film up to this location, as

$$\Gamma_c = [(\rho_f - \rho_g)\rho_f/3\mu]\delta^3 g(x) \tag{5}$$

Since the temperature distribution can be assumed linear,

$$h\Delta T = k\Delta T/\delta = \frac{h_{fg}'}{2\pi R(x)}\frac{d[\Gamma_c 2\pi R(x)]}{dx} \tag{6}$$

Substituting equation (5) in the right-hand equation of (6) gives

$$3A = \frac{3(\delta[gR]^{1/3})^3 d(\delta[gR]^{1/3})}{g^{1/3}R^{4/3}\,dx} \tag{7}$$

where $A \equiv \mu k\Delta T/(\rho_f - \rho_g)\rho_f h_{fg}'$. Integrating equation (7) subject to the boundary condition $\delta(x = 0) = 0$ gives

$$\frac{4A}{(gR)^{4/3}}\int_0^x g^{1/3}R^{4/3}\,dx = \delta^4 \tag{8}$$

Thus

$$\delta = \left[\frac{4\mu k\Delta T x}{(\rho_f - \rho_g)\rho_f h_{fg}' g_{\mathrm{eff}}}\right]^{1/4} \tag{9}$$

where

$$g_{\text{eff}} \equiv \frac{x(gR)^{4/3}}{\int_0^x g^{1/3} R^{4/3}\, dx} \tag{10}$$

Finally, we can write the local Nusselt number as

$$\text{Nu} = \frac{(k/\delta)x}{k} = \left[g_{\text{eff}} \frac{(\rho_f - \rho_g)\rho_f h_{fg}' x^3}{4\mu k \Delta T} \right]^{1/4} \tag{11}$$

With the exception of the use of an effective gravity, this is identical to equation (1). In terms of A, it can be written as

$$\text{Nu} = 0.707 \left[g_{\text{eff}} \frac{x^3}{A} \right]^{1/4} \tag{11a}$$

Examples of Applications

Equations (10) and (11) provide a convenient and versatile method for handling a wide variety of problems. We shall illustrate their use with several examples. Each example will be generally restricted to low $c_p\Delta T/h_{fg}$ or, for larger $c_p\Delta T/h_{fg}$, to Prandtl numbers on the high side of unity.

1 Vertical Flat Plate, Constant Gravity. In this case R is a constant which approaches infinity and equation (10) gives $g_{\text{eff}} = g$. Thus equation (11) reduces to equation (1).

2 Horizontal Cylinder. Again R is a constant approaching infinity, and the local x component of gravity, $g \sin (2x/D)$, should be used for $g(x)$ in equation (10). When g_{eff} is evaluated numerically, and the resulting value of h, obtained from equation (11), is averaged over the circumference of the cylinder, the result can be used to write a Nusselt number based on the diameter, D,

$$\text{Nu}_D = 0.729[gD^3/A]^{1/4} \tag{12}$$

which compares extremely well with the accepted value of $0.728[gD^3/A]^{1/4}$. Presumably Nusselt would also have obtained $C = 0.729$ had he had a digital computer to work with.

3 Upper Half of a Horizontal Cylinder. A similar integration halfway around the cylinder gives

$$\text{Nu}_D = 0.866[gD^3/A]^{1/4} \tag{13}$$

as compared with Nusselt's value of $0.861[gD^3/A]^{1/4}$.

4 Lower Half of a Horizontal Cylinder. If condensation begins at the middle of the tube and continues around the bottom, or if it simply continues around the bottom from the top, the results are fortuitously identical to three decimal places

$$\text{Nu}_D = 0.592[gD^3/A]^{1/4} \tag{14}$$

Nusselt obtained 0.589 for the numerical factor.

5 Rotating Horizontal Disk. In this case $g = \omega^2 x$ and $R = x$. Equation (10) gives $g_{\text{eff}} = 3\omega x/8$ and

$$\text{Nu} = 0.9036[(\mu/\rho_f)^2/A]^{1/4} \tag{15}$$

which agrees with Sparrow and Gregg's result.

6 Stationary Cone. Here we have a gravity of $g \cos (\alpha/2)$, where $R = x \sin (\alpha/2)$. This gives $g_{\text{eff}} = (7/3)\, g \cos (\alpha/2)$, and

$$\text{Nu} = 0.874[\cos (\alpha/2)]^{1/4}[gx^3/A]^{1/4} \tag{16}$$

7 Stationary Sphere. The gravity is $g \sin (2x/D)$ as it was for the horizontal cylinder but R is now $(D/2) \sin (2x/D)$. This, like the horizontal cylinder, requires a straightforward numerical integration. The result is

$$\text{Nu}_D = 0.785[gD^3/A]^{1/4} \tag{17}$$

8 Rotating Plate. The original motivation for undertaking this study was the problem of predicting condensation on a rotating plate aligned on a radial plane with its top located a distance X from the axis of rotation. In this case, R is a constant approaching infinity and $g = \omega^2 X + \omega^2 x$. Equation (10) gives

$$g_{\text{eff}} = \frac{4x\omega^2/3}{1 - [X/(X + x)]^{4/3}} \tag{18}$$

Accordingly the film thickness is

$$\delta = \left\{ \frac{3}{A\omega^2} [1 - (X/[X + x])^{4/3}] \right\}^{1/4} \tag{19}$$

When X is shrunk to zero, $\delta \to (3/A\omega^2)^{1/4}$ which (like δ for the rotating disk) is constant. The local Nusselt number in this case is

$$\text{Nu} \equiv \frac{h}{k} \left(\frac{\mu}{\rho_f \omega} \right)^{1/2} = 0.760[(\mu/\rho_f)^2/A]^{1/4} \tag{20}$$

which is of the same general form as the rotating disk result, with a smaller constant.

An Application to Film Boiling

Clearly a table of examples could be proliferated *ad nauseam*. The method is sufficiently simple that it is not necessary to do so, however. But an interesting experimental verification can be made for case 7 with the aid of data for film boiling on a sphere:

Several years ago Bromley [7] viewed film boiling on horizontal cylinders as the inverse of the condensation process and used equation (4), with a slightly modified value of h_{fg}', to describe it.[4] Since a portion of the vapor film at the top is inactive in the heat removal process owing to the bubble release process, C should be less than 0.728. Bromley's experiments showed it to be 0.62 or *85.2 percent* of the value for condensation.

We can also use equation (17) to predict the heat transfer during film boiling from a sphere. If we multiply it by the same correction factor of 85.2 percent, and change k and μ to the values for vapor, we get

$$\text{Nu}_D = 0.67[gD^3/A]^{1/4} \tag{21}$$

But this is *exactly* the expression that Frederking and Daniels [8] found would correlate their data for heat transfer during film boiling from spheres.[5]

Conclusion

The local Nusselt number for an axisymmetric body in a nonuniform gravity field is

$$\text{Nu} = 0.707[g_{\text{eff}} x^3/A]^{1/4}$$

where

$$g_{\text{eff}} = \frac{x(gR)^{4/3}}{\int_0^x g^{1/3} R^{4/3} dx}$$

These expressions are, practically speaking, valid for all but liquid metals applications.

References

1 Nusselt, W., "Die Oberflächenkondensation des Wasserdampfes," Z. *Ver. Deutsch. Ing.*, Vol. 60, 1916, pp. 541–6, 569–75.

2 Rohsenow, W. M., "Heat Transfer and Temperature Distribution in Laminar Film Condensation," TRANS. ASME, Vol. 78, 1956, pp. 1645–48.

[4] The viscosity and thermal conductivity are now those for the *vapor* film instead of for saturated liquid.

[5] The prediction of Nu for film boiling is actually a little more complicated than we have indicated here. A recent study of film boiling from spheres by Hendricks and Baumeister [9] shows that the portion of the film not contributing strongly to heat transfer should actually vary slightly with A, and it shows that the liquid can exert significant traction on the film. However, it also shows that equation (21) gives generally good results.

3 Sparrow, E. M., and Gregg, J. L., "A Boundary-Layer Treatment of Laminar-Film Condensation," JOURNAL OF HEAT TRANSFER, TRANS. ASME, Series C, Vol. 81, No. 1, Feb. 1959, pp. 13–18.

4 Sparrow, E. M., and Gregg, J. L., "A Theory of Rotating Condensation," JOURNAL OF HEAT TRANSFER, TRANS. ASME, Series C, Vol. 81, No. 2, May 1959, pp. 113–120.

5 Sparrow, E. M., and Gregg, J. L., "Laminar Condensation Heat Transfer on a Horizontal Cylinder," JOURNAL OF HEAT TRANSFER, TRANS. ASME, Series C, Vol. 81, No. 3, Nov. 1959, pp. 291–296.

6 Chen, M. M., "An Analytical Study of Laminar Film Condensation, Parts 1 and 2," JOURNAL OF HEAT TRANSFER, TRANS. ASME, Series C, Vol. 83, No. 1, Feb. 1961, pp. 48–60.

7 Bromley, L. A., "Heat Transfer in Stable Film Boiling," *Chem. Engr. Prog.*, Vol. 46, 1950, p. 221.

8 Frederking, T. H. K., and Daniels, D. J., "The Relation Between Bubble Diameter and Frequency of Removal from a Sphere During Film Boiling," JOURNAL OF HEAT TRANSFER, TRANS. ASME, Series C, Vol. 88, No. 1, Feb. 1966, pp. 87–93.

9 Hendricks, R. C., and Baumeister, K. J., "Film Boiling from Submerged Spheres," NASA TN-D-5124, June 1969.

KENNETH A. RATHJEN
Senior Thermodynamicist,
Grumman Aerospace Corporation,
Bethpage, N. Y.
Mem. ASME

LATIF M. JIJI
Professor of Mechanical Engineering,
The City University of New York,
New York, N. Y.

Heat Conduction With Melting or Freezing in a Corner[1]

This paper presents an analytical solution to the two-dimensional free boundary problem of solidification of a liquid, initially at a uniform temperature and filling the quarter-space $x, y > 0$, subject to a constant wall temperature. The problem is the two-dimensional analog of Neumann's freezing problem. The solution is characterized by similarity in the variables $x/t^{1/2}$, $y/t^{1/2}$ and is obtained by treating the heat of solidification as a moving heat source. A nonlinear, singular, integro-differential equation for the solid-liquid interface is thereby derived and used to establish superhyperbolas to approximate the interface position. Results are presented for a range of the two dimensionless parameters of the problem. The accuracy of the superhyperbolic representation of the interface position is determined by comparison with a finite-difference solution. Equations are given for the calculation of the temperature fields in the solid and liquid regions that are valid for all time (i.e., they are not necessarily short- or long-time solutions).

Introduction

A LARGE number of technically important problems involve solution of the equation describing diffusion of heat, mass, or some other scalar quantity, subject to boundaries that are neither fixed in space nor known a priori. Appropriately, much work has been done in treating these free boundary problems. Boley [1],[2] Bankoff [2], and Muehlbauer and Sunderland [3] cite many references in their comprehensive literature surveys.

With few exceptions, the problems considered thus far have been one-dimensional, with most solutions obtained via approximate and numerical methods. This is due to the nonlinearity of such problems, which enters as a boundary condition at the free boundary.

In the 1860's Neumann [4, p. 282] presented an exact solution to the solidification of the initially liquid half-space $y > 0$ with the surface $y = 0$ maintained at a lower than fusion temperature. Neumann's solution, which is one of the few exact solutions available, has become a classic and is frequently used to check approximate solutions of problems that in some limit become the Neumann problem; cf. references [5–8]. It has also been useful for starting numerical or approximate analyses to related problems [4, p. 476; 9].

This paper considers the two-dimensional analog of Neumann's problem—the solidification of the initially liquid quarter-space $x, y > 0$ with the surfaces $x = 0$ and $y = 0$ maintained at a lower than fusion temperature.

To date, few solutions of two-dimensional free boundary problems have been published. Allen and Severn [10] using a relaxation method treated the inward solidification of a uniform prism having a square cross section, subjected to a constant boundary temperature. The liquid phase was assumed to be at the fusion temperature, thereby removing it from further consideration.

Poots [11] considered the same problem as Allen and Severn [10] using the approximate integral methods of boundary layer theory in fluid mechanics that are associated with the names of von Kármán-Pohlhausen and Tani. The location and time history of the free boundary for a specific liquid are given in tabular and graphical form and show reasonable agreement with those obtained by Allen and Severn.

Springer and Olson [12] considered the two-dimensional problem of axisymmetric freezing and melting of materials contained between two concentric cylinders of finite length. The descriptive differential equations of the system were approximated by finite-difference equations which were solved on a digital computer.

Using an embedding technique, Sikarskie and Boley [13] found short-time series solutions for two problems where two-dimensional effects were introduced by spatial variations of heating or cooling conditions along one boundary surface of a slab.

---

[1] Abstracted from the thesis submitted by Dr. Rathjen in partial fulfillment of the requirements for the PhD degree at The City University of New York.

[2] Numbers in brackets designate References at end of paper.

Contributed by the Heat Transfer Division for publication (without presentation) in the JOURNAL OF HEAT TRANSFER. Manuscript received by the Heat Transfer Division, June 3, 1968; revised manuscript received, June 29, 1970. Paper No. 70-HT-Q.

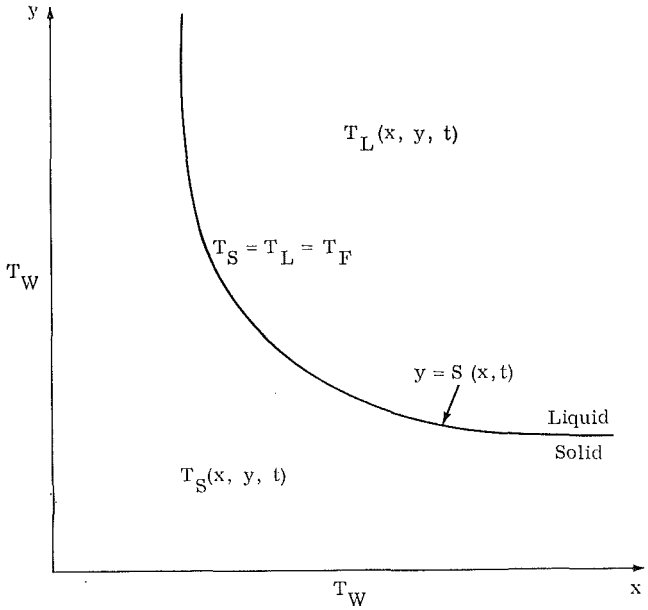

Fig. 1 Two-dimensional solidification problem

The Mathematical Problem

The problem under consideration is the initially liquid quarter-space $x, y > 0$ at a constant temperature T_i, which is greater than or equal to the fusion temperature T_F. For time $t \geq 0$, the surfaces $x = 0$ and $y = 0$ are maintained at a constant temperature T_W that is lower than T_F. At time $t = 0$, a change of phase occurs along the surfaces $x = 0$ and $y = 0$; at time $t > 0$, the phase change occurs at the free boundary, which is expressed by $y = S(x, t)$; see Fig. 1. The temperature fields $T_S(x, y, t)$ and $T_L(x, y, t)$ in the solid and liquid regions are to be found, as is the interface position $S(x, t)$.

The following dimensionless temperatures are adopted:

$$T_S^* = \frac{(T_S - T_F)}{(T_F - T_W)}$$

$$T_L^* = \frac{k_L(T_L - T_F)}{k_S(T_F - T_W)}$$

$$T_i^* = \frac{k_L(T_i - T_F)}{k_S(T_F - T_W)}$$

where k_S and k_L denote respectively the thermal conductivity in the solid and liquid regions.

In terms of the dimensionless temperatures, the descriptive equations for the problem are

$$\frac{\partial^2 T_S^*}{\partial x^2} + \frac{\partial^2 T_S^*}{\partial y^2} = \frac{1}{\alpha}\frac{\partial T_S^*}{\partial t} \quad \text{for } 0 < x < \infty \text{ and } 0 < y < S(x, t) \tag{1}$$

$$\frac{\partial^2 T_L^*}{\partial x^2} + \frac{\partial^2 T_L^*}{\partial y^2} = \frac{1}{\alpha}\frac{\partial T_L^*}{\partial t} \quad \text{for } 0 < x < \infty \text{ and } S(x, t) < y < \infty \tag{2}$$

$$T_S^*(0, y, t) = -1 \tag{3}$$

$$T_S^*(x, 0, t) = -1 \tag{4}$$

$$T_L^*(x, y, t) = T_i^* \quad \text{for } x \to \infty \text{ and } y \to \infty \tag{5}$$

$$T_L^*(x, y, 0) = T_i^* \tag{6}$$

$$T_S^*(x, S(x, t), t) = T_L^*(x, S(x, t), t) = 0 \tag{7}$$

$$k_S\left[\frac{\partial T_S^*}{\partial y} - \frac{\partial T_L^*}{\partial y}\right]\left[1 + \left(\frac{\partial S}{\partial x}\right)^2\right] = \frac{\rho L}{T_F - T_W}\frac{\partial S}{\partial t} \quad \text{for } y = S(x, t) \tag{8}$$

Nomenclature

c = specific heat
C = constant in superhyperbola = $(x_0^{*m} - \lambda^m)^2$
f = interface position in x^*, y^* domain
k = thermal conductivity
L = latent heat of fusion
m = exponent in superhyperbola
S = interface position in x, y, t domain
t = time
t' = integration variable
T = dimensionless temperature field = $U + V$
T_F = fusion temperature
T_i = initial temperature
T_i^* = dimensionless initial temperature $= \frac{k_L}{k_S}\left[\frac{T_i - T_F}{T_F - T_W}\right]$
T_L = temperature field in liquid region
T_L^* = dimensionless temperature field in liquid region $= \frac{k_L}{k_S}\left[\frac{T_L - T_F}{T_F - T_W}\right]$
T_S = temperature field in solid region
T_S^* = dimensionless temperature field in solid region $= \frac{T_S - T_F}{T_F - T_W}$
T_W = wall temperature
U = dimensionless temperature field in rectangular corner with boundary temperature of -1 and initial temperature T_i^*
V = dimensionless temperature field in rectangular corner with boundary and initial temperature zero and with a moving heat source
w_i = Gaussian weighting factors
x = coordinate
x^* = dimensionless coordinate = $x/(4\alpha t)^{1/2}$
x' = integration variable
x_0 = intersection of line $y = x$ and interface curve in x, y, t domain
x_0^* = intersection of line $y^* = x^*$ and interface curve in x^*, y^* domain
x_1^* = x^* value corresponding to $f = (x_0^* + \lambda)/2$
y = coordinate
y^* = dimensionless coordinate = $y/(4\alpha t)^{1/2}$
α = thermal diffusivity, when used without subscript $\alpha = \alpha_S = \alpha_L$
β = latent to sensible heat ratio = $L/[c_S(T_F - T_W)]$
η = integration variable
λ = constant in one-dimensional solution—stationary interface position
Λ = dimensionless constant such that $f(x^* > \Lambda) \approx \lambda$
ξ_i = zeros of Legendre polynomials
ρ = density
τ = integration variable = t'/t

Subscripts

F = fusion quantity
L = liquid region quantity
S = solid region quantity
W = wall quantity

Functions

erf x = error function $= \frac{2}{\pi^{1/2}}\int_0^x e^{-p^2}dp$
erfc x = complementary error function $= 1 - \text{erf}\, x$
exp x = exponential function $= e^x$
$G(x', t'; x; t) \equiv$ exp $[-(x - x')^2/4\alpha(t - t')]$ − exp $[-(x + x')^2/4\alpha(t - t')]$
$E(\tau; \Lambda; x^*) \equiv$ erf $[(x^* - \Lambda\tau^{1/2})/(1 - \tau)^{1/2}]$ + erf $[(x^* + \Lambda\tau^{1/2})/(1 - \tau)^{1/2}]$
$K(\eta, \tau; x^*) \equiv$ exp $[-(x^* - \tau^{1/2}\eta)^2/(1 - \tau)]$ − exp $[-(x^* + \tau^{1/2}\eta)^2/(1 - \tau)]$

$$S(x, 0) = 0 \qquad \text{for } x > 0 \tag{9}$$

Here L is the latent heat of fusion, ρ is the density which is assumed to be the same for both phases so that volumetric effects may be neglected, and α is the thermal diffusivity which is assumed to be the same for both phases so that the two diffusion equations are identical.

Equation (8), which is derived in the Appendix and asserts conservation of energy at the interface, relates the velocity of the free boundary to the rate at which energy diffuses toward the boundary; equation (9) gives the initial position of the free boundary.

Interchanging subscripts S and L shows that the melting problem (i.e., the quarter-space is initially solid rather than liquid, and $T_W > T_F \geq T_i$) is mathematically equivalent to the solidification problem. With reference to equation (8), the latent heat L is negative for the melting problem.

Equations (1)–(9), with slight modifications and changes in notation, describe the isothermal transformation of a superconducting material to a normal conductor due to a magnetic field applied normal to the x, y plane [15]. They also describe some molecular diffusion problems that include instantaneous irreversible reactions [15]. In the magnetic problem, the free boundary is the interface between the superconductor and the normal conductor, while in the chemical problem, it is the reaction site.

Solution

To solve equations (1)–(9), we consider the superposition of two problems: first, a normal heat conduction problem without change of phase, and second, the problem of a distributed moving source of heat in a medium initially at temperature zero with boundaries maintained at zero. This concept of representing the heat of fusion by a moving source was first used by Lightfoot [4, pp. 293–294; 16] to solve Neumann's problem. Lightfoot assumed that the thermal conductivities, specific heats, and thermal diffusivities are equal in the liquid and solid regions.

In extending Lightfoot's moving source approach to the two-dimensional case, it will not be necessary to assume that the conductivities and specific heats are equal, but only that the ratio k/c is the same for two phases. This is a consequence of our choice of dimensionless temperature, and in particular the inclusion of the conductivity ratio k_L/k_S in the definition of T_L^*. This assumption of equal k/c ratios, however, is not necessary for the case where the liquid is initially at the fusion temperature.

We proceed systematically by considering

$$T(x, y, t) = U(x, y, t) + V(x, y, t) \tag{10}$$

where

$$T_S^*(x, y, t) = T(x, y, t) \text{ when } y < S(x, t)$$

and

$$T_L^*(x, y, t) = T(x, y, t) \text{ when } y > S(x, t)$$

Letting

$$U(0, y, t) = -1$$

$$U(x, 0, t) = -1$$

$$U(x, y, 0) = T_i^*$$

and

$$U(x, y, t) = T_i^* \qquad \begin{matrix} \text{for } x \to \infty \\ \text{and } y \to \infty \end{matrix}$$

the following conditions on V are established from equations (3)–(6) and (10):

$$V(0, y, t) = 0$$

$$V(x, 0, t) = 0$$

$$V(x, y, 0) = 0$$

and

$$V(x, y, t) = 0 \qquad \begin{matrix} \text{for } x \to \infty \\ \text{and } y \to \infty \end{matrix}$$

Equation (7) gives

$$U(x, S(x, t), t) + V(x, S(x, t), t) = 0 \tag{11}$$

If we require $\partial U/\partial y$ to be continuous for all x, y, $t > 0$, then from equation (8), it follows that $\partial V/\partial y$ is to be discontinuous for $y = S(x, t)$ such that

$$k_S\left[\left.\frac{\partial V}{\partial y}\right|_{y=S^-} - \left.\frac{\partial V}{\partial y}\right|_{y=S^+}\right]\left[1 + \left(\frac{\partial S}{\partial x}\right)^2\right] = \frac{\rho L}{T_F - T_W}\frac{\partial S}{\partial t}$$

Additionally, we require the functions U and V to satisfy the partial differential equations

$$\frac{\partial^2 U}{\partial x^2} + \frac{\partial^2 U}{\partial y^2} = \frac{1}{\alpha}\frac{\partial U}{\partial t}$$

and

$$\frac{\partial^2 V}{\partial x^2} + \frac{\partial^2 V}{\partial y^2} = \frac{1}{\alpha}\frac{\partial V}{\partial t}$$

U Solution. Clearly, the function U is the solution to the heat conduction problem in the rectangular corner x, $y > 0$ with boundary temperature -1 and initial temperature T_i^*. Carslaw and Jaeger [4, p. 171, equation (2)] give the solution to the problem with zero wall temperature and unit initial temperature. From this, it is an easy matter to establish that

$$U(x, y, t) = -1 + (1 + T_i^*)\operatorname{erf}[x/(4\alpha t)^{1/2}]\operatorname{erf}[y/(4\alpha t)^{1/2}] \tag{12}$$

V Solution. The function V can be obtained by considering the curve $y = S(x, t)$ to represent a line source of heat moving through the quadrant x, $y > 0$. The strength of the source varies both with the position x and the time t. To deduce the strength of the source we note that in a dx' element, located at the abscissa x', there is contained a source of length

$$dl = \left[1 + \left(\frac{\partial S}{\partial x'}(x', t')\right)^2\right]^{1/2} dx'$$

at time t'. The normal velocity of this infinitesimal line element is

$$\frac{\partial S}{\partial t'}(x', t') \Big/ \left[1 + \left(\frac{\partial S}{\partial x'}(x', t')\right)^2\right]^{1/2}$$

therefore, the area covered by dl during the time period dt' is $\partial S/\partial t'\, dx'\, dt'$. Now we associate with this area the quantity of liquid that solidifies, liberating $\rho L/(T_F - T_S)\, \partial S/\partial t' dx' dt'$ units of heat. The factor $(T_F - T_W)^{-1}$ is present because of the dimensionless temperature scale being used. By definition, the strength of a source is set equal to the number of units of heat divided by ρc_S. It follows that the strength of the differential source located at the point $[x', S(x', t')]$ at time t' is $\beta\, \partial S(x', t')/\partial t' dx' dt'$, where β is defined as $L/[c_S(T_F - T_W)]$. The symmetry of the problem about the line $y = x$ indicates that at the point $[S(x', t'), x']$ there is a corresponding differential source of equal strength.

The function V is determined by summing the contributions of all the differential sources. To this end, we note that for the rectangular corner x, $y > 0$, with zero surface temperature and zero initial temperature, the temperature field due to an instantaneous unit source at (x', y'), time t' is given in [4, p. 361, equation (2)] as

$$\frac{1}{4\pi\alpha(t-t')}\,G(x',t';\ x;\ t)\,G(y',t';\ y;\ t)$$

where for convenience in writing we have defined the function

$$G(x',t';\ x;\ t) = \exp\left[-(x-x')^2/4\alpha(t-t')\right] - \exp\left[-(x+x')^2/4\alpha(t-t')\right]$$

It follows that the temperature field due to the differential sources located at $[x', S(x',t')]$ and $[S(x',t'), x']$, time t' is

$$\beta\,\frac{\partial S\,(x',t')}{\partial t'}\,\frac{}{4\pi\alpha(t-t')}\,dx'\,dt'\,[G(x',t';\ x;\ t)\,G\,(S(x',t'),t';\ y;\ t) + G(S(x',t'),t';\ x;\ t)\,G(x',t';\ y;\ t)]$$

To obtain V we must integrate the above with respect to x' and t' between the limits of $x_0 \le x' \le \infty$ and $0 \le t' \le t$. The lower limit on x' is the intersection of line $y = x$ and the interface curve at any instant of time; it is an unknown function of t'. Thus V is given by

$$V(x,y,t) = \frac{\beta}{4\pi\alpha}\int_0^t\int_{x_0}^{\infty}\frac{\partial S\,(x',t')}{\partial t'}[G(x',t';\ x;\ t) \times G(S(x',t'),t';\ y;\ t) + G(S(x',t'),t';\ x;\ t) \times G(x',t';\ y;\ t)]dx'\,\frac{dt'}{(t-t')} \quad (13)$$

Reference [15] shows that the temperature field can be expressed as a function of the two variables x^* and y^* and that the interface position can be expressed by $y^* = f(x^*)$, where $x^* = x/(4\alpha t)^{1/2}$ and $y^* = y/(4\alpha t)^{1/2}$. If x^*, y^*, and the following variables

$$\eta = x'/(4\alpha t')^{1/2}$$
$$\tau = t'/t$$
$$f(\eta) = S(x',t')/(4\alpha t')^{1/2}$$
$$x_0^* = x_0/(4\alpha t')^{1/2}$$

are introduced in equation (13) we obtain

$$V(x^*,y^*) = \frac{\beta}{2\pi}\int_0^1\int_{x_0^*}^{\infty}\left[f(\eta) - \eta\,\frac{df(\eta)}{d\eta}\right] \times [K(\eta,\tau;\ x^*)\,K(f(\eta),\tau;\ y^*) + K(f(\eta),\tau;\ x^*)\,K(\eta,\tau;\ y^*)] \times d\eta\,\frac{d\tau}{1-\tau} \quad (14)$$

where

$$K(\eta,\tau,x^*) = \exp\left[-(x^* - \tau^{1/2}\eta)^2/(1-\tau)\right] - \exp\left[-(x^* + \tau^{1/2}\eta)^2/(1-\tau)\right]$$

Equation (14) is a more convenient form than equation (13) on two counts: first, the integration with respect to t' from 0 to t (an indefinite quantity) has been replaced by an integration with respect to τ between the definite limits 0 and 1. Second, the interface position, now expressed by f, is a function of only one of the integration variables (η) in equation (14), while in equation (13) it is a function of both integration variables.

Numerical integration will be required to evaluate $V(x^*, y^*)$, and it is therefore desirable to eliminate the infinite limit in equation (14). This can be accomplished by dividing the interval (x_0^*, ∞) into the two intervals (x_0^*, Λ) and (Λ, ∞), and selecting Λ such that for $\eta \ge \Lambda$, $f(\eta) \approx \lambda$ and $df(\eta)/d\eta \approx 0$. Here λ is the one-dimensional stationary interface position of Neumann's solution in the y^* domain and is found from the following transcendental equation (reference [15])

$$\frac{\exp(-\lambda^2)}{\operatorname{erf}\lambda} - \frac{T_i^*\exp(-\lambda^2)}{\operatorname{erfc}\lambda} = \pi^{1/2}\beta\lambda \quad (15)$$

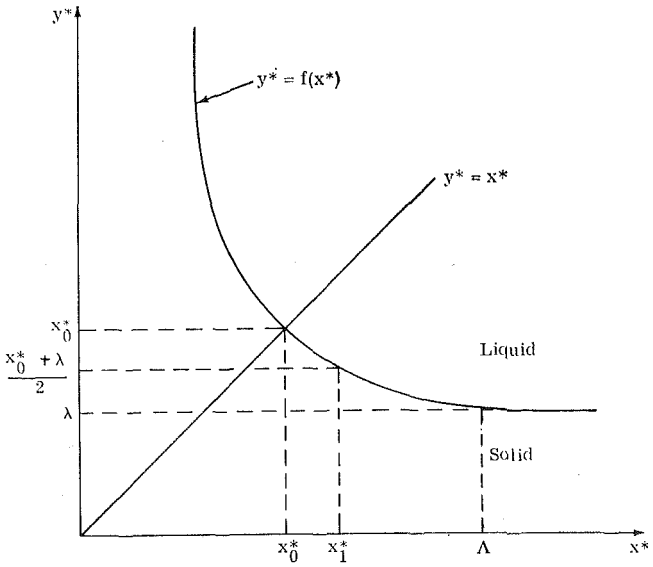

Fig. 2 Schematic showing x_0^*, x_1^*, λ, and Λ

It can be shown a posteriori that generally for $\Lambda > 3\lambda$ the above conditions are satisfied. However for $T_i^* > 1.0$ with $\beta > 1.0$, a value $\Lambda > 5\lambda$ is a better choice; this is a change from reference [15].

When the integration with respect to η in the interval (Λ, ∞) is performed, equation (14) becomes

$$V(x^*,y^*) = \frac{\beta}{2\pi}\int_0^1\int_{x_0^*}^{\Lambda}\left[f(\eta) - \eta\,\frac{df(\eta)}{d\eta}\right] \times [K(\eta,\tau;\ x^*)\,K(f(\eta),\tau;\ y^*) + K(f(\eta),\tau;\ x^*)\,K\,(\eta,\tau;\ y^*)] \times d\eta\,\frac{d\tau}{1-\tau} + \frac{\beta\lambda}{4\pi^{1/2}}\int_0^1 [K(\lambda,\tau;\ y^*)\,E(\tau;\ \Lambda;\ x^*) + K(\lambda,\tau;\ x^*)\,E(\tau;\ \Lambda;\ y^*)]\,\frac{d\tau}{\tau^{1/2}(1-\tau)^{1/2}} \quad (16)$$

where

$$E(\tau;\ \Lambda;\ x^*) = \operatorname{erf}\left[(x^* - \Lambda\tau^{1/2})/(1-\tau)^{1/2}\right] + \operatorname{erf}\left[(x^* + \Lambda\tau^{1/2})/(1-\tau)^{1/2}\right]$$

We have thus established the solution of the moving source problem (i.e., V) in terms of the interface position expressed by the function f, which will be determined from (11). Recalling that $S(x,t)$ maps into $f(x^*)$ in the x^*, y^* domain, we have from equations (11), (12), and (16)

$$0 = -1 + (1 + T_i^*)\operatorname{erf}(x^*)\operatorname{erf}(f(x^*)) + \frac{\beta}{2\pi}\int_0^1\int_{x_0^*}^{\Lambda}\left[f(\eta) - \eta\,\frac{df(\eta)}{d\eta}\right][K(\eta,\tau,x^*)\,K(f(\eta),\tau;\ f(x^*)) + K(f(\eta),\tau;\ x^*)\,K(\eta,\tau;\ f(x^*))]\,d\eta\,\frac{d\tau}{1-\tau} + \frac{\beta\lambda}{4\pi^{1/2}}\int_0^1 [K(\lambda,\tau;\ f(x^*))\,E(\tau;\ \Lambda;\ x^*) + K(\lambda,\tau;\ x^*)\,E(\tau,\Lambda;\ f(x^*))]\,\frac{d\tau}{\tau^{1/2}(1-\tau)^{1/2}} \quad (17)$$

Due to the appearance of f in the functions erf and K, and the singularity of the integrand of the double integral at the point ($\tau = 1$, $\eta = x^*$), no attempt will be made to obtain an exact solution of this nonlinear, singular, integro-differential equation for f. Instead we proceed as follows: Assume a functional form for f

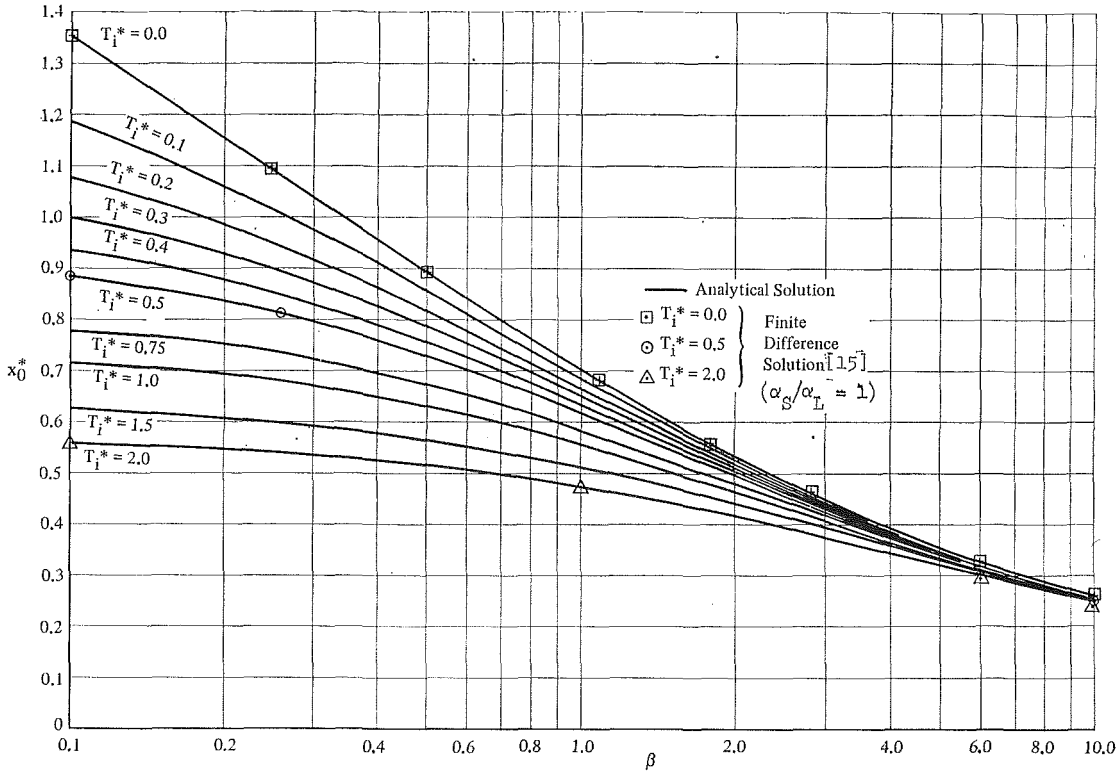

Fig. 3 x_0^* versus β

that: (1) exhibits the proper asymptotic behavior for large x^* or y^*, (2) is symmetrical about the line $y^* = x^*$, and (3) contains arbitrary constants; and then determine the constants by satisfying equation (17) at particular points (i.e., at particular values of x^*). We shall take the functional form of f to be that of the superhyperbola which in explicit form is

$$f(x^*) = \left[\lambda^m + \frac{C}{x^{*m} - \lambda^m}\right]^{1/m}$$

To determine C and m we shall require that $f(x_0^*) = x_0^*$ and $f(x_1^*) = (x_0^* + \lambda)/2$; see Fig. 2. Therefore, in essence x_0^* and x_1^* are the principal unknowns; C and m are determined once x_0^* and x_1^* are specified. If equation (17) is written twice, once with $x^* = x_0^*$ and once with $x^* = x_1^*$, two simultaneous equations in the two unknowns are produced. When the integrals are replaced with quadrature formulas, nonlinear algebraic equations are obtained, which can be solved using a trial and error procedure on a digital computer.

Results

Figs. 3 and 4 present solutions for x_0^* and x_1^* for a range of values of β and T_i^*, the two dimensionless parameters of the problem. Gauss' quadrature formula [17] was used with 20 points in each of the subintervals $0 \le \tau \le 0.9$, $0.9 \le \tau \le 1.0$, $x_0^* \le \eta \le x_1^*$ and $x_1^* \le \eta \le \Lambda$. Because of the previously mentioned singularity at the point ($\tau = 1$, $\eta = x^*$), Gauss' method, which does not use the end points of an integration interval, is quite suitable.

Fig. 5 presents the asymptote λ of the superhyperbola, as obtained from equation (15), and the constants C and m are established from

$$C = (x_0^{*m} - \lambda^m)^2$$

and

$$(x_0^{*m} - \lambda^m)^2 = [x_1^{*m} - \lambda^m]\left[\left(\frac{x_0^* + \lambda}{2}\right)^m - \lambda^m\right]$$

Fig. 6 gives the solution m of the above nonlinear equation for values of x_0^*/λ and x_1^*/λ.

Thus, Figs. 3–6 establish the superhyperbola to represent the interface position $f(x^*)$ for given values of β and T_i^*. With $f(x^*)$ determined, the temperature field T can be calculated from the sum of equations (12) and (16), which, after applying Gauss' quadrature formula with 20 points in each of the aforementioned subintervals, can be written as

$$\begin{aligned} T(x^*, y^*) = {} & -1 + (1 + T_i^*)\,\mathrm{erf}\,x^*\,\mathrm{erf}\,y^* \\ & + \frac{\beta}{2\pi}\sum_{i=1}^{40}\sum_{j=1}^{40} w'_i\tilde{w}_j\left[f(\eta_j) - \eta_j\frac{df(\eta_j)}{d\eta}\right] \\ & \times [K(\eta_j, \tau_i;\ x^*)\,K(f(\eta_j), \tau_i;\ y^*) + K(f(\eta_j), \tau_i;\ x^*) \\ & \times K(\eta_j, \tau_i;\ y^*)]\,(1 - \tau_i)^{-1} \\ & + \frac{\beta\lambda}{4\pi^{1/2}}\sum_{i=1}^{40} w'_i[K(\lambda, \tau_i;\ y^*)\,E(\tau_i;\ \Lambda;\ x^*) \\ & + K(\lambda, \tau_i;\ x^*)\,E(\tau_i;\ \Lambda;\ y^*)]\,\tau_i^{-1/2}\,(1 - \tau_i)^{-1/2} \end{aligned} \quad (18)$$

where the "adjusted" weighting factors w'_i and $\tilde{w}_j$ are given by

$$w'_i = \left(\frac{0.9 - 0}{2}\right)w_i = 0.45\,w_i \qquad i = 1, 2, \ldots, 20$$

$$w'_{41-i} = \left(\frac{1.0 - 0.9}{2}\right)w_i = 0.05\,w_i \qquad i = 1, 2, \ldots, 20$$

$$\tilde{w}_i = \left(\frac{x_1^* - x_0^*}{2}\right)w_i \qquad i = 1, 2, \ldots, 20$$

$$\tilde{w}_{41-i} = \left(\frac{\Lambda - x_1^*}{2}\right)w_i \qquad i = 1, 2, \ldots, 20$$

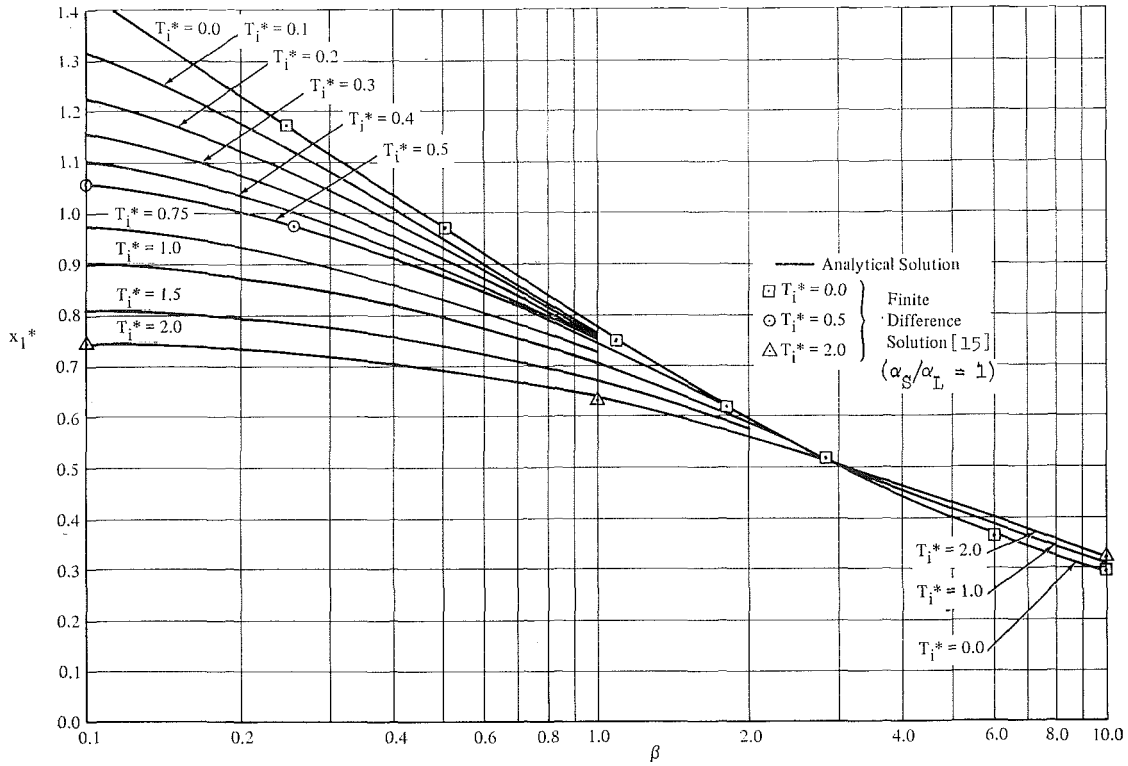

Fig. 4 x_1^* **versus** β

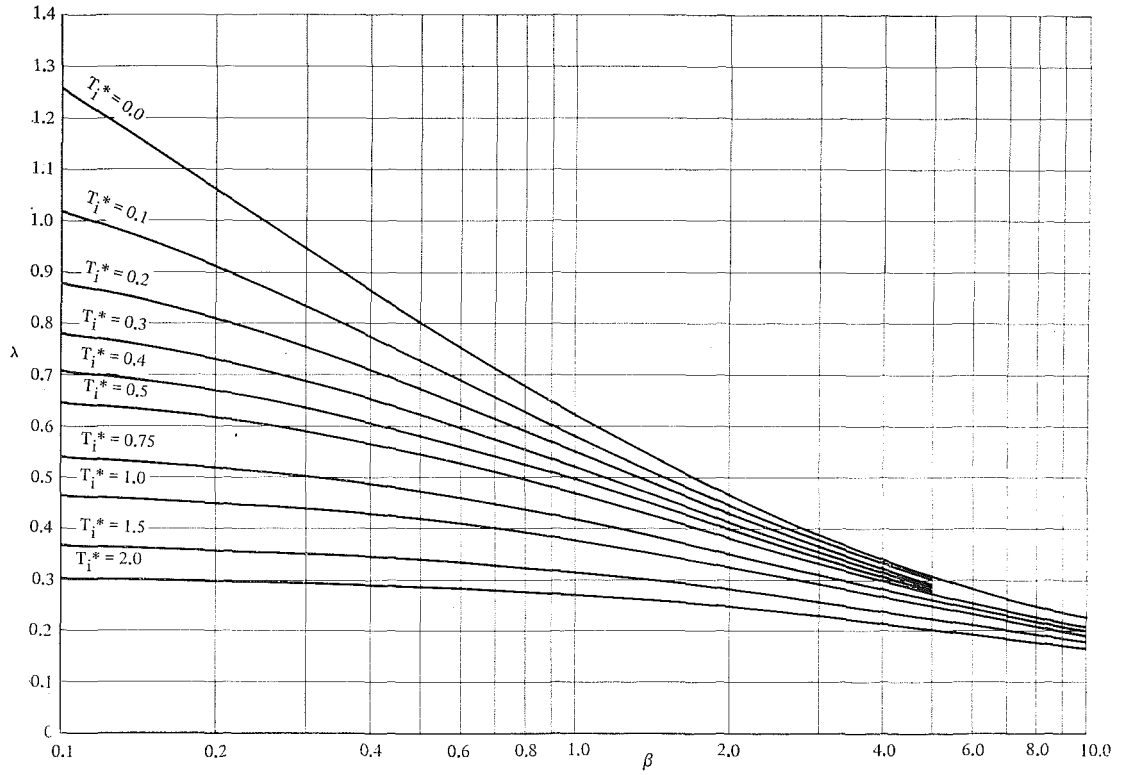

Fig. 5 Solution of equation (15)

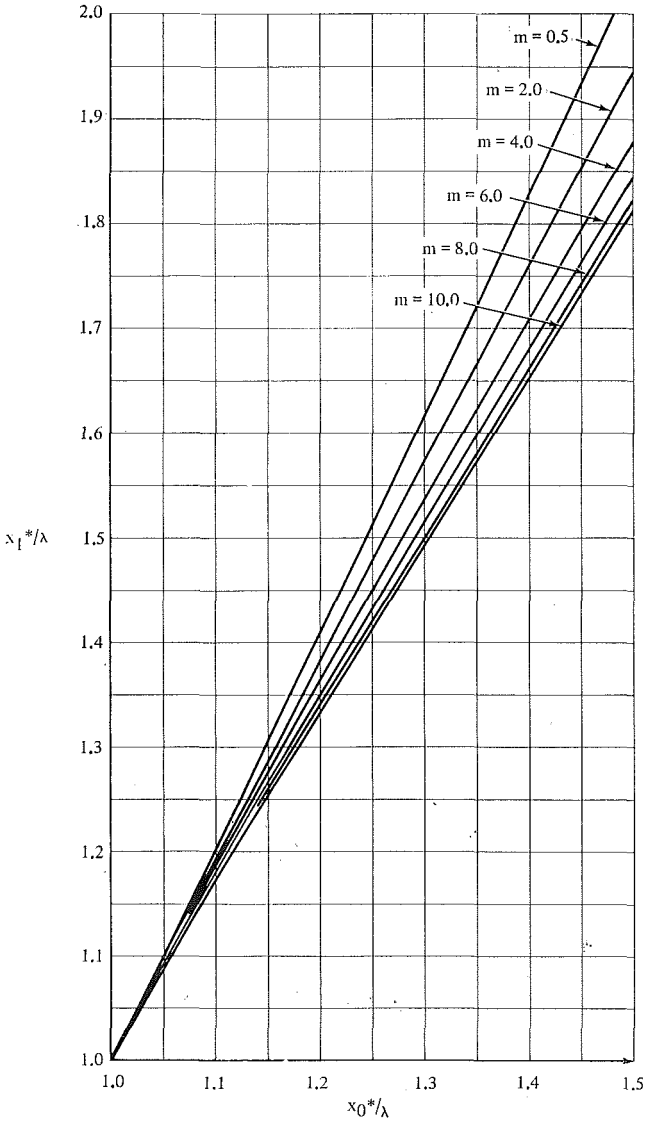

Fig. 6 Solution of $[x_0^{*m} - \lambda^m]^2 = [x_1^{*m} - \lambda^m]\left[\left(\frac{x_0^* + \lambda}{2}\right)^m - \lambda^m\right]$

w_i = weighting factor as given in Table 1, and the abscissas τ_i and η_j are given by

$$\tau_i = \left(\frac{0.9 - 0}{2}\right)\xi_i + \left(\frac{0.9 + 0}{2}\right) = 0.45\xi_i + 0.45 \qquad i = 1, 2, \ldots, 20$$

$$\tau_{41-i} = \left(\frac{1.0 - 0.9}{2}\right)\xi_i + \left(\frac{1.0 + 0.9}{2}\right) = 0.05\xi_i + 0.95 \qquad i = 1, 2, \ldots, 20$$

$$\eta_i = \left(\frac{x_1^* - x_0^*}{2}\right)\xi_i + \left(\frac{x_1^* + x_0^*}{2}\right) \qquad i = 1, 2, \ldots, 20$$

$$\eta_{41-i} = \left(\frac{\Lambda - x_1^*}{2}\right)\xi_i + \left(\frac{\Lambda + x_1^*}{2}\right) \qquad i = 1, 2, \ldots, 20$$

ξ_i = abscissa as given in Table 1;

also,

$$f(\eta_j) = \left[\lambda^m + \frac{C}{\eta_j^m - \lambda^m}\right]^{1/m}$$

Table 1 Abscissas and weighting factors for Gaussian integration

$\pm\xi_i$	w_i
0.0765265	0.1527534
0.2277859	0.1491730
0.3737061	0.1420961
0.5108670	0.1316886
0.6360537	0.1181945
0.7463319	0.1019301
0.8391170	0.0832767
0.9122344	0.0626720
0.9639719	0.0406014
0.9931286	0.0176140

Table 2 Comparison of x_0^* and λ for water

	$T_i^* = 1.35$, $\beta = 33.9$	$T_i^* = 0.55$, $\beta = 22.4$	$T_i^* = 0.25$, $\beta = 19.6$	$T_i^* = 0$, $\beta =$ any value
$\frac{x_0^* \text{ (anal., } \alpha_S/\alpha_L = 1)}{x_0^* \text{ (f.d., } \alpha_S/\alpha_L = 9.2)}$	1.18	1.10	1.06	1
$\frac{x_0^* \text{ (exp., } \alpha_S/\alpha_L = 9.2)}{x_0^* \text{ (f.d., } \alpha_S/\alpha_L = 9.2)}$	0.94	0.89	0.86	—
$\frac{\lambda \text{ (Neumann's, } \alpha_S/\alpha_L = 1)}{\lambda \text{ (Neumann's, } \alpha_S/\alpha_L = 9.2)}$	1.29	1.16	1.08	1

Comparisons

To demonstrate the accuracy of the assumed superhyperbolic form for the interface position $f(x^*)$, comparisons of the analytical solutions with finite-difference solutions for various values of β and T_i^* have been made [15]. The finite-difference formulation was based on equations (1)–(9) with no assumptions regarding the interface shape; it therefore provided an independent check of the analytical results. Figs. 3 and 4 show the good agreement between the two methods so far as x_0^* and x_1^* are concerned. Fig. 7 gives a comparison of the interface position and temperatures, for the case $\beta = 0.25$, $T_i^* = 0.3$, at the nodal points of the finite-difference method and in the x^*, y^* domain where the solutions are not explicitly dependent on t. The same good agreement was obtained in the other cases compared in reference [15].

As was previously noted, the analytic solution assumes that α_S/α_L equals 1, and thus the comparisons given in Figs. 3, 4, and 7 are based on finite-difference solutions with $\alpha_S/\alpha_L = 1$. The error introduced by this assumption depends on the values of β and T_i^*. Computations of x_0^* were made for water ($\alpha_S/\alpha_L = 9.2$) at four values of β and T_i^* using the analytic solution ($\alpha_S/\alpha_L = 1$) and the finite-difference solution with $\alpha_S/\alpha_L = 9.2$. Table 2 presents the results. It is noted that the error decreases as T_i^* is decreased. For $T_i^* = 0$ the analytic solution becomes exact for all values of β. This is a special case of a liquid which is initially (and subsequently) at the fusion temperature. Since no diffusion of heat takes place in the liquid phase under this condition, the solution is independent of the parameter α_S/α_L.

A measure of the effect of the value of α_S/α_L on the solution to the two-dimensional problem can be obtained by its effect on Neumann's one-dimensional problem [4, p. 285]. Table 2 gives the ratio of λ, the one-dimensional interface location in the stationary plane, for $\alpha_S/\alpha_L = 1$ to its value for $\alpha_S/\alpha_L = 9.2$. The error in λ using $\alpha_S/\alpha_L = 1$ follows the same trend as that of x_0^* with the error in λ somewhat larger than that for x_0^*. Thus, Neumann's solution can be used as a conservative guide on the magnitude of the error introduced in the analytic solution for substances with $\alpha_S/\alpha_L \neq 1$.

Comparison with experimental data for x_0^* from [14] is also shown in Table 2. The disagreement shown may be due to free convection effects and phase kinetics.

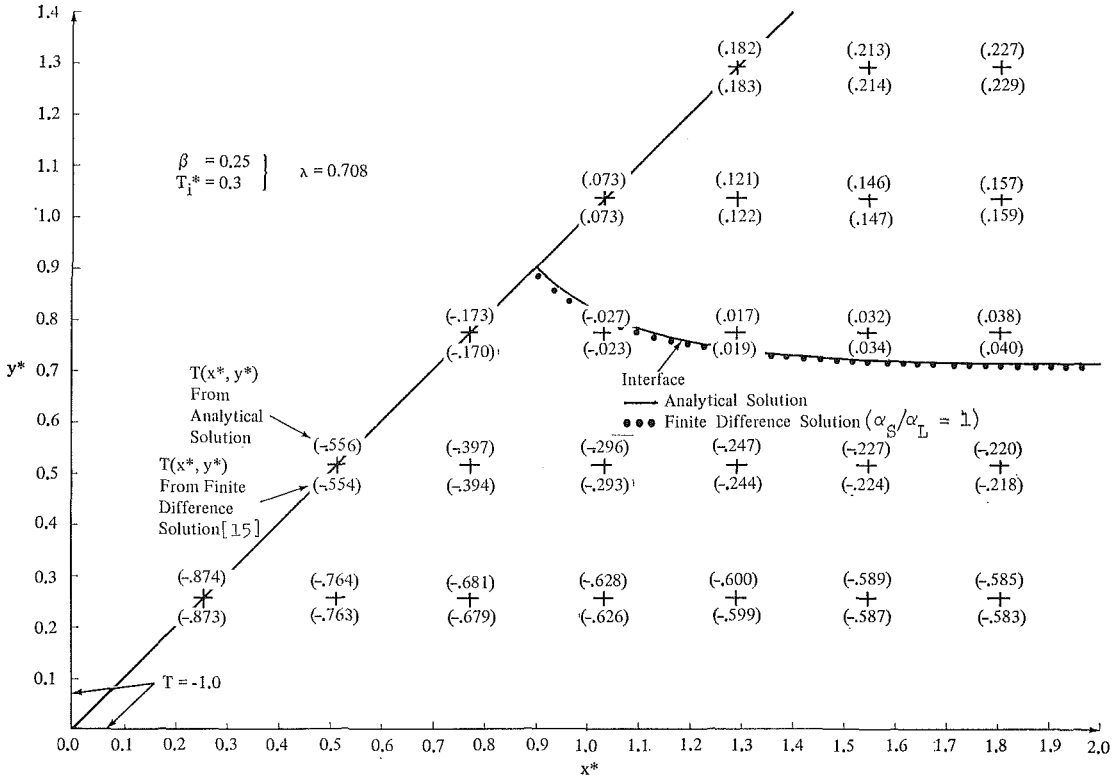

Fig. 7 Comparison of analytical and finite-difference solutions

Concluding Remarks

The nonlinear, singular, integro-differential equation, (17) for the interface position $f(x^*)$ that was derived herein, was used to establish superhyperbolas to represent the interface. This representation for the free boundary, and the ensuing temperature field were demonstrated to be accurate to within five units in the third decimal place by comparison with a finite-difference solution. Equation (18), which gives the temperature field, is valid for all t (i.e., it is not necessarily a short- or long-time solution). The results presented in Figs. 3–6 yield the interface position for a range of the two dimensionless parameters of the problem. Inspection of Fig. 3 reveals: (1) that as β or T_i^* increases, the freezing rate as measured by x_0^* decreases (the distance along the 45 deg line from the origin to the interface is given by $(8\ \alpha\ t)^{1/2}x_0^*$), and (2) that as β increases, the relative importance of T_i^* decreases.

Acknowledgment

The support of the Grumman Aerospace Corporation, and of the National Science Foundation under Grant GK-1281, is gratefully acknowledged.

References

1 Boley, B. A., "The Analysis of Problems of Heat Conduction and Melting," *High Temperature Structures and Materials, Proc. 3rd Symp. on Naval Structural Mech.*, edited by A. M. Freudenthal, B. A. Boley, and H. Liebowitz, Pergamon, New York, N. Y., 1963, pp. 260–315.

2 Bankoff, S. G., "Heat Conduction or Diffusion with Change of Phase," *Advances in Chemical Engineering*, edited by T. B. Drew, J. W. Hoopes, and T. Vermeulen, Academic Press, New York, N. Y., Vol. V, 1964, pp. 75–150.

3 Muehlbauer, J. C., and Sunderland, J. E., "Heat Conduction with Freezing or Melting," *Applied Mechanics Reviews*, Vol. 18, No. 12, Dec. 1965, pp. 951–959.

4 Carslaw, H. S., and Jaeger, J. C., *Conduction of Heat in Solids*, 2nd ed., Oxford at the Clarendon Press, 1959.

5 Goodman, T. R., "The Heat-Balance Integral and Its Application to Problems Involving a Change of Phase," TRANS. ASME, Vol. 80, 1958, pp. 335–342.

6 Selig, F., "Notes on the Problem of Stefen," (in German) *Öst. Ing.-Arch.*, Vol. 10, 1956, pp. 277–280.

7 Yang, K. T., and Szewczyk, A., "An Approximate Treatment of Unsteady Heat Conduction in Semi-Infinite Solids With Variable Thermal Properties," JOURNAL OF HEAT TRANSFER, TRANS. ASME, Series C, Vol. 81, No. 3, Aug. 1959, pp. 251–252.

8 Lardner, T. J., "Approximate Solutions for Melting and Ablation Problems," Polyt. Inst. of Brooklyn PIBAL Rep. No. 654, June 1962.

9 Citron, S. J., "On the Conduction of Heat in a Melting Slab," *Proceedings of the 4th U. S. Congress of Applied Mechanics*, ASME, June 1962, pp. 1221–1227.

10 Allen, D. N. de G., and Severn, R. T., "The Application of Relaxation Methods to the Solution of Non-Elliptic Partial Differential Equations; III. Heat Conduction, with Change of State, in Two Space Dimensions," *Quart. J. Mech. Appl. Math.*, Vol. 15, 1962, pp. 53–62.

11 Poots, G., "An Approximate Treatment of a Heat Conduction Problem Involving a Two-Dimensional Solidification Front," *International Journal of Heat and Mass Transfer*, Vol. 5, May 1962, pp. 339–348.

12 Springer, G. S., "Solidification and Melting of Materials in Finite Systems with Cylindrical Symmetry" PhD thesis, Yale University, New Haven, Conn., 1962; see also Springer, G. S., and Olson, D. R., "Method of Solution of Axisymmetric Solidification and Melting Problems," ASME Paper No. 62-WA-246, 1962; and Springer, G. S., and Olson, D. R., "Axisymmetric Solidification and Melting of Materials," ASME Paper No. 63-WA-185, 1963.

13 Sikarskie, D. L., and Boley, B. A., "The Solution of a Class of Two-Dimensional Melting and Solidification Problems," *International Journal of Solids Structures*, Vol. 1, No. 2, May 1965, pp. 207–234.

14 Jiji, L. M., Rathjen, K. A., and Drzewiecki, T., "Two-Dimensional Solidification in a Corner," *International Journal of Heat and Mass Transfer*, Vol. 13, No. 1, Jan. 1970, pp. 215–218.

15 Rathjen, K. A., "Heat Conduction with Melting or Freezing in a Corner," PhD thesis, The City University of New York, New York, N. Y., 1968.

16 Lightfoot, N. M. H., "The Solidification of Molten Steel," *Proc. London Math. Soc.*, Vol. 31, April 1929, pp. 97–116.

17 Lanczos, C., *Applied Analysis*, Prentice-Hall, Inc., Englewood Cliffs, N. J., 1956, p. 396.

APPENDIX

Derivation of Energy Equation at Free Boundary

An observer situated on the free boundary at the point $S(x', t)$ moves with the velocity $\partial S/\partial t$ in the y direction. During the time interval δt he observes $\rho\ \partial S/\partial t\ \delta x \delta t$ amount of mass change phase in the interval $x' - \delta x/2 \leq x \leq x' + \delta x/2$. The heat liberated because of the change of phase is $\rho L\ \partial S/\partial t\ \delta x \delta t$ and must equal the net heat conducted away from the interface between $x' - \delta x/2$ and $x' + \delta x/2$ during time δt. The heat conducted away from the interface in the y direction is given by

$$\left\{-k_L \frac{\partial T_L}{\partial y} - \left(-k_S \frac{\partial T_S}{\partial y}\right)\right\} \delta x \delta t \qquad \text{for } y = S(x', t)$$

and in the x direction by

$$\left\{-k_L \frac{\partial T_L}{\partial x} - \left(-k_S \frac{\partial T_S}{\partial x}\right)\right\} \left\{-\frac{\partial S}{\partial x}\, \delta x\, \delta t\right\} \qquad \text{for } y = S(x', t)$$

Equating the net heat conducted away from the interface and the heat liberated due to phase change gives, after dividing by $\delta x\, \delta t$, the following

$$k_S \frac{\partial T_S}{\partial y} - k_L \frac{\partial T_L}{\partial y} + k_L \frac{\partial T_L}{\partial x}\frac{\partial S}{\partial x} - k_S \frac{\partial T_S}{\partial x}\frac{\partial S}{\partial x} = \rho L \frac{\partial S}{\partial t} \qquad \text{for } y = S(x', t) \quad \text{(A1)}$$

In general, it is true that

$$dT_S = \frac{\partial T_S}{\partial x}\, dx + \frac{\partial T_S}{\partial y}\, dy + \frac{\partial T_S}{\partial t}\, dt$$

However, along the interface T_S equals T_F (a constant) and therefore we have

$$0 = \frac{\partial T_S}{\partial x}\, dx + \frac{\partial T_S}{\partial y}\, dy + \frac{\partial T_S}{\partial t}\, dt \qquad \text{for } y = S(x, t) \quad \text{(A2)}$$

Also, along the interface we have

$$dy = \frac{\partial S}{\partial x}\, dx + \frac{\partial S}{\partial t}\, dt \qquad \text{for } y = S(x, t) \quad \text{(A3)}$$

Substitution of equation (A3) in equation (A2) yields

$$\left\{\frac{\partial T_S}{\partial x} + \frac{\partial T_S}{\partial y}\frac{\partial S}{\partial x}\right\} dx + \left\{\frac{\partial T_S}{\partial t} + \frac{\partial T_S}{\partial y}\frac{\partial S}{\partial t}\right\} dt = 0 \qquad \text{for } y = S(x, t) \quad \text{(A4)}$$

Since x and t are independent, equation (A4) gives

$$\frac{\partial T_S}{\partial x} = -\frac{\partial T_S}{\partial y}\frac{\partial S}{\partial x} \qquad \text{for } y = S(x, t) \quad \text{(A5)}$$

and

$$\frac{\partial T_S}{\partial t} = -\frac{\partial T_S}{\partial y}\frac{\partial S}{\partial t} \qquad \text{for } y = S(x, t) \quad \text{(A6)}$$

Similarly we can obtain

$$\frac{\partial T_L}{\partial x} = -\frac{\partial T_L}{\partial y}\frac{\partial S}{\partial x} \qquad \text{for } y = S(x, t) \quad \text{(A7)}$$

and

$$\frac{\partial T_L}{\partial t} = -\frac{\partial T_L}{\partial y}\frac{\partial S}{\partial t} \qquad \text{for } y = S(x, t) \quad \text{(A8)}$$

Substituting equations (A5) and (A7) into (A1), introducing the definition of the dimensionless temperatures $T_S{}^*$ and $T_L{}^*$, and noting that x' is a general coordinate, we obtain

$$k_S\left[\frac{\partial T_S{}^*}{\partial y} - \frac{\partial T_L{}^*}{\partial y}\right]\left[1 + \left(\frac{\partial S}{\partial x}\right)^2\right] = \frac{\rho L}{T_F - T_W}\frac{\partial S}{\partial t} \qquad \text{for } y = S(x, t) \quad \text{(A9)}$$

ROBERT J. KASPER
Senior Engineer,
Tocco Division,
Park-Ohio Industries, Inc.,
Cleveland, Ohio
Mem. ASME

Transient Temperature Distribution in Round and Slab-Type Loads Heated by Electric Induction

Equations are derived for the transient temperature distribution in a round or slab-type load with a radiation boundary condition, as required for a thermal analysis of large steel sections heated for forging, by electric induction. The load is assumed to be initially at a uniform temperature and then has heat generated in it by the induction process. Initial distribution curves of the derived transient corrections are compared with the steady-state induced thermal wave shapes that would exist at various heating frequencies if not dampened by the transient correction.

Introduction

THE PURPOSE of this paper, which is a continuation of the previous work [1],[1] is to document a solution of the transient diffusivity correction factors required to accurately analyze the temperature distributions in both round and slab-type loads or workpieces, when heated by the electric induction process.

The study of electric induction heating, like other methods of heating, is influenced by unsteady-state conditions. These conditions are most pronounced when analyzing relatively short cycle times for nonmagnetic induction heating applications, the use of very high surface power densities for surface hardening of carbon steel, or multi-stage heating of very heavy steel sections for forging.

The previous work done by the author [1, 10] describes an approximate method which was used to compensate a thermal analysis for unsteady conditions. We will herein study a more exact method to correct the temperature distribution in a round load, as well as a flat or slab-type load, allowing for radiation loss from the surface and conduction into the center of the load.

A complete physical description of the electric induction heating process, due to its highly complex nature, is far beyond the scope of this paper. The brief description following is merely intended to introduce the reader to the electromechanical terminology used in the mathematical derivation of the transient equations.

Reference Depth. A conventional induction heating system consists of a round solenoidal coil surrounding a coaxial metallic load. Alternating current is caused to flow in the coil and its resulting electric field action induces a corresponding current flow in the load. The depth of the d-c equivalent of this current is called the reference depth D_2. This parameter is one of the most important variables in the study of electric heating and is defined as

$$D_2 = 3.158(R_2/uf)^{1/2} \tag{1}$$

It is significant to note that as the heating power is applied at higher frequencies, the majority of the current flows in a shallower band around the load. The same applies when heating magnetic materials where permeability $u > 1$. The reference depth is further described in Fig. 1 as the point in the load where the induced current is 36.7 percent of the surface value I_s.

Further use is made of depth D_2 in defining argument Z of the Bessel equations which describe the electrical field effects in a round load

$$Z = \frac{\sqrt{2}}{D_2} \cdot \frac{A_0}{2} \tag{2}$$

Argument Z increases with frequency of the power supply.

Power Terms. Also shown in Fig. 1 is a typical temperature profile resulting from the application of P_0 w/sq in. of electric power at the load surface for some time t. Of this power, P_1 w/sq in. is lost by radiation from the surface, leaving P_2 w/sq in. as heat in the load. The ratio of the heating power to the induced power is the thermal efficiency of the load

[1] Numbers in brackets designate References at end of paper.

Contributed by the Heat Transfer Division for publication (without presentation) in the JOURNAL OF HEAT TRANSFER. Manuscript received by the Heat Transfer Division, September 10, 1969; revised manuscript received, June 17, 1970. Paper No. 70-HT-S.

$$\eta = P_2/P_0 \tag{3}$$

which also appears in the equations following. For simplification, net power P_2 is assumed held constant in this analysis.

Temperatures. The previously cited work [1] states that the surface-to-center temperature difference of a cylinder can be determined by

$$T_2 - T_0 = \frac{P_2 A_0}{4K} F_2 \tag{4}$$

while the temperature difference from the average value to the center is

$$T_1 - T_0 = \frac{P_2 A_0}{4K} F_3 \tag{5}$$

where the center-to-surface factor F_2 and the center-to-average factor F_3 are mathematically defined as

$$F_2 = 1 - \frac{1}{\eta}\frac{1}{Z}\frac{Z_0 - 1}{Z_1} \tag{6}$$

$$F_3 = \frac{1}{2} - \frac{1}{\eta}\frac{1}{Z^2}\frac{2Z_2 - Z}{Z_1} \tag{7}$$

The average temperature T_1 of a round load can also be expressed in power terms via an energy balance

$$Q = WC(T_1 - T_a) \tag{8}$$

rearranging,

$$T_1 - T_a = \frac{Q}{WC}$$

where

$Q = P_2 \cdot 2\pi a \cdot L \cdot t$ w·sec
$W = \pi a^2 \cdot L \cdot d$ lb
$T_a = 0$ deg F per definition of mean specific heat C

therefore

$$T_1 = \frac{P_2 a}{K} \cdot \frac{2Kt}{dCa^2} = \frac{P_2 a}{K} \cdot 2\frac{kt}{a^2}$$

Nomenclature

a = radius of cylindrical load, in.
A_0 = diameter of cylindrical load, in.
A_n = coefficient of general Fourier expression
b = substitution constant = Z_s/l
B = substitution constant = αr
C = mean specific heat of load from 0 deg F, w·sec/lb·deg F
d = density of load, lb/cu in.
D_2 = reference depth of equivalent current flow in load, in.
e = 2.7183 constant
f = heating frequency, Hz
$f(r)$ = temperature variation with respect to distance r
$f(x)$ = temperature variation with respect to distance x
F_2 = temperature difference factor, center to surface
F_3 = temperature difference factor, center to average
h = surface (boundary) radiation factor
= H/K, or surface conductance/thermal conductivity
H_2 = slab total thickness ($2l$), in.
$J_0(\alpha r)$ = zero-order Bessel function of αr
$J_1(\alpha r)$ = first-order Bessel function of αr
$J_2(\alpha r)$ = second-order Bessel function of αr
k = thermal diffusivity constant = K/dC, sq in./sec
K = mean thermal conductivity, w/sq in·deg F/in.
l = half-thickness of slab, in.
L = length of load, in.
m = summation integer
M = odd integration power = $4m + 1$
n = summation integer
P_0 = total power induced at load surface, w/sq in.
P_1 = power lost by surface radiation, w/sq in.
P_2 = net power generated in the load, w/sq in.
Q = heat content of the load, w·sec
Q_1, Q_2, Q_3, Q_4 = integration constants
r = radial distance from center to any point in round load, in.
r/a = dimensionless distance ratio, variable
R_2 = electrical resistivity of the load, μohm·in.
S_0 = transient summation term at center of load
S_2 = transient summation term at surface of load
t = total time of heating, variable, sec
T = dimensionless time parameter for rounds = kt/a^2
T_s = dimensionless time parameter for slabs = kt/l^2
T_a = load temperature at start (ambient), deg F
$T_{r/a}$ = load temperature at point r/a, deg F
$T_{x/l}$ = load temperature at point x/l, deg F
T_0 = load temperature at center, deg F
T_1 = load temperature, average, deg F
T_2 = load temperature at surface, deg F
T_9 = time of heating to a temperature condition, sec
u = magnetic permeability of the load, gauss/oersted
W = weight of load, lb
W_2 = width of load, in.
x = linear distance from center to any point in slab load, in.
x/l = dimensionless distance ratio, variable
X_n = coefficient of general Fourier expression
$X(Zr/a)$ = Bessel function for round load, variable
= $Ber^2 Zr/a + Bei^2 Zr/a$
$X(Z_s x/l)$ = trigonometric function for slab load, variable
= $\cosh Z_s x/l + \cos Z_s x/l$
Z = argument of round load, constant
= $\sqrt{2}\, a/D_2 = 0.707A_0/D_2$
Z_0 = $Ber^2 Z + Bei^2 Z$, constant
Z_1 = $Ber\ Z\ Ber'\ Z + Bei\ Z\ Bei'\ Z$, constant
Z_2 = $Ber\ Z\ Bei'\ Z - Bei\ Z\ Ber'\ Z$, constant
Z_s = argument of slab load, constant
= $2l/D_2 = H_2/D_2$
Z_{s0} = $\cosh Z_s + \cos Z_s$, constant
Z_{s1} = $\sinh Z_s - \sin Z_s$, constant
Z_{s2} = $\sinh Z_s + \sin Z_s$, constant
α, α_n = roots of general boundary equations
η = thermal efficiency of the load-coil system = P_2/P_0
π = 3.14159 constant

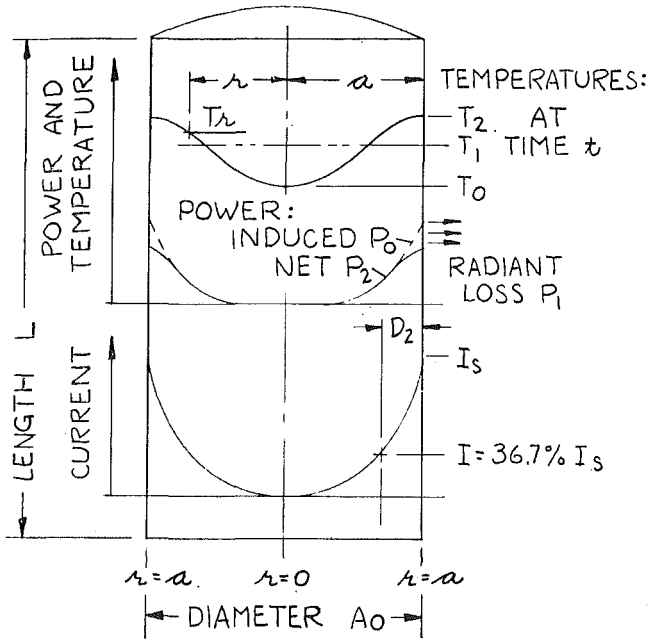

Fig. 1 Temperature, power, and current terminology for a cylindrical section

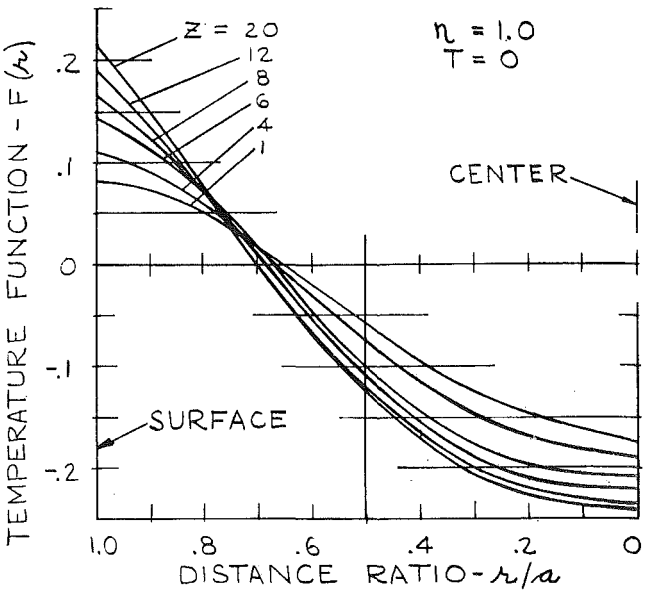

Fig. 2 Round-load temperature function f(r) versus ratio r/a

$$= \frac{P_2 a}{K} \cdot 2T \tag{8a}$$

where the diffusivity $k = K/dC$.

We also define a dimensionless time parameter T as

$$T = \frac{kt}{a^2} \tag{9}$$

Approach

We will first determine the equation of the steady-state profile or wave shape of the temperature distribution within a round load infinitely long and heated by electric induction as a function of the radial distance ratio r/a from the center out.

A Fourier series equation will then be derived for this wave shape which when added to the steady-state wave at time $t = 0$ will result in a constant initial temperature $T_2 = T_1 = T_0$ throughout the load.

The radiation boundary conditions used in this problem will be identified for future reference.

A similar equation for the slab-type loads will be examined in a like manner later in this paper. Simplified steady-state temperature equations for slabs are included in Appendix 3 for comparison with those of a cylindrical-shaped load.

Round Loads

Wave Shape. A fine analysis of the subject of induction heating was done by Dreyfus [2] where the temperature difference between any point r/a and the average temperature of the load is established. However, his transient correction was not explained in any great detail, which is one of the reasons for this paper.

Rewriting Dreyfus's expression in present terminology by means of simple algebra

$$T_{r/a} - T_1 = \frac{P_2 a}{K}\left[\frac{1}{2}\frac{r^2}{a^2} - \frac{1}{4} + \frac{1}{2}\frac{1}{\eta}\frac{2Z_2 - Z \cdot X(Zr/a)}{Z^2 Z_1}\right] \tag{10}$$

Now, adding the average temperature T_1 per equation (8a), we have the steady-state temperature at any point r/a and at any time t

$$T_{r/a} = \frac{P_2 a}{K}\left[2T + \frac{1}{2}\frac{r^2}{a^2} + \frac{1}{2}\frac{1}{\eta}\frac{2Z_2 - Z \cdot X(Zr/a)}{Z^2 Z_1} - \frac{1}{4}\right] \tag{11}$$

Transient Correction. The transient correction will be of the Fourier-Bessel form

$$\Delta T_{r/a} = \sum_{n=1}^{\infty} A_n J_0(\alpha r) e^{-k\alpha^2 t} \tag{12}$$

Referring to Carslaw and Jeager [3] and Churchill [4], A_n and α are coefficients as defined by the boundary conditions. In our problem of induction heating an infinite cylinder, we can write the equations for temperature v as follows

$$\frac{\partial v}{\partial t} = k\left(\frac{\partial^2 v}{\partial r^2} + \frac{1}{r}\frac{\partial v}{\partial r}\right), \qquad 0 < r < a$$

with radiation at the surface $r = a$ into medium at zero temperature, the boundary condition is

$$\frac{\partial v}{\partial r} + hv = 0, \qquad r = a$$

and for $J_0(\alpha r)$ to be a solution, α must be a positive root of

$$\alpha J_0'(\alpha a) + hJ_0(\alpha a) = 0 \tag{13}$$

We will also assume that the general equation for the coefficient A_n is

$$A_n = \frac{2\alpha^2}{(\alpha^2 a^2 + 0 - 0)J_0^2(\alpha a)} \int_0^a r J_0(\alpha r) f(r) dr \tag{14}$$

The thermal wave shape of equation (11) which requires dampening to zero at starting time $t = 0$ is the temperature function $f(r)$

$$f(r) = \frac{1}{2}\frac{r^2}{a^2} + \frac{1}{2}\frac{1}{\eta}\frac{2Z_2 - Z \cdot X(Zr/a)}{Z^2 Z_1} - \frac{1}{4} \tag{15}$$

By specifying the exact shape of the temperature wave as $f(r)$ per equation (15), the wave shape is compensated for radiation by efficiency term η, so we are treating the surface of the cylinder as being insulated as far as the boundary condition is concerned. This is the same as putting the radiation factor $h = 0$ in equation (13), so the boundary condition and its first derivative is now

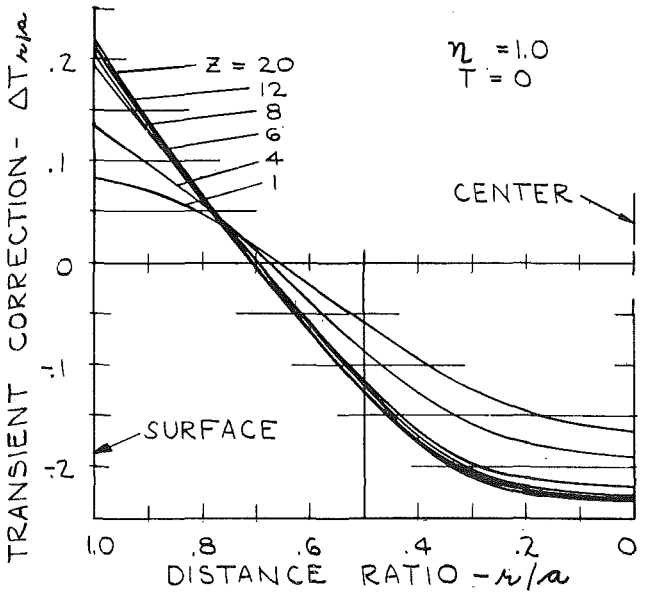

Fig. 3 Round-load transient correction factor $\Delta T_{r/a}$ versus ratio r/a

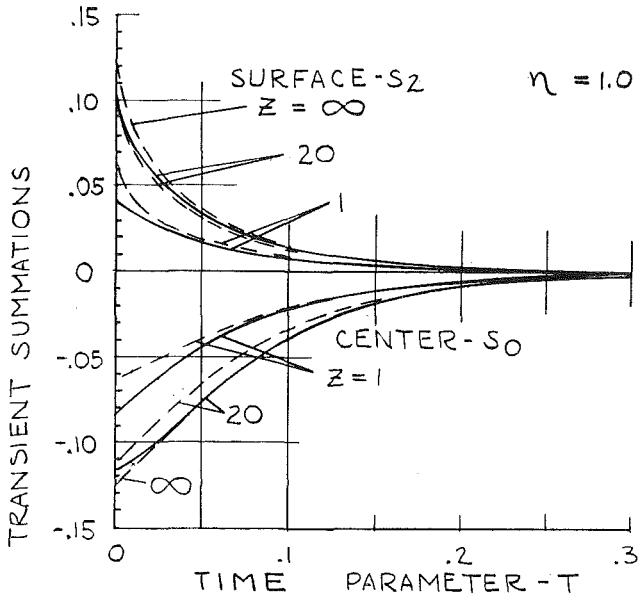

Fig. 4 Round-load transient summation terms versus parameter T; dash curves are for reference to earlier work

$$J_0'(\alpha a) = 0$$
$$-J_1(\alpha a) = 0 \qquad (13a)$$

Function $f(r)$ is plotted for reference in Fig. 2 at various values of Z and at $\eta = 100$ percent, as would be the case at the start of a heating cycle.

After using $f(r)$ of equation (15) in the expression for A_n in equation (14) and integrating per Appendix 1, we get for coefficient A_n

$$A_n = \frac{2}{(\alpha a)^2 J_0(\alpha a)} \left\{1 + \frac{[8/(\alpha a)^2 - 1]Z^3}{16\eta Z_1}\right\} \qquad (16)$$

Substituting the equivalent ratio α_n/a for α, and placing A_n defined by (16) into the Fourier-Bessel equation (12) we have for the transient correction

$$\Delta T_{r/a} = 2 \sum_{n=1}^{\infty} e^{-k\alpha_n^2 t/a^2} \frac{J_0(\alpha_n r/a)}{\alpha_n^2 J_0(\alpha_n)} \left\{1 + \frac{(8/\alpha_n^2 - 1)Z^3}{16\eta Z_1}\right\} \qquad (17)$$

Results. Our boundary condition per (13a) is $J_1(\alpha_n) = 0$, so the first five roots of the summation are

n =	1	2	3	4	5
α_n =	3.832	7.016	10.17	13.32	16.47
$J_0(\alpha_n)$ =	−0.4027	+0.3000	−0.2497	+0.2184	−0.1960

As a test of this derivation, $\Delta T_{r/a}$ of equation (17) is plotted in Fig. 3 at various values of argument Z, at a zero radiation level $\eta = 100$ percent, and for time $t = 0$ (where exponential $e^{-T\alpha_n^2} = 1$). We see that these wave shapes will readily cancel the shapes of Fig. 2 at each respective value of Z.

Note that the zero axis of both plots coincides with the average temperature of the load. Also, note that for large values of argument $Z > 50$ in equation (17), the value of $Z_1 \to \infty$ in the denominator causing the second term in the bracket to become zero; thus the summation becomes

$$\Delta T_{r/a} = 2 \sum_{n} e^{-T\alpha_n^2} \frac{J_0(\alpha_n r/a)}{\alpha_n^2 J_0(\alpha_n)}$$

which is the same as the transient correction used by Carslaw and Jeager [5] for constant flux at the surface of a cylinder.

By subtracting the transient correction $\Delta T_{r/a}$ of (17) from the bracket term of equation (11) we have the complete expression for the temperature at any point r/a in a round load heated by induction

$$T_{r/a} = \frac{P_2 a}{K}\left[2T + \frac{1}{2}\frac{r^2}{a^2} + \frac{1}{2}\frac{1}{\eta}\frac{2Z_2 - Z\cdot X(Zr/a)}{Z^2 Z_1} - \frac{1}{4} - 2\sum_{n} e^{-T\alpha_n^2}\frac{J_0(\alpha_n r/a)}{\alpha_n^2 J_0(\alpha_n)}\left\{1 + \frac{(8/\alpha_n^2 - 1)Z^3}{16\eta Z_1}\right\}\right] \qquad (18)$$

For reference, Fig. 4 is a plot of the center S_0 ($r = 0$) and surface S_2 ($r = a$), values of the summation term in equation (18) versus time parameter T, for arguments $Z = 20$ and 1, and at a zero radiation level $\eta = 100$ percent. The actual temperature correction can be obtained by multiplying S_0 or S_2 by $2\cdot P_2 a/K$, as the variables exist at time T.

Slab Loads

Wave Shape. To differentiate between the round system of mathematics and the slab system, a letter s will be suffixed to the arguments and their function in the following equations. Fig. 5 will also help identify other slab terminology and its boundaries.

Rewriting the Dreyfus expression for the temperature in a slab [2] in present terminology

$$T_{x/l} - T_1 = \frac{P_2 l}{K}\left[\frac{1}{2}\frac{x^2}{l^2} - \frac{1}{6}\frac{1}{\eta}\frac{Z_{s2} - Z_s\cdot X(Z_s x/l)}{Z_s^2 Z_{s1}}\right] \qquad (19)$$

The average temperature energy equivalent (assuming the width of the slab W_2 as being much greater than its height or thickness $2l$) can be derived in a similar fashion as that for a round load by using equation (8); therefore

$$T_1 = Q/(WC)$$

where

$Q = 2P_2 W_2 L t$ w·sec (neglecting edge heat)

$W = W_2 2lLd$ lb

so

$$T_1 = \frac{P_2 l}{K}\frac{Kt}{dCl^2} = \frac{P_2 l}{K}\cdot\frac{kt}{l^2}$$

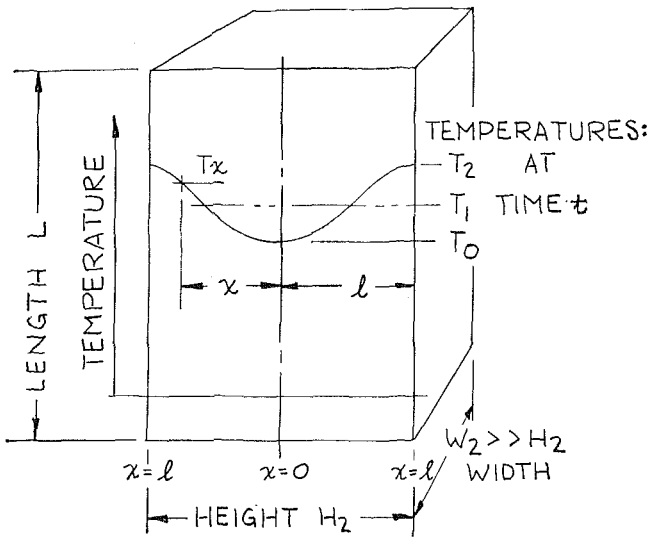

Fig. 5 Temperature terminology for a slab-type section

$$= \frac{P_2 l}{K} T_s \tag{20}$$

where the dimensionless time parameter T_s for a slab is

$$T_s = \frac{kt}{l^2}$$

Adding T_1 to equation (19), we get the steady-state temperature at any point x/l and at any time t

$$T_{x/l} = \frac{P_2 l}{K}\left[T_s + \frac{1}{2}\frac{x^2}{l^2} + \frac{1}{\eta}\frac{Z_{s2} - Z_s \cdot X(Z_s x/l)}{Z_s^2 Z_{s1}} - \frac{1}{6}\right] \tag{21}$$

Transient Correction. The Fourier expression to be used is

$$\Delta T_{x/l} = \sum_{n=1}^{\infty} A_n X_n e^{-k\alpha^2 t} \tag{22}$$

Referring to Carslaw and Jeager [6], A_n, X_n, and α are coefficients defined by the boundary conditions.

In our problem of induction heating an infinite slab, we can write equations for temperature v as follows

$$\frac{\partial v}{\partial t} = k\frac{\partial^2 v}{\partial x^2}, \qquad 0 < x < l$$

For radiation at the surface $x = l$ into medium at zero and zero heat flow across axis $x = 0$, the only boundary condition is

$$\frac{\partial v}{\partial x} + hv = 0, \qquad x = l$$

For the case of radiation from the faces at l, and for an initial temperature distribution defined by

$$f(x) = A_1 X_1 + A_2 X_2 + \ldots$$

coefficient X_n is defined as

$$X_n = \cos \alpha x + \frac{h}{\alpha} \sin \alpha x$$

the values α_1, α_2, α_3, etc., are n roots of boundary condition

$$\tan \alpha l = \frac{2\alpha h}{\alpha^2 - h^2} \tag{23}$$

Once again, we are compensating the power induced in the slab

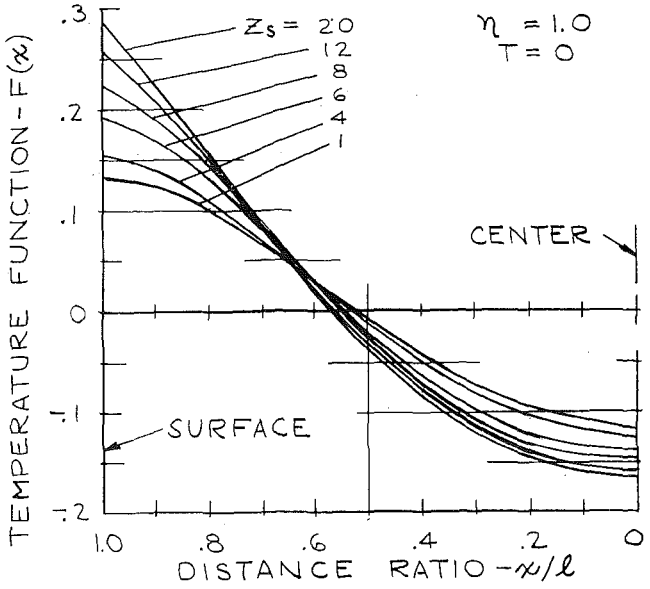

Fig. 6 Slab-load temperature function $f(x)$ versus ratio x/l

for radiation loss by $P_2 = P_0 - P_1$, so the radiation factor $h = 0$, and the boundary condition becomes

$$\tan \alpha l = 0 \tag{23a}$$

from which we get

$$\alpha = n\pi/l \tag{23b}$$

$$\sin \alpha l = 0 \tag{23c}$$

For $h = 0$, we also have coefficient X_n become

$$X_n = \cos \alpha x = \cos n\pi x/l \tag{24}$$

and the general expression for coefficient A_n becomes

$$A_n = \frac{2\alpha^2}{(\alpha^2 + 0)l + 0}\int_0^l \cos \alpha x f(x) dx \tag{25}$$

The thermal wave shape of equation (21) which requires dampening to zero at time $t = 0$ is the temperature function $f(x)$

$$f(x) = \frac{1}{2}\frac{x^2}{l^2} + \frac{1}{\eta}\frac{Z_{s2} - Z_s \cdot X(Z_s x/l)}{Z_s^2 Z_{s1}} - \frac{1}{6} \tag{26}$$

This function is plotted in Fig. 6, for reference, at various values of Z.

Placing $f(x)$ of equation (26) into the expression for A_n in equation (25) and integrating per Appendix 2, we get for coefficient A_n

$$A_n = 2\frac{\cos \alpha l}{n^2\pi^2}\left\{1 + \frac{[6/(n\pi)^2 - 1]Z_s^3}{3\eta Z_{s1}}\right\} \tag{27}$$

using $\alpha = n\pi/l$, $T_s = kt/l^2$, and $\cos \alpha l = (-1)^n$ (to keep the cosine terms even with period 2π so that the summation will converge), and substituting into equation (22), our transient correction becomes

$$\Delta T_{x/l} = 2\sum_{n=1}^{\infty}\frac{(-1)^n}{(n\pi)^2} e^{-T_s(n\pi)^2} \cos n\pi x/l \times \left\{1 + \frac{[6/(n\pi)^2 - 1]Z_s^3}{3\eta Z_{s1}}\right\} \tag{28}$$

Results. As a test of this derivation, $\Delta T_{x/l}$ of equation (28) is plotted in Fig. 7, at various values of argument Z_s. A severe distortion of the wave shape is noted when compared to Fig. 6, as the

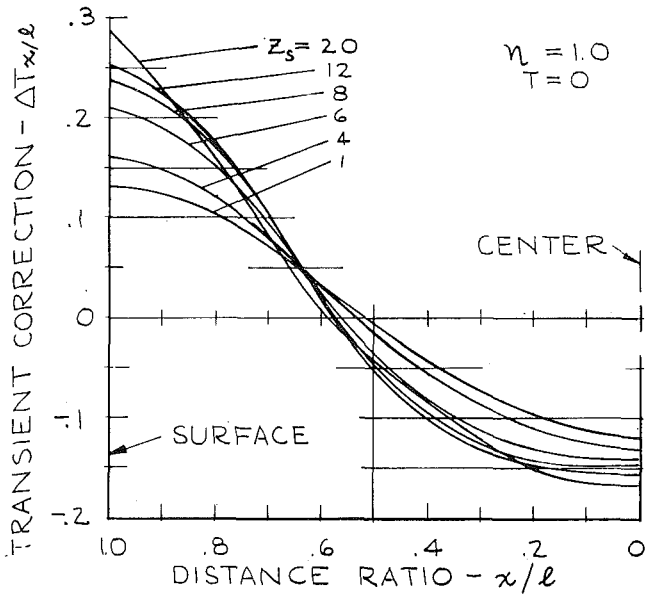

Fig. 7 Slab-load transient correction factor $\Delta T_{x/l}$ versus ratio x/l

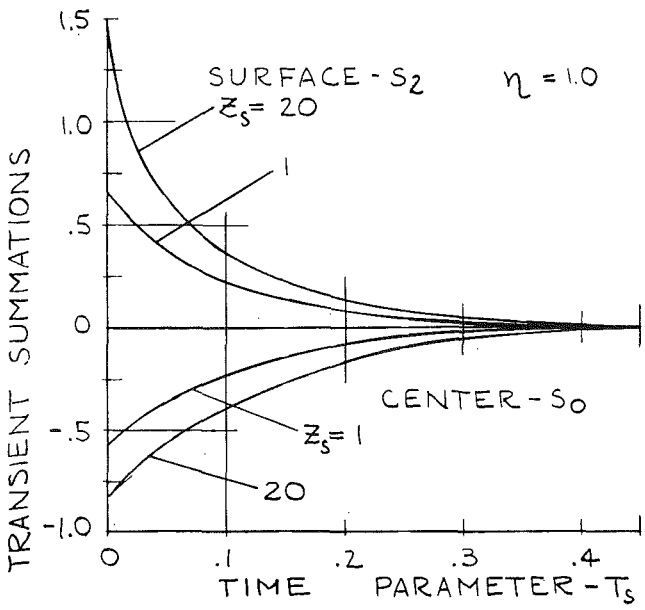

Fig. 8 Slab-load transient summation terms versus parameter T_s

argument Z increased, and it is minimized by increasing the number of summations made per

argument Z_s	summation terms n
1 to 12	2
20	4
50	10

This distortion may be due to using only 4 terms of the series in equation (38) of Appendix 2.

For large values of argument $Z_s > 50$ in equation (28), the value of $Z_{s1} \rightarrow \infty$ in the denominator of the bracket and causes the summation to become

$$\Delta T_{x/l} = 2 \sum_n \frac{(-1)^n}{(n\pi)^2} e^{-T_s(n\pi)^2} \cos n\pi x/l$$

which is the same as the transient correction used in reference [7] for constant flux at the surface of a slab.

By subtracting the transient correction from the bracket term of equation (21) we get the complete expression for the temperature at any point x/l in a slab heated by induction

$$T_{x/l} = \frac{P_2 l}{K}\left[T_s + \frac{1}{2}\frac{x^2}{l^2} + \frac{Z_{s2} - Z_s \cdot X(Z_s x/l)}{\eta Z_s^2 Z_{s1}} - \frac{1}{6} - 2\sum_n \frac{(-1)^n}{(n\pi)^2} e^{-T_s(n\pi)^2} \cos n\pi x/l \left\{1 + \frac{[6/(n\pi)^2 - 1]Z_s^3}{3\eta Z_{s1}}\right\}\right] \quad (29)$$

For additional reference, Fig. 8 is a plot of the slab's center summation term $S_0(x = 0)$ and surface summation term $S_2(x = l)$, of equation (29) versus parameter T_s, for two arguments ($Z = 20$, $Z = 1$) and at a zero radiation level

$$\eta = 100 \text{ percent}$$

Discussion

The round and slab load transient corrections plotted in Figs. 3 and 7, respectively, are shown for a thermal efficiency $\eta = 100$ percent, which is representative of the exact starting conditions where no radiation loss exists, i.e., the induced power P_0 equals the net power P_2, and radiation power P_1 equals zero.

The shape of the round load transient distribution has a slight distortion in the argument Z range of 4 and 12 at the surface and center locations, while the slab load distribution has good correlation at the surface and center but includes a slight distortion between 0.8 and 0.2 distance ratio in the same argument range.

For the general application of induction heating of nonmagnetic materials, especially those whose resistivity R_2 does not vary greatly with temperature, such as titanium alloys, copper alloys, 300 series stainless, nichrome, and monel, the frequency of the power supply will be selected so that the heating system will operate with an argument Z ($\sim$ load-thickness/reference-depth ratio) between 1 and 4, thus minimizing the difference between the surface and center temperature, while the heating of magnetic materials such as most iron and steel alloys will operate with an argument Z greater than 20 during the initial portion of the heating cycle, due to the extremely shallow reference depth D_2 caused by the load's magnetic permeability. Therefore, most applications of the derived transient corrections fall in their most accurate range of correlation.

Further, as the heating progresses and the radiation loss increases due to a higher surface temperature T_2, the efficiency η gradually decreases toward a typical value of 0.7, which in turn causes all of the temperature corrections to decrease in magnitude and shift toward the zero value of average temperature axis.

Simultaneously, as the heating time (parameter T) increases, the effect of the exponential multiplier also causes the transient correction factor to decrease as is shown in Figs. 4 and 8. However, the heating of a large section size ($T = kt/a^2$) will greatly reduce this effect and is the reason that this analysis is important to the study of induction heating large shapes such as steel ingots.

As an example, the heating of a 25-in-dia steel ingot with an average diffusivity of 0.02 sq in/sec for 10 min will have a value of T per equation (9)

$$T = 0.02 \cdot (60 \cdot 10)/12.5^2$$
$$= 0.077$$

For this example, the surface may be magnetic or nonmagnetic depending upon the power density P_0 induced in the ingot by the coil's power supply, but in either case $T < 0.1$ and the exact solution of the transient correction as outlined herein should be used.

Conclusion

Nonsteady-state temperature wave shapes for induction-heated round and slab-type loads have been mathematically de-

fined and their respective Fourier equations have been derived and plotted. The work is treated as a radiation boundary problem with the radiation factor h set to zero.

An accurate temperature distribution can now be calculated at any instant of a heating cycle for these type loads.

This work can now be extended to the transient analysis of a multi-stage induction heating system, where the steady-state temperature profile of a secondary power level must be corrected by its diffusivity transient effect as well as the residual heat effect of the primary power level as contained by the load when it is transferred from an initial stage of heating (or cooling in the case of a casting) to the following stage of induction heating.

Another extension of this work could be to study the exact cooling nature of a load once it has been heated by the electric induction process.

References

1 Kasper, R. J., "Temperature Distributions for Induction Through-Heating of Magnetic Materials to Forging Temperatures," ASME Paper No. 68-HT-30, 1968.

2 Dreyfus, L. A., "High Frequency Heating and Temperature Distributions in Surface Hardening of Steel," Proceedings NR 208, Royal Swedish Academy of Engineering Sciences, Stockholm, 1952, p. 92.

3 Carslaw and Jeager, *Conduction of Heat in Solids*, 2nd ed., Oxford University Press, London, 1959, pp. 195–196.

4 Churchill, R. V., *Fourier Series and Boundary Value Problems*, McGraw-Hill, New York, 1941, p. 166.

5 Carslaw and Jeager, loc. cit., p. 203.

6 Carslaw and Jeager, loc. cit., pp. 115, 118.

7 Carslaw and Jeager, loc. cit., p. 112.

8 Watson, G. N., *A Treatise on the Theory of Bessel Functions*, 2nd ed., University Press, Cambridge, 1966, p. 148.

9 McLachlan, N. W., *Bessel Functions for Engineers*, 2nd ed., Clarendon Press, Oxford, 1961, p. 72.

10 Kasper, R. J., "Temperature Distribution for Induction Through Heating of Titanium," *IEEE Transactions*, 69TP 114-IGA.

APPENDIX 1

The integration of the following round-load integral will be made by parts

$$\int_0^a rJ_0(\alpha r)\left[\frac{1}{2}\frac{r^2}{a^2}+\frac{Z_2}{\eta Z^2 Z_1}-\frac{1}{4}-\frac{X(Zr/a)}{2\eta Z Z_1}\right]dr \qquad (30)$$

Substituting $B = \alpha r$, $r = B/\alpha$, $dr = dB/\alpha$

$$\textbf{Part 1} = \frac{1}{2a^2}\int_0^a r^3 J_0(\alpha r)dr = \frac{1}{2a^2\alpha^4}\int_0^a B^3 \cdot J_0 B dB \qquad (31)$$

$$= \frac{1}{2a^2\alpha^4}\left|B^3 J_1 B - 2B^2 J_2 B\right|_0^a$$

$$= \frac{1}{2a^2\alpha^4}\left|\alpha^3 r^3 J_1(\alpha r) - 2\alpha^2 r^2 J_2(\alpha r)\right|_0^a$$

$$= \frac{1}{2a^2\alpha^4}\left[\alpha^3 a^3 J_1(\alpha a) - 2\alpha^2 a^2 J_2(\alpha a) - 0\right]$$

per $J_1(0) = 0$ and $J_2(0) = 0$ by definition

$$= -\frac{J_2(\alpha a)}{\alpha^2}$$

per boundary condition (13a), $J_1(\alpha a) = 0$

$$\therefore \quad \text{Part 1} = \frac{J_0(\alpha a)}{\alpha^2}$$

per recurrence equation, $J_2 Y = \frac{2}{Y} J_1 Y - J_0 Y$, where $J_1 Y = 0$ due to our boundary condition (13a) for $Y = \alpha a$.

$$\textbf{Part 2} = \left[\frac{Z_2}{\eta Z^2 Z_1}-\frac{1}{4}\right]\int_0^a rJ_0(\alpha r)dr \qquad (32)$$

Let Q_1 be the constant quantity in brackets and substitute $B = \alpha r$

$$= Q_1\frac{1}{\alpha^2}\int_0^a BJ_0 B dB = Q_1\frac{1}{\alpha^2}\left|BJ_1 B\right|_0^a$$

$$= Q_1\frac{1}{\alpha^2}\left|\alpha r J_1(\alpha r)\right|_0^a = Q_1\frac{1}{\alpha^2}\left[aJ_1(\alpha a) - 0\right]$$

per $J_1(0) = 0$ by definition

$$\therefore \quad \text{Part 2} = 0 \qquad (32a)$$

per boundary condition $J_1(\alpha a) = 0$.

$$\textbf{Part 3} = -\frac{1}{2\eta Z Z_1}\int_0^a rX(Zr/a)J_0(\alpha r)dr \qquad (33)$$

Let Q_2 be the constant quantity and enter the correct expression for the X factor

$$= -Q_2\int_0^a r(Ber^2\, Z\, r/a + Bei^2\, Z\, r/a)J_0(\alpha r)dr$$

No exact solution could be found for the $(Ber^2 + Bei^2)$ integration, so the term was replaced by its expansion per Watson [8]

$$= -Q_2\int_0^a r\left[1+\sum_{m=1}^{\infty}\frac{\left(\frac{Zr}{2a}\right)^{4m}}{m!^2(2m)!}\right]J_0(\alpha r)dr$$

Integrating by parts and moving summation constants outside of the second integral

$$= -Q_2\int_0^a rJ_0(\alpha r)dr - Q_2\sum_m \frac{1}{m!^2(2m)!}\left(\frac{Z}{2a}\right)^{4m}\int_0^a r^{4m+1}J_0(\alpha r)dr$$

The first integral is zero, per integration of a constant by Part 2 above.

Substituting $B = \alpha r$ in the second integral

$$= -Q_2\sum_m \frac{1}{m!^2(2m)!}\left(\frac{Z}{2a}\right)^{4m}\frac{1}{\alpha^{4m+2}}\int_0^a B^{4m+1}J_0 B dB$$

A solution for the remaining integral is per McLachlan [9] which is of the form

$$\int_0^Z Z^M J_0(Z)dZ = \left|J_1 Z[Z^M - (M-1)^2 Z^{M-2} + \ldots] + J_0 Z[(M-1)Z^{M-1} - (M-1)^2(M-3)Z^{M-3} + \ldots]\right|_0^Z$$

Constant M must be odd, as is the case of $M = 4m + 1$. Applying the limits to the coefficient of the first expansion, at limit $= a$, $J_1(\alpha a)[BRK1] = 0$ due to the boundary condition, and at limit $= 0$, $J_1(0)[BRK2] = 0$ by definition. Applying the limits to the second expansion, Part 3 becomes

$$= -Q_2\sum_m \frac{1}{m!^2(2m)!}\left(\frac{Z}{2a}\right)^{4m}\frac{1}{\alpha^{4m+2}}\left|J_0 B[(4m+1-1)B^{4m} - (4m)^2(4m-2)B^{4m-2} + \ldots]\right|^a$$

Dropping all of the remaining terms in the expansion, substituting $B = \alpha r$, and applying limit $= a$

$$= -Q_2\sum_m \frac{1}{m!^2(2m)!}\left(\frac{Z}{2a}\right)^{4m}\frac{1}{\alpha^{4m+2}}\left\{J_0(\alpha a)[4m(\alpha a)^{4m} - (4m)^2(4m-2)(\alpha a)^{4m-2}]\right\}$$

At limit $= 0$, $J_0(0) = 1$, but the bracket term is zero. Now taking the first summation for $m = 1$

$$= -Q_2 \frac{1}{1\cdot 2}\left(\frac{Z}{2a}\right)^4 \frac{1}{\alpha^6}\{J_0(\alpha a)[4(\alpha a)^4 - 16(2)(\alpha a)^2]\}$$

$$= +Q_2 \frac{Z^4 J_0(\alpha a)4(\alpha a)^4}{32\alpha^2(\alpha a)^4}[8/(\alpha a)^2 - 1]$$

$$\therefore \quad \text{Part 3} = \frac{[8/(\alpha a)^2 - 1]Z^3}{16\eta Z_1}\cdot\frac{J_0(\alpha a)}{\alpha^2} \tag{33a}$$

Collecting all 3 parts, the integral finally becomes

$$\int_0^a rJ_0(\alpha r)f(r)dr = \frac{J_0(\alpha a)}{\alpha^2}\left[1 + 0 + \frac{[8/(\alpha a)^2 - 1]Z^3}{16\eta Z_1}\right] \tag{34}$$

APPENDIX 2

The integration of the following slab-load integral will be made by parts

$$\int_0^l \cos\alpha x\left[\frac{1}{2}\frac{x^2}{l^2} + \frac{Z_{s2}}{\eta Z_s{}^2 Z_{s1}} - \frac{1}{6} - \frac{X(Z_s x/l)}{\eta Z_s Z_{s1}}\right]dx \tag{35}$$

$$\textbf{Part 1} = \frac{1}{2l^2}\int_0^l x^2\cos\alpha x dx = \frac{1}{2l^2}\left|\frac{2x}{a^2}\cos\alpha x - \frac{2}{\alpha^3}\sin\alpha x + \frac{x^2}{\alpha}\sin\alpha x\right|_0^l \tag{36}$$

$$= \frac{1}{2l^2}\left[\frac{2l}{\alpha^2}\cos\alpha l - \frac{2}{\alpha^3}\sin\alpha l + \frac{l^2}{\alpha}\sin\alpha l - 0 + \frac{2}{\alpha^3}\sin 0 - 0\right]$$

$$= \frac{\cos\alpha l}{\alpha^2 l}$$

per $\sin 0 = 0$, and boundary condition (23c) $\sin\alpha l = 0$

$$\therefore \quad \text{Part 1} = \frac{l}{(n\pi)^2}\cos\alpha l \tag{36a}$$

per condition (23b) $\alpha = n\pi/l$.

$$\textbf{Part 2} = \left[\frac{Z_{s2}}{\eta Z_s{}^2 Z_{s1}} - \frac{1}{6}\right]\int_0^l \cos\alpha x dx = Q_3\left|\frac{1}{\alpha}\sin\alpha x\right|_0^l \tag{37}$$

$$= Q_3\left[\frac{\sin\alpha l}{\alpha} - 0\right]$$

$$\therefore \quad \text{Part 2} = 0 \tag{37a}$$

per boundary condition (23c) $\sin\alpha l = 0$.

$$\textbf{Part 3} = -\frac{1}{\eta Z_s Z_{s1}}\int_0^l \cos\alpha x(\cosh Z_s x/l + \cos Z_s x/l)dx \tag{38}$$

This integral is solved by letting $b = Z_s/l$ and using the series summations

$$\cosh bx = 1 + \frac{(bx)^2}{2!} + \frac{(bx)^4}{4!} + \frac{(bx)^6}{6!} + \ldots$$

$$\cos bx = 1 - \frac{(bx)^2}{2!} + \frac{(bx)^4}{4!} - \frac{(bx)^6}{6!} + \ldots$$

Adding the first four terms we get

$$\cosh bx + \cos bx = 2\left[1 + \frac{(bx)^4}{4!}\right]$$

substituting back into Part 3 integral with $Q_4 = -\dfrac{2}{\eta Z_s Z_{s1}}$

$$= -Q_4\int_0^l \cos\alpha x\left[1 + \frac{(bx)^4}{4!}\right]dx$$

Solving this new integral by parts

$$\textbf{Part 3a} = -Q_4\int_0^l \cos\alpha x dx = -Q_4\left|\frac{\sin\alpha x}{\alpha}\right|_0^l$$

$$\therefore \quad \text{Part } 3a = 0$$

$$\textbf{Part 3b} = -Q_4\frac{b^4}{4!}\int_0^l x^4\cos\alpha x dx \tag{38a}$$

$$= -Q_4\frac{b^4}{4!}\left|\frac{1}{\alpha}x^4\sin\alpha x - \frac{4}{\alpha}\int_0^l x^3\sin\alpha x dx\right|_0^l$$

The first term disappears per $\sin\alpha l = 0$ and $\sin 0 = 0$

$$= \frac{4}{\alpha}Q_4\frac{b^4}{4!}\left|\frac{3x^2}{\alpha^2}\sin\alpha x - \frac{6}{\alpha^4}\sin\alpha x - \frac{x^3}{\alpha}\cos\alpha x + \frac{6x}{\alpha^3}\cos\alpha x\right|_0^l$$

The first two terms disappear as above, the last two terms are zero at limit = 0, so the remainder is

$$= \frac{4}{\alpha}Q_4\frac{b^4}{4!}\left[-\frac{l^3}{\alpha} + \frac{6l}{\alpha^3}\right]\cos\alpha l$$

$$\therefore \quad \text{Part } 3b = Q_4\frac{lb^4}{\alpha^2 3!}\left[\frac{6}{\alpha^2} - l^2\right]\cos\alpha l \tag{38b}$$

Collecting all parts of Part 3 and using (23b), $\alpha = n\pi/l$

$$\text{Part 3} = \frac{l^3 b^4 l^2}{3(n\pi)^2\eta Z_s Z_{s1}}[6/(n\pi)^2 - 1]\cos\alpha l$$

substituting $b = Z_s/l$

$$= \frac{l}{(n\pi)^2}\frac{[6/(n\pi)^2 - 1]Z_s{}^3}{3\eta Z_{s1}}\cos\alpha l \tag{38c}$$

Now collecting all 3 parts, the integral becomes

$$\int_0^l \cos\alpha x f(x)dx = \frac{l}{(n\pi)^2}\left\{1 + 0 + \frac{[6/(n\pi)^2 - 1]Z_s{}^3}{3\eta Z_{s1}}\right\}\cos\alpha l \tag{39}$$

APPENDIX 3

The simplified surface T_2 and center T_0 steady-state temperatures of an infinitely long slab of width W_2 and thickness $H_2 = 2l$ can be determined by substituting $x = l$ and $x = 0$, respectively, into equation (21)

$$T_2 = \frac{P_2 l}{K}\left[T_s + \frac{1}{3} + \frac{Z_{s2} - Z_s\cdot Z_{s0}}{\eta Z_s{}^2 Z_{s1}}\right] \tag{40}$$

$$T_0 = \frac{P_2 l}{K}\left[T_s - \frac{1}{6} + \frac{Z_{s2} - 2Z_s}{\eta Z_s{}^2 Z_{s1}}\right] \tag{41}$$

Subtracting the center temperature from the surface temperature

$$T_2 - T_0 = \frac{P_2 l}{K}\left[\frac{1}{2} - \frac{Z_{s0} - 2}{\eta Z_s Z_{s1}}\right]$$

$$= \frac{P_2 H_2}{4K} F_2 \tag{42}$$

where

F_2 = slab center to surface temperature factor

$$= 1 - 2(Z_{s0} - 2)/(\eta Z_s Z_{s1}) \tag{43}$$

Now subtracting the center temperature from the slab's average temperature equation (20)

$$T_1 - T_0 = \frac{P_2 l}{K}\left[\frac{1}{6} - \frac{Z_{s2} - 2Z_s}{\eta Z_s^2 Z_{s1}}\right]$$

$$= \frac{P_2 H_2}{4K} F_3 \tag{44}$$

where

F_3 = slab center to average temperature factor

$$= 1/3 - 2(Z_{s2} - 2Z_s)/(\eta Z_s^2 Z_{s1}) \tag{45}$$

APPENDIX 4

Fig. 4 also shows the comparison between the earlier approximation (dash curves) of the transient correction [1] and [10] and the correction as derived in this paper (solid curves) for round loads calculated at $\eta = 100$ percent.

At the starting time $T = 0$, the error for the magnetic case of $Z \approx 20$ was -9 percent at the center and surface of the load while the error for the nonmagnetic case of $Z \approx 1$ was -33 percent at the center and $+33$ percent at the surface.

At values of $T > 0.1$ the error becomes insignificant and the approximation is adequate.

K. T. SHIH
Senior Research Engineer,
Thermodynamics,
Convair Aerospace Division,
General Dynamics,
San Diego, Calif.

R. DETHLEFSEN[1]
Manager of Electrophysics,
Allis-Chalmers Research,
Milwaukee, Wisc.

Anode Heat Flux Density of High-Current Arcs

The anode heat flux density of high-current arcs was determined by measuring the time from striking an arc to the onset of surface melting. Data were taken using argon and nitrogen with different metals, pressures, and anode surface temperatures. The anode heat flux density was found to be between 10^4 and 10^6 w/cm² for arc currents of 50 to 2000 amp*; these values increased with increasing arc current and gas pressure and were higher in nitrogen than in argon. The initial anode surface temperature also had a strong effect on the anode attachment spot.*

Introduction

THE DEVELOPMENT of electric-arc devices and switch gear is limited by electrode erosion, with the major share of erosion usually occurring at the anode of a high-current arc. This erosion is correlated with the fact that the anode generally receives a large heat flux from the arc. The amount of erosion can be reduced if the arc is moved rapidly across the electrode surface by an applied magnetic field or by a gas flow.

In an earlier phase of the present work [1],[2] it was demonstrated that the moving arc attaches momentarily in one or several simultaneous attachment spots on the anode surface. The lifetime of these attachment spots was found to be in the range from 1 to 20 μsec. Localized electrode erosion—in the form of small craters—was caused by these attachment spots. Observations of these craters indicate that the primary destructive effect on the anode was local melting and other effects of highly localized heating. It became apparent that measurements of the heat flux into the anode were desirable. The average rate of heat transfer to the anode of arc devices has been determined by several laboratories from an energy balance of the coolant [2]. For anode erosion due to a moving arc, the local maximum value, not the average heat flux, is the important parameter. To the best of our knowledge, this value had not yet been measured.

In this work, a test facility was built to duplicate, under controlled conditions, the stationary attachment spots of a moving arc. A variable-pulse-length arc discharge was generated in a predetermined position on an anode test plate and the local maximum value of the heat flux density was determined from the time it took the anode metal to start melting. Pulse times of the stationary arc were chosen according to the range observed from high-speed films of the traveling arc [1]. Experiments were conducted in argon and nitrogen atmospheres with various anode metals, at varied pressure levels. These measurements may be of value as input data to the design of water-cooled anodes for fast-moving, high-current arcs. A futher application may exist in assessing the possible damage to aerospace structures due to atmospheric lightning [3, 4].

It should be kept in mind that the measurements on a pulsed stationary arc are supposed to simulate the conditions at the stationary attachment spots of magnetically driven arcs. Conditions at the anode attachment of a steady and stationary arc discharge are likely to be different—due to either the higher pressure inside an impulsive discharge, or the effect of an applied magnetic field.

[1] Formerly Staff Scientist, Space Science Laboratory, Convair Division, General Dynamics Corporation, San Diego, Calif.

[2] Numbers in brackets designate References at end of paper.

Contributed by the Heat Transfer Division and presented at the Winter Annual Meeting, Los Angeles, Calif., November 16–20, 1969, of THE AMERICAN SOCIETY OF MECHANICAL ENGINEERS. Manuscript received by the Heat Transfer Division, July 20, 1970. Paper No. 69-WA/HT-57.

Nomenclature

b = thickness of the anode foil, cm
B = magnetic field strength, gauss
c = heat capacity, w·sec/g·deg K
d = diameter, cm
I = arc current, amp
j = electric current density, amp/cm²
j_{cr} = critical current density defined by equation (3), amp/cm²
l = thermal diffusion depth, cm
q = anode heat flux density, w/cm²
r = radius, cm
t = time, sec
T = temperature, deg K
ΔT = temperature rise of the metal at the surface, deg K
λ = thermal conductivity, w/cm·deg K
ρ = specific density, g/cm³
τ = characteristic time, sec
σ = electrical conductivity, 1/ohm·cm
α = thermal diffusivity, cm²/sec

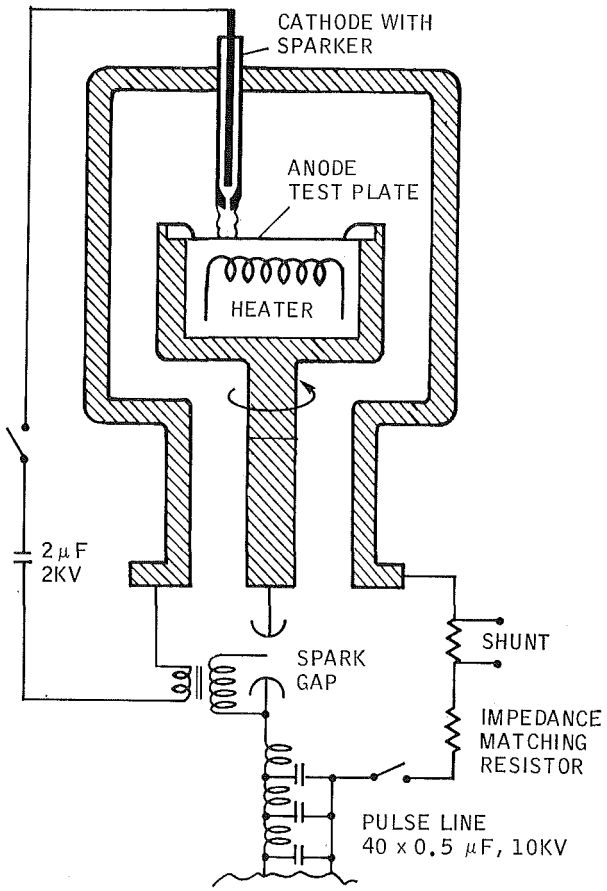

Fig. 1 Schematic setup for the pulsed arc; electrode assembly is mounted in an environmental chamber

Analytical Considerations

The basis for analyzing the data is the equation of transient heat conduction. Heat is transmitted from the plasma through the attachment surface into the metal, and is also generated inside the metal by Joule heating. The differential balance of heat flux is described by the equation

$$\rho c \frac{\partial T}{\partial t} = \lambda \nabla^2 T + \frac{j^2}{\sigma}. \tag{1}$$

A dimensional analysis of the terms leads to simple relations which describe their relative importance. Comparing the transient with the steady-state conduction term and inserting characteristic variables of time τ and length l for the derivatives gives

$$\frac{c\rho \dfrac{\partial T}{\partial t}}{\lambda \nabla^2 T} \propto \frac{c\rho T l^2}{\tau \lambda T}.$$

This relationship yields a useful expression for the thermal diffusion depth

$$l = \sqrt{\frac{\lambda \tau}{c\rho}} = \sqrt{\alpha \tau}. \tag{2}$$

When the Joule heating term is compared with the thermal conduction term, and the Wiedemann-Franz-Lorentz law [5]

$$\frac{\lambda}{\sigma} = L \times T \quad \text{with} \quad L = 2.24 \times 10^{-8} \left(\frac{\text{volt}}{\text{deg K}}\right)^2$$

is introduced, we obtain

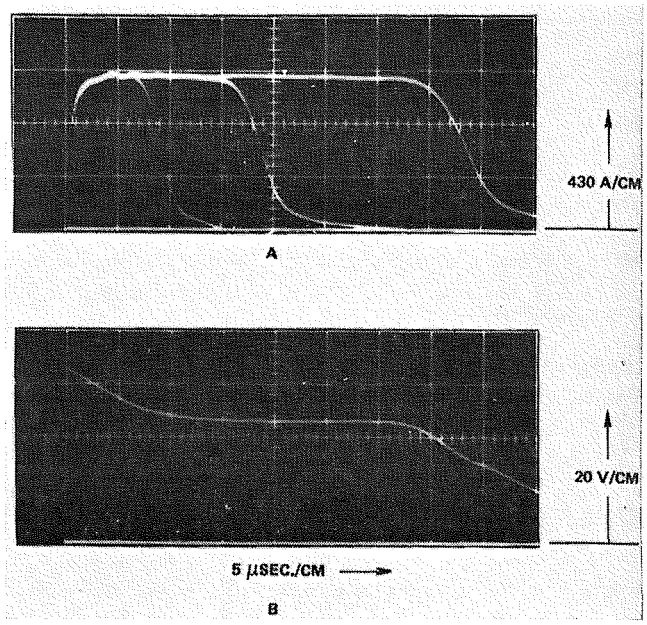

Fig. 2 (A) Pulsed arc current for varied number of sections in the lumped-parameter discharge line (9,18, and 40 sections); charging voltage 2.5 kv; (B) arc voltage oscillogram; nitrogen arc, 5-mm gap, 1 atm, 1.25 kA, copper anode

$$\frac{j^2}{\sigma \lambda \nabla^2 T} \propto \frac{j^2 l^2}{\sigma \lambda T} = \frac{j^2 l^2 L}{\lambda^2}.$$

The effect of Joule heating in the metal thus can be neglected for

$$j < j_{cr} = \frac{\lambda}{l} \sqrt{\frac{1}{L}}. \tag{3}$$

An analytical solution to the equation of transient heat conduction relevant to our problem is given in reference [6]. Under the assumptions of a semi-infinite solid body with constant heat flux into the interface, Joule heating neglected, one-dimensional propagation, and constant properties of the metal, heat flux density is given by

$$q = (\rho c \lambda \pi / t)^{1/2} \Delta T / 2. \tag{4}$$

The one-dimensionality assumption is satisfied if the attachment spot diameter is larger than the thermal diffusion depth l [7]. If this is not fulfilled, the above relation will yield too small a value of heat flux density. The characteristic length l for all materials tested in this work has the order of 10^{-3} cm for a residence time of the arc attachment spot of 10^{-5} sec.

The current density j_{cr}, above which Joule heating in the metal becomes a significant contribution, ranges from 2.4×10^6 amp/cm^2, for low-conductivity materials like tantalum, to 25×10^6 amp/cm^2, for high-conductivity materials such as copper. Current densities of such magnitude are reported to exist only in the cathode spot.

The anode test plates generally had a thickness of about 1 mm. To gain a check on the heat flux data calculated from equation (4), very thin (10^{-3} cm) anode foils were used. The heat transfer then was calculated from the equation:

$$q = \rho c b \Delta T / t. \tag{5}$$

The underlying assumption is that the heated part of the thin foil is spacewise isothermal; Joule heating is also neglected.

Experimental Apparatus and Measurement Procedure

Fig. 1 shows the low-inductance, coaxial-electrode geometry used to generate the pulsed arc. The coaxial electrodes were

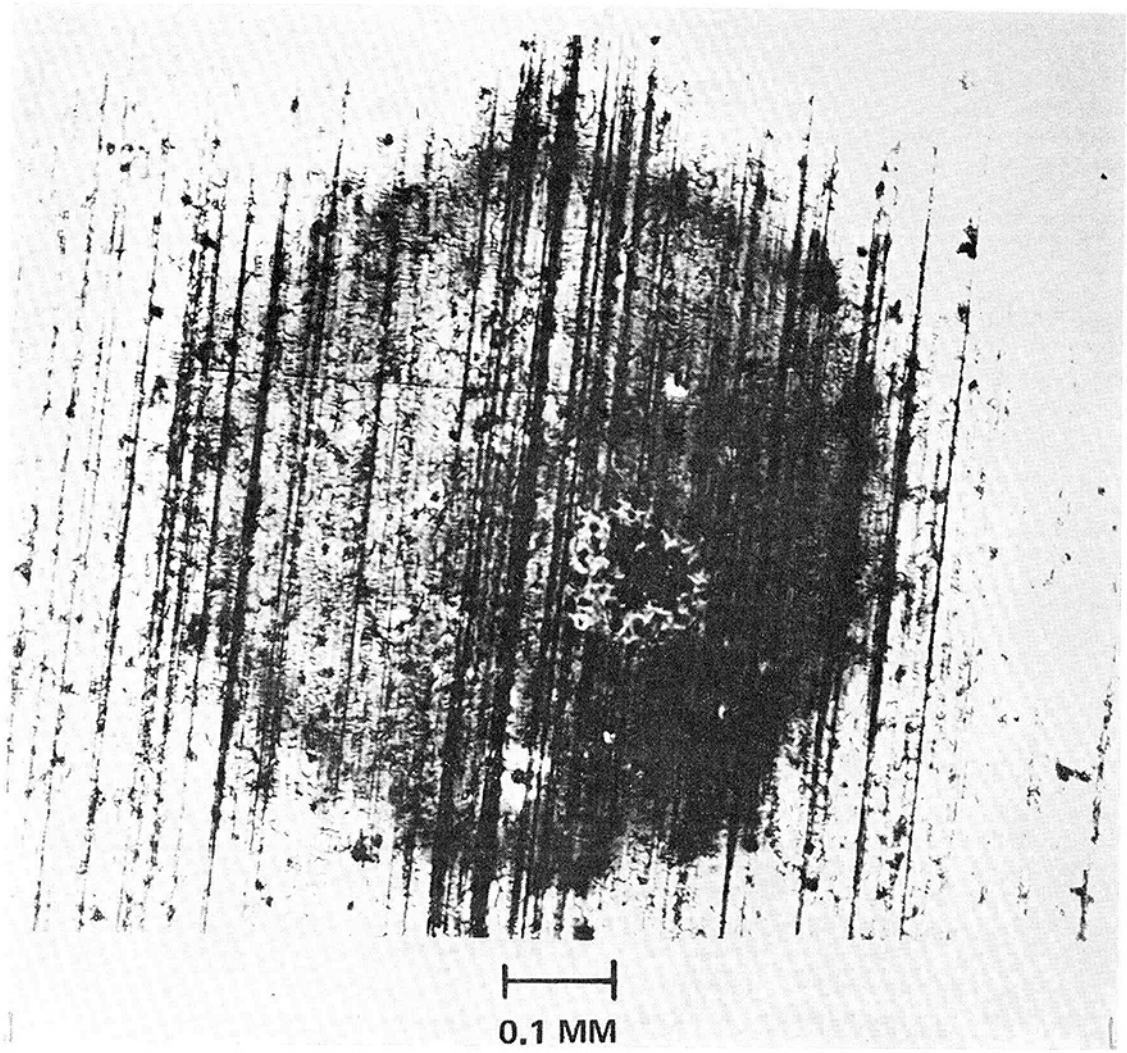

Fig. 3 Anode attachment on copper plate; nitrogen arc, 2 atm, 0.6 kA, 17 μsec, 5-mm gap

mounted in an environmental chamber. The inner electrode (presently the anode) received the erosion test plates, which could be rotated from outside the environmental chamber. This made it feasible to collect the traces of about eight arcs on the test plate without opening the environmental chamber. Triggering was initiated by a spark emitted through a 0.15-cm-dia channel in the tip of the tungsten cathode. This condition was very similar to the condition of the moving arc where a forward attachment spot was formed by the breakdown between a stream of plasma and the electrode surface. A spark gap in the main current circuit was necessary to prevent accidental breakdown at high voltages and low pressure.

A nearly rectangular arc current pulse was obtained from a lumped-parameter capacitor discharge line that can deliver a pulse current up to 5 kA with a pulse length variable between 2 and 40 μsec. Fig. 2 shows the oscilloscope traces of the arc current pulse for the three values of pulse length, plus a trace of the arc voltage. Examination of both current and voltage traces shows that a steady state was reached at about 5 μsec.

Because surface condition had a strong influence on the threshold for the occurrence of anode erosion, all test plates were carefully polished and deoxidized. Experiments were conducted in argon and nitrogen at pressures between 0.25 and 3 atm.

The anode heat flux density of the pulsed-arc discharges is determined from equations (4) or (5). ΔT is taken as the difference between the melting temperature of the anode material and the initial temperature of the anode metal before the pulsed discharge. Thermal properties of the anode metal were chosen corresponding to a temperature of about $^2/_3$ that of the melting temperatures. Thermal properties and the relative ability to withstand impulsive and steady heat loads have been compiled in reference [1] for many possible anode materials. The time t of equations (4) and (5) is taken as the pulse time of the discharge.

Experimentally, it was more convenient to vary the arc current than to change the pulse time. Hence the melting threshold was found by increasing the arc current for successive discharges with constant pulse duration. Since arc attachment occurs at predetermined positions it was easy to determine by microscopic observation what arc current and given set of other parameters correspond to incipient melting. An example of the anode attachment marks on a copper anode is shown in Fig. 3. The observed erosion marks are very similar to those observed for the magnetically driven arc. The heat flux density was determined from these observations using the equation of unsteady heat conduction. By varying the pulse time and by choosing metals with different thermal properties, different magnitudes of heat flux density can be evaluated.

The estimated accuracy of the measurements is given in the following discussion. Gas pressure was measured with a Wallace and Tiernan gauge with an accuracy of better than 1 percent. The pulse length was determined from the number of sections in the lumped-parameter discharge line. Fig. 2 shows oscilloscope traces of the arc current pulse for three values of pulse length.

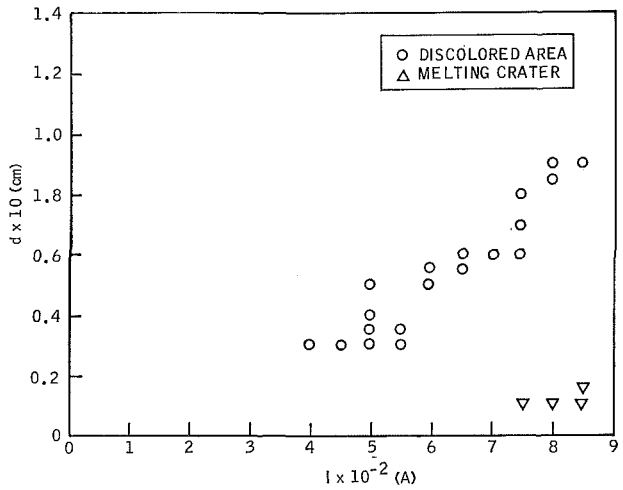

Fig. 4 Diameter of erosion tracks on copper plate as a function of the arc current; nitrogen arc, 0.5 atm, 17 μsec, 5-mm gap

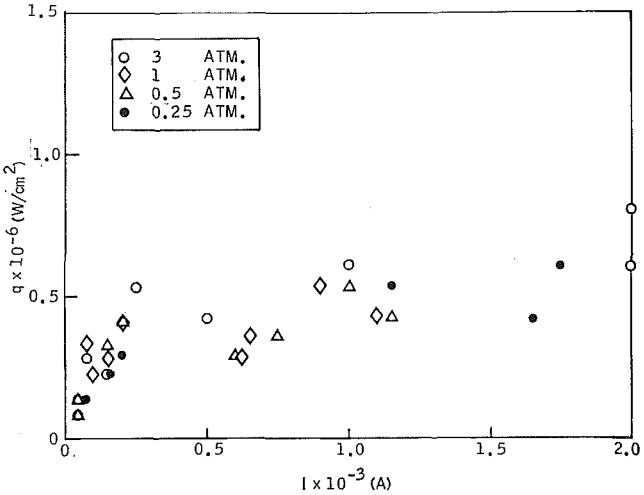

Fig. 6 Anode heat flux density as a function of the arc current; argon arc, 5-mm gap

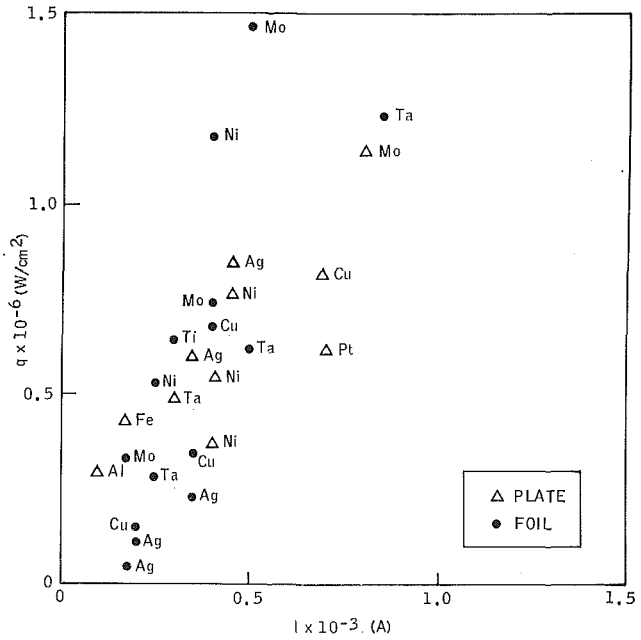

Fig. 5 Comparison between two different methods of measuring the anode heat flux density; nitrogen arc, 1 atm, 5-mm gap, anode metal is indicted by chemical symbol

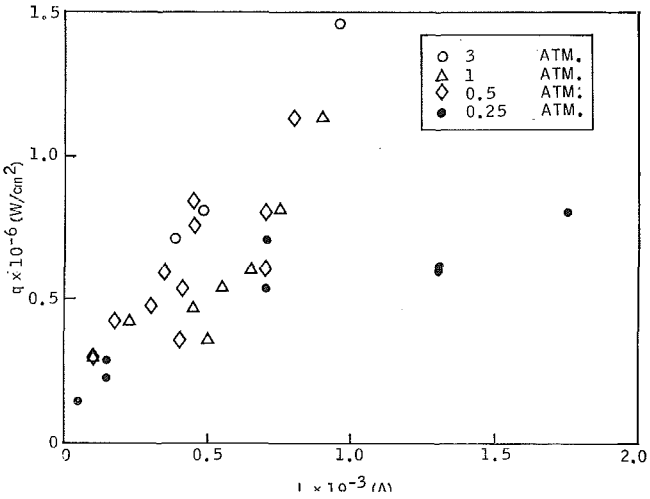

Fig. 7 Anode heat flux density as a function of the arc current; nitrogen arc, 5-mm gap

In performing the routine experiments, arc current amplitude was determined by measuring the capacitor charging voltage. This was permissible because any possible variations in arc impedance were small in relation to that of the discharge line and the ballast resistor. A current-measuring shunt was also used, which had been calibrated with high-precision instruments of better than 1 percent accuracy. The charging voltage was measured with a field-service-type voltmeter of about ± 5 percent accuracy.

The values of arc current (threshold current) in Figs. 5–7 correspond to those values where incipient melting could be observed. Because determination of incipient melting requires tedious scrutiny of the metal surface under a microscope, the estimated uncertainty of the arc current in the graphs is ± 15 percent. Determination of the maximum local value of heat flux depends on a knowledge of the thermal properties of the metal. Temperature-averaged values have been used in the evaluation. A further uncertainty was introduced by the difficulty of completely removing all surface layer on the various anode metals. Different grain sizes also added to the uncertainty.

Experimental Results

Fig. 3 shows a typical anode attachment track formed on copper in a nitrogen atmosphere. The dark circular area consists of a colorful deposit believed to be a thin coating of copper oxide. Near the center of the track in Fig. 3, there is a 0.14-mm-dia melting crater surrounded by a few pits of 0.01-mm diameter, which also show melting in an incipient stage. These small individual pits are the starting phase of anode erosion and occur above a certain value of current. Their number increases with increasing current, and also seems to increase with increasing pulse length. At higher currents, individual pits band together to form a large melting crater. It seems that the small pits correspond to anode attachment with strong constriction. The diameter of the discolored area depends on pulse duration. A 20 percent increase in diameter was observed when the pulse length was varied from 5 to 38 μsec. The discolored area corresponds to the area of contact between the copper and the arc plasma. Within this area, the current distribution seems to be strongly nonuniform. Fig. 4 shows an increase of the discolored area with

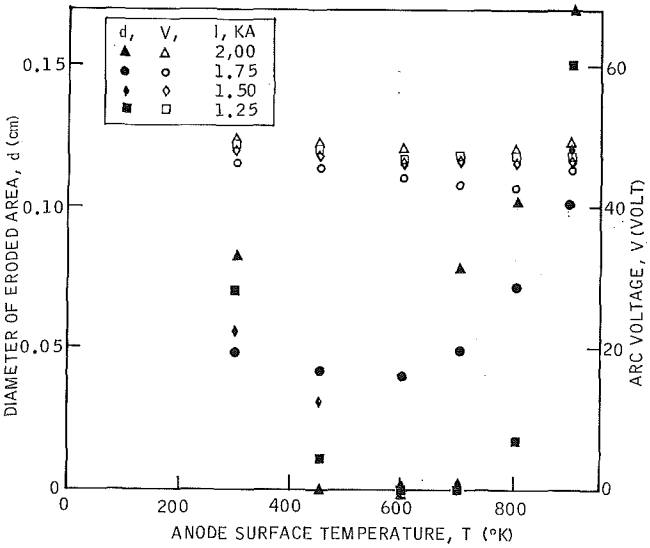

Fig. 8 Effect of surface temperature on copper anode erosion and arc voltage; nitrogen arc, 1 atm, 17 μsec, 5-mm gap

increasing current. Melting craters with a diameter of about 0.1 mm start to form at a current of 750 amp.

A comparison of local maximum values of heat flux density taken with thick plates and thin foils is shown in Fig. 5. Arc pulse time was varied between 8.5 and 38 μsec. The various anode metals used are indicated by their chemical symbols in the graph. The data show considerable scatter, but no consistent discrepancy between data taken with an anode plate, equation (4), or the anode foil, equation (5), can be seen.

Data obtained with argon and nitrogen using an anode plate, equation (4), at different pressures, are collected in Figs. 6 and 7. Some valuable information can be drawn from these heat flux data:

1 Measured values of heat flux density are between 10^4 and 10^6 w/cm^2.

2 Heat flux density is higher in nitrogen than in argon by a factor of two.

3 Heat flux density increased with increasing total arc current and gas pressure.

The measured values of heat flux density were in good agreement with the analysis of Cobine and Burger [8].

The effect of initial anode surface temperature was also studied. In these experiments, the anode plate was preheated with an electric heater installed underneath the plate, see Fig. 1. A thermocouple was attached to the edge of the plate to measure the temperature. Precaution was taken to check the temperature distribution on the plate. With a copper plate, it was found that the maximum temperature difference between the center and the edge of the plate was about 15 deg K for the temperature range covered by the present study. Arcs of various current magnitude had been struck on anodes in a nitrogen atmosphere, while the anode surface was held at constant temperature within the range from 300 to 900 deg K. For a copper anode, the coloration area which was formed normally in nitrogen and air was increased and became more and more faint with increasing anode surface temperature. At 600 deg K a very faint coloration area of 0.5-cm diameter was observed. With a further increase in anode surface temperature, the discolored area completely disappeared. Fig. 8 illustrates the variation of eroded area, and arc voltage, with anode surface temperature. At temperatures of 300 deg K and 900 deg K, the eroded area increased with increasing arc current as expected. However, at temperatures between 450 deg K and 800 deg K the trend was either reversed or became irregular. This irregularity may have been caused by a movement of the anode attachment spot at higher currents, which was indicated by the shape of the discolored area. The arc voltage first decreased, then increased, as the initial anode surface temperature was increased.

Brichkin, et al. [9] also observed that the arc anode attachment became more diffuse at higher anode surface temperatures. The inherent physical reason is not yet understood. One explanation may be that close to a heated anode, the gas density, ρ, is lower, and the anode attachment becomes more diffuse because $r(t) \propto \rho^{-n}$, where n has a value about 0.3 [10]. Also, there may be some effects on the changes of anode surface conditions, which may be due to the process of outgassing or growth in the grain size, etc.

Since a metal surface at higher temperature can withstand only transient heat loads of decreased magnitude, it is conceivable that an optimum value of anode temperature for the condition of minimized erosion exists. An optimum thickness of the water-cooled anode can then be estimated using a simple heat-conduction equation. For a copper anode, with a surface temperature on plasma side of 700 deg K, and on water side of 370 deg K, a heat flux density of 10^6 w/cm^2 gives an optimum thickness of 0.15 cm.

Conclusions

A method has been developed to measure the anode heat flux density of the high-current arc. Anode heat flux density was found to be between 10^4 and 10^6 w/cm^2. It increased with increasing arc current and gas pressure and it is higher in nitrogen than in argon. This high value of anode heat flux causes a frequent anode erosion, which first decreased and then increased when the initial anode surface temperature was increased.

Acknowledgments

The reported work was performed under Contract F33615-67-C-1386 for the Aerospace Research Laboratories, Office of Aerospace Research, United States Air Force. The authors wish to acknowledge many stimulating discussions with A. V. Larson, E. E. Soehngen, H. O. Schrade, and W. C. Roman. Special acknowledgment is due J. P. Tinkham for contributing to the design, for building the test facility, and for performing part of the measurements.

References

1 Dethlefsen, R., "Investigation of Electrode Erosion in High Current Electric Arcs," ARL Report 68-0112, 1968.

2 Eckert, E. R. G., and Pfender, E., "Advance in Plasma Heat Transfer," *Advances in Heat Transfer*, Vol. 4, Academic Press, New York, 1967, pp. 229–316.

3 Schneider, K. H., "Stosstromeinwirkung auf ebene Metallflachen," ETZ-A Bd. 89, H. 11, 1968, pp. 254–259.

4 Kofoid, M. J., "Lightning Discharge Heating of Titanium Aircraft Skins," Boeing Sci. Res. Lab., D1-82-0752, 1968.

5 Joos, G., *Lehrbuch der Theoretischen Physik*, Akademische, Frankfurt, 1959, p. 148.

6 Carslaw, H. S., and Jaeger, J. C., *Conduction of Heat in Solid*, Oxford, London, 1959, p. 75.

7 Cramer, K. R., and Roman, W. C., "Electrode Design Based on Transient Thermal Analysis," ASME Paper No. 69-WA/HT-52, 1969.

8 Cobine, J. D., and Burger, E. E., "Analysis of Electrode Phenomena in the High-Current Arc," *Journal of Applied Physics*, Vol. 26, July 1955, pp. 895–900.

9 Brichkin, A. V., Bolotov, A. V., and Borisova, T. V., "Dynamics of Electrode Spots in an Electric Arc," *Soviet Physics—Technical Physics*, Vol. 11, Jan. 1967, pp. 929–934.

10 Somerville, J. M., *The Electric Arc*, Methuen, London, 1959, p. 110.

journal of heat transfer

discussion

Heat Transfer to Horizontal Gas-Solid Suspension Flows[1]

W. J. Danziger.[2] The values of Nu in Figs. 5 and 7 show considerable difference from published data for vertical flow of air-solids mixtures. In [1][3] it was shown that up to W_s/W_a of about 1.0 there was little effect of the solids (although there was a tendency toward a slight increase in Nu), and that over W_s/W_a of 2.0, Nu varied as $(W_s/W_a)^{0.45}$. In [7] it was reported that Nu varied as $Re^{0.66}$.

Fig. 7, however, shows zero effect of W_s/W_a, and indicates values of Nu for air-solids mixtures only 80–90 percent of those for solids–free-air instead of approximately 230 percent that would be predicted for the maximum solids concentration used. Fig. 5 shows some points that indicate no dependence on either W_s/W_a *or* Re, and others that indicate no dependence on Re but show a greater effect of W_s/W_a than would be predicted. Both [1] and [7] were based on cracking catalyst of about 50μ average particle diameter, but extrapolation to either 30μ or 200μ average diameter glass particles could not be expected to introduce errors of the magnitude of the discrepancies indicated, and change from vertical to horizontal flow would not change the relationships noted as long as no solids accumulated on the bottom of the tube.

At least some of the discrepancy results from use of $(T_w - T_{mm})$ in calculation of the heat transfer coefficient. This gives a false value of h, since it is $(T_w - T_a)$ that represents the true driving force for transfer of heat from the hot surface. Though T_a wasn't measured, T_{mm} wasn't measured either, and only incorrect values of h can be calculated with it. It is suggested that useful information might be derived from the data by use of the equation given in [7] for the MTD between air and a solid particle, together with a heat balance, to estimate T_a. The possible error in the assumed value of h between gas and particle will result in some possible error in the calculated value of T_a, and therefore of h between fluid and wall, but h so calculated will still be more correct than the value used by the authors.

It it is assumed that a higher temperature at the top of the tube would stem from stratification, the reduced heat capacity of the resulting solids-poor mixture at the top of the constant-flux tube would require that the air temperature be higher there than that in the lower portion, thus intensifying the error in h calculated on the basis of T_{mm}. However, it is inconceivable that gas flowing at a given mass rate does not prevent stratification of small beads yet does prevent stratification of beads of perhaps 300 times the mass of the small beads. A more reasonable explanation of the temperature discrepancy, top versus bottom, affecting the small bead but not the large bead might be that an electrostatic charge on the beads caused fines to plate out on the upper tube surface. At the bottom of the tube there would be enough scouring action to prevent such plating, whereas at the top of the tube the scouring would be less intense, with gravity acting to reduce particle impact, thus allowing an insulating coating to remain. Even the smallest diameter sphere in the size range of the large bead, however, is many times larger than any particle that would be expected to adhere to the wall because of its charge.

Fig. 8 shows pressure drop at Re of 30,000 remaining unchanged, whether air-only or the same quantity of air with up to about 4 lb of 30μ beads per pound of air was flowing. Such constancy would seem to be more indicative of manometer leads plugged with beads than of a novel flow effect.

Authors' Closure

The authors wish to thank Mr. Danziger for his suggestion. The influence of the estimated mean air temperature on the evaluation of Nu is being studied, and the results will be presented along with additional data in the near future. More recent pressure-drop data have confirmed the previous findings, and plugged pressure taps can be ruled out as a possibility.

[1] By C. A. Depew and E. R. Cramer, published in the February, 1970, issue of the JOURNAL OF HEAT TRANSFER, TRANS. ASME, Series C, Vol. 92, No. 1, pp. 77–82.

[2] The M. W. Kellogg Company, New York, N. Y.

[3] Numbers in brackets designate References at end of article under discussion.

Heat Flux Through a Strip-Heated Flat Plate[1]

Frederick A. Costello.[2] An exact solution to the subject problem that is more convenient than that presented by Schmitz [8][3] can be obtained by use of the Schwarz-Christoffel transformation [9]. A typical section of the strip-heated plate is shown in Fig. 1. The transformation is given by $(d > 1)$

$$\frac{dz}{d\tau} = K \frac{1}{\sqrt{\tau(\tau - 1)(\tau - d)}} \tag{1}$$

An elliptic integral of the first kind, defined by

$$F(k, \sin^{-1} R) \equiv \int_0^R \frac{dr}{\sqrt{(1 - r^2)(1 - k^2 r^2)}} \tag{2}$$

results, with the one complication that the second argument is complex.

[1] By R. A. Schmitz, published in the February, 1970, issue of the JOURNAL OF HEAT TRANSFER, TRANS. ASME, Series C, Vol. 92, No. 1, pp. 201–202.

[2] Associate Professor, University of Delaware, Newark, Del.

[3] Numbers in brackets designate Additional References at end of Discussion.

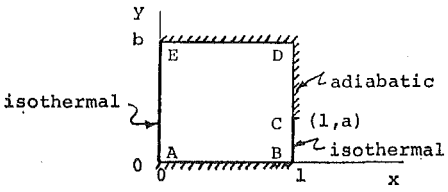

Fig. 1 Typical section

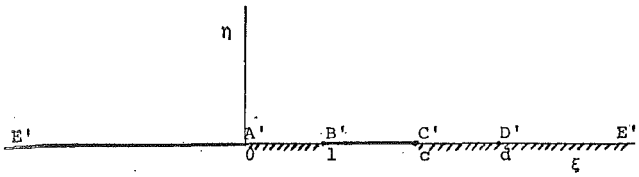

Fig. 2 Mapping onto upper half-plane

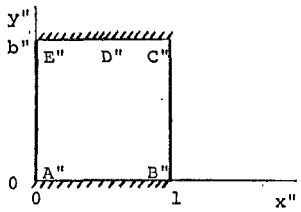

Fig. 3 Inverse mapping

The integral of equation (1) can be expressed in terms of elliptic integrals if the following transformation is used:

$$\tau = r^2$$

Then, for $\tau < 1$ and for $\tau = 0$ corresponding to $z = 0$,

$$z = \frac{2K}{\sqrt{d}} F\left[\frac{1}{\sqrt{d}}, \sin^{-1}(\sqrt{\tau})\right]$$

For $\tau > 1$, a second transformation is required:

$$d - r^2 = (d - 1)w^2$$

so that

$$z = \frac{2K}{\sqrt{d}} F\left(\frac{1}{\sqrt{d}}, \frac{\pi}{2}\right) - \frac{2K}{\sqrt{d}} i\left[F\left(\sqrt{\frac{d-1}{d}}, \sin^{-1}\left(\sqrt{\frac{d-\tau}{d-1}}\right)\right) - F\left(\sqrt{\frac{d-1}{d}}, \frac{\pi}{2}\right)\right]$$

For $z = 1$ to map onto $\tau = 1$ and for $z = 1 + ib$ to map onto $\tau = d$,

$$\frac{\sqrt{d}}{2K} = F\left(\frac{1}{\sqrt{d}}, \frac{\pi}{2}\right) \tag{3}$$

$$b = \frac{2K}{\sqrt{d}} F\left(\sqrt{\frac{d-1}{d}}, \frac{\pi}{2}\right) = F\left(\sqrt{\frac{d-1}{d}}, \frac{\pi}{2}\right) \Big/ F\left(\frac{1}{\sqrt{d}}, \frac{\pi}{2}\right) \tag{4}$$

The location of C' can be determined from the known value of $z(= 1 + ia)$ at C:

$$a = \left[F\left(\sqrt{\frac{d-1}{d}}, \frac{\pi}{2}\right) - F\left(\sqrt{\frac{d-1}{d}}, \sin^{-1}\sqrt{\frac{d-c}{d-1}}\right)\right] \Big/ F\left(\frac{1}{\sqrt{d}}, \frac{\pi}{2}\right) \tag{5}$$

The conductance of the strip heater as shown in Fig. 1 can be determined from the above transformation as follows:

1 The value of d is determined from equation (4) for the known value of b.

2 The value of c is determined from equation (5) for the known values of a and d.

3 The mapping in the $(\xi - \eta)$ plane, Fig. 2, is transformed via the same equations to the $(x'' - y'')$ plane shown in Fig. 3 to a problem with known conductance. The location of b'' is found from equation (4)

$$b'' = F\left(\sqrt{\frac{c-1}{c}}, \frac{\pi}{2}\right) \Big/ F\left(\frac{1}{\sqrt{c}}, \frac{\pi}{2}\right)$$

4 The conductance of Fig. 1 is calculated from [2]

$$\frac{Q}{k(\Delta T)} \equiv S = b''$$

It appears that the above solution is the only closed-form solution to the subject problem expressible in terms of tabulated functions.

Additional References

8 Schmitz, R. A., "Heat Flux Through a Strip-Heated Flat Plate," JOURNAL OF HEAT TRANSFER, TRANS. ASME, Series C, Vol. 92, No. 1, Feb. 1970, pp. 201–202.

9 Carslaw, H. S., and Jaeger, J. C., "Conduction of Heat in Solids," Oxford University Press, Oxford, England, 1959.

Taylor-Goertler Vortices and Their Effect on Heat Transfer[1]

Arun S. Mujumdar.[2] Although boundary layer development over curved surfaces is of great practical importance, to my knowledge there are no accurate prediction methods available which incorporate transverse and/or streamwise curvature effects. The effect of surface curvature is, of course, a special case of the more general effect of streamline curvature [12].[3] The curvature effects could be significant even on plane walls near separation. The problem dealt with by Professor McCormack and his coworkers is, therefore, a significant contribution to the existing literature, and will provide guidelines for future work in this area.

---

[1] By P. D. McCormack, H. Welker, and M. Kelleher, published in the February, 1970, issue of the JOURNAL OF HEAT TRANSFER, TRANS. ASME, Series C, Vol. 92, No. 1, pp. 101–112.

[2] Mechanical Engineer, Research Division, Carrier Corp., Syracuse, N. Y.

[3] Numbers in brackets designate Additional References at end of Discussion.

The authors have shown that a linear analysis is not physically realistic. In fact, the nonlinear mechanism of vortex stretching seems to be crucial to all flows near walls; the viscous sublayer is perhaps a classical example [13]. A nonlinear analysis similar to that carried out by Sutera, Kestin, and Maeder would probably explain the increased heat transfer rates. The authors may be aware of the work of Williams [14] who solved the vortex-stretching model on an IBM computer using the versatile CSMP (Continuous System Modeling Program) language. The frequently awkward time and amplitude scaling procedures are not required in this digital equivalent of an analog computer. A major problem encountered in solving boundary-value problems numerically is that of searching the right initial conditions. I have successfully used a very elegant least-squares method proposed by Nachtsheim and Swigert [15] to obtain rapid convergence in the solution of boundary-layer-type equations. The technique is relatively insensitive to the initial guess.

Secondly, I wish to suggest that the 3 percent free-stream turbulence level could enhance the heat transfer rate appreciably if a streamwise pressure gradient exists [16]. Curiously enough, it appears that the physical mechanisms responsible for the transport phenomena are basically different depending on whether or not the flow contains oscillations of a discrete frequency (e.g., Taylor-Goertler vortices) or a wideband spectrum of frequencies (e.g., turbulence). Although only remotely analogous, one may consider the observations of Smith [17] with regard to the effect on heat transfer of the wake-induced periodicity near the forward stagnation point of a circular cylinder in a turbulence-free stream. His hot-wire data indicated that the wake induced periodic fluctuations (at Strouhal frequency) of about 12 percent of the mean velocity just outside the boundary layer. Suppression of these periodic oscillations by placing a splitter-plate in the near wake did not affect the heat transfer in the stagnation region (Re $\simeq$ 50,000). My own experiments at lower Reynolds numbers (5000–10,000), however, indicated a definite effect of these oscillations (up to 15 percent), the effect being more pronounced at lower free-stream turbulence levels and lower Reynolds numbers [18]. It is not intended to suggest or imply that the Taylor-Goertler vortices are similar to the stationary, three-dimensional vortex structures along the stagnation line induced by free-stream vorticity [19, 20]. The effects of the two, however, are curiously alike, and would certainly justify attempts to carry out a nonlinear analysis.

In this connection I would like to point out Karlsson's [21] analytical and experimental study of a flat-plate turbulent boundary layer when the free stream fluctuates sinusoidally about a constant mean. He showed that the periodic and mean motions become uncoupled (neglecting compressibilty) for small amplitude oscillations or higher amplitude oscillations at higher frequencies, i.e., nonlinearity may be neglected. In the case of the Taylor-Goertler vortices, the amplitudes and frequencies probably lie in the intermediate range where nonlinearity cannot be ignored.

Additional References

12 Bakewell, H. P., and Lumley, J. L., "Viscous Sublayer and Adjacent Wall Region in Turbulent Pipe Flow," *Phys. Fluids*, Vol. 10, No. 9, 1967, pp. 1880–1889.

13 Patel, V. C., "The Effects of Curvature on the Turbulent Boundary Layer," ARC 30427, 1968.

14 Williams, G., "Enhancement of Heat and Mass Transfer in a Stagnation Region by Free Stream Vorticity," ARL 68-0022, 1968.

15 Nachtsheim, P. R., and Swigert, P., "Satisfaction of Asymptotic Boundary Conditions in Numerical Solution of Systems of Non-Linear Equations of Boundary-Layer Type," NASA TN D-3004, 1965.

16 Kestin, J., *Advances in Heat Transfer*, Vol. 3, Academic Press, N. Y., 1966.

17 Smith, M. C., "Wake-Induced Effects Near the Forward Stagnation Point of a Circular Cylinder," *Phys. Fluids*, Vol. 11, No. 8, 1968, pp. 1618–1620.

18 Mujumdar, A. S., PhD thesis, McGill University, Montreal, 1970.

19 Brun, E. A., Diep, G. B., and Kestin, J., *J. Compt. Rend. Acad. Sci.*, Paris, Vol. 263, 1966, pp. 742–745.

20 Sadeh, W. Z., Sutera, S. P., and Maeder, P. F., Brown University, Div. of Eng. Rept. AF 1754/4, 1968.

21 Karlsson, S. K. F., *Journal of Fluid Mechanics*, Vol. 5, 1959, p. 622.

Authors' Closure

The contribution of Dr. Mujumdar is a very useful one. There appears to be a general consensus now that the non-linear mechanism of vortex stretching is necessary to explain the heat transfer effect found experimentally. The question of the similarity between Taylor-Goertler vortices and the stationary three-dimensional vortex structures along stagnation lines which occur in flow past cylinders and also past conical-shaped nose cones (in supersonic flow) is one that has yet to be resolved. There is one school of thought which considers that both effects are just pressure oscillations in the boundary layer. If this is so, then the periodic and mean motions should be decoupled. An experimental program to check this might be able to establish the difference between these two boundary-layer flows. In the Taylor-Goertler case, the periodic and mean motions are definitely coupled.

Hyperbolic Heat-Conduction Equation—A Solution for the Semi-Infinite Body Problem[1]

K. J. Baumeister[2] and T. D. Hamill.[3]

In reference [1],[4] a step change in temperature was applied to a semi-infinite medium and the following equations and boundary conditions were considered:

$$\frac{1}{C^2}\frac{\partial^2 T}{\partial t^2} + \frac{1}{\alpha}\frac{\partial T}{\partial t} = \nabla^2 T \tag{1}$$

$$\frac{\alpha}{C^2}\frac{\partial \mathbf{q}}{\partial t} + \mathbf{q} = -k\nabla \mathsf{T} \tag{2}$$

with the boundary conditions on temperature

$$T = T_0 \left.\frac{\partial T}{\partial t}\right|_{\substack{t=0\\x>0}} = 0 \quad \text{at } t = 0 \qquad x > 0 \tag{3}$$

$$T = T_w \quad \text{at} \quad z = 0 \qquad t > 0 \tag{4}$$

$$T \to T_0 \qquad x \to \infty \qquad t > 0 \tag{5}$$

In addition, the initial heat flux was assumed intuitively to be

$$q = 0 \qquad t = 0 \qquad x \geq 0 \tag{6}$$

---

[1] By K. J. Baumeister and T. D. Hamill, published in the November, 1969, issue of the JOURNAL OF HEAT TRANSFER, TRANS. ASME, Series C, Vol. 91, No. 4, pp. 543–548.

[2] Lewis Research Center, Cleveland, Ohio.

[3] McDonnell Douglas, Huntington Beach, Calif.

[4] Numbers in brackets designate References at end of article under discussion.

The authors have shown that a linear analysis is not physically realistic. In fact, the nonlinear mechanism of vortex stretching seems to be crucial to all flows near walls; the viscous sublayer is perhaps a classical example [13]. A nonlinear analysis similar to that carried out by Sutera, Kestin, and Maeder would probably explain the increased heat transfer rates. The authors may be aware of the work of Williams [14] who solved the vortex-stretching model on an IBM computer using the versatile CSMP (Continuous System Modeling Program) language. The frequently awkward time and amplitude scaling procedures are not required in this digital equivalent of an analog computer. A major problem encountered in solving boundary-value problems numerically is that of searching the right initial conditions. I have successfully used a very elegant least-squares method proposed by Nachtsheim and Swigert [15] to obtain rapid convergence in the solution of boundary-layer-type equations. The technique is relatively insensitive to the initial guess.

Secondly, I wish to suggest that the 3 percent free-stream turbulence level could enhance the heat transfer rate appreciably if a streamwise pressure gradient exists [16]. Curiously enough, it appears that the physical mechanisms responsible for the transport phenomena are basically different depending on whether or not the flow contains oscillations of a discrete frequency (e.g., Taylor-Goertler vortices) or a wideband spectrum of frequencies (e.g., turbulence). Although only remotely analogous, one may consider the observations of Smith [17] with regard to the effect on heat transfer of the wake-induced periodicity near the forward stagnation point of a circular cylinder in a turbulence-free stream. His hot-wire data indicated that the wake induced periodic fluctuations (at Strouhal frequency) of about 12 percent of the mean velocity just outside the boundary layer. Suppression of these periodic oscillations by placing a splitter-plate in the near wake did not affect the heat transfer in the stagnation region (Re $\simeq$ 50,000). My own experiments at lower Reynolds numbers (5000–10,000), however, indicated a definite effect of these oscillations (up to 15 percent), the effect being more pronounced at lower free-stream turbulence levels and lower Reynolds numbers [18]. It is not intended to suggest or imply that the Taylor-Goertler vortices are similar to the stationary, three-dimensional vortex structures along the stagnation line induced by free-stream vorticity [19, 20]. The effects of the two, however, are curiously alike, and would certainly justify attempts to carry out a nonlinear analysis.

In this connection I would like to point out Karlsson's [21] analytical and experimental study of a flat-plate turbulent boundary layer when the free stream fluctuates sinusoidally about a constant mean. He showed that the periodic and mean motions become uncoupled (neglecting compressibilty) for small amplitude oscillations or higher amplitude oscillations at higher frequencies, i.e., nonlinearity may be neglected. In the case of the Taylor-Goertler vortices, the amplitudes and frequencies probably lie in the intermediate range where nonlinearity cannot be ignored.

Additional References

12 Bakewell, H. P., and Lumley, J. L., "Viscous Sublayer and Adjacent Wall Region in Turbulent Pipe Flow," *Phys. Fluids*, Vol. 10, No. 9, 1967, pp. 1880–1889.

13 Patel, V. C., "The Effects of Curvature on the Turbulent Boundary Layer," ARC 30427, 1968.

14 Williams, G., "Enhancement of Heat and Mass Transfer in a Stagnation Region by Free Stream Vorticity," ARL 68-0022, 1968.

15 Nachtsheim, P. R., and Swigert, P., "Satisfaction of Asymptotic Boundary Conditions in Numerical Solution of Systems of Non-Linear Equations of Boundary-Layer Type," NASA TN D-3004, 1965.

16 Kestin, J., *Advances in Heat Transfer*, Vol. 3, Academic Press, N. Y., 1966.

17 Smith, M. C., "Wake-Induced Effects Near the Forward Stagnation Point of a Circular Cylinder," *Phys. Fluids*, Vol. 11, No. 8, 1968, pp. 1618–1620.

18 Mujumdar, A. S., PhD thesis, McGill University, Montreal, 1970.

19 Brun, E. A., Diep, G. B., and Kestin, J., *J. Compt. Rend. Acad. Sci.*, Paris, Vol. 263, 1966, pp. 742–745.

20 Sadeh, W. Z., Sutera, S. P., and Maeder, P. F., Brown University, Div. of Eng. Rept. AF 1754/4, 1968.

21 Karlsson, S. K. F., *Journal of Fluid Mechanics*, Vol. 5, 1959, p. 622.

Authors' Closure

The contribution of Dr. Mujumdar is a very useful one. There appears to be a general consensus now that the non-linear mechanism of vortex stretching is necessary to explain the heat transfer effect found experimentally. The question of the similarity between Taylor-Goertler vortices and the stationary three-dimensional vortex structures along stagnation lines which occur in flow past cylinders and also past conical-shaped nose cones (in supersonic flow) is one that has yet to be resolved. There is one school of thought which considers that both effects are just pressure oscillations in the boundary layer. If this is so, then the periodic and mean motions should be decoupled. An experimental program to check this might be able to establish the difference between these two boundary-layer flows. In the Taylor-Goertler case, the periodic and mean motions are definitely coupled.

Hyperbolic Heat-Conduction Equation—A Solution for the Semi-Infinite Body Problem[1]

K. J. Baumeister[2] and T. D. Hamill.[3]

In reference [1],[4] a step change in temperature was applied to a semi-infinite medium and the following equations and boundary conditions were considered:

$$\frac{1}{C^2}\frac{\partial^2 T}{\partial t^2} + \frac{1}{\alpha}\frac{\partial T}{\partial t} = \nabla^2 T \tag{1}$$

$$\frac{\alpha}{C^2}\frac{\partial \mathbf{q}}{\partial t} + \mathbf{q} = -k\nabla \mathsf{T} \tag{2}$$

with the boundary conditions on temperature

$$T = T_0 \left.\frac{\partial T}{\partial t}\right|_{\substack{t=0\\x>0}} = 0 \quad \text{at } t = 0 \qquad x > 0 \tag{3}$$

$$T = T_w \quad \text{at} \quad z = 0 \qquad t > 0 \tag{4}$$

$$T \to T_0 \qquad x \to \infty \qquad t > 0 \tag{5}$$

In addition, the initial heat flux was assumed intuitively to be

$$q = 0 \qquad t = 0 \qquad x \geq 0 \tag{6}$$

---

[1] By K. J. Baumeister and T. D. Hamill, published in the November, 1969, issue of the JOURNAL OF HEAT TRANSFER, TRANS. ASME, Series C, Vol. 91, No. 4, pp. 543–548.

[2] Lewis Research Center, Cleveland, Ohio.

[3] McDonnell Douglas, Huntington Beach, Calif.

[4] Numbers in brackets designate References at end of article under discussion.

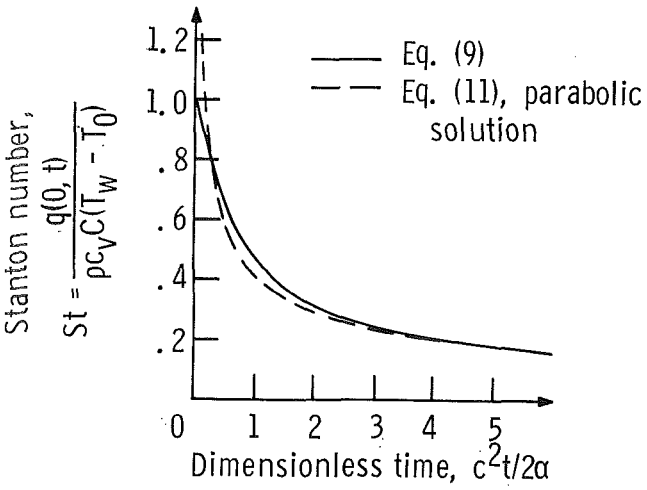

Fig. 1 Heat flux at wall as a function of time

where T is temperature, t is time, q is heat flux, C is speed of heat propagation, α is thermal diffusivity, k is thermal conductivity, and x is position.

We were interested in seeing how the effect of the second derivative of temperature and the thermal inertia term, $\frac{\alpha}{C^2}\frac{\partial q}{\partial t}$, affected the temperature and heat flux distribution. It turns out that equation (6) is an unnecessary constraint, which overspecified the problem, as will now be shown.

The general solution to equation (2) is given in reference [1] as

$$q = -\frac{C^2 k}{\alpha} e^{-C^2 t/\alpha} \int_0^t \frac{\partial T}{\partial x} e^{C^2 \xi/\alpha} d\xi \tag{7}$$

and the solution for the temperature distribution is given in reference [1] as

$$\frac{T(x,t) - T_0}{T_w - T_0} = u(Ct - x) \left\{ \exp\left(\frac{-Cx}{2\alpha}\right) + \int_{x/C}^{t} \frac{Cx}{2\alpha} \exp\left(\frac{-C^2\tau}{2\alpha}\right) \frac{I_1\left[\frac{C^2}{2\alpha}\sqrt{\tau^2 - \left(\frac{x}{C}\right)^2}\right] d\tau}{\sqrt{\tau^2 - \left(\frac{x}{C}\right)^2}} \right\} \tag{8}$$

Differentiating equation (8) and substituting the temperature gradient into equation (7) gives the heat flux as a function of x and t. The differentiation of the unit step function gives a contribution only when $x = Ct$. For the special case of x equal to zero, $q(0, t)$ is

$$\mathrm{St} = \frac{q(0,t)}{\rho C_v C(T_w - T_0)} = e^{-C^2 t/2\alpha} I_0(C^2 t/2\alpha) \tag{9}$$

in terms of a conduction Stanton number.

At t equal to zero the Stanton number equals 1; thus, the above solution predicts a unit jump in the Stanton number associated with a step change in temperature. This differs from the incorrect solution for Stanton number given in reference [1] which satisfied equation (6) and gave a value of zero. Equation (9) is shown in Fig. 1 along with the conventional parabolic solution to the same problem.

For large times, the zeroth-order term of an asymptotic expansion of I_0 is of the form

$$I_0\left(\frac{C^2 t}{2\alpha}\right) \sim \frac{\exp\left(\frac{C^2 t}{2\alpha}\right)}{\sqrt{2\pi\left(\frac{C^2 t}{2\alpha}\right)}} \tag{10}$$

thus for large times

$$\mathrm{St} = \frac{1}{\sqrt{2\pi(C^2 t/2\alpha)}} \tag{11}$$

which is the usual heat parabolic conduction solution.

Free Convection From a Two-Dimensional Finite Horizontal Plate[1]

Zeëv Rotem.[2] The author considers free convective heat transfer from a horizontal, downward-facing plate. Reference is made to previous work by Schmidt [2],[3] interpreted as demonstrating the existence of a type of stagnation-point flow below the plate, and of Suriano and Yang [3] who are reported to have shown the existence of this flow by numerical computation.

The author then applies a similarity transform which in actual fact is a boundary layer transformation.[4] The result is a set of three simultaneous ordinary differential equations. The transformation can, of course, only be used for two-dimensional flows or three-dimensional flows with rotational symmetry where a Stokes stream function may be assumed.

It has recently been pointed out [12, 13] that Schmidt's flow is not of the type stipulated by Chen; also, that Suriano and Yang's [3] solution was erroneous in principle [14], quite apart from the fact that it referred to a plate heated on *both* its sides, for values of the Grashof number for which the transformation of Chen does not apply.

Further, the proof that there is no flow of the type stipulated by Chen for free convection from underneath a horizontal plate heated and facing downward seems to be well established [15, 16]. Therefore correlations will have to be based on careful tests alone and/or on solutions of the complete equations (2) through (5) of Chen, using a numerical technique which is properly conservative [14].

Additional References

12 Rotem, Z., and Claassen, L., "Natural Convection above Unconfined Horizontal Surfaces," *Journal of Fluid Mechanics*, Vol. 38, 1969, pp. 173–192.

---

[1] By Ching-Jen Chen, published in the Aug. 1970 issue of the JOURNAL OF HEAT TRANSFER, TRANS. ASME, Series C, Vol. 92, No. 3, p. 548.

[2] Professor, University of British Columbia, Vancouver, B. C., Canada.

[3] Numbers in brackets designate References continued from original paper.

[4] When λ is finite (!). λ is a measure of plate width.

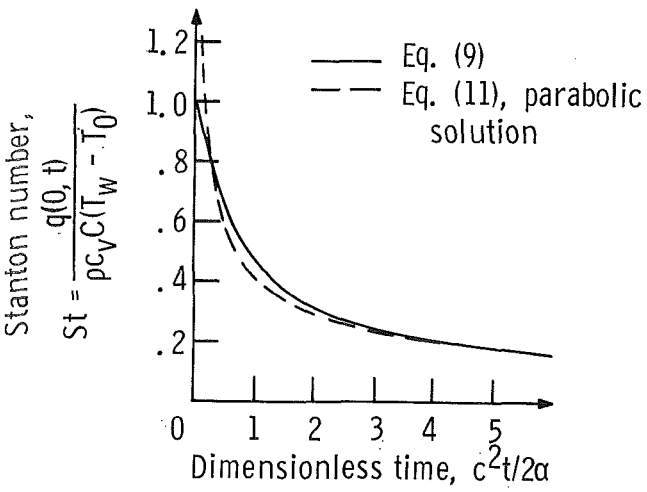

Fig. 1 Heat flux at wall as a function of time

where T is temperature, t is time, q is heat flux, C is speed of heat propagation, α is thermal diffusivity, k is thermal conductivity, and x is position.

We were interested in seeing how the effect of the second derivative of temperature and the thermal inertia term, $\frac{\alpha}{C^2}\frac{\partial q}{\partial t}$, affected the temperature and heat flux distribution. It turns out that equation (6) is an unnecessary constraint, which overspecified the problem, as will now be shown.

The general solution to equation (2) is given in reference [1] as

$$q = -\frac{C^2 k}{\alpha} e^{-C^2 t/\alpha} \int_0^t \frac{\partial T}{\partial x} e^{C^2 \xi/\alpha} d\xi \tag{7}$$

and the solution for the temperature distribution is given in reference [1] as

$$\frac{T(x,t) - T_0}{T_w - T_0} = u(Ct - x) \left\{ \exp\left(\frac{-Cx}{2\alpha}\right) + \int_{x/C}^{t} \frac{Cx}{2\alpha} \exp\left(\frac{-C^2\tau}{2\alpha}\right) \frac{I_1\left[\frac{C^2}{2\alpha}\sqrt{\tau^2 - \left(\frac{x}{C}\right)^2}\right] d\tau}{\sqrt{\tau^2 - \left(\frac{x}{C}\right)^2}} \right\} \tag{8}$$

Differentiating equation (8) and substituting the temperature gradient into equation (7) gives the heat flux as a function of x and t. The differentiation of the unit step function gives a contribution only when $x = Ct$. For the special case of x equal to zero, $q(0, t)$ is

$$\mathrm{St} = \frac{q(0,t)}{\rho C_v C(T_w - T_0)} = e^{-C^2 t/2\alpha} I_0(C^2 t/2\alpha) \tag{9}$$

in terms of a conduction Stanton number.

At t equal to zero the Stanton number equals 1; thus, the above solution predicts a unit jump in the Stanton number associated with a step change in temperature. This differs from the incorrect solution for Stanton number given in reference [1] which satisfied equation (6) and gave a value of zero. Equation (9) is shown in Fig. 1 along with the conventional parabolic solution to the same problem.

For large times, the zeroth-order term of an asymptotic expansion of I_0 is of the form

$$I_0\left(\frac{C^2 t}{2\alpha}\right) \sim \frac{\exp\left(\frac{C^2 t}{2\alpha}\right)}{\sqrt{2\pi\left(\frac{C^2 t}{2\alpha}\right)}} \tag{10}$$

thus for large times

$$\mathrm{St} = \frac{1}{\sqrt{2\pi(C^2 t/2\alpha)}} \tag{11}$$

which is the usual heat parabolic conduction solution.

Free Convection From a Two-Dimensional Finite Horizontal Plate[1]

Zeëv Rotem.[2] The author considers free convective heat transfer from a horizontal, downward-facing plate. Reference is made to previous work by Schmidt [2],[3] interpreted as demonstrating the existence of a type of stagnation-point flow below the plate, and of Suriano and Yang [3] who are reported to have shown the existence of this flow by numerical computation.

The author then applies a similarity transform which in actual fact is a boundary layer transformation.[4] The result is a set of three simultaneous ordinary differential equations. The transformation can, of course, only be used for two-dimensional flows or three-dimensional flows with rotational symmetry where a Stokes stream function may be assumed.

It has recently been pointed out [12, 13] that Schmidt's flow is not of the type stipulated by Chen; also, that Suriano and Yang's [3] solution was erroneous in principle [14], quite apart from the fact that it referred to a plate heated on *both* its sides, for values of the Grashof number for which the transformation of Chen does not apply.

Further, the proof that there is no flow of the type stipulated by Chen for free convection from underneath a horizontal plate heated and facing downward seems to be well established [15, 16]. Therefore correlations will have to be based on careful tests alone and/or on solutions of the complete equations (2) through (5) of Chen, using a numerical technique which is properly conservative [14].

Additional References

12 Rotem, Z., and Claassen, L., "Natural Convection above Unconfined Horizontal Surfaces," *Journal of Fluid Mechanics*, Vol. 38, 1969, pp. 173–192.

---

[1] By Ching-Jen Chen, published in the Aug. 1970 issue of the JOURNAL OF HEAT TRANSFER, TRANS. ASME, Series C, Vol. 92, No. 3, p. 548.

[2] Professor, University of British Columbia, Vancouver, B. C., Canada.

[3] Numbers in brackets designate References continued from original paper.

[4] When λ is finite (!). λ is a measure of plate width.

13 Rotem, Z., and Claassen, L., "Free Convection Boundary-Layer Flow Over Horizontal Plates and Discs," *Canadian Journal of Chemical Engineering*, Vol. 47, 1969, pp. 461–468.
14 Panton, R., "Laminar Free Convection along a Vertical Plate at Extremely Small Grashof Numbers," *International Journal of Heat and Mass Transfer*, Vol. 11, 1968, pp. 615–616.
15 Gill, W. N., Zeh, D. W., and Del-Casal, E., "Free Convection on a Horizontal Plate," *Z.A.M.P.*, Vol. 16, 1965, pp. 539–541.
16 Rotem, Z., "Free Convection from Heated, Horizontal Downward-Facing Plates," *Z.A.M.P.*, Vol. 21, 1970, pp. 472–475.

Author's Closure

To discuss Professor Rotem's comments we recognize the following points:

1 The theoretical solution obtained in my case is for a finite, horizontal plate (i.e., a plate with two edges) heated facing downward or cooled facing upward, while the case solved by Rotem and Claassen [12, 13, 16] or the proof of Gill, Zeh, and Del-Casal [15] are for a semi-infinite plate (i.e., a plate with one edge). We must be very careful in applying the semi-infinite plate solution to a finite, horizontal plate since the existence of continuous flow at $X \to \infty$ now must be stipulated at the midpoint of the finite plate. For a heated finite plate facing upward the lighter fluid at the midpoint may move upward to give a flow that approximates the condition at $X \to \infty$. However, for a heated finite plate facing downward, the lighter fluid at the midpoint will be stagnated near the wall and remain there because the heavier fluid is below it. Therefore, the semi-infinite plate solution does not apply to the heated (or cooled) finite plate facing downward (or upward).

2 Experimentally, for a heated, finite plate facing downward to exhibit a stagnation point flow was well demonstrated by Kraus' direct measurement of the flow direction (see Figs. 22 and 23 of [1]). Consider Fig. 12 of Schmidt [2]. If the air near the midpoint were to move down on the underside of the plate the photo would not show smooth isothermal lines near it. Furthermore, a stagnation-point flow for a heated, finite plate facing downward was made visually by Singh and Birkebak.[5] Note that $\lambda \simeq 2.5$ is also applicable in Singh and Birkebak's photo.

3 I agree with Panton's [14] comment on the work of Suriano and Yang [3] that to treat an infinite domain by a finite domain will introduce errors in numerical values because of the uncertainty in the temperature gradient at the wall. In fact, I was unable to plot Suriano and Yang's [3] data in my Fig. 3.

[5] See Fig. 4, *Z. angew. Math. Phys.*, Vol. 20, 1969, p. 454.

ERRATA

Frank Kreith, "Thermal Design of High-Altitude Balloons and Instrument Packages," published in the August, 1970, issue of the JOURNAL OF HEAT TRANSFER, TRANS. ASME, Series C, Vol. 92, No. 3, pp. 307–332.

On page 329 immediately preceding the section "Summary" the following paragraph should be inserted:

The thermal analysis presented in this paper was modified as shown in reference [97] to design and test two balloon-borne instrument packages. A test flight was made by NCAR on April 24, 1968, with a 30,000-cu-ft balloon to an altitude of 70,000 ft, carrying two simulated instrument packages with different coatings. The instrument packages are shown schematically in Fig. 26 with the left side of the platform covered with aluminum foil and the right side covered with a mylar-aluminum laminate. On both sides, the temperatures at the top and the bottom surface of the styrofoam body were measured by means of thermistors. The results of these tests are described in detail in reference [97], and Fig. 27 presents a summary of the temperature versus time history of the balloon package at float. The greatest sources of uncertainty in predicting the temperatures were the values for the absorptances and emittances of the aluminum foil and mylar-aluminum laminate covering the surfaces. Within the uncertainty introduced by the lack of precision with which these properties were known, the temperature measurements obtained in this experimental flight agreed with the analytically predicted results.